CENTRO INTERNACIONAL DE ESTUDOS
DE DOUTORAMENTO E AVANZADOS
DA USC (CIEDUS)

TESE DE DOUTORAMENTO

JET QUENCHING AND HEAVY ION COLLISIONS

Víctor Vila Pérez

ESCOLA DE DOUTORAMENTO INTERNACIONAL

PROGRAMA OFICIAL DE DOUTORAMENTO EN FÍSICA NUCLEAR E DE PARTÍCULAS

SANTIAGO DE COMPOSTELA

2020

USC
UNIVERSIDADE
DE SANTIAGO
DE COMPOSTELA

DECLARACIÓN DO AUTOR DA TESE

[JET QUENCHING AND HEAVY ION COLLISIONS]

Para defensas telemáticas

D. Víctor Vila Pérez

Presento a miña tese, seguindo o procedemento axeitado ao Regulamento, e declaro que:

1) A tese abarca os resultados da elaboración do meu traballo.
2) De selo caso, na tese faise referencia ás colaboracións que tivo este traballo.
3) A tese é a versión definitiva presentada para a súa defensa e coincide coa versión enviada en formato electrónico.
4) Confirmo que a tese non incorre en ningún tipo de plaxio doutros autores nin de traballos presentados por min para a obtención doutros títulos.

E comprométome a presentar o exemplar impreso da tese no prazo dun mes dende que a EDIUS mo requira, así como o Compromiso Documental de Supervisión no caso de que o orixinal non estea na Escola.

En Santiago de Compostela, a 10 de Xullo de 2020

Asdo. Víctor Vila Pérez

USC
UNIVERSIDADE
DE SANTIAGO
DE COMPOSTELA

AUTORIZACIÓN DO DIRECTOR / TITOR DA TESE

[JET QUENCHING AND HEAVY ION COLLISIONS]

D. Carlos A. Salgado López

INFORMA:

Que a presente tese, correspóndese co traballo realizado por D. Víctor Vila Pérez, *baixo a miña dirección, e autorizo a súa presentación, considerando que reúne os requisitos esixidos no Regulamento de Estudos de Doutoramento da USC, e que como director desta non incorre nas causas de abstención establecidas na Lei 40/2015.*

En Santiago de Compostela, a 10 de Xullo de 2020

Asdo. Carlos A. Salgado López

USC
UNIVERSIDADE
DE SANTIAGO
DE COMPOSTELA

A mis padres, mi hermano y mis abuelos.

USC
UNIVERSIDADE
DE SANTIAGO
DE COMPOSTELA

Agradecimientos

En primer lugar, quiero expresar mi profundo agradecimiento a Carlos Salgado, por dirigir mis trabajos desde las etapas previas a esta tesis doctoral hasta la conclusión de la misma, dándome así la oportunidad de poder aprender de él en el día a día desde un trato personal muy cercano y de confianza. Su dedicación a la Física por encima de todas sus responsabilidades ha sido una gran inspiración, y su sabiduría y gran intuición una fuente constante de aprendizaje durante todos estos años. Gracias por todo.

Sería injusto no dedicar unas líneas de agradecimiento al resto de personas que codirigieron los proyectos que componen este manuscrito. A Konrad Tywoniuk, con el que tuve la oportunidad de trabajar desde mi estancia en el CERN. Su pasión y ambición inagotables, sus grandes conocimientos y su buena metodología han sido un estímulo motivacional muy fuerte. A Fabio Domínguez, supervisor de mis estudios durante la mayor parte de esta tesis doctoral, por su disposición a discutir y proponer soluciones ingeniosas a los problemas en los que trabajamos juntos. Y a Cyrille Marquet, por recibirme en la École Polytechnique de París e iniciarme en un ámbito de estudio prácticamente nuevo para mí aportando todo su conocimiento. Por encima de todo les agradezco su sencillez y naturalidad en el trato. Quiero dar las gracias también al resto de personas con las que he colaborado o que han aportado su grano de arena a esta tesis doctoral a través de discusiones fructíferas, como Guilherme Milhano, João Barata, Anderson Kendi o Néstor Armesto, entre otros.

A mis amigos de toda la vida, con los que llegué a Santiago de Compostela hace ya una década, y a todas las personas que desde entonces han formado parte de mi día a día. No habría sido lo mismo sin todas ellas. Tampoco sería justo no destinar una línea a mencionar otra de mis pasiones, el tenis, incluyendo el entorno de gente tan saludable que rodea a este deporte, ya que creo que indirectamente me ha ayudado a ordenar y aclarar muchas ideas en la cabeza.

Por último, es difícil encontrar las palabras adecuadas para agradecer a mis padres y a mi hermano su apoyo en cada una de las decisiones que me han llevado hasta este punto. Siempre preocupados porque disponga de la atmósfera adecuada para centrarme en mis propios intereses sin pedir nada a cambio, sobra decir que esta tesis doctoral no sería posible ni tendría sentido sin ellos a mi lado. No me olvido de mis abuelos, siempre pendientes de mis actividades con esa curiosidad que les caracteriza. Gracias de corazón.

I acknowledge the financial support given by the European Research Council under the projects HotLHC ERC-2011-StG-279579 and YoctoLHC ERC-2018-ADG-835105, Xunta de Galicia (Consellería de Educación) under the fellowship ED481A-2017/089 and Ministerio de Educación, Cultura y Deporte under the fellowship FPU16/02236.

USC
UNIVERSIDADE
DE SANTIAGO
DE COMPOSTELA

Abstract

The study of heavy-ion collisions (HICs) at very high colliding energies has dramatically changed the big picture of the theory of strong interactions under extreme conditions of temperature and density, the so-called hot and dense Quantum Chromodynamics (QCD). Heavy-ion physics ranges from a bath of strongly interacting gluons at lower energy scales to highly energetic quarks and gluons ruled by QCD in its perturbative regime (pQCD). These gluons quickly thermalize and form a state of strongly interacting matter in which quarks and gluons are no longer confined within hadrons and become free to traverse this soup – the widely-known Quark-Gluon Plasma (QGP), so that they end up in a cascade of particles known as jets. This thesis is intended to shed light on the underlying mechanisms responsible for jet energy loss and medium response to jet propagation as well. During jet evolution through QCD deconfined matter, the multiple scattering interaction of partons with the medium results into the modification of their dynamics, leading to parton energy loss, commonly referred to as jet quenching. This manuscript also provides insight on the phenomenon of color coherence in multi-gluon radiation for a plethora of parton branching processes and its effects on multi-jet final states, which plays a central role in the description of the *quenched* jets. Finally, although this thesis is aimed primarily at looking into final state effects such as the abovementioned, with regard to initial state effects an analysis of angular correlations between gluons produced in high energy hadronic collisions within the Color Glass Condensate framework (CGC) is performed as well.

Keywords: HICs, pQCD, QGP, jet quenching, CGC.

USC
UNIVERSIDADE
DE SANTIAGO
DE COMPOSTELA

Víctor Vila Pérez

Resumen

El estudio de colisiones de iones pesados (HICs) a energías de colisión muy altas ha cambiado radicalmente el panorama de la teoría de las interacciones fuertes bajo condiciones extremas de temperatura y densidad, la llamada Cromodinámica Cuántica (QCD) caliente y densa. La física de iones pesados se extiende desde un baño de gluones fuertemente interactuantes a escalas de energía más bajas hasta quarks y gluones altamente energéticos gobernados por la QCD en su régimen perturbativo (pQCD). Estos gluones termalizan rápidamente y forman un estado de materia fuertemente interactuante en la que los quarks y los gluones ya no están confinados dentro de los hadrones y se vuelven libres para atravesar esta sopa – muy conocida como Plasma de Quarks y Gluones (QGP), de forma que acaban en una cascada de partículas conocidas como *jets*. Esta tesis está destinada a arrojar luz sobre los mecanismos subyacentes responsables de la pérdida de energía de los *jets* y también de la respuesta del medio a la propagación de los mismos. Durante la evolución de los *jets* a través de la materia QCD deconfinada, la interacción por dispersión múltiple de los partones con el medio resulta en la modificación de sus dinámicas, llevando a la pérdida de energía de los partones, comúnmente conocida como *jet quenching*. Este manuscrito también profundiza en el fenómeno de coherencia de color en la radiación múltiple de gluones para una plétora de procesos de *branching* de partones y sus efectos en estados finales de multi-*jets*, que juega un papel central en la descripción de los *quenched jets*. Finalmente, aunque esta tesis está dirigida principalmente a investigar efectos de estado final como los mencionados anteriormente, en lo relativo a efectos de estado inicial también se realiza un análisis de correlaciones angulares entre gluones producidos en colisiones hadrónicas de altas energías en el marco *Color Glass Condensate* (CGC).

Palabras clave: HICs, pQCD, QGP, *jet quenching*, CGC.

USC
UNIVERSIDADE
DE SANTIAGO
DE COMPOSTELA

Resumo

O estudo de colisións de ións pesados (HICs) a enerxías de colisión moi altas cambiou radicalmente o panorama da teoría das interaccións fortes baixo condicións extremas de temperatura e densidade, a chamada Cromodinámica Cuántica (QCD) quente e densa. A física de ións pesados esténdese desde un baño de gluóns fortemente interactuantes a escalas de enerxía máis baixas ata quarks e gluóns altamente enerxéticos gobernados pola QCD no seu réxime perturbativo (pQCD). Estes gluóns termalizan rapidamente e forman un estado de materia fortemente interactuante na que os quarks e os gluóns xa non están confinados dentro dos hadróns e vólvense libres para atravesar esta sopa – moi coñecida como Plasma de Quarks e Gluóns (QGP), de forma que acaban nunha fervenza de partículas coñecidas como *jets*. Esta tese está destinada a arroxar luz sobre os mecanismos subxacentes responsables da perda de enerxía dos *jets* e tamén da resposta do medio á propagación dos mesmos. Durante a evolución dos *jets* a través da materia QCD deconfinada, a interacción por dispersión múltiple dos partóns co medio resulta na modificación das súas dinámicas, levando á perda de enerxía dos partóns, comunmente coñecida como *jet quenching*. Este manuscrito tamén profundiza no fenómeno de coherencia de cor na radiación múltiple de gluóns para unha plétora de procesos de *branching* de partóns e os seus efectos en estados finais de multi-*jets*, que xoga un papel central na descrición dos *quenched jets*. Finalmente, aínda que esta tese está dirixida principalmente a investigar efectos de estado final como os mencionados anteriormente, no relativo a efectos de estado inicial tamén se realiza unha análise de correlacións angulares entre gluóns producidos en colisións hadrónicas de altas enerxías no marco *Color Glass Condensate* (CGC).

Palabras chave: HICs, pQCD, QGP, *jet quenching*, CGC.

USC
UNIVERSIDADE
DE SANTIAGO
DE COMPOSTELA

Contents

List of Figures

USC
UNIVERSIDADE
DE SANTIAGO
DE COMPOSTELA

Motivation

There is a growing interest and knowledge in *heavy-ion collisions* (HICs) since it gave a completely new way of understanding the successful theory of strong interactions under conditions that become more and more extreme, the hot and dense *Quantum Chromodynamics* (QCD). This theory underwent numerous tests in particle accelerators over more than 40 years regarding the behaviour of hadrons in vacuum. More recently, strong interactions have started to be probed in a medium as well, reaching critical values of temperature and density which bring us to an energy scale that favours the deconfinement of quarks and gluons. These conditions make way to the formation of the so-called *Quark-Gluon Plasma* (QGP), a new state of matter that can behave in unexpected ways due to collective effects.

According to the current description of the evolution of the early universe, the *Big Bang* theory, $10^{-5}s$ after the explosion a soup of QGP went through a phase transition to confined hadrons, the first hint of a QCD transition. Deepening and broadening knowledge on this transition involves studying the inner structure of matter under extreme conditions of temperature and density. From a theoretical perspective, the overriding challenge is to achieve a robust formulation of in-medium quantum field theory using QCD. However, the theory is non-perturbative at the relevant scales, thus constraining analytic methods. One way to make progress in the knowledge of its properties is to address the QGP as an almost perfect liquid whose ingredients interact strongly.

An intense activity of research is being carried out in this respect. In fact, exploring the plasma has long been established as one of the main aims of the Relativistic Heavy Ion Collider (RHIC) at Brookhaven National Laboratory (BNL) and the Large Hadron Collider (LHC) program at the Conseil Européen pour la Recherche Nucléaire (CERN). In order to characterize this novel phase of matter under laboratory conditions, various probes are handled in HICs. *Hard probes* (HP) are created in the early stages of the collision after hard scattering processes and are therefore key probes for infering the medium properties by means of quantifying their modifications. *Jets* are natural hard probes: due to the hard scale of these high-transverse momentum sprays of collimated particles, the production cross-sections can be addressed purely within the perturbative domain of QCD (pQCD). While jets propagate throughout the deconfined QCD medium, the multiple scattering interaction of the hard partons that make them up with the medium constituents results into the modification of their dynamics and leads to parton energy loss, commonly referred to as *jet quenching*.

The successes of jet quenching testify to the drawing power of hard probes when describing the QGP. The measurement of the di-jet asymmetry at the LHC was one of the clearest experimental evidences of this suppression, which is expected to be enhanced with the medium temperature and the path length of the parton within the medium.

With the final goal of establishing a fully comprehensive theoretical framework behind experimental observations, one of the proposed ideas was that this suppression is due to the partonic energy loss in the QCD matter formed in the collisions. Despite the fact that several approaches try to provide a complete understanding of jet propagation in matter, much still remains to be done in order to accomplish a deeper understanding of the underlying mechanisms responsible for in-medium jet interactions.

Generally speaking, this thesis aims precisely to shed light on the mechanisms responsible for jet quenching and medium response to jet propagation as well.

One of the key sources responsible for the modifications suffered by an energetic jet as a result of its interaction with the medium ingredients is *medium-induced radiation*, which can be computed in the framework of different general approaches within pQCD as the BDMPS-Z/ ASW formalism, GLV or AMY, among others. These approaches are nothing more than the generalization of the Landau-Pomeranchuk-Migdal (LPM) effect to pQCD. Moreover, jet quenching Monte Carlo (MC) generators happened to be extremely effective tools toward a better linking between theoretical implementations and experiments.

Due to their perturbative calculability, high-transfer momentum processes are computed from first principles in the absence of medium effects. In the presence of a medium the formulation is not so different, which motivates one to make use of jet substructure techniques to provide further details on the interplay between essential qualitative features as energy loss, medium-induced radiation and *color coherence*. In fact, one of the basic aspects of the parton shower process is color coherence in multi-parton splittings, a central challenge present in the current status of the theory and phenomenology of jet evolution and radiative processes in matter. Many attemps to make progress in this respect have been actively addresed in the last few years, but only considering a frozen configuration for the emitters. In this context, a number of works on the quark-antiquark *antenna* radiation set up a relevant insight on the description of partonic in-medium propagation. In particular, they have highlighted the importance of interference effects when addressing jet showering inside the medium. The notion of loss of memory of color connections due to color screening between the parent partons and the offspring is proven by introducing decoherence in a dense medium, which results in independent radiation off the emitters.

The main body of this manuscript gives a wider and novel insight into the phenomenon of color coherence in multi-gluon radiation for different parton branching processes and its effects on multi-jet final states by putting forward an extension of previous derivations performed in this context, which plays a central role in the description of the *quenched* jets. Handling multiple emissions configurations hinder the discussions since interferences among different processes might become important.

In the vacuum shower color is preserved, what leads to angular ordering. However, when considering an in-medium partonic setup, motivated by medium-induced gluon radiation, interference patterns might gradually alter the color coherence of the system over a time scale known as the decoherence time, which governs the decoherence regime. As will be shown later, it follows that in this regime the antennas experience a prompt color decorrelation as they travel over the medium, thus loosing memory of their origin.

As stated above, this thesis is primarily intended to look into the final state picture of HICs via the study of effects such as the abovementioned. However, initial stages have also their place in this work. The relation between the two types of effects concerning the collisions is discussed before anything else.

The understanding of the structure of the wave functions of the colliding nuclei is of paramount importance, typically encoded in their nuclear *parton distribution functions* (nPDFs), which characterize the partonic structure and dynamics of the nuclei. At high energies, nuclei do not behave as a mere incoherent superposition of their constituents. Instead, coherence effects become important. Not only do they modify their partonic content, but also the underlying dynamics of particle production in scattering processes. PDFs (nPDFs) are not computable within the perturbative approach since they carry a long distance (low energy) part of the cross-section. They are usually fitted from experimental data. There is thus a distinction between such *initial state* effects (IS), which are a prelude to thermalization, from those giving rise to the presence of a QGP, the *final state* effects (FS). Stressing the difference between both is of vital importance for an appropriate characterization of the matter produced in HICs, as sometimes they may lead to qualitative similar phenomena with regard to interesting observables.

Another important subject line is the analysis of those collective phenomena framed in the context of the *Color Glass Condensate* effective theory (CGC), which is currently the most universally accepted approach to describe *small Bjorken-x* degrees of freedom. It incorporates non-linear recombination effects both at the level of particle production and also in the quantum evolution of hadronic wave functions. Hence, disentangling CGC from other effects demands the analysis of more exclusive observables. One of the first and captivating observations in this respect was the finding of long-range two-particle correlations in *pp* collisions at the LHC. Similar correlations had been noticed before at RHIC. An accepted explanation for the observed events is related to collective flow in QGP. Nonetheless, this is still an open question. The long-range rapidity correlations may not be linked to the origin of the QGP as they spread out over a very large rapidity interval, concluding that they may originate at very early stage of the collision. In support of this view, as a final piece of this thesis an analysis of angular correlations between gluons produced in high-energy hadronic collisions within the CGC is performed as well, proving that the emitted gluons are necessarily correlated both in rapidity and the emission angle.

The thesis is organized as follows: Section 1 is intended to contextualize the current work by means of giving a broad insight into the theory and phenomenology of QCD. In Section 2 a formal description of the general formalism framework for describing highly energetic particles propagating in matter is presented. Background on both jet quenching and CGC theoretical tools and methods is provided in this chapter too, notably by focusing the attention on the different techniques required for performing the derivations carried out in the main body of this manuscript. Three different studies are developed within the jet quenching sector. Both the first and the second provide support to the jet quenching picture towards understanding parton shower evolution at all stages. Since they pose a generalization of previous studies of the problem of color coherence in parton radiation, earlier results are restored when setting the appropriate limits. The third one presents a first attempt at introducing color coherence effects into the evolution equation for medium-induced probabilistic branchings, implicitly encapsulating the implementation of the spectrum for the undertaken branching scenario. The forthcoming section is aimed at deciphering the origin of the correlations arising between produced particles at high energies. The calculations conducted in this chapter lie within the CGC effective theory work context. Albeit it is assumed a simple picture for the origin of the correlations, they are to be expected on very general grounds. Lastly, a summary of the main lines of discussion wraps up this thesis.

1

Introduction

This chapter is devoted to contextualize the core content of this thesis by touching upon the highlights which will be of crucial importance for building up the successive chapters. Even though it covers a great deal of the basics of theory and phenomenology of QCD, this section is not in itself sufficient so as to achieve a detailed picture of QCD. For this kind of review, references such as [1–6] should lead readers to a somewhat deeper level.

More specifically, after a short introduction on the very early days of the theory of strong interactions, both its gauge structure and central features are discussed. General points regarding QCD at high temperature and density are addressed as well. While not entering into too much detail on the partonic energy loss picture since a more involved development is undergone in subsequent chapters, a few guidelines concerning jet quenching in the Quark-Gluon Plasma and on the Color Glass Condensate effective theory are also presented.

1.1 Basics of QCD

QCD is the theory that accounts for the strong interactions and, more particularly, the interaction between the quarks which ultimately build up all the particles that strongly interact, hadrons, whether as mesons where a quark and an antiquark interact, $q\bar{q}$, or baryons where three quarks interact with each other, qqq.

The interaction between quarks is effected through the exchange of gluons, which are the bearers of a further new quantum number, the color. Color was first introduced by Greenberg precisely to restore the Pauli Principle: since quarks are 1/2 spin particles, two of the same type could not have the same quantum numbers. However, there are in fact three baryons, Δ^{++}, Δ^{-} and Ω^{-}, composed by three quarks, uuu, ddd, and sss respectively. Thus, it is necessary to associate a new quantum number to each quark, the color, so that each quark has three different possible values. Han and Nambu introduced it on an dynamical basis, and later, this group and two others independently (D. Gross and F. Wilczek in Princeton, and D. Politzer in Harvard – [7] and [8], respectively) showed that the interaction between quarks and gluons vanishes over short distances, explaining why quarks are behaving as nearly free inside the proton, as revealed by Stanford data regarding electron-proton deep-inelastic scattering (DIS). This phenomenon has been of major importance and is termed asymptotic freedom. It enabled H. Fritzsch, M. Gell-Mann and H. Leutwyler to deliver the QCD Lagrangian in 1973 [9].

1.2 The QCD Lagrangian

The Lagrangian describing Quantum Electrodynamics (QED) can be inferred by imposing a certain symmetry, called gauge invariance, to the Lagrangian for a free particle. Indeed, the Lagrangian

$$\mathcal{L} = \bar{\psi}(i\gamma^{\mu}\partial_{\mu} - m)\psi \tag{1.1}$$

describes the field ψ of a free electron, where γ^{μ} are the Dirac matrices that satisfy the anticommutator

$$\{\gamma^{\mu}, \gamma^{\nu}\} = 2g^{\mu\nu}, \tag{1.2}$$

with $g^{\mu\nu}$ the metric tensor. Gauge invariance of such Lagrangian is preserved under the transformations

$$\begin{aligned} \psi \rightarrow \psi' &= \exp[iq\alpha(x)]\psi, \\ \bar{\psi} \rightarrow \bar{\psi}' &= \exp[-iq\alpha(x)]\bar{\psi}, \end{aligned} \tag{1.3}$$

where $\alpha(x)$ is a function and q the charge associated to the quark. By introducing now the photon vector field $A_{\mu}(x)$, which transforms under the gauge transformation as

$$A_{\mu} \rightarrow A'_{\mu} = A_{\mu} - \partial_{\mu}\alpha(x), \tag{1.4}$$

and replacing in eq. (1.1) the ∂_{μ} derivative by the covariant derivative

$$D_{\mu} = \partial_{\mu} + iqA_{\mu}, \tag{1.5}$$

the new Lagrangian reads

$$\mathcal{L}_{\text{QED}} = \bar{\psi}(i\gamma^\mu D_\mu - m)\psi = i\bar{\psi}\gamma^\mu\partial_\mu\psi - m\bar{\psi}\psi - q\bar{\psi}\gamma^\mu A_\mu\psi. \tag{1.6}$$

It is gauge invariant and clearly contains the free Lagrangian $\mathcal{L}_0$ plus an interaction,

$$\mathcal{L}_{\text{QED}} = \mathcal{L}_0 - j^\mu A_\mu,\ j^\mu = q\bar{\psi}\gamma^\mu\psi. \tag{1.7}$$

It should therefore be borne in mind that the gauge symmetry determines the interaction. In order to get the entire QED Lagrangian, the term describing the free electromagnetic field needs to be added,

$$-\frac{1}{4}F^{\mu\nu}F_{\mu\nu},\ F_{\mu\nu} = \partial_\mu A_\nu - \partial_\nu A_\mu. \tag{1.8}$$

It is worth noting that if the photon had mass, the term $\frac{1}{2}m_\gamma^2 A^\mu A_\mu$, which is not gauge invariant, should be added, meaning that the gauge invariance implies $m_\gamma = 0$.

QCD is formulated as a gauge theory in analogy with QED: quarks correspond to electrons, gluons to photons and color to electric charge. The sole but key difference is that the underlying group is the non-abelian $SU(3)$ color group, in which appears eight functions $\alpha_a(x)$, $a = 1, 2, ..., 8$, and eight gauge fields G_μ^a corresponding to the eight gluons – as in the case of QCD the constituents come in three different colors, $N_c = 3$. Conversely, QED displays $U(1)$ symmetry, what does that on the gauge transformations (1.3) and (1.4) both the function $\alpha(x)$ and only one gauge field $A_\mu(x)$ show up.

Proceeding in the same way as QED, the free quark Lagrangian reads

$$\mathcal{L} = \sum_q \bar{\psi}_q^j i\gamma^\mu\partial_\mu\psi_q^k - \sum_q m_q\bar{\psi}_q^j\psi_q^j, \tag{1.9}$$

where the indices j, k indicate the color, $j, k = 1, 2, 3$, and $q = u, d, c, s, t, b$ the quark flavor. For the sake of simplicity, only one quark flavor is written down and the color index is omitted as well.

The gauge transformation for the quark fields is given by

$$\psi_q(x) \to \psi'(x) = \exp[ig_s\alpha_a(x)T_a]\psi_q(x), \tag{1.10}$$

where g_s is the strong interaction coupling constant, and T_a are 3×3 null trace matrices, generators of the SU(3) group that satisfy

$$[T^a, T^b] = if_{abc}T_c, \tag{1.11}$$

where f_{abc} are the structure constants of the group. In the interest of guaranteeing the gauge invariance, eight gauge fields must be introduced, the gluon fields, which transform as

$$G_\mu^a \to G_\mu^{a'} = G_\mu^a - \partial_\mu \alpha_a(x) - g_s f_{abc} \alpha_b(x) G_\mu^c, \tag{1.12}$$

and by replacing now in eq. (1.9) ∂_μ by the covariant derivative D_μ,

$$D_\mu = \partial_\mu + i g_s T_a G_\mu^a, \tag{1.13}$$

the Lagrangian has the form

$$\mathcal{L}_{\text{QCD}} = \bar{\psi}_q i\gamma^\mu D_\mu \psi_q - m_q \bar{\psi}_q \psi_q = \bar{\psi}_q i\gamma^\mu \partial_\mu \psi_q - g_s \bar{\psi}_q i\gamma^\mu \psi_q T^a G_\mu^a - m_q \bar{\psi}_q \psi_q, \tag{1.14}$$

to which eventually the following term has to be added,

$$-\frac{1}{4} F_a^{\mu\nu} F_{\mu\nu}^a, \;\; F_{\mu\nu}^a = \partial_\mu G_\nu^a - \partial_\nu G_\mu^a - g_s f_{abc} G_\mu^b G_\nu^c. \tag{1.15}$$

In the preceding equation, the extra term compared to the QED one (1.8) comes from the additional piece appearing on the transformation of the gluon field G_μ^a in (1.12) compared to that of the photon A_μ in (1.4). This further term is necessary so that the Lagrangian is invariant since, being the symmetry non-abelian, an extra piece emerges when introducing (1.10) in eq. (1.9). Looking at the interaction, it is important to emphasize that besides the quark-antiquark-gluon vertex, analogous to the fermion-antifermion-photon coupling, according to (1.15), the possibility of coupling between gauge fields themselves does exist too, as shown in Fig. 1.1 via the three- and four-gluon vertices. The latter two possibilities present in the QCD context make a vital difference in contrast to what occurs in QED, the key to understand their different behaviours in both theories: gluons radiate too, which stems from the non-abelian behaviour of the SU(3) symmetry group of QCD.

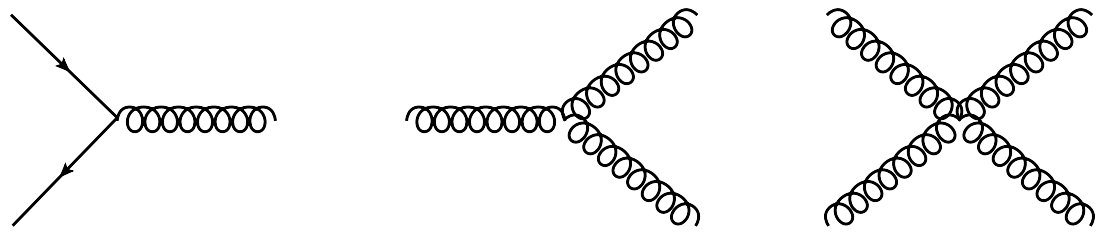

Figure 1.1: The basic interaction vertices in QCD.

1.3 Asymptotic freedom

In QCD, unlike what occurs with photons, gluons themselves carry the color charge of the strong interactions and can therefore interact between them. Consequently, diagrams of the type of Fig. 1.2(c) – in which gluons recombine among themselves to form a gluon – have to be added to those depicted in Figs. 1.2(a) and 1.2(b) – similar to the existing ones in QED. The contribution of the diagram 1.2(c) has the opposite sign to the 1.2(b) one in such a way that, given a small value for the coupling at a specific energy scale Q^2 – the renormalization scale μ^2, the behaviour of the coupling constant $\alpha_s = g_s^2/4\pi$ at a different scale reads

$$\alpha_s(Q^2) = \frac{\alpha_s(\mu^2)}{1 + \frac{\alpha_s(\mu^2)}{12\pi}(11N_c - 2n_f)\ln(Q^2/\mu^2)}, \tag{1.16}$$

provided that the coupling does not get too large, as in such a case it would not be possible to use perturbative techniques. As $(11N_c - 2n_f)$ is positive – the number of colors is $N_c = 3$ and the number of flavors $n_f = 6$, in the limit of small distances (high energies) it is verified that $\alpha_s(Q^2) \to 0$, meaning that there is no interaction, a phenomenon known as asymptotic freedom. This behaviour is illustrated in Fig. 1.3.

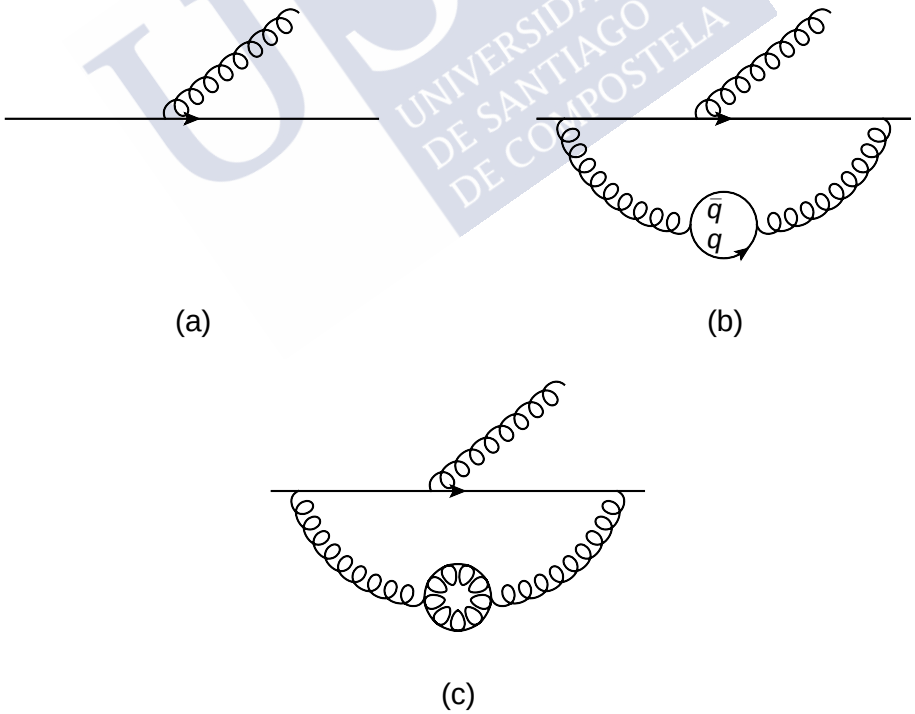

Figure 1.2: Charge renormalization in QCD.

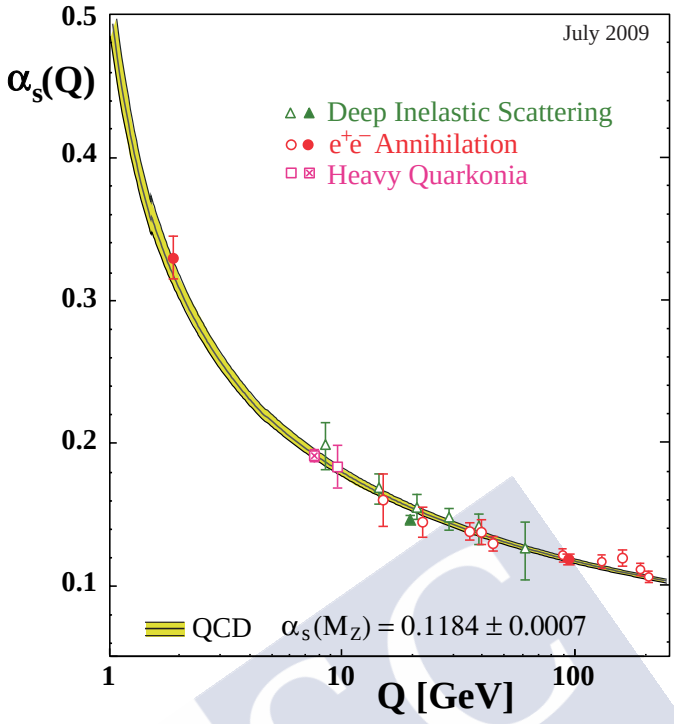

Figure 1.3: A compilation of data regarding the behaviour of the strong coupling constant α_s with the momentum $Q \propto 1/r$ (taken from [11]).

Asymptotic freedom is in addition the basic principle behind jet formation. The process $e^+e^- \rightarrow$ hadrons takes place via the diagram pictured in Fig. 1.4, where the intermediate photon produces a quark-antiquark pair. When these partons pull away, they neutralize their color via gluon radiation which, in turn, will produce more gluons and $q\bar{q}$ pairs, recombining amongst themselves to result in the hadrons that are measured in the final state. These hadrons are not uniformly distributed in all possible directions but instead they are mostly clustered in two directions, forming two jets of collimated hadrons. The demonstration of the existence of jets is credited to G. Sterman and S. Weinberg [12]. Today, jet physics is a topic of great interest given both its importance for QCD studies and Beyond the Standard Model physics searches.

1.4 Confinement

Quarks and gluons, the Lagrangian fields of QCD, in contrast to what occurs in other gauge field theories, are not observed in free states – at least at normal temperature and pressure – but that they are caught up within hadrons. This is referred to as confinement.

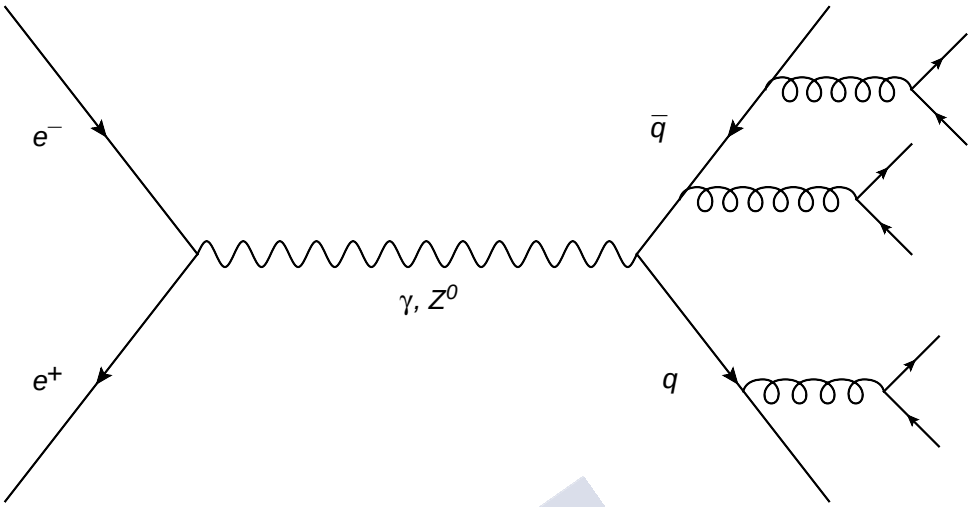

Figure 1.4: Hadron production from e^+e^- collisions.

Though this central feature of the theory of strong interactions has so far not been proven from an analytical point of view, there exist numerical lattice calculations which enable to reproduce some of its consequences, namely the hadron masses [13].

1.5 Lepton-hadron deep-inelastic scattering (DIS)

The evidence of the existence of quarks and gluons as elemental constituents of matter precedes the formulation of QCD and has its roots in the lepton-hadron collision experiments where the outgoing lepton is detected at large angles. These experiments involve a highly virtual photon exchange and are called deep-inelastic scattering experiments (DIS), pictured in Fig. 1.5. The total cross-section can be written in terms of two Lorentz invariant quantities known as structure functions, F_1 and F_2.

These functions depend on two variables, currently chosen as

$$Q^2 = -q^2 > 0,\ x = Q^2/(2p \cdot q). \tag{1.17}$$

Both functions were first measured in the late 1960s, resulting into a couple of substantial findings. Amongst other important relations,

$$F_1(x, Q^2) = F_1(x),\ F_2(x, Q^2) = F_2(x), \tag{1.18}$$

that is to say, the structure functions only depend on x, the so-called Bjorken scaling [14], and

$$2xF_1(x, Q^2) = F_2(x, Q^2), \tag{1.19}$$

the Callan-Gross relation, which evidences that the hadron constituents probed by the photon have spin 1/2. Subsequently, these constituents were identified with the quarks, giving rise to the parton model.

1.6 The parton model

In the parton model – see [15, 16] for more detail, a parton is described, in a given reference frame in which its momentum becomes very large, as an incoherent superposition of elemental constituents called partons. The variables x and $1/Q$ can be interpreted respectively as the hadron's momentum fraction that carries the parton probed by the photon, and the transverse resolution with which the hadron is probed. Then, the previously introduced structure function F_2 can be written as sum – weighted according to the momentum fraction and the squared charge e_f^2 – of the probabilities $f(x, Q^2)$ to find a parton f with momentum fraction x when the hadron is probed with a resolution $1/Q$. These are no more than the so-called parton distribution functions (PDFs):

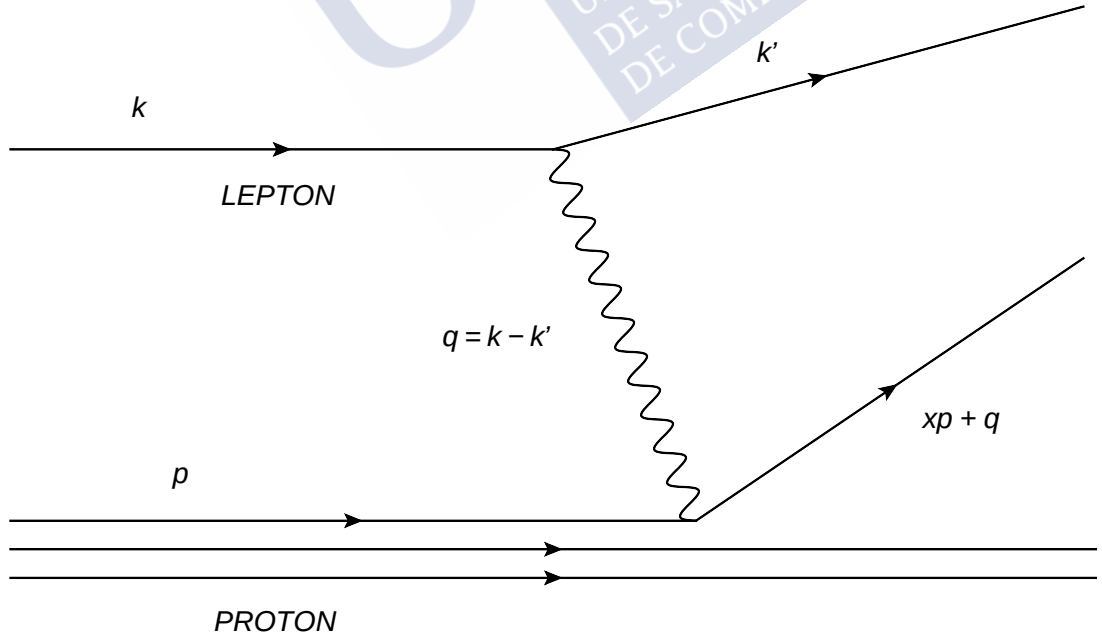

Figure 1.5: Schematic depiction of a lepton-hadron deep-inelastic scattering.

$$F_2(x) = \sum_f e_f^2 x f(x, Q^2). \tag{1.20}$$

The parton model quite naturally finds its deepest meaning in the QCD context. Electrically charged partons are identified with quarks. Furthermore, gluons turn up as a quark from the hadron with momentum fraction z can radiate a gluon, thus giving rise to the quark with momentum fraction $x < z$ which is probed by the photon. This radiation leads to a soft evolution – logarithmic in the PDFs [17].

At present, the determination of the PDFs in hadrons and nuclei is actively on course – see, for example, [18] and [19]. It is of key importance for both its interest in getting to know the hadron's structure and its practical usefulness for calculating the particle production in collisions which involve hadrons via the well-known factorization theorems [20]. Since the PDFs hold information about short- and large-distance scales, it is not possible to address the situation in a perturbative way, that is to say, it is not yet known how to compute them from first principles owing to the non-perturbative nature of the hadron as QCD bound state. Instead, factorization theorems, valid at any pQCD order, enable to split the problem in two clearly separate parts. The first is perturbative and hence calculable in the pQCD work frame. In particular, it describes the lepton-hadron scattering process. The second part, of a non-perturbative nature, provides the distribution of a parton i within the hadron N at a given energy scale, namely the already introduced PDFs.

In both DIS processes and pp collisions at high energies the initial state must be described by using PDFs. They can be determined by global fits to all available data from both DIS and hard scatterings. Global fits can be performed at leading order (LO), next-to-leading order (NLO) or next-to-next-to-leading order (NNLO) in the strong coupling constant α_s. In recent years, precision has been optimized and an extension in the kinematic range of experimental measurements for many of these processes have been carried out as well. Moreover, new theoretical developments increase the reliability of global fits. The precision of contemporary experiments demands the use of theoretical implementations at least at NLO and preferably at NNLO in comparisons between theory and experiments.

Nevertheless, PDFs hold the major advantage of being completely independent of the process under study in such a way that once extracted for a particular process it is not required to perform the calculation once again. Additionally, known at a given energy scale, PDFs can be derived for any other value of Q^2 through the use of QCD-based series of evolution equations, the so-called Dokshitzer-Gribov-Lipatov-Altarelli-Parisi (DGLAP) evolution equations [17, 21, 22].

1.7 Hot and dense QCD

It has been more than four decades since T. D. Lee and G. Wick pointed to the possibility of exploring new physics by distributing a large nuclear matter density or a large energy density within a relatively large volume to create new states of dense nuclear matter [23]. It soon became apparent that asymptotic freedom implies the existence of a highly dense form of nuclear matter made up by deconfined quarks and gluons [24], later renamed Quark-Gluon Plasma (QGP). The energy density has been studied and discussed in detail following finite temperature lattice QCD calculations. The results show a rapid increase from a low energy density state to a high energy density one, as one would expect in the phase transition from a state of confined quarks and gluons to deconfined [25]. Indeed, only at temperatures much higher than the critical temperature the (almost free) QGP predicted by aysmptotic freedom will pop up. For moderate temperatures, lattice QCD points towards a QGP with strong residual interactions, the strongly coupled QGP (scQGP), where the phase transition to QGP may seem to be a cross-over. Lattice QCD calculations also reckon with a first order phase transition for high densities of baryons μ_β and low temperature, whilst at high temperature and low baryonic density would lead to the above-mentioned cross-over. Accordingly, the phase diagram would present a critical point, as shown in Fig. 1.6.

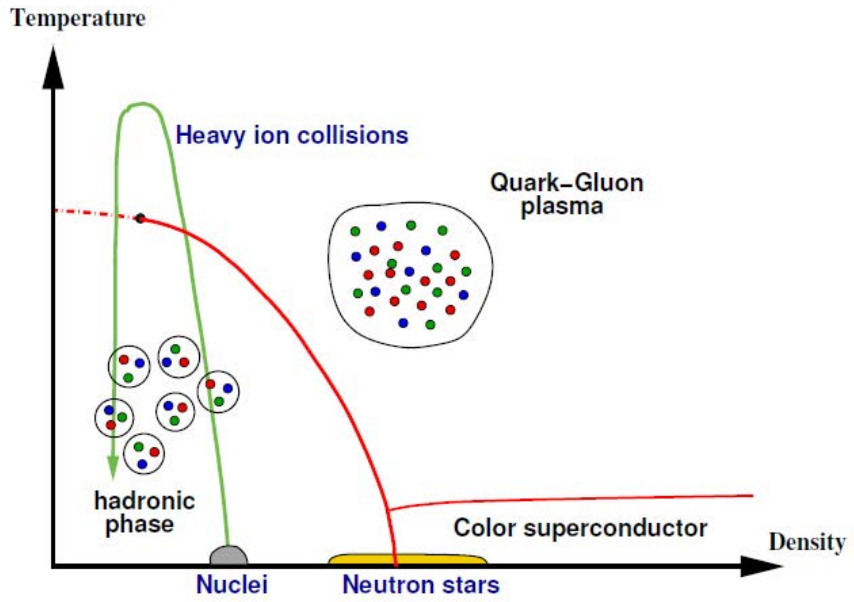

Figure 1.6: A sketch of the QCD phase diagram (extracted from [26]).

The quest for the QGP is not just important because it is the QCD state of matter at high temperature or high baryonic density that was present during the first microseconds after the Big Bang. What is more, it can exist in neutron stars, and even brings unique information on the origin of most of the ordinary mass and the confinement of quarks and gluons [27]. During the last decades considerable effort has been expended in experiments focused on achieving the QGP in the laboratory. Firstly, the Intersecting Storage Rings (ISR) experiments at the Conseil Européen pour la Recherche Nucléaire (CERN) explored light-ion collisions, just as the Alternating Gradient Synchroton (AGS) program at Brookhaven National Laboratory (BNL) was focused on looking deeply into the low energy regime. Later on, both Super Proton Synchrotron (SPS) experiments at CERN and Relativistic Heavy Ion Collider (RHIC) tests at BNL fully studied a wide range of centralities and observables at $\sqrt{s} \approx 20$ GeV and $\sqrt{s} \approx 200$ GeV per nucleon, respectively. Since then, experiments at CERN's Large Hadron Collider (LHC) have taken the lead in HICs studies.

RHIC data [28–31] showed phenomena such as a strong suppression of high-transverse momentum particles produced in collisions between gold ions to the number that would be expected, provided by the product of the number of nucleon-nucleon collisions with the proton-proton production relying on theoretical considerations. Indeed, STAR and PHENIX experiments at BNL found the first evidence for jets. These showed a significant difference from those seen in simpler collisions. STAR observed that one of the two back-to-back jets was invariably *quenched*, sometimes weakened and sometimes wholly extinguished. In this way, jets are *hard probes* (HP), by nature interacting through the strong force but moving so fast and with so much energy that they are often not completely absorbed by the surrounding quarks and gluons in the QGP. The degree of jet quenching – sketched in Fig. 1.7, a phenomenon that emerges in data from millions of collisions events, makes it possible to unveil some key information on the QGP, making it possible to deliver its properties.

The most frequent explanation put forward for this suppression is medium-induced radiative energy loss [33–35], by far the most recurrent topic addressed in the ensuing chapters of this thesis. Nevertheless, radiative energy loss models are not the only ones. Models also exist that consider collisional energy loss, approaches that assume an inmediate hadronization of partons and a few others. In order to differentiate between the different types of models it appears necessary to have a closer look at observables such as correlations between the produced particles within a reconstructed jet.

High-transverse momentum particle suppression as a result of energy loss owing to in-medium interactions had been foretold by Bjorken for nearly 40 years. More recently, the ALICE, ATLAS and CMS experiments at CERN's LHC have confirmed the existence of jet quenching in HICs. The much greater collision energies at the LHC push measurements to much higher jet energies, giving way to more detailed characterization of the QGP.

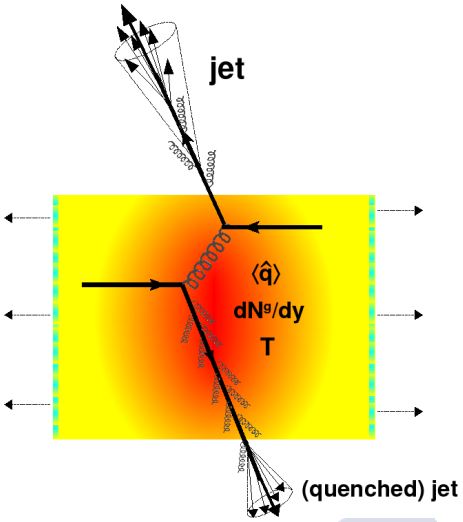

Figure 1.7: Jet quenching in a head-on nucleus-nucleus collision (illustration from [32]).

Theoretical understanding of these measurements is challenging, however, and is one of the most important problems in QCD today.

With regard to the initial stage in relativistic nuclear collisions, it might be described by parton saturation models such as the so-called Color Glass Condensate (CGC) [36–39], a state hydrodynamically described as a perfect fluid with very low viscosity. The CGC effective theory has been constructed for organizing the calculation of processes characterized by a large gluon occupation number by means of considering non-linear recombination effects, which factually turn out to be significant when nuclei are proven at sufficiently small values of Bjorken-x.

In the small-x regime, the occupation number of gluons becomes large in such a way that gluon self-interactions are of considerable significance, logically leading to gluon saturation – the gluon density proves to be inversely proportional to the strong coupling constant α_s. Note that as depicted in Fig. 1.8, there is an increase in the number of gluons on account of the rising of the energy, thus making smaller values of x kinematically accessible. This approach provides a framework for computing particle distributions and their dynamics prior to thermalization.

As stated above, all these detailed on-the-ground findings point to the creation of high-density matter. Due to the presence of this medium consisting on a near perfect partonic fluid with high density, high-transverse momentum particle propagation undergones significant changes with regard to vacuum propagation. LHC data available so far appear to be in conformity with these conclusions [41–45].

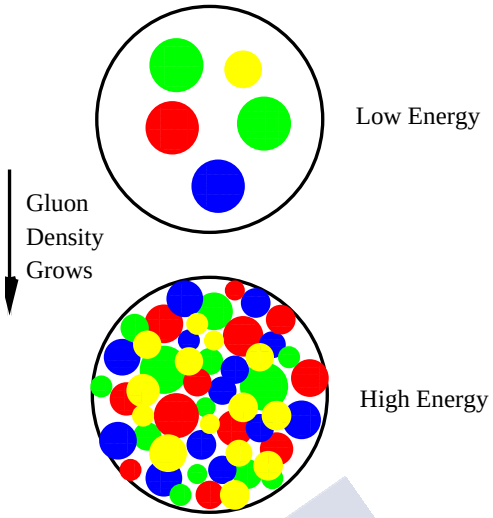

Figure 1.8: Phase-space gluon density in a hadron (picture from [40]).

USC
UNIVERSIDADE
DE SANTIAGO
DE COMPOSTELA

2

The formalism framework

This chapter provides an explicit basis and back-up for describing the nature and challenges associated with the phenomena of interest covered in the chapters that follow. Both the theoretical tools that underpin the presented developments, together with existing models rooted in these analytic methods, and the assumptions and expectations to critically evaluate the topics raised in this thesis are discussed. The main purpose is therefore not only to create a clear framework upon which to build the analyses and studies carried out, but also about highlighting how the undertaken approaches might differ and under what circumstances, eventually toward testing the validity of the interpretations set out in order to make broader generalizations at later stages. In short, this chapter fulfills the primary purpose of articulating the overarching theoretical environment guided by well-established models that best fit the physical scenarios to be dealt with.

As it was formerly mentioned in the motivation of this manuscript, the three subsequent chapters are encompassed within the in-medium jet evolution field. To get a sense of the in-medium evolution-based framework and provide extended discussions between energy loss approaches linked back to these theoretical schemes, it is fitting to start this episode by conducting thorough reviews both on vacuum and in-medium jet propagation, putting emphasis on parton energy loss models within the pQCD frame. In this context, theoretical and methodological tools as the Lund jet plane, which provides a powerful visual representation of the radiation within any given jet, thus allowing for an exhaustive comparison of jet quenching models, are also introduced. Furthermore, since the kinematical Lund diagram has a broad scope for constraining Monte Carlo simulations, it naturally leads to discuss how to exploit sophisticated jet substructure observables.

Finally, as the concluding portions of this chapter are intended to study particle correlations in saturated matter, it is in fact necessary to lay the foundations concerned with small-x physics, parton saturation and the Color Glass Condensate (CGC). These topics also fall within the main scope of this thesis since particle correlations may render possible further tests of the physics underlying jet quenching.

2.1 Fundamentals of jet evolution

The guiding principle is to think of the evolution of a jet as a pattern of parton branchings, qualitatively, the parton shower picture. This way of proceeding could raise doubt about the validity of this approach since one might mistakenly think that it leads to a disregard of higher corrections when addressing multi-parton phenomena. They, indeed, can be included to quantitatively predict multi-jet scenario properties with improved accuracy.

The probabilistic picture of jet evolution constitutes one of the cornerstones for further discussion. At this stage of handling parton evolution, interference effects have an important role to play. Among them are coherence phenomena, contemplated for the first time in the QCD context in the early eighties [46, 47]. From the experience with jet evolution in vacuum, one knows that coherence manifestations lead to angular ordering (AO) of the sequential parton decays, what provided the base for Monte Carlo simulations of jet physics in vacuum [48]. Nevertheless, a total understanding of jet evolution depends to a great extent in being able to fully grasp how these collimated multiparticle sprays behave when they go through a dense medium as the QGP, which is still not wholly under control.

2.1.1 Jet evolution in vacuum

As noted just above, the first manifestation of coherence is angular ordering. It is therefore worthwhile to elucidate the physical origin of AO from a simple model of the jet cascade, namely, the radiation pattern of soft gluons produced by a singlet quark-antiquark *antenna*. The question is to what extent the quark and the antiquark independently emit gluons. To this end, the calculation of the amplitude based on the diagrams sketched out in Fig. 2.1, which include the emission of a gluon with momentum k and polarization vector ϵ from both the quark and the antiquark, is performed – for further details, see [48]. It reads

$$\mathcal{M}_{q\bar{q}g} = -\bar{u}(p_1) i g_s \not{\epsilon} t^a \frac{i(\not{p}_1 + \not{k})}{(p_1+k)^2} i e \gamma_\mu v(p_2) + \bar{u}(p_1) i e \gamma_\mu \frac{i(\not{p}_2 + \not{k})}{(p_2+k)^2} i g_s \not{\epsilon} t^a v(p_2), \tag{2.1}$$

where $\bar{u}(p_1)$ and $v(p_2)$ are the spinors for the outgoing quark and antiquark, respectively, e is the quark's electric charge and γ_μ are the Dirac matrices. Here the former term corresponds to the emission from the quark, while the latter accounts for the emission from the antiquark.

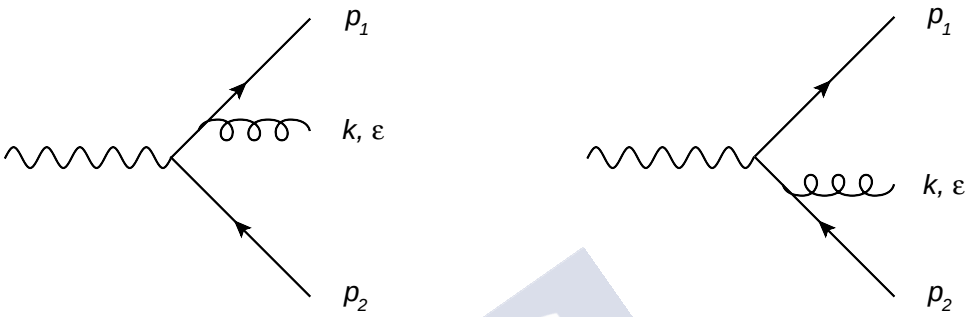

Figure 2.1: Diagrammatic representation of the $\gamma^* \to q\bar{q}g$ process.

After some algebraic manipulations, eq. (2.1) results in

$$\mathcal{M}_{q\bar{q}g} \simeq \bar{u}(p_1) ie\gamma_\mu t^a v(p_2) \cdot g_s \left(\frac{p_1 \cdot \epsilon}{p_1 \cdot k} - \frac{p_2 \cdot \epsilon}{p_2 \cdot k} \right). \tag{2.2}$$

It is worth noting that the first factor in the equation above has the same Lorentz structure – apart from the soft-gluon emission matrix – as the amplitude for the singlet quark-antiquark antenna production without considering further radiative processes off the leading partons, $\mathcal{M}_{q\bar{q}}$. Squaring and summing over both polarization and color states give rise to

$$|\mathcal{M}_{q\bar{q}g}|^2 \simeq |\mathcal{M}_{q\bar{q}}|^2 C_F g_s^2 \frac{2p_1 \cdot p_2}{(p_1 \cdot k)(p_2 \cdot k)}. \tag{2.3}$$

A key point in the above result is that in the soft limit, the squared amplitude for the undertaken process factorizes into the squared amplitude for the singlet antenna production plus a piece with a rather simple dependence on the gluon momentum, as the phase space does it too,

$$d\Phi_{q\bar{q}g} \simeq d\Phi_{q\bar{q}} \frac{d^3\vec{k}}{(2\pi)^3 2\omega}, \tag{2.4}$$

where ω is the energy of the gluon with momentum k.

By virtue of this factorization, one can write down the full differential cross-section for the production of the singlet antenna along with a radiated gluon as the product of the singlet antenna production matrix element and phase space – $|\mathcal{M}_{q\bar{q}}|^2 d\Phi_{q\bar{q}}$ – multiplied by a soft gluon emission probability $d\mathcal{S}$. Explicitly,

$$|\mathcal{M}_{q\bar{q}g}|^2 d\Phi_{q\bar{q}g} \simeq |\mathcal{M}_{q\bar{q}}|^2 d\Phi_{q\bar{q}} d\mathcal{S}. \tag{2.5}$$

Using now $d^3k = \omega^2 d\omega \; d\Omega$ – here $d\Omega = d\cos\theta \; d\phi$ is the differential solid angle, where θ and ϕ are the polar and azimuthal angles of the gluon with respect to the leading partons, respectively – and $\alpha_s = g_s^2/4\pi$, $d\mathcal{S}$ results in

$$d\mathcal{S} = \omega d\omega \; \frac{d\Omega}{2\pi} \cdot \frac{\alpha_s C_F}{2\pi} \frac{2p_1 \cdot p_2}{(p_1 \cdot k)(p_2 \cdot k)}. \tag{2.6}$$

It is helpful to define the radiation function $W_{q\bar{q}}$,

$$W_{q\bar{q}} := 2\omega^2 \frac{p_1 \cdot p_2}{(p_1 \cdot k)(p_2 \cdot k)}, \tag{2.7}$$

and rewrite it in terms of the polar angles as follows,

$$W_{q\bar{q}} = \frac{2(1 - \cos\theta_{q\bar{q}})}{(1 - \cos\theta_{qg})(1 - \cos\theta_{\bar{q}g})}, \tag{2.8}$$

where $\theta_{q\bar{q}}$ is the $q\bar{q}$-antenna opening angle, related with the virtuality of the off-shell particle in the hard scattering, and $\theta_{qg(\bar{q}g)}$ is the gluon emission angle off the quark (antiquark) – the angle of the new antenna.

Now, the radiation function can be easily separated into two parts containing collinear singularities along the lines i and j sketched in Fig. 2.2 in a way that $W_{q\bar{q}} = W_{q\bar{q}}^{[i]} + W_{q\bar{q}}^{[j]}$, with

$$\begin{aligned} W_{q\bar{q}}^{[i]} &:= \frac{1}{2}\left(W_{q\bar{q}} + \mathcal{R}_q - \mathcal{R}_{\bar{q}}\right), \\ W_{q\bar{q}}^{[j]} &:= \frac{1}{2}\left(W_{q\bar{q}} + \mathcal{R}_{\bar{q}} - \mathcal{R}_q\right), \end{aligned} \tag{2.9}$$

where $\mathcal{R}_q$ and $\mathcal{R}_{\bar{q}}$ are defined as

$$\mathcal{R}_q := \frac{2}{1 - \cos\theta_{qg}}, \;\; \mathcal{R}_{\bar{q}} := \frac{2}{1 - \cos\theta_{\bar{q}g}}, \tag{2.10}$$

accounting for the independent radiation off each of the partons.

Turning now to eq. (2.6) and expressing it as a function of eqs. (2.9), it results

$$d\mathcal{S} = \frac{d\omega}{\omega} \; \frac{d\Omega}{2\pi} \; \frac{\alpha_s C_F}{2\pi} \left(W_{q\bar{q}}^{[i]} + W_{q\bar{q}}^{[j]}\right). \tag{2.11}$$

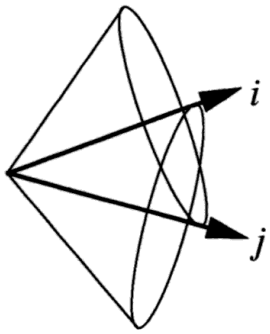

Figure 2.2: Soft radiation confining cone around leading partons i and j (sketch from [2]).

In order to properly interpret the obtained result it is convenient to reorganize the preceding equation as a combination of independent radiation off the leading partons and the interference between them. Under these changes, the soft gluon radiation probability from the antenna setup reads

$$d\mathcal{S} = \frac{d\omega}{\omega}\,\frac{d\Omega}{2\pi}\,\frac{\alpha_s C_F}{2\pi}\left(\mathcal{R}_q + \mathcal{R}_{\bar{q}} - 2\mathcal{J}\right), \tag{2.12}$$

where

$$\mathcal{J} := \frac{1}{2}\left(\mathcal{R}_q + \mathcal{R}_{\bar{q}}\right) - \frac{1}{2}W_{q\bar{q}} \tag{2.13}$$

describes the interference between the two partonic sources.

Finally, performing the angular integration in eq. (2.11) with respect to each line direction of Fig. 2.2 gives [2]

$$\int_0^{2\pi}\frac{d\phi_q^{[i]}}{2\pi}W_{q\bar{q}}^{[i]([j])} = \frac{2}{1-\cos\theta_{qg(\bar{q}g)}}\Theta\left(\cos\theta_{q\bar{q}} - \cos\theta_{qg(\bar{q}g)}\right). \tag{2.14}$$

A clear analysis of eqs. (2.12) and (2.14) is absolutely essential to fully understand the parton cascade picture in QCD. Eq. (2.12) states that the spectrum contains two types of non-integrable singularities. In a first step, the spectrum is divergent as long as the energy of the emitted gluon becomes soft, the soft or infrared divergence. It also contains two leading collinear singularities, namely, provided the gluon is collinearly radiated off either the quark – $\theta_{qg} \to 0$ – or the antiquark – $\theta_{\bar{q}g} \to 0$, the collinear divergence. Furthermore, radiation is suppressed at large angles due to destructive interferences – $\mathcal{R}_{q(\bar{q})}$ is roughly equal to $\mathcal{J}$ for large-angle radiation. Though derived via the $e^+e^- \to q\bar{q}$ production process, the soft and collinear divergences are a general property of QCD.

In turn, looking at eq. (2.14), after azimuthal averaging, the contribution from the term $W_{q\bar{q}}^{[i]}$ is confined to a cone, centred on the direction of line i, extending in angle as far as the direction of line j. Similarly, the contribution $W_{q\bar{q}}^{[j]}$, after averaging over $\phi_{\bar{q}}^{[j]}$, is confined to a cone centred on line j extending as far as line i, a remarkable property known as angular ordering. As suggested by the resulting Heaviside step function showed in eq. (2.14), decreasing emission angles are implied, meaning that the radiation pattern of soft gluons is angular-ordered in QCD, an example of a coherence effect common to all gauge theories, see Fig. 2.3.

Glancing back again at eq. (2.12), it is open to a heuristic interpretation based on the coherence of the system. In the perturbative approach, the amplitudes to some configurations, particularly those with large angle radiation, interfere rather than add incoherently. Making interpretation of this outcome is easy: at certain opening angles, the resolution of the color configurations of the emitters is hindered from a large distance unless they are sufficiently appart, and their net behaviour is rather similar to the radiation from the parent parton. Otherwise, they shall behave in an incoherent way, that is to say, as isolated emitters. Producing a gluon with energy ω and transverse momentum $k_\perp$ takes a formation time $t_f \simeq 2\omega/k_\perp^2$ during which the transverse size of the antenna is $r_\perp(t) \simeq \theta_{q\bar{q}} t$, whence $r_\perp(t_f) \simeq 2\theta_{q\bar{q}}/\omega\theta_{qg(\bar{q}g)}^2$ as $k_\perp \simeq \omega\theta_{qg(\bar{q}g)}$. A further scale on account is the transverse resolution of the radiated gluon at the time of formation, $\Lambda_\perp \simeq 1/k_\perp$, so $\Lambda_\perp \simeq 1/\omega\theta_{qg(\bar{q}g)}$. When the two scales are compared, an easy interpretation pops up: when the transverse size of the pair is smaller than the gluon transverse resolution – $\theta_{q\bar{q}} < \theta_{qg(\bar{q}g)}$, the radiated parton cannot resolve the antenna, thus behaving as an individual body in a color singlet state, meaning that no radiation is expected. In short, the cascading of a jet, initiated by a hard parton, shall occur in a coherent manner. Conversely, when $r_\perp > \Lambda_\perp$ – $\theta_{q\bar{q}} > \theta_{qg(\bar{q}g)}$, the gluon is able to resolve the dipole so that coherence does not play a key role. All in all, the interference is important only for gluon emissions at relatively large angles, outside of the dipole cone. In this way, the interpretation of the results obtained in eqs. (2.12) and (2.14) constitutes the basic building block for the construction of a coherent parton branching formalism.

It is noticeable that although the calculation performed in this subsection is carried out for the case of a color singlet antenna, the essence of the findings is not modified for other color configurations such as the color octet since they only imply color conservation issues.

Once having reviewed the building block of parton evolution in the abscence of a medium, now is the moment to take a closer look at the modifications that hard probes can undergo when interacting with color charges in a medium as the QGP.

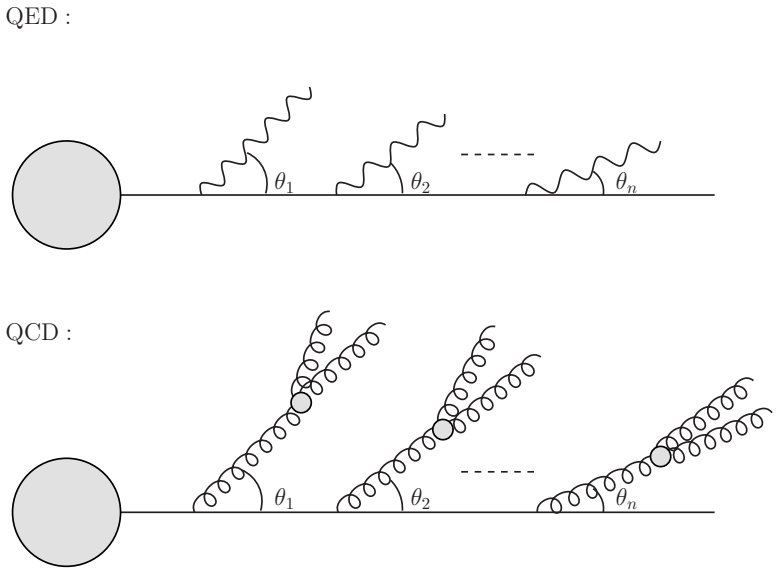

Figure 2.3: Diagrammatic depiction of angular-ordered emissions in both QED and QCD (drawn out from [50]).

2.1.2 In-medium jet evolution

Several approaches try to probe the physics behind jet evolution in matter, but the latest studies on jet substructure are the ones which do it in more detail. However, it lacks an accurate description for jet propagation and fragmentation in a medium as the problem of parton splittings is crucial in a wide range of high-energy physics scenarios. For instance, the development of a Monte Carlo QCD parton shower requires the splitting vertex along with a calculation of the available phase space. After all, there are still many questions left unanswered to gain a full understanding of the processes that underly jet modifications and energy loss, and hence a better characterization of the medium properties, which plays a key role in addressing coherence phenomena. This subsection presents the nature of the energy loss experienced by hard probes when traversing the hot QCD medium. Introducing the leading models attempting to cover parton energy loss within the pQCD frame also falls under this piece.

Jet energy loss

Hard partonic jets might lose energy by means of a combination of both elastic and inelastic collisions with the deconfined partons within the QGP. The energy loss arising as a result of elastic scatterings is known as collisional energy loss. Unlike the former, the latter is due to multiple scatterings with the medium constituents, which may induce additional radiation, thus taking away a fraction of the energy from the leading parton.

This is called radiative energy loss. Assuming a dominance of medium-induced radiation, experimental findings tend to be interpreted in terms of purely radiative processes.

Collisional energy loss

Collisional energy loss of hard partons was initially proposed by Bjorken in the early eighties [51]. Later on, several attemps at developing a more thorough analysis beyond the starter model were made by taking notice of novel considerations and effects [52–56].

As is discussed below in more depth, when addressing in-medium parton propagation, in most current approaches for radiative energy loss the medium is modeled as an assembly of heavy static scattering centers in such a way as recoil effects are neglected, hence omitting any reference to collisional energy loss for the leading partons. Indeed, collisional and radiative energy loss are added separately in these frameworks. When comparing collisional and radiative effects, collisional energy loss usually shows less impact for light flavor leading partons – particularly for high jet energies [57], whereas it is meant to be the controlling mechanism for heavy quark energy loss within the low and intermediate energy regimes [58]. In the high-energy regime, heavy quarks become ultrarelativistic and radiative effects become more significant [59].

All in all, collisional energy loss plays a subdominant role with respect to radiative energy loss and will be disregarded throughout this thesis.

Radiative energy loss

Radiative energy loss has been deemed as the major ingredient when addressing both parton energy loss and jet quenching in relativistic HICs. Due to the presence of the QGP, parton splitting processes are altered with regard to vacuum propagation since they experience ongoing rescatterings with the medium constituents.

As mentioned earlier, interference effects play a crucial role when dealing with parton evolution, and within them coherence phenomena are some of the most visible. In this respect, the Landau-Pomeranchuk-Migdal (LPM) effect, first demonstrated experimentally at SLAC [60], constitutes a marked effect when handling medium-induced gluon radiation in the course of parton propagation. In the fifties, Landau, Pomeranchuk and Migdal predicted that the cross-section for bremsstrahlung from highly relativistic particles in dense media is suppressed due to interference caused by multiple in-medium scatterings [61,62]. More specifically, for the radiation process to take place it is required a finite time, marked by the formation time of the producing gluon, $t_f \simeq 2\omega/k_\perp^2$, where ω and $k_\perp$ are the energy and transverse momentum of the collinear radiated gluon. By comparing the two scales,

it is appraised that whenever the gluon formation time t_f is larger than the mean free path λ of the propagating parton, the rescatterings experienced by the hard parton can no longer be considered as independent. This quantum interference effect amongst consecutive scatterings resulting from the LPM effect gives rise to a suppression in the radiation spectrum as against the Bethe-Heitler (BH) bremsstrahlung spectrum, which assumes incoherent rescatterings[1] [63].

Several different model frameworks for studying medium-induced gluon radiation in hot and dense matter within pQCD have been developed over the past two and a half decades. Among them the following stand out: BDMPS-Z [64–68], ASW [69–73], GLV [74–77], AMY [78–80] and HT [81–85].

All the models listed above rely on the standard assumption that interactions among the leading parton and the emitted gluon with the medium can be computed within pQCD, whether or not the medium properties can be addressed perturbatively. It is within this context that diverse approaches arise with the final goal of calculating the radiative energy loss of the energetic parton. Brief comments on the basic information of these formalisms are provided further below. However, first of all it is worth stressing the common assumptions and approximations amongst them concerning the branching of the leading parton, the medium model or the kinematical considerations for the parton-medium interactions.

- The parton splitting is affected by the medium in such a way that interactions between both the high-energy parton and the offspring with the medium become important. As the transverse momentum of the daughter parton $k_\perp$ is quite less than its energy ω, only collinear radiation off the emitters takes place. In the wake of this condition, the two partons involved in each splitting take similar paths, giving way to the LPM effect previously introduced in this section.

- It is assumed that the momentum transfer between the hard parton and the medium is localized, meaning that the mean free path of the incoming parton λ is much larger than the color screening length of the medium, which is proportional to the inverse of the Debye screening mass μ_D.

- The *eikonal* picture is implemented: the interaction of the projectile partons with the medium is assumed to be eikonal, that is to say, they propagate through the medium without changing their transverse position. Kinematically speaking, what all this adds up to is that the energy of the leading parton E is far greater than the transverse momentum exchanged with the medium $q_\perp$.

[1] The independent Bethe-Heitler gluon spectrum reads $\omega dI_{\rm rad}/d\omega \simeq L^2/\omega$, with ω the energy of the radiated parton and L the medium length.

Despite common assumptions, in a practical sense each model framework description conducts a particular set of approximations with regard to certain points about the in-medium parton branching or the medium model. However, as each formalism allude to a great number of common ingredients in order to fully model this complex physical scenario, addressing each of them separately does not come easily. Following is a small report on each one – see [86] for a more thorough balance at comparing the specific implementations amongst themselves. Attention is being paid to the BDMPS-Z/ASW formalisms as they constitute the building block that enables to perform the calculations presented in the three main strands of this manuscript.

The BDMPS-Z and ASW formalisms
[Baier-Dokshitzer-Mueller-Peigné-Schiff-Zakharov / Armesto-Salgado-Wiedemann]

BDMPS-Z was the very first of the in-medium radiative energy loss formalisms. It is developed in a purely path-integral formulation that accounts for the resummation of the scatterings on multiple heavy static colored centers. U. A. Wiedemann enclosed the interference between vacuum and medium-induced radiation in the existing framework at a later stage [70, 71]. The most common model approach for analytical and numerical studies is the *saddle* point approximation. This involves assuming that the high-energy parton interacts with the medium by way of multiple soft scattering processes, commonly known as either multiple soft scattering or dipole approximation. Numerical analysis implementing this approximation within the BDMPS-Z approach were undertaken by C. A. Salgado and U. A. Wiedemann on the basis of calculating the in-medium splitting gluon probabilities, the so-called *quenching weights* [72]. Alternatively, M. Gyulassy, P. Levai and I. Vitev (GLV) and U. A. Wiedemann (independently) [70, 76] presented another approximation based on a systematic expansion over the number of scatterings experienced by the incoming parton, the opacity expansion, characterized by the density ρ of scattering centers – or the mean free path of the leading parton λ – and the Debye screening mass μ_D. In some phenomenological calculations the single hard scattering limit is implemented, that is to say, only the leading term of the summation ($N = 1$) is taken since it is assumed that there is only one dominant hard scattering. Multiple gluon emission scenarios are addressed by iterating the single gluon emission kernel by means of a Poisson convolution, which assumes that the number of radiated partons in a given path responds to a Poisson distribution.

The GLV formalism [Gyulassy-Levai-Vitev]

The GLV frame is based on the opacity expansion – as just stated, two different model implementations (independently developed) exist for this approach. As also noted above, some phenomenological studies restrict themselves to the single hard scattering limit. Higher orders in opacity were, however, considered by GLV and S. Wicks [77, 87].

The AMY formalism [Arnold-Moore-Yaffe]

The AMY approach was developed to study parton energy loss in a weakly-coupled medium being in thermal equilibrium. While it was primarily formulated on the assumption that the leading parton passes through an infinite size QCD medium, including the effect of finite medium length was a recent addition by S. Caron-Huot and C. Gale [88]. With regard to the case of multiple gluon emissions, AMY uses a set of rate evolution equations so designed as to the radiation probability evolves with the primary hard parton energy loss.

The HT formalism [Higher-Twist]

The original development of the higher-twist approach was led by X.-f. Guo and X.-N. Wang [81,82]. In this formalism, higher-twist matrix elements analytically characterize the medium properties. Typically, nuclear PDFs factorize out from those matrix elements, thus enabling the latter to fully describe the high-energy parton-medium interaction. As is the case for the most of the other approaches, HT was first developed for single hard scattering until A. Majumder extrapolated the work frame to the case of multiple scatterings later on [85]. Parton branching evolution is performed via medium-modified DGLAP evolution equations.

As seen in the main approaches conceived from the perspective of understanding the suppression of high-p_T hadrons in ultrarelativistic HICs, parton energy loss in QCD matter proves to be an intriguing task which requires the modeling at various stages, just as identifying the dominant mechanism responsible for the observed modifications. In the initial stage of each energy loss formalism high-energy partons are formed in a primary collision, while in the final state they ultimately fragment into hadrons. Between these two stages parton-medium interactions take place, giving rise to the parton cascade. As can be guessed, the evolution of scales that leads to parton showering is suitable to computer simulation using Monte Carlo techniques, which is the focus of the following piece of this section.

2.1.3 Parton showers from a phenomenological insight

The parton showering scenario is a Markov process that Monte Carlo (MC) techniques can cover very efficiently. A Markov chain MC allows to estimate *a posteriori* branching probabilities by assuming that the next branching depends only on the previous one and is randomly generated. Nevertheless, improving the treatment of each regime is required as higher-order perturbative calculations and more sophisticated hadronization models emerge.

Not only is a MC event generator surely able to run simulations suitable for a wide scope of processes taking place in particle physics experiments, but also provides well-founded information for designing new experimetal setups. In the context of QCD, once the partonic structure of hadrons was known, MC generators started to surface. Indeed, important tools to test QCD as DIS can be understood in terms of parton interactions. Set forth below a more detailed discussion of the physics behind parton showering involved in MC event generators.

Getting back to eq. (2.6), it seems to be something that might be implemented and iterated in a MC algorithm. As a matter of fact, it constitutes the starting point to write an iterative algorithm since it provides a general expression for a hard process together with a collinear splitting. The picture is becoming even clearer: it is therefore possible to iterate an expression for the soft emission probability in order to generate a collinear splitting and then prompt it to handle the final state of that splitting as a new hard process, generating an even more collinear splitting from it and so forth, that is to say, the building block to iteratively attach extra partons one by one. In short, a collinear parton shower algorithm is capable of encapsulating soft gluon effects as long as the opening angle is set as the evolution scale.

While in the absence of medium effects the MC technique is extensively used for simulating final state parton showers [89, 90], perturbative-based jet quenching MC event generators are more challenging as they constitute the baseline for characterizing medium-modified multi-particle final states, as well as a basic tool to describe parton-medium interactions and test medium properties. In recent years, several MC generators implementing partonic energy loss have been developed. Prominent amongst them are PQM [91], using the BDMPS quenching weights, PYQUEN [92], which modifies the standard PYTHIA 6.2 jet events [90] via both a reduction in the energy of the partons involved in the cascade and by adding additional gluons to that shower, Q-PYTHIA [93], including medium-induced gluon radiation within the BDMPS-Z approach, JEWEL [94], whose interest lies in going deeper into the relationship between parton energy loss and some of its specific features as $p_\perp$-broadening or recoil momentum, or MARTINI [95, 96], taking advantage of the set of rate evolution equations from AMY [80].

Discussions on MC parton shower algorithms encourage to dip into the kinematical Lund diagram [97] – see [98] to find out more about the standards of the scheme, which constitutes a structured representation of the phase-space within jets and thus make application possible for radiation pattern implementations run by MC event generators. The Lund diagram easily fits in the context of in-medium parton splittings as it renders an important starting point for having an overall vision of what regimes react more to medium effects. Details on the construction of this diagram can be found below since this tool is used to map the radiation spectrum of the splitting process addressed in one of the most relevant chapters of this thesis.

The Lund plane encompasses the emission kinematics as a function of two variables: the Y-axis represents the emission tranverse momentum $k_\perp$ with respect to the jet axis, whereas the inverse of the radiation angle θ with respect to the jet axis is plotted along the X-axis – the natural logarithmic scale is used for both axis. To be clearer, the Lund diagram can be exploited in terms of different variables, but in any case, taking advantage of the fact that ordinary $1 \to 2$ QCD splittings lead to the infrared and collinear divergencies, both encapsulated in eq. (2.6). For the purpose of describing how to proceed further with the filling of the Lund diagram it is helpful to handle the most convenient expression for the splitting probability. A little algebra reshapes eq. (2.6) to an equivalent form,

$$d\mathcal{S} = \bar{\alpha} \cdot \frac{d\omega}{\omega} \frac{d\theta}{\theta}, \tag{2.15}$$

where $\bar{\alpha}$ is defined as $\bar{\alpha} := 2\alpha_s C_i/\pi$ (with $C_i = C_F$ for a quark splitting).

After this, it is also appropriate to define certain quantities that directly fall under the Lund map, namely, the jet invariant mass, an important observable in jet physics since it represents the prototype of a jet substructure observable, which in the collinear limit reads

$$M^2 = z(1-z)p_\perp^2\theta^2, \tag{2.16}$$

where z represents the energy fraction carried away by one of the emitted partons and $p_\perp$ accounts for the total momentum of the dipole jet, or the formation time, the characteristic time-scale of the splitting taking place,

$$t_f = \frac{2z(1-z)p_\perp}{k_\perp^2}, \tag{2.17}$$

with $k_\perp = z(1-z)p_\perp\theta$.

Then, in the double-logarithmic approximation (DLA) – where $\mathcal{O}(1-z)$ corrections can be neglected[2], the Lund parton splitting map can be chart in terms of kinematical variables such as $z\theta$ versus $1/\theta$ in logarithmic scaling – or $\ln(1/z)$ versus $\ln(1/\theta)$ and the like, depending on which suits best. In this way, the Lund map can be filled by virtue of eq. (2.15) for the probability that one splitting takes place,

$$d\mathcal{S} = \bar{\alpha} \cdot d\ln z\theta \; d\ln\frac{1}{\theta}, \tag{2.18}$$

or also

$$d\mathcal{S} = \bar{\alpha} \cdot d\ln\frac{1}{z} \; d\ln\frac{1}{\theta}. \tag{2.19}$$

[2]This makes it possible to approximate $p_\perp \simeq zE\theta$, $k_\perp \simeq zp_\perp\theta$ and such.

Figure 2.4 shows a sketch of the Lund map expanded accordingly to eq. (2.18)[3], where both soft and large-angle emissions and hard and collinear radiation regimes are explicitly identified within the plane. A couple of clarifications with regard to Fig. 2.4 are necessary. It is noticeable that, according to eqs. (2.18) and (2.19), the Lund diagram is uniformly filled with a density $\rho \simeq \bar{\alpha}$. Moreover, higher-order corrections in the strong coupling α_s emerge when multiple splittings effects are taken into account.

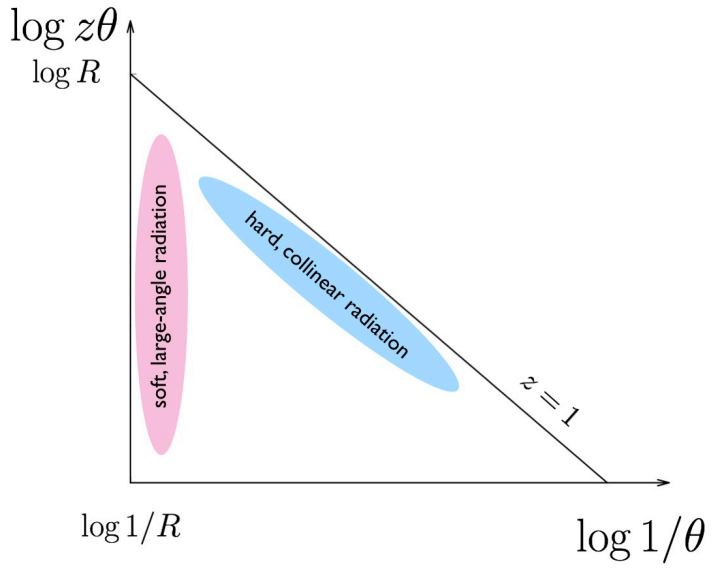

Figure 2.4: The Lund diagram filled by means of eq. (2.18). Here R is the jet opening angle (courtesy of [99]).

The process for populating the map consists on matching each branching with a point within the Lund map, which consequently displays lines of constant formation times with a slope one parametrized by solving

$$\ln z\theta = \ln \frac{1}{\theta} + \ln \frac{1}{p_\perp t} \tag{2.20}$$

for $t = t_f$.

The next step is to discuss the Lund diagram for in-medium splittings, a study thoroughly conducted in Chapter 4 for a real and collinear parton splitting inside a medium.

[3]Note that eqs. (2.18) and (2.19) are restricted to the singlet case. For the octet case, C_F must be replaced by $C_A = N_c$.

Based on the introduced background, it is easy to deduce that medium modifications are expected to arise from the baseline $t_f = L$ upwards, that is to say, medium effects events show up, by all means, inside the medium of length L. This line can be estimated by imposing $t = L$ in eq. (2.20). Furthermore, as will be seen in greater depth in Chapter 4, other characteristic time scales related to decoherence and broadening of partons in the medium arise in the addressed physical scenario. They are equally represented as straight lines within the graph, thus dividing the plane in different regimes. Given the presence of various relevant scales, this naturally leads to a careful discussion rooted in the different ordering of the time scales themselves, eventually gaining a clear insight into medium modifications regarding the nature of the splittings and the coherence of the system.

As can be seen, Lund diagrams are suitable as a theoretical representation of the phase-space within jets, and not just that but also have been raising attention as a powerful tool in discussions of MC parton shower algorithms since they carry wide-ranging information on jets, including the potential for exploiting their internal structure [99,100]. The MC technique is extensively used for the simulation of final state parton showers in vacuum, whereas in the presence of medium effects, the generalization to multiple splittings is a challenge that remains open whilst some steps forward have been achieved in this respect – [101] is one of the latest.

A jet definition, understood as a well-defined procedure to reconstruct jets from the set of hadrons in the final state of the collision, is a means of connecting theoretical models with experimental observables. As a first step, one might think of jets as being in one to one correspondence with the produced partons in a hard scattering. Nevertheless, in a hadron collider environment the actual identification of jets is non-trivial since it is not always true that hadrons are associated with a particular jet. This situation may occur, for example, when jets partially overlap. In view of this situation, several algorithms for identifying jets on a hard scattering have been currently developed. An important requirement for jet algorithms is to be infrared and collinear (IRC) safe, that is, for any partonic configuration, replacing any parton with a collinear set of partons with the same total momentum, or adding any number of infinitely soft partons in any directions, should produce identical result. The two main types are cone algorithms and sequential recombination algorithms. The older cone algorithms [12] define a jet as those hadrons lying within some distance from the jet center. However, not all cone algorithms fulfill IRC safety[4]. Most LHC studies use sequential recombination algorithms as the generalized-k_t algorithm [102], the k_t algorithm [103,104], the Cambridge-Aachen (C/A) algorithm [105] or the anti-k_t algorithm [106], which stem from the approach that, from the pQCD point of view, jets are essentially the product of successive parton branchings.

[4]In fact, IRC safety is not so much required to find jets, but to deal with them within the pQCD framework. Away from the purpose of comparing theoretical models with experimental data, an IRC-unsafe jet algorithm fits just as well.

So, what the algorithm basically do is to invert the process outlined above by successively recombining two particles into one. Moreover, the process can be repeated again, for example, in jet substructure studies. In a first step, the anti-k_t algorithm is used to reconstruct jets, while another sequential-recombinational algorithm reclusters the constituents of that jet to study its internal structure. Finally, it is also important to perform numerical implementations of the algorithms. At the moment, the standard package for jet clustering is FastJet since it provides an implementation of all the cited recombination algorithms [102].

Novel jet substructure variables have been recently defined. Many of them are IRC safe, thus enabling to use perturbative methods. Jet substructure techniques are designed in such a way that the constituents of a jet are reorganized into a hierarchical tree where the nodes account for the successive splitting processes, which is a starting point for the future analysis using techniques such as jet grooming or tagging algorithms. The former concerns a reorganization of the tree by discarding radiation that fails to pass a given criteria, while the latter is undertaken in order to identify the very first splitting that passes a given requirement, thereby splitting a jet into two sub-jets. Over the last years, much has been accomplished on using these techniques for many jet substructure observables, which in turn open new doors of opportunity to explore unknown physics domains – see [100] for a very detailed compilation of standards and resources in jet algorithms and jet substructure phenomenology.

2.2 Radiative energy loss in the BDMPS-Z/ASW approach

Just as was stated earlier in this section, a number of formalisms for radiative energy loss of an energetic parton inside hot and dense matter have been put forward over recent decades. This piece is now intended to delve deeply into the details referring to the BDMPS-Z/ASW approach, as this formalism is the backbone of the studies developed in the succeeding chapters. At the beginning, general considerations for analytically describing the hard partonic interaction with the colored medium are introduced, as well as the relevant assumptions about the branching of the incoming parton, the nature of the medium or the kinematical approximations for the projectile parton. Then, the single-inclusive particle spectrum is revisited as the prelude to a review of the medium modification undergone by the gluon spectrum off a quark-antiquark antenna along the same line followed in the vacuum case. All these contribute to set an overall knowledge regarding in-medium parton energy loss as also unravels the basic procedures and techniques which prove necessary to support further studies on parton showering presented in this manuscript.

2.2.1 High-energy parton propagation through a medium

In an attempt to answer the question of how an energetic parton created in the early stages of heavy-ion collisions traverses a dense medium the most widespread picture used is presented here. Noteworthy is that it is built on the basis of a semi-classical approach that neglects the modifications undergone by the medium configuration as a result of the passage of the incoming parton, namely the recoil of the scattering centers. In particular, to put this into practice the medium is modeled as a background field understood as a collection of static colored scattering centers with a specified density distribution along the trajectory of the projectile. For its part, the propagation of the fast parton throughout this medium field $A^-(x^+, \boldsymbol{x}_\perp)$ is fittingly implemented in terms of Wilson lines in the fundamental representation,

$$W(L^+, x_0^+; \boldsymbol{x}_\perp) = \mathcal{P} \exp\left[ig \int_{x_0^+}^{L^+} dx^+ \; A^-(x^+, \boldsymbol{x}_\perp)\right], \tag{2.21}$$

where $\boldsymbol{x}_\perp$ is the transverse position of the hard parton and the boundaries are set in the light-cone space, which is very useful in the context of high-energy collisions. In particular, the light-cone variables are defined as

$$x^\pm = \frac{1}{\sqrt{2}}(x_0 \pm x_3), \; p^\pm = \frac{1}{\sqrt{2}}(p_0 \pm p_3). \tag{2.22}$$

The scalar product reads

$$p \cdot x = p^+ x^- + p^- x^+ - \boldsymbol{p}_\perp \cdot \boldsymbol{x}_\perp, \tag{2.23}$$

while the rapidity is defined to be

$$y = \frac{1}{2} \ln\left(\frac{p_0 + p_3}{p_0 - p_3}\right) = \frac{1}{2} \ln\left(\frac{p^+}{p^-}\right). \tag{2.24}$$

As mentioned above, adequately addressing the picture of parton eikonal propagation in matter involves the use of Wilson lines, which in this context can be straightforwardly derived from first principles by assuming the leading parton experiences multiple scatterings as it travels across the medium. This approach is displayed in Fig. 2.5, where x_1 to x_n account for the position of the scattering centers within the background field[5].

Now, having fixed everything with regard to the passage of the parton through the medium field, the scattering matrix for one kick reads as [35]

$$S_1(p', p) = \int d^4x \; e^{i(p'-p)\cdot x} \; \bar{u}(p') \; igA_\mu^a(x) T^a \gamma^\mu \; u(p), \tag{2.25}$$

[5]The movement of the energetic quark is set in positive x_3-direction.

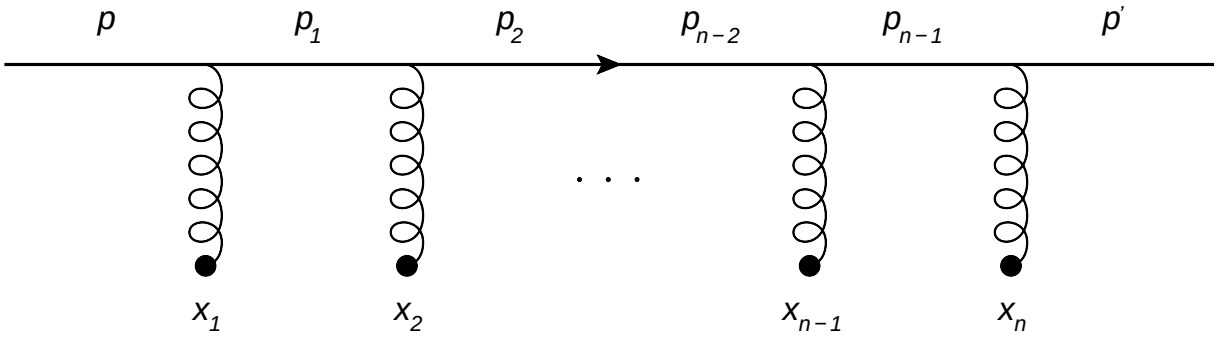

Figure 2.5: Diagram showing a multiple scattering eikonal trajectory.

where T^a stands for the corresponding color matrix. Implementing the eikonal limit in the above equation – $p^+ \simeq p'^+$ – gives rise to

$$S_1(p',p) \simeq 2\pi\delta(p'^+ - p^+)2p^+ \int d\boldsymbol{x}_\perp \; e^{-i(\boldsymbol{p}'_\perp - \boldsymbol{p}_\perp)\cdot\boldsymbol{x}_\perp} \left[ig \int dx^+ \; A^-(x^+, \boldsymbol{x}_\perp) \right]. \qquad (2.26)$$

Here the color matrix has been absorbed into the medium color field, $A^- := T^a A^{(-)a}$. For the generalization of the preceding expression to n-scatterings a recurrence relationship must be found by adding one scattering per step – see [35] for the whole derivation. After this, the S-matrix generalized to n-scatterings is given by

$$S_n(p',p) \simeq 2\pi\delta(p'^+ - p^+)2p^+ \int d\boldsymbol{x}_\perp \; e^{-i(\boldsymbol{p}'_\perp - \boldsymbol{p}_\perp)\cdot\boldsymbol{x}_\perp} \frac{1}{n!} \mathcal{P} \left[ig \int dx^+ \; A^-(x^+, \boldsymbol{x}_\perp) \right]^n, \quad (2.27)$$

such that the total scattering matrix proves to be

$$S_n(p',p) = \sum_{n=0}^{\infty} S_n(p',p) \simeq 2\pi\delta(p'^+ - p^+)2p^+ \int d\boldsymbol{x}_\perp \; e^{-i(\boldsymbol{p}'_\perp - \boldsymbol{p}_\perp)\cdot\boldsymbol{x}_\perp} \; W(x_n^+, x_1^+; \boldsymbol{x}_\perp), \quad (2.28)$$

where $W(x_n^+, x_1^+; \boldsymbol{x}_\perp)$ is given by eq. (2.21).

Eq. (2.28) characterizes the scattering process suffered by a hard parton – a quark or a gluon[6] – as it crosses a color deconfined medium. The response of the medium is made manifest by inducing color rotation at each kick so that the incoming parton keeps propagating through the medium rotating in color space. The amount of energy loss is assumed to be negligible, so the leading particle moves along a straight line path.

[6]Likewise, the same procedure may be followed to obtain the total scattering matrix for the case of a high-energy gluon via writing the external fields encapsulated in eq. (2.21) in the adjoint representation.

However, if appropriate, easing eikonality restrictions enables the propagating particle to spread in the transverse plane. This does apply, for example, to the medium-induced gluon radiation. In such a case, the gluon exhibits Brownian motion in the transverse plane and instead of the standard Wilson line introduced in eq. (2.21), the Green's function propagator describes both the color rotation and the Brownian motion experienced by the interacting gluon,

$$\mathcal{G}(L^+,\boldsymbol{x}_\perp;x_0^+,\boldsymbol{x}_{0\perp}|p^+)=\int_{\boldsymbol{r}_\perp(x_0^+)=\boldsymbol{x}_{0\perp}}^{\boldsymbol{r}_\perp(L^+)=\boldsymbol{x}_\perp}\mathcal{D}\boldsymbol{r}_\perp(\xi)\ \exp\left[i\frac{p^+}{2}\int_{x_0^+}^{L^+}d\xi\ \dot{\boldsymbol{r}}_\perp^2(\xi)\right] \times W(L^+,x_0^+;\boldsymbol{r}_\perp(\xi)), \tag{2.29}$$

where both the longitudinal medium boundaries (L^+, x_0^+) and the transverse position of the gluon $(\boldsymbol{x}_\perp, \boldsymbol{x}_{0\perp})$ have been set. It is worth noting that in the infinite-energy limit, the integrand within the path-integral describing the parton's trajectory in the transverse plane vanishes, thus recalling the single straight classical trajectory defined by the eikonal Wilson line,

$$\lim_{p^+\to\infty}\ \mathcal{G}(L^+,\boldsymbol{x}_\perp;x_0^+,\boldsymbol{x}_{0\perp}|p^+)=W(L^+,x_0^+;\boldsymbol{x}_\perp)\ \delta^{(2)}(\boldsymbol{x}_\perp-\boldsymbol{x}_{0\perp}). \tag{2.30}$$

Again, for a detailed derivation of eq. (2.29), the reader is referred to [35].

2.2.2 The medium averaging procedure

To provide the cross-section for particle production it is necessary to carry out an averaging process over all possible medium color configurations since the total scattering matrices presented above only work for a specific configuration of the fields. Two of the main prescriptions regarding the averaging method are discussed herein: the opacity expansion [70, 77] and the multiple soft scattering approximation [71] – a few guidelines on the two were given when introducing the different formalisms for studying medium-induced gluon radiation in hot and dense matter. As already outlined earlier as well, both approaches view the medium as a set of discrete scattering centers randomly distributed throughout the longitudinal and transverse directions and separated by a minimum distance equivalent to the Debye screening length $1/\mu_D$, with μ_D being the Debye screening mass.

In this context, each hard parton crossing the static colored medium field contributes to the scattering amplitude with a Wilson line written in the appropriate representation[7] at a fixed position in the transverse plane. The aforementioned averaging procedure gives rise to the non-trivial correlations amongst the fields encapsulated within the Wilson lines.

[7]Quarks go in the fundamental representation whilst gluons fall within the adjoint one.

Regardless of the approach under consideration for the computation of such medium averages, as the number of Wilson lines involved in the calculation increases, so too does the complexity of the calculation of higher point correlators. The simplest correlation function is the two-point correlator,

$$\frac{1}{N}\mathrm{Tr}\Big\langle W^{\dagger}(\boldsymbol{x}_{\perp})W(\boldsymbol{y}_{\perp})\Big\rangle, \tag{2.31}$$

where the average over initial color indices is implicit. Whereas the preceding expression is restricted to quark propagation, the same holds true for gluons just placing $1/(N^2-1)$ instead of $1/N$ in front of the trace, which in this case would involve Wilson lines in the adjoint representation.

By using the general definition of the Wilson line (2.21), the two-point correlator (2.31) can be written as

$$\begin{aligned}\frac{1}{N}\mathrm{Tr}\Big\langle W^{\dagger}(\boldsymbol{x}_{\perp})W(\boldsymbol{y}_{\perp})\Big\rangle = \frac{1}{N}\mathrm{Tr}\Bigg\langle \exp\left\{-ig\int dx^{+}A^{(-)\dagger}(x^{+},\boldsymbol{x}_{\perp})\right\} \\ \times \exp\left\{ig\int dx^{+}A^{-}(x^{+},\boldsymbol{x}_{\perp})\right\}\Bigg\rangle.\end{aligned} \tag{2.32}$$

Now implementing a series expansion of the exponentials falling inside the trace – known as Gaussian approximation, one cannot but notice that the linear terms are cancelled out on account of the color trace, thus causing the dominant contribution to be given by the second-order terms arising from the series,

$$\begin{aligned}\frac{1}{N}\mathrm{Tr}\Big\langle W^{\dagger}(\boldsymbol{x}_{\perp})W(\boldsymbol{y}_{\perp})\Big\rangle = \mathcal{P}\Bigg\langle 1 + \frac{(ig)^2}{2}\left[\int dx^{+}A^{(-)\dagger}(x^{+},\boldsymbol{x}_{\perp})\right]^2 + \\ + \frac{(ig)^2}{2}\left[\int dx^{+}A^{-}(x^{+},\boldsymbol{y}_{\perp})\right]^2 \\ - (ig)^2\left[\int dx^{+}A^{(-)\dagger}(x^{+},\boldsymbol{x}_{\perp})\right]\left[\int dx^{+}A^{-}(x^{+},\boldsymbol{y}_{\perp})\right]\Bigg\rangle,\end{aligned} \tag{2.33}$$

where the path ordering $\mathcal{P}$ makes sure that the potentials are ordered along the longitudinal axis.

The above result suggests a direct interpretation linked to the two-scattering diagrams drawn in Fig. 2.6 since the first two dominant contributions, also known as *contact terms*, are not able to resolve the transverse size of the dipole, as is clear after some algebra manipulations.

First, it is appropriate to write the gluon field as the Fourier transform of the scattering potentials at positions (x_i^+, x_n^+) as

$$A^-(x^+, \boldsymbol{x}_\perp) = \sum_n \int \frac{d^2\boldsymbol{q}_\perp}{(2\pi)^2}\, e^{i(\boldsymbol{x}_\perp - \boldsymbol{x}_{n\perp})\cdot\boldsymbol{q}_\perp}\; a^{(-)}(\boldsymbol{q}_\perp)\; \delta(x^+ - x_n^+). \tag{2.34}$$

Besides that, performing the medium averages requires the integration on both the longitudinal and transverse coordinates of the medium constituents. Taking as an example one of the leading terms inside the correlation function, it follows that

$$\begin{aligned} &\int dx^+ dx_n^+ d\boldsymbol{x}_{n\perp} \int \frac{d^2\boldsymbol{q}_{1\perp}}{(2\pi)^2}\frac{d^2\boldsymbol{q}_{2\perp}}{(2\pi)^2}\; e^{-i(\boldsymbol{x}_\perp - \boldsymbol{x}_{n\perp})\cdot\boldsymbol{q}_{1\perp}}\; e^{i(\boldsymbol{y}_\perp - \boldsymbol{x}_{n\perp})\cdot\boldsymbol{q}_{2\perp}} \\ &\times a^{(-)*}(\boldsymbol{q}_1)\; a^-(\boldsymbol{q}_2)\; \delta(x^+ - x_n^+) = \int dx^+ \int \frac{d^2\boldsymbol{q}_\perp}{(2\pi)^2}\; e^{i(\boldsymbol{y}_\perp - \boldsymbol{x}_\perp)\cdot\boldsymbol{q}_\perp}\; |a(\boldsymbol{q}_\perp)|^2. \end{aligned} \tag{2.35}$$

By proceeding in the same way for each of the remaining terms, eq. (2.33) reads

$$\frac{1}{N}\mathrm{Tr}\Big\langle W^\dagger(\boldsymbol{x}_\perp)W(\boldsymbol{y}_\perp)\Big\rangle = 1 - C_F \int \frac{d^2\boldsymbol{q}_\perp}{(2\pi)^2}\; |a(\boldsymbol{q}_\perp)|^2\; \left(1 - e^{i(\boldsymbol{y}_\perp - \boldsymbol{x}_\perp)\cdot\boldsymbol{q}_\perp}\right), \tag{2.36}$$

where the color factor comes from summing over final and averaging over initial color states[8].

At this point, it is convenient to define the dipole cross-section as

$$\sigma(\boldsymbol{y}_\perp - \boldsymbol{x}_\perp) = 2\int \frac{d^2\boldsymbol{q}_\perp}{(2\pi)^2}\; |a(\boldsymbol{q}_\perp)|^2\; \left(1 - e^{i(\boldsymbol{y}_\perp - \boldsymbol{x}_\perp)\cdot\boldsymbol{q}_\perp}\right). \tag{2.37}$$

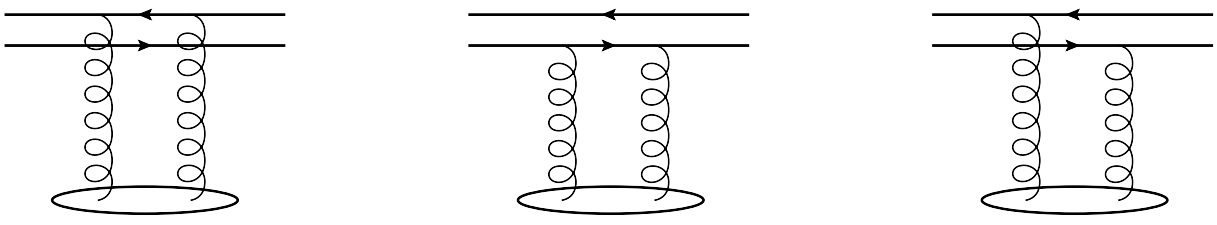

Figure 2.6: Diagrammatic representation of the different contributions to the two-point correlator within the Gaussian approximation framework.

[8] Again, for the gluon case the resulting color factor is C_A.

It is worthwhile to emphasize that over this derivation an assumption about the distribution of the scattering centers has been implicitly carried out. As previously stated, the scattering centers are meant to be located each other at a distance corresponding to the Debye screening length, what is effected via introducing the longitudinal density of scattering centers, $n(x^+) = \sum_n \delta(x^+ - x_n^+)$. Finally, under the embodied assumptions, the correlation function (2.31) proves to be

$$\frac{1}{N}\mathrm{Tr}\Big\langle W^\dagger(\boldsymbol{x}_\perp)W(\boldsymbol{y}_\perp)\Big\rangle_{\text{(one scattering)}} = 1 - C_F \int dx^+\; n(x^+)\sigma\left(\boldsymbol{y}_\perp - \boldsymbol{x}_\perp\right), \tag{2.38}$$

where the quark and the antiquark are placed at $\boldsymbol{y}_\perp$ and $\boldsymbol{x}_\perp$ respectively.

The preceding equation represents nothing but the result of cutting out the above-mentioned opacity expansion [70, 76] at first order, that is to say, when allowing the energetic parton to scatter at most once. This is also known as the single hard scattering approximation (SHSA), expected to be significant for mean free paths much longer than the length of the medium, which accordingly is assumed to be dilute. When the all-order resummation is effected, the series converges to

$$\frac{1}{N}\mathrm{Tr}\Big\langle W^\dagger(\boldsymbol{x}_\perp)W(\boldsymbol{y}_\perp)\Big\rangle = \exp\left\{-\frac{C_F}{2}\int dx^+\; n(x^+)\sigma(\boldsymbol{y}_\perp - \boldsymbol{x}_\perp)\right\}, \tag{2.39}$$

as it emerges from the multiple soft scattering approximation (MSSA), collectively referred to as the BDMPS-Z/ASW approach [64–67, 72, 73]. It is particularly interesting to note that the opacity expansion can be traced back as a limit for the solution of the BDMPS–Z path integral. With a strong presence in the literature, both approximations are the major prescriptions to take density effects into account as a conduct for building the medium-induced branching. The most relevant points on each are given below.

In the context of the opacity expansion approach, one way to justify the independent nature of the collection of static sources which comprise the medium is to model the scattering centers as screened Yukawa type potentials with Debye screening length $1/\mu_D$,

$$|a^-(\boldsymbol{q}_\perp)|^2 = \frac{\mu_D^2}{\pi(\boldsymbol{q}_\perp^2 + \mu_D^2)^2}. \tag{2.40}$$

As was stated when computing the two-point correlator, the opacity expansion is a power series expansion built on the basis of the effective number of scatterings defined within the integrand function $[n(\xi)\sigma(\boldsymbol{y}_\perp - \boldsymbol{x}_\perp)]^N$ in eqs. (2.38) and (2.39). Staring at each nth-order of the series, one sees that the zeroth order stands for the vacuum-like input, while $N = 1$, explicitly shown in eq. (2.38), determines the leading contribution according to the predicted medium modifications.

At this stage, beyond first order any contribution is subleading and accounts for the interference effects arising between the medium constituents, thus supporting an overall understanding of the model based on hard momentum transfers off the medium. However, the greater the density of scattering centers, the less accurate it will be to discard higher-order corrections to the opacity expansion so that a resummation over the whole perturbative series is required. The MSSA – sometimes also referred to as dipole approximation, valid for opaque media, takes on this role by resumming high-density effects to all orders. More specifically, under the assumption that low momentum transfer processes in each scattering dominate the cross-section, the dipole cross-section, which determines the strength of a single elastic scattering, can be approximated by [66]

$$\sigma(\boldsymbol{r}_\perp) \simeq k\boldsymbol{r}_\perp^2, \tag{2.41}$$

known as the harmonic oscillator approximation, where the details about the specific properties of the medium enter into the proportionality factor through the transport coefficient, $\hat{q}(\xi) := 2\sqrt{2}n(\xi)k$. It is used as the phenomenological basis to be inferred from data [107, 108], thus constituting the appropriate baseline parameter to test the actual theoretical predictions [109]. Furthermore, as a gluon receives random kicks from the medium constituents, with each kick transferring a momentum squared $\sim \mu_D^2$, one can estimate the also called jet quenching parameter $\hat{q}$ as the growth rate of the average transverse momentum squared, namely the momentum broadening per mean free path,

$$\frac{d\langle k_\perp^2\rangle}{dt} \simeq \frac{\mu_D^2}{\lambda} := \hat{q}. \tag{2.42}$$

In view of the above discussion, it is implied that both the SHSA and the MSSA fall within the same picture: in the former approximation one hard scattering is included, while in the latter multiple soft scatterings are resummed to all orders. The dipole approximation can, however, be interpreted as meaning that the whole medium acts coherently as a single scattering center with a Gaussian momentum distribution. Approaches that interpolate between these two extreme scenarios have recently become available [110–112].

To wrap up this piece it is important to stress that besides the correlator of two Wilson lines handled above within the Gaussian approximation, higher-point correlation functions naturally arise when computing cross-sections for processes involving more particles in the final state. In such cases, the large-N_c limit, an useful and predictive expansion for understanding high-energy QCD dynamics, is often undertaken as an attempt to simplify the treatment in such a way that only a few of the explicit contributions become important. More specifically, once this approximation is implemented some of the correlations are suppressed by powers of N_c as compared to the dipole amplitude. In the coming chapters these sort of correlators are faced in depth as they inexorably emerge when addressing more challenging physical scenarios.

2.2.3 The medium-induced gluon radiation spectrum

Following the introduction of the BDMPS-Z/ASW approach, the medium-induced radiation amplitude corresponding to the splitting of a quark into a quark-gluon antenna is now considered. As a result of the hard process which materializes within the medium the energetic quark that splits is produced, then experiencing multiple scatterings together with the emitted gluon, which takes away a minor fraction of energy off the parent parton – $p^+ \gg k^+$. In accordance to the soft limit, the path followed by the incoming quark both before and after the splitting is eikonal and can therefore be described by the classical Wilson line (2.21), while the trajectory undergone by the radiated parton is encapsulated in the Green function (2.29) since it includes higher-order transverse corrections to the eikonal trajectory. The raised scenario is depicted in Fig. 2.7, where h represents the hard process giving rise to the leading parton, and the multiple scatterings suffered by the propagating partons are also shown.

Two leading contributions, allowing the gluon to exhibit vacuum-like propagation or in-medium rescattering, have to be considered in order to compute the total radiation amplitude [35]. They read, respectively,

$$\mathcal{M}_q \simeq -2gT^a \, \frac{\boldsymbol{k}_\perp \cdot \boldsymbol{\epsilon}_\perp}{k_\perp^2} \int d\boldsymbol{x}_\perp \, e^{-i\boldsymbol{k}_\perp \cdot \boldsymbol{x}_\perp} \, W(L^+, x_0^+; \boldsymbol{x}_\perp), \tag{2.43}$$

where x_0^+ and L^+ determine the longitudinal boundaries of the medium, and $\boldsymbol{k}_\perp$ and $\boldsymbol{\epsilon}_\perp$ accounts for, respectively, the momentum and polarization of the gluon radiated outside the medium, and

$$\begin{aligned} \mathcal{M}_g \simeq -\frac{2g}{k^+} \int dx^+ d^2\boldsymbol{x}_\perp \, e^{-i\boldsymbol{k}_\perp \cdot \boldsymbol{x}_\perp} \, W(x^+, x_0^+; \boldsymbol{0}) T^b \\ \times \boldsymbol{\epsilon}_\perp \cdot \frac{\partial}{\partial \boldsymbol{y}_\perp} \, \mathcal{G}^{ba}(L^+, \boldsymbol{x}_\perp; x^+, \boldsymbol{0}|k^+) \, W(L^+, x^+; \boldsymbol{0}). \end{aligned} \tag{2.44}$$

Here $\boldsymbol{y}_\perp$ has been set to zero to ensure the eikonality of the leading quark. The total amplitude is therefore the sum of eqs. (2.43) and (2.44),

$$\mathcal{M}_{\text{rad}} = \mathcal{M}_q + \mathcal{M}_g. \tag{2.45}$$

Squaring eq. (2.45) gives way to three different contributions according to the position of the radiation vertex in both amplitude and its complex conjugate, as can be seen from the diagrams presented in Fig. 2.8, where the contribution from vacuum radiation,

$$k^+ \frac{dI^{\text{vac}}}{dk^+ d^2\boldsymbol{k}_\perp} = \frac{\alpha_s C_F}{\pi^2} \frac{1}{k_\perp^2}, \tag{2.46}$$

pops up as well as expected. Singling out the remainder purely medium-induced gluon radiation contributions to the squared amplitude produces the result [35]

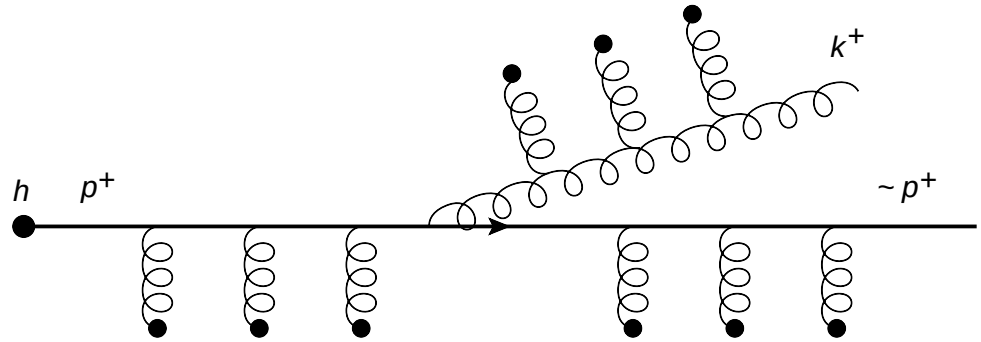

Figure 2.7: The medium-induced gluon radiation diagram within the soft approximation.

$$k^+\frac{dI^{\mathrm{med}}}{dk^+d^2\boldsymbol{k}_\perp}=\frac{\alpha_s C_F}{(2\pi)^2k^+}\,2\mathrm{Re}\Bigg\{\frac{1}{k^+}\int dx^+d\bar{x}^+d^2\boldsymbol{x}_\perp\; e^{-i\boldsymbol{k}_\perp\cdot\boldsymbol{x}_\perp}\; e^{-\frac{1}{2}\int_{x^+}^{L^+}d\xi\; n(\xi)\sigma(\boldsymbol{x}_\perp)}$$
$$\times\frac{\partial}{\partial\boldsymbol{y}_\perp}\cdot\frac{\partial}{\partial\boldsymbol{x}_\perp}\,\mathcal{K}(\bar{x}^+,\boldsymbol{x}_\perp;x^+,\boldsymbol{y}_\perp=\boldsymbol{0}|k^+) \tag{2.47}$$
$$+\int dx^+d^2\boldsymbol{x}_\perp\; e^{-i\boldsymbol{k}_\perp\cdot\boldsymbol{x}_\perp}\;2\frac{\boldsymbol{k}_\perp}{k_\perp^2}\cdot\frac{\partial}{\partial\boldsymbol{y}_\perp}\,\mathcal{K}(L^+,\boldsymbol{x}_\perp;x^+,\boldsymbol{y}_\perp=\boldsymbol{0}|k^+)\Bigg\},$$

with x^+ and $\bar{x}^+$ referring to the longitudinal coordinates in amplitude and complex-conjugate amplitude respectively, and $\mathcal{K}$ encapsulating the medium-averages to be performed,

$$\mathcal{K}(y^+,\boldsymbol{y}_\perp;x^+,\boldsymbol{x}_\perp|k^+)=\frac{1}{N^2-1}\mathrm{Tr}\Big\langle\mathcal{G}(y^+,\boldsymbol{y}_\perp;x^+,\boldsymbol{x}_\perp|k^+)W^\dagger(y^+,x^+;\boldsymbol{0})\Big\rangle, \tag{2.48}$$

which in this case will entail solving the two-dimensional path-integral

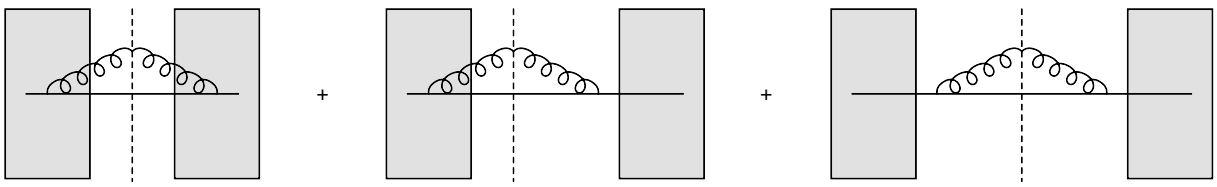

Figure 2.8: Schematic view of the diagrams corresponding to the three terms that emerge when computing the squared amplitude of the medium-induced gluon radiation in the soft limit. The dashed line sets the amplitude apart from its complex conjugate.

$$\mathcal{K}(y^+,\boldsymbol{y}_\perp;x^+,\boldsymbol{x}_\perp|k^+)=\int_{\boldsymbol{r}_\perp(x^+)=\boldsymbol{x}_\perp}^{\boldsymbol{r}_\perp(y^+)=\boldsymbol{y}_\perp}\mathcal{D}\boldsymbol{r}_\perp(\xi)\\ \times\exp\left\{\int_{x^+}^{y^+}d\xi\ \left[i\frac{k^+}{2}\dot{\boldsymbol{r}}_\perp^2-\frac{1}{2}n(\xi)\sigma(\boldsymbol{r}_\perp)\right]\right\}. \tag{2.49}$$

Then, using eq. (2.41), in the MSSA the preceding path-integral is equivalent to that of a harmonic oscillator,

$$\mathcal{K}(y^+,\boldsymbol{y}_\perp;x^+,\boldsymbol{x}_\perp|k^+)=\int_{\boldsymbol{r}_\perp(x^+)=\boldsymbol{x}_\perp}^{\boldsymbol{r}_\perp(y^+)=\boldsymbol{y}_\perp}\mathcal{D}\boldsymbol{r}_\perp(\xi)\\ \times\exp\left\{i\frac{k^+}{2}\int_{x^+}^{y^+}d\xi\ \left[\dot{\boldsymbol{r}}_\perp^2+i\frac{\hat{q}(\xi)}{2\sqrt{2}k^+}\boldsymbol{r}_\perp^2\right]\right\}. \tag{2.50}$$

Both [35] and [113] provide an instructive discussion on the solution of eq. (2.50) and the corresponding spectrum (2.47). Numerical results on the double-differential medium-induced gluon radiation spectrum for a quark crossing a static medium are shown in Fig. 2.9. A brief discussion on these results is featured below from a qualitative perspective.

The results contained therein are presented on the basis of the variables ω_c and κ, defined in terms of the medium properties – the medium transport parameter $\hat{q}$ and the length of the medium L – as follows,

$$\omega_c:=\frac{1}{2}\hat{q}L^2,\ \kappa:=\frac{k_\perp^2}{\hat{q}L}, \tag{2.51}$$

where ω_c corresponds to the maximal possible value for the gluon frequency. For its part, the formation time of the emitted gluon within the medium,

$$t_f\simeq\frac{2\omega}{k_\perp^2}, \tag{2.52}$$

can be read off on the propagator (2.50) describing non-eikonal corrections. It is instructive to compare this time scale with the medium length for the proper interpretation of the big picture. In cases where the formation time is much shorter than the length of the medium, $t_f\ll L$, consecutive incoherent scatterings take place as the spectrum is proportional to L/t_f. In the opposite limit, $t_f\gg L$, the entire medium acts as a single scattering center in a coherent way, thereby leading to a significant reduction of the medium-induced gluon radiation, which is nothing more than a manifestation of the already discussed LPM effect [66]. This can be noted clearly in Fig. 2.9 as a suppression of the spectrum for small values of κ. As a consequence, the examined spectrum shows neither collinear nor infrared divergencies, as opposed to the vacuum case one (2.15).

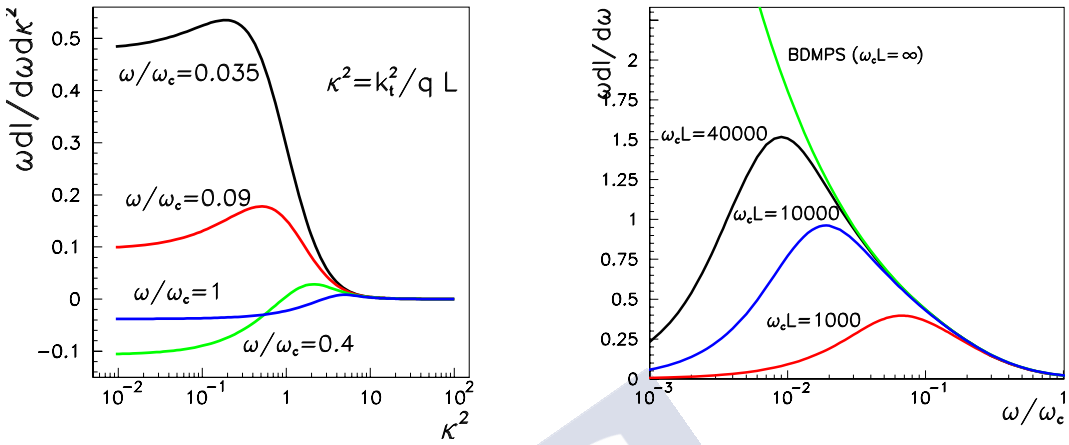

Figure 2.9: A numerical evaluation of the medium-induced gluon radiation spectrum (2.47) for a high-energy quark propagating through a static medium as a function of the variables (2.51) (results from [35]).

In closing, it is important to state that in real-life heavy-ion collisions the created collective medium is dynamically evolving and spreading out itself. Such a scenario can be transferred directly into the framework via assuming a time-dependent longitudinal density of scattering centers. A straightforward way of modeling the evolution of the medium is by parameterizing this density in terms of a power-dependence regarding the diluteness of the medium as it expands, $n(\xi) \simeq 1/\xi^{\alpha}$, with α the dilution factor. [35] also presents the corresponding spectra for different values of α.

2.2.4 The radiation spectrum off a $q\bar{q}$-antenna in a dense medium

As has been presented in the previous subsection, the medium-induced gluon radiation spectrum off a single parton does not exhibit any of the divergencies evidenced in the vacuum case. Additionally, the spectrum is strongly suppressed for formation times of the emitted partons larger than the length of the medium, thus showing a major contribution at a characteristic energy and radiation angle on grounds of the medium properties. This proves certainly well that the dense medium is responsible for the energy loss undergone by the leading parton attributable to the radiative process. However, the role of the physical scenario revisited above is limited since it does not incorporate the interference effects that emerge when studying medium-induced radiation off multiple emitters, the block for building up the partonic cascade in the presence of a medium.

As earlier noted too when discussing the different models for studying medium-induced radiation in hot and dense matter, several approaches have been developed for addressing multiple emissions setups. For example, HT includes the medium-induced radiation spectrum as a modification of the standard Altarelli-Parisi splitting function in vacuum, the higher-twist medium-modified DGLAP evolution equation [82]. Nevertheless, an accurate description for jet evolution in matter requires the analysis of coherence effects between subsequent emitters, as the vacuum case makes clear inasmuch as interference contributions are responsible for angular ordering.

With the above picture in view, some key points on a well-known study that seeks to mitigate the discussed limitations are presented in this piece [114–116]. More specifically, the gluon emission off a quark-antiquark antenna in a medium is reviewed to set the stage for the development of the studies which constitute the heart of this thesis. As will be seen, they are heading in exactly the same direction but somehow one step further in terms of getting close to a real-life parton shower.

Along the same line of argument proposed in subsection 2.1.1 for studying the radiation spectrum off a $q\bar{q}$-dipole propagating in vacuum, medium effects on the gluon radiation spectrum off the pair are discussed here. The physical scenario consists of a color singlet or octet antenna with an opening angle $\theta_{q\bar{q}}$ travelling through a static deconfined medium as a result of the decay of a highly virtual photon or gluon, respectively. Returning to the vacuum case that has been introduced earlier – eq. (2.12), the spectrum of radiated gluons with energy ω and transverse momentum k reads, for a singlet dipole,

$$\omega \frac{dN^{\text{vac}}_{\text{sing}}}{d^3k} = \frac{\alpha_s C_F}{(2\pi)^2 \omega^2} W_{q\bar{q}}, \tag{2.53}$$

with $W_{q\bar{q}} = \mathcal{R}_q + \mathcal{R}_{\bar{q}} - 2\mathcal{J}$, so that the spectrum is given by the independent radiation off the antenna constituents and the interferences between them. Incorporating the medium into this picture allows for the possibility of both the leading and the emitted partons to interact with the background field.

In a similar fashion to the medium-induced gluon radiation spectrum off a single parton, three different contributions have to be taken into account – displayed in Fig. 2.10. Below is an anticipation of the outcome for the interference spectrum assuming eikonality for the leading partons whilst relaxing the eikonal approximation for the emitted gluon [114, 116],

$$\begin{aligned}\mathcal{J} = \text{Re} \int_0^\infty dt' \int_0^{t'} dt \ & [1 - \Delta_{\text{med}}(t)] \\ & \times \int d^2\boldsymbol{z} \ \exp\left[-i\boldsymbol{\kappa}\cdot\boldsymbol{z} - \frac{1}{2}\int_{t'}^\infty d\xi \ n(\xi)\sigma(\boldsymbol{z}) + i\frac{\omega}{2}\delta\boldsymbol{n}^2 t\right] \\ & \times (\boldsymbol{\partial}_y - i\omega \ \delta\boldsymbol{n})\cdot\boldsymbol{\partial}_z \ \mathcal{K}(t', \boldsymbol{z}; t, \boldsymbol{y}|\omega)|_{\boldsymbol{y}=\delta\boldsymbol{n}t} + \text{sym.},\end{aligned} \tag{2.54}$$

where $\boldsymbol{\kappa} = \boldsymbol{k} - x\boldsymbol{p}$ ($\bar{\boldsymbol{\kappa}} = \boldsymbol{k} - \bar{x}\bar{\boldsymbol{p}}$), $x = \omega/p^+$, is the gluon transverse momentum with respect to the quark (antiquark) and $\delta\boldsymbol{n} := \delta\boldsymbol{k}/\omega$, with $\delta\boldsymbol{k} := \boldsymbol{\kappa} - \bar{\boldsymbol{\kappa}}$ the relative transverse momentum of the $q\bar{q}$-antenna, being closely associated with the opening angle of the pair as $|\delta\boldsymbol{n}| \simeq \sin\theta_{q\bar{q}}$. The symmetrical term comes from switching $\boldsymbol{\kappa} \to \bar{\boldsymbol{\kappa}}$ and, accordingly, $\delta\boldsymbol{n} \to -\delta\boldsymbol{n}$.

The independent components, $\mathcal{R}_q$ and $\mathcal{R}_{\bar{q}}$, can be traced from the preceding expression for the interference spectrum via taking $\delta\boldsymbol{n} \to 0$. As an example, the quark component is given by

$$\begin{aligned}\mathcal{R}_q = 2\mathrm{Re}\int_0^\infty dt' \int_0^{t'} dt \int d^2\boldsymbol{z} \exp\left[-i\boldsymbol{k}\cdot\boldsymbol{z} - \frac{1}{2}\int_{t'}^\infty d\xi\; n(\xi)\sigma(\boldsymbol{z})\right] \\ \times\, \boldsymbol{\partial}_y \cdot \boldsymbol{\partial}_z \mathcal{K}(t', \boldsymbol{z}; t, \boldsymbol{y}|\omega)\Big|_{\boldsymbol{y}=0},\end{aligned} \tag{2.55}$$

in this way supporting the result for the medium-induced gluon radiation spectrum shown in the previous subsection, eq. (2.47). An analogous expression holds for the antiquark component, $\mathcal{R}_{\bar{q}}$.

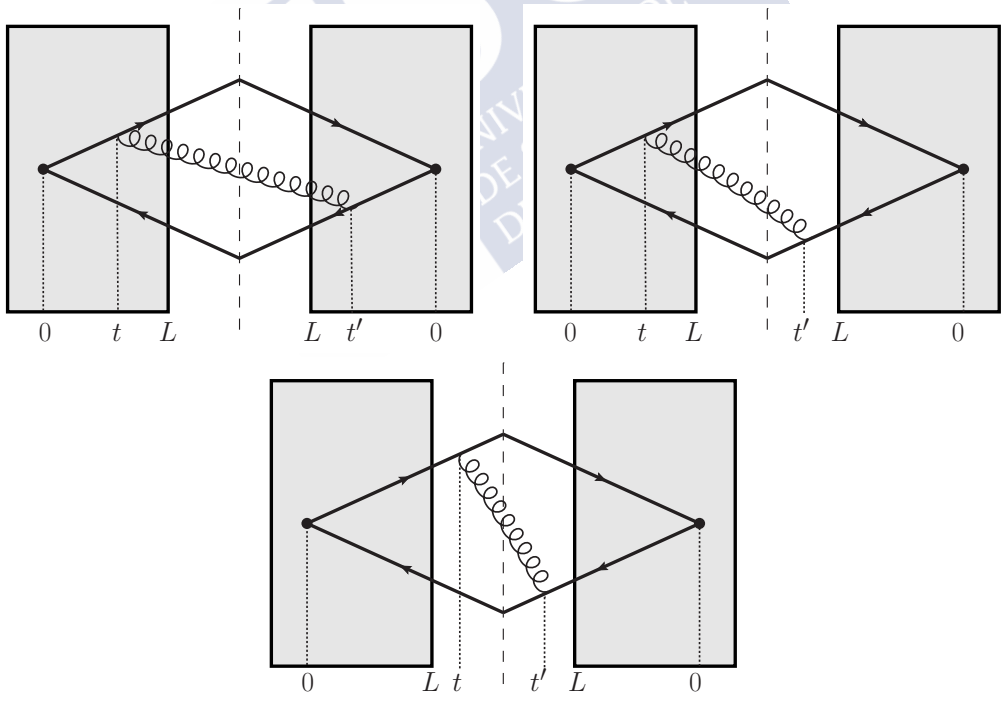

Figure 2.10: The three diagrams contributing to the gluon spectrum off the antenna in the medium case. Both the *in-in* and *in-out* components are sketched in the panels at top, whereas the bottom one is identified with the vacuum contribution (diagrams taken from [116]).

Eq. (2.54) characterizes the radiation off the quark-antiquark pair at various stages of its progress through the medium, as further described herein. At the beginning, the two-parton system originated from the splitting of a parent parton in a color singlet state, $\gamma^* \to q\bar{q}$, is assumed to form at the origin of the coordinate space, spreading over the medium until the gluon emission takes place. In the interim, the antenna-medium interaction is described by the survival probability [116]

$$\mathcal{S}_{(t,0)} := 1 - \Delta_{\text{med}}(t,0) = \exp\left[-\frac{1}{2}\int_0^t d\xi\ n(\xi)\sigma(\delta\boldsymbol{n}\ \xi)\right], \tag{2.56}$$

where $\sigma(\delta\boldsymbol{n}\ \xi)$ is the dipole-medium cross-section. The preceding equation describes the rate of color decoherence of the pair as a result of color interactions with the deconfined medium before the emission occurs. The decoherence parameter $\Delta_{\text{med}}(t,0)$, implicit in the definition of the survival probability $\mathcal{S}_{(t,0)}$, determines the decoherence time t_d, a physical time-scale that governs the color decoherence of the dipole inside the medium. In this way, $t \gg t_d$ implies that the $q\bar{q}$-system decoheres in color and the interference contribution is therefore suppressed. At this stage, the gluon is produced at time t in the amplitude and t' in its complex conjugate. Within the time-like separation between those times, better known as the formation time, the dynamics of the emerging dipole system is characterized by

$$\mathcal{K}(t',\boldsymbol{z};t,\boldsymbol{y}|\omega) = \int \mathcal{D}[\boldsymbol{r}]\ \exp\left\{\int_t^{t'} d\xi\ \left[i\frac{\omega}{2}\dot{\boldsymbol{r}}^2(\xi) - \frac{1}{2}n(\xi)\sigma(\boldsymbol{r})\right]\right\}, \tag{2.57}$$

the same two-dimensional path-integral arising when performing the medium averages for computing the medium-induced gluon radiation spectrum, eq. (2.49), which encompasses the Brownian motion exhibited by the gluon in the transverse plane from time t to t'. It arises as a result of the accumulation of momentum from the medium and leads to a change of the dipole size from $\boldsymbol{r}(t) = \boldsymbol{y}$ to $\boldsymbol{r}(t') = \boldsymbol{z}$. Moving forward on the dynamics picture, the characterization of further propagation from time t' onward is present in the middle term of the second line in eq. (2.54). More specifically, it accounts for the additional momentum accumulated from the medium by the gluon. Finally, the last term in the second line of eq. (2.54) proves to be independent of the medium attributes.

Before going deeper in discussing the uprising regimes for in-medium gluon emissions, it is particularly important to define the previous quantities in the context of the already introduced harmonic oscillator approximation (2.41),

$$n(t)\sigma(\boldsymbol{r}) \simeq \frac{1}{2}\hat{q}(t)\boldsymbol{r}^2, \tag{2.58}$$

valid within the multiple soft scattering approximation framework. In this approximation,

the decoherence parameter (2.56) is given by

$$\Delta_{\text{med}}(t) = 1 - \exp\left[-\frac{1}{12}\hat{q}\ \delta\boldsymbol{n}^2 t^3\right], \tag{2.59}$$

since the antenna is assumed to linearly grow with time. It is possible now to read the decoherence time t_d off the equation above as looking back at eq. (2.56) it unambiguously stems from the solution of

$$\frac{1}{2}\int_0^{t_d} d\xi\ n(\xi)\sigma(\delta\boldsymbol{n}\ \xi) = 1, \tag{2.60}$$

so for this specific case the time-scale for decoherence of the pair takes the form

$$t_d \simeq \left(\frac{1}{\hat{q}\theta_{q\bar{q}}^2}\right)^{1/3}. \tag{2.61}$$

Likewise, the formation time of a medium-induced gluon can be identified in eq. (2.57). Further, it can be heuristically estimated in terms of the medium transport parameter $\hat{q}$ since within a time t_f, the gluon acquires a transverse momentum squared $k_f^2 \simeq \hat{q}t_f$, where $t_f \simeq 2\omega/k_\perp^2$, thus deducing

$$t_f \simeq \left(\frac{2\omega}{\hat{q}}\right)^{1/2}, \tag{2.62}$$

so that the formation time in vacuum entered in subsection 2.1.1, $t_f \simeq 2/(\omega\theta^2)$, is greater for soft gluons emitted at a fixed angle θ. Indeed, recalling the heuristic interpretation raised throughout the bottom part of the 2.1.1 piece, conducted to properly understand and reflect on the gluon radiation spectrum in vacuum, encourages a similar discussion based on the relevant scales of the current problem. In particular, the characteristic scales that matter in this context are the transverse size of the antenna, $r_\perp = \theta_{q\bar{q}}L$, where $\theta_{q\bar{q}}$ is the antenna opening angle, and the tranverse color screening length of the medium, given by the inverse of the characteristic medium scale, Q_s^{-1}, which, by definition, is the maximal transverse momentum that can be accumulated by an induced parton when crossing the whole medium. Intuitively, this scale is also known as the saturation momentum, and it is achieved for a gluon with a frequency ω_c, the maximal gluon frequency already introduced in (2.51) as $\omega_c = (1/2)\hat{q}L^2$. For a dense medium, it reads $Q_s^2 = \hat{q}L$.

Following closely the discussion conducted in [116], it is therefore natural to consider two different regimes on the grounds of the following expression for the medium decoherence parameter (2.56),

$$1 - \Delta_{\text{med}} \simeq e^{-Q_s^2 r_\perp^2}. \tag{2.63}$$

To start with, in the cases of small antenna sizes, $r_\perp < Q_s^{-1}$, the medium cannot resolve the inner structure of the system, thus interacting as a coherent ensemble. This is referred to as the dipole regime. In terms of the characteristic time scales, this condition is equivalent to say that the decoherence time is much greater than the medium length, $t_d \gg L$. It is even possible to decipher the puzzle on the basis of angular scales. Specifically, the aforementioned conditions can also be translated into the context in which the opening angle of the pair is smaller than some critical angle θ_c,

$$\theta_c = \frac{Q_s}{\omega_c} = \frac{2}{(\hat{q}L^3)^{1/2}}, \tag{2.64}$$

the formation angle for a gluon with the maximal frequency ω_c, in accordance to the relations above. In short, in this regime jet-medium interactions induce coherent radiation because the antenna probes the medium, being the interference spectrum directly proportional to

$$\Delta_{\text{med}} = \frac{1}{12} Q_s^2 r_\perp^2. \tag{2.65}$$

Alternatively, if $r_\perp > Q_s^{-1}$ is fulfilled, the medium probes the inner structure of the antenna. In such a situation, very little time passes until the antenna constituents decorrelate themselves from the moment they enter the medium. This is the so-called decoherence regime, which occurs for $t_d < L$, meaning that the two-parton system decoheres at a finite distance within the medium. The spectrum therefore consists of independent radiation off each of the emitters since interferences are strongly suppressed in a way that the decoherence parameter reaches its highest value, $\Delta_{\text{med}} = 1$.

A precise derivation of the three different components which constitute the radiation spectrum off the two color charges crossing the medium has been carried out in [116] within the harmonic oscillator approximation. A numerical study also supports the two-regimes picture commented on above. In order to complete this piece and with a view towards linking with the physical scenario addressed in the chapter that follows the *out-out* component, responsible for the decoherence of the vacuum radiation, is discussed.

Emissions taking place outside the medium correspond to the diagram illustrated in the panel at bottom of Fig. 2.10. Within the harmonic oscillator approximation, it reads [116]

$$\mathcal{J}^{out-out} = [1 - \Delta_{\text{med}}(L, 0)]\, 4\omega^2 \frac{\boldsymbol{\kappa} \cdot \bar{\boldsymbol{\kappa}}}{\boldsymbol{\kappa}^2 \bar{\boldsymbol{\kappa}}^2} \cos\left[\frac{(\boldsymbol{\kappa} + \bar{\boldsymbol{\kappa}}) \cdot \boldsymbol{r}}{2}\right], \tag{2.66}$$

where $\boldsymbol{r} = \delta \boldsymbol{n} L$.

It is of upmost importance to notice that the preceding expression is directly proportional to the vacuum interference emission pattern encapsulated in the radiation function (2.7), which displays the angular ordering property between subsequent emissions,

$$W_{q\bar{q}} = 2\omega^2 \frac{p_1 \cdot p_2}{(p_1 \cdot k)(p_2 \cdot k)}, \tag{2.67}$$

bearing in mind that p_1 and p_2 are the four-momenta of the outgoing quark and antiquark, respectively, and ω is the energy of the gluon with momentum k. To prove that, it is enlightening to rewrite the preceding expression in terms of the variables present in eq. (2.66) as follows,

$$W_{q\bar{q}} = 4\omega^2 \frac{\delta\boldsymbol{\kappa}^2}{\boldsymbol{\kappa}^2\bar{\boldsymbol{\kappa}}^2} = 4\omega^2 \left(\frac{1}{\boldsymbol{\kappa}^2} + \frac{1}{\bar{\boldsymbol{\kappa}}^2} - 2\frac{\boldsymbol{\kappa} \cdot \bar{\boldsymbol{\kappa}}}{\boldsymbol{\kappa}^2\bar{\boldsymbol{\kappa}}^2} \right), \tag{2.68}$$

recalling that $\boldsymbol{\kappa}$ ($\bar{\boldsymbol{\kappa}}$) is the gluon transverse momentum with respect to the quark (antiquark), and $\delta\boldsymbol{\kappa}$ is the relative transverse momentum of the pair. This arrangement is exactly the decomposition of the spectrum (2.12) into the independent components and the interferences,

$$W_{ij} = \mathcal{R}_q + \mathcal{R}_{\bar{q}} - 2\mathcal{J}, \tag{2.69}$$

as has been shown in detail in subsection 2.1.1. Here both $\mathcal{R}_q := 4\omega^2/\boldsymbol{\kappa}^2$ and $\mathcal{R}_{\bar{q}} := 4\omega^2/\bar{\boldsymbol{\kappa}}^2$ account for the radiation spectrum off the independent constituents of the antenna, and $\mathcal{J} := 4\omega^2 \frac{\boldsymbol{\kappa}\cdot\bar{\boldsymbol{\kappa}}}{\boldsymbol{\kappa}^2\bar{\boldsymbol{\kappa}}^2}$ describes the two-parton system interference.

Accordingly, it can be said that the *out-out* component therefore controls the decoherence of the vacuum radiation as it only entails the two-parton interaction with the medium. In fact, one might reasonably expect that in view of the corresponding diagram – at the bottom of Fig. 2.10. Most remarkably, it constitutes the leading term in the soft limit, as will be shown in greater detail in the next chapter.

Finally, albeit limited to the color singlet configuration as it greatly simplifies the color algebra, it is possible to extrapolate these findings to other color configurations of the final state by proceeding in the same way. As an example, the creation of the $q\bar{q}$-antenna from an octet source is physically a more prominent scenario. In pure vacuum, the cross-section for the color octet case reads [1]

$$\omega \frac{dN^{\text{vac}}_{\text{octet}}}{d^3k} = \frac{\alpha_s}{(2\pi)^2\omega^2} \left(C_F \mathcal{R}_{\text{sing}} + C_A \mathcal{J} \right), \tag{2.70}$$

where the radiation function W_{ij} given by eq. (2.69) has been renamed as $\mathcal{R}_{\text{sing}}$ to clearly trace the singlet component back. Contrary to the singlet case (2.53), the additional contribution, with $\mathcal{J}$ defined just below eq. (2.69), gives rise to large-angle emissions in what is seen as the radiation off the total charge of the pair, meaning radiation off the parent parton imagined to be on-shell – zero for a virtual photon or C_A for a virtual gluon,

thus retaining the angular-ordered pattern. In the medium context, the octet contribution to the total antenna radiation spectrum goes along the same line of reasoning and is given by the interference term. The discussion under way on the next chapter about the medium-induced radiation spectrum off the antenna in the soft limit will generate further evidence on this trend.

This last part of the present section served to set the foundations of medium-induced radiation within the BDMPS-Z/ASW approach. The consequences of the mechanism responsible for in-medium radiation have been studied throughout different physical scenarios. In particular, the radiation spectrum produced by a two-parton system has proven very successful to describe the first steps of the showering of highly virtual partons originated from the initial stages of heavy-ion collisions, seeking to anchor the debate on the nature of in-medium energy loss or the medium response to jet propagation. Working on the base of these works, Chapters 3, 4 and 5 of this manuscript reflect upon further dynamical setups, always trying to approach the maximum the standard of real-life parton cascades.

2.3 Small-x physics in pQCD

This final piece of this chapter is devoted to lay the ground for a proper understanding of the quantitative study conducted in Chapter 6 relying on angular correlations arising in the spectrum of gluons produced in HICs. Particle correlations lead to the underlying dynamics responsible for two separate substantive phenomena that are currently under study since they can give answers to many of the raised questions regarding the nature of hot and dense deconfined matter. One is the phenomenon of perturbative saturation, which carries valuable information about the early stages of the collisions, and the other is jet quenching, the main topic of this thesis, thoroughly discussed throughtout this manuscript. The Color Glass Condensate (CGC) provides a framework to study the approach to saturation, as well as the subsequent evolution of the gluon distribution into the saturation regime [37, 38, 118–125]. A number of review papers play just on this subject, giving full details of the formalism [40, 126, 127]. It is revisited herein, placing emphasis on applications as the one provided in Chapter 6.

As the elementary degrees of freedom in QCD are partons, the quark and gluon content within the hadrons involved in hadronic collisions is a matter of high importance. At very high energies, the geometry of the nucleon changes because of Lorentz contraction in a way that it appears to be two-dimensional in the laboratory frame of reference. At the same time, the internal time-scales of the nucleon, such as the short-term fluctuations[9]

[9]Initial state fluctuations into states having additional gluons and quark-antiquark pairs can occur. They are short lived, namely with a lifetime inversely proportional to their energy.

or the lifespan of the interactions between the constituents, are multiplied by the same Lorentz factor. Upon this time dilation, the nucleon ingredients are displayed as free during the high-energy collision. What is more, more fluctuations are revealed, thus increasing the number of gluons seen in the reaction, as observed experimentally in DIS at HERA [128].

Such growth on the gluon distribution at small-x leads one to think of discarding perturbative approaches when addressing hadronic interactions in the high-energy limit. Parton distributions saturate under these circumstances in a way that, when the gluon occupation number is of order $1/\alpha_s$, multiple interactions are important at each order and special care must be taken in applying perturbative methods [36]. Given the situation requiring the resummation of different components that come from multiple interactions, many interesting implications have to be put in perspective within the big picture.

In this regard, possibilities have been opened since it was first proposed to use weak-coupling methods as a comprehensive manner of targeting this situation, in particular, through the generation of the saturation momentum scale Q_s, a scale that can be much greater than the non-perturbative scale Λ_{QCD}. It arises as a consequence of non-linear interactions between gluons and is defined as the product of the coupling constant α_s multiplied by the gluon density per unit area, thus measuring the strength of the gluon recombination processes that take place as the gluon density grows [36, 129]. The CGC approach provides a physical picture which allows to organize the calculation of these processes in the saturation regime, and thereby contributes to guess what diagrams are relevant and have to be included in the resummation.

2.3.1 BFKL dynamics

Considering this boost-like evolution of the nucleon structure leads to understand the evolution of the gluon content at small-x as a cascade of gluons, initiated by each valence quark, that have increasingly small longitudinal momenta as one moves down in the cascade. Provided that these gluon cascades do not interact, the evolution can be expressed in terms of a linear equation for the gluon distribution, the Balitsky-Fadin-Kuraev-Lipatov (BFKL) equation [130, 131]. The derivation of the BFKL equation in transverse coordinate space is straightforward to follow in terms of the dipole model [132]. Considering the dipole splitting depicted in Fig. 2.11 in the large-N_c limit – in which the emitted gluons are replaced by quark-antiquark pairs, the corresponding evolution equation reads [133]

$$\frac{\partial}{\partial Y} n(x_0 - x_1, x, Y) = \frac{\alpha_s C_F}{\pi^2} \int d^2x_2 \frac{(x_0 - x_1)^2}{(x_0 - x_2)^2 (x_1 - x_2)^2} \times \left[n(x_0 - x_2, x, Y) + n(x_2 - x_1, x, Y) - n(x_0 - x_1, x, Y) \right], \tag{2.71}$$

where $n(x_0 - x_1, x, Y)$ accounts for the number density of dipoles of size x in an onium state of size $(x_0 - x_1)$ at rapidity Y. It is intuitive to match-up each of the different pieces of the preceding equation with the ingredients present in the physical scenario.

Figure 2.11: A color dipole splitting into two new dipoles in the large-N_c limit.

First, it is natural to find the soft emission probability in transverse coordinate space, also known as the dipole kernel, within the integral since the evolution stems from soft gluon emissions. Besides that, the first two terms in the brackets are the densities of the two new color dipoles, whilst the remaining term corresponds to a virtual correction that illustrates the loss of the initial dipole after the soft gluon emission occurs. Although the large-N_c limit is undertaken for computing the evolution equation only in terms of dipole densities, finite-N_c corrections do not modify its structure within the leading logarithmic approximation – in which the longitudinal momentum of the emitted gluon is much softer than the leading partons.

Also noteworthy is that the forward scattering amplitude of a dipole consisting on a quark and an antiquark with transverse coordinates x_0 and x_1, respectively, evaluated at rapidity Y, $N(x_0, x_1, Y)$, satisfies the BFKL equation as well,

$$\frac{\partial}{\partial Y} N(x_0, x_1, Y) = \frac{\alpha_s C_F}{\pi^2} \int d^2 x_2 \frac{(x_0 - x_1)^2}{(x_0 - x_2)^2 (x_1 - x_2)^2} \times \left[N(x_0, x_2, Y) + N(x_2, x_1, Y) - N(x_0, x_1, Y) \right], \tag{2.72}$$

as $N(x_0, x_1, Y)$ results from convoluting the dipole density n with the amplitude of scattering of a dipole from a nucleon integrated over the nuclear length. Although variations exist when it comes to solving the BFKL equation ([131, 134, 135], amongst others), generic solutions grow exponentially with rapidity, which leads to a violation of unitarity. This asymptotic increase can be related back to the growth of the gluon distribution at small-x. Given this, the Balitsky-Kovchegov (BK) equation was introduced to mitigate this problem.

2.3.2 BK equation and gluon saturation

As noted above, the BFKL equation presents a continuous increase of the gluon density, meaning that it does not account for the interactions between the gluons from different cascades that pop up at the stage where gluons become densely packed in the wavefunction of a nucleon. Balitsky and Kovchegov independently included for the first time nonlinear effects in the BFKL formalism [136–139].

On the basis of eq. (2.72), these mergings of gluons from different cascades slow down the growth in the gluon distribution at small-x by including a term where both dipoles can interact with the nucleus, so that the modified equation reads [133]

$$\begin{aligned}\frac{\partial}{\partial Y}N(x_0,x_1,Y) = \frac{\alpha_s C_F}{\pi^2}\int d^2x_2 \frac{(x_0-x_1)^2}{(x_0-x_2)^2(x_1-x_2)^2}\,[N(x_0,x_2,Y) \\ + N(x_2,x_1,Y) - N(x_0,x_1,Y) - N(x_0,x_2,Y)N(x_2,x_1,Y)],\end{aligned} \tag{2.73}$$

the Balitsky-Kovchegov (BK) equation, which fixes the limitations highlighted in the BFKL framework. Solutions to the BK equation show an exponential increase with Y that eventually saturates. The interpretation of this outcome is fairly intuitive: in the dilute regime, which corresponds to small scattering amplitudes, only valence quarks are probed. As the rapidity increases, the dipole can go deeply and also interact with gluons emitted off the valence quarks. In the regime of larger rapidities, these gluons radiate more and more gluons in ladder-like diagrams as the one pictured in Fig. 2.12. It is at this point when nonlinearities become important, thus controlling the increase in the gluon density in such a way that the scattering amplitude is bounded. Herewith emerges the phenomenon of gluon saturation, previously represented in Fig. 1.8.

It is important to establish the onset from which the impact of gluon saturation is relevant. The standard criterion can be written in terms of the gluon resolution scale Q as follows [127],

$$Q^2 \leq Q_s^2 \simeq \frac{\alpha_s x G(x,Q_s^2)}{\pi R_A^2}, \tag{2.74}$$

where $xG(x,Q_s^2)$ is the gluon distribution and R_A is the radius of the nucleus. The second member of the preceding inequality is the already introduced saturation momentum scale. Gluon saturation effects become important below this scale, thus becoming more evident for larger Q_s's. It is also possible to express the inequality above as a function of the mass number A and x since the gluon distribution of a nucleus is approximately proportional to A and its radius to $A^{1/3}$, and the x dependence can be extracted from experimental data. On this basis, the introduced criterion reads now

$$Q^2 \leq Q_s^2 \simeq A^{1/3}x^{-0.3}, \tag{2.75}$$

which is consistent with the fact that the gluon distribution in nucleons at small-x grows as $1/x$.

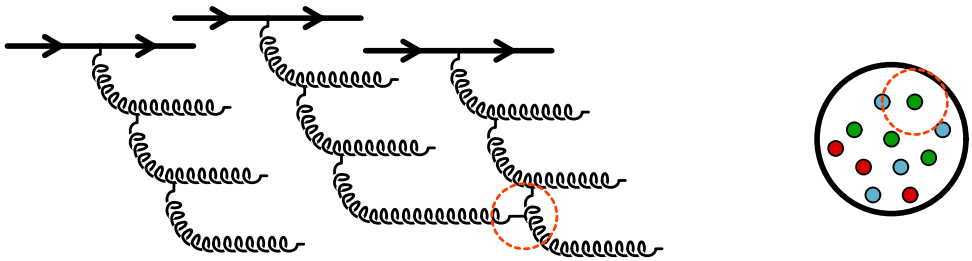

Figure 2.12: Different gluon showers originated from valence quarks within a nucleon (figure from [127]).

2.3.3 The Color Glass Condensate

Recalling that the CGC effective theory builds on the fact that the parton dynamics at small-x is slowed down by Lorentz time dilation, it is natural to treat such partons as time independent objects advancing at the speed of light along the light-cone. Hence, the only relevant point is the color charge they carry with, encapsulated in a color current as

$$J_a^\mu = \delta^{\mu+}\rho_a(x^-, \boldsymbol{x}_\perp), \tag{2.76}$$

where all components of the current except the longitudinal one have been ignored as it is the only enhanced by the Lorentz factor. Noteworthy is that the source current is independent of x^+ as color charges are assumed to be time independent. ρ_a represents the color charge density both in x^- and $\boldsymbol{x}_\perp$.

Finding a solution to the target field is not straightforward because this involves solving the classical Yang-Mills equation of motion with an external source,

$$[D_\mu F^{\mu\nu}]_a(x) = J_a^\nu(x). \tag{2.77}$$

However, in the Lorentz gauge – $\partial_\mu A^\mu = 0$, it is possible to find an analytical solution for the defined current, giving rise to

$$A_a^-(x) = A_a^i(x) = 0, \quad A_a^+(x) = -\frac{1}{\nabla_\perp^2}\rho_a(x^-, \boldsymbol{x}_\perp), \tag{2.78}$$

so it emerges very clearly from this result that specifying the ensemble of target fields is equivalent to specify the ensemble of the densities, what reasonates with the need to define a probability distribution $W[\rho_a]$ within the CGC approach. The McLerran-Venugopalan (MV) model [37–39] provides an approach of the functional $W[\rho_a]$ for large nuclei based on the assumption that color charge densities at two distinct points in the transverse plane are uncorrelated. This can be regarded as a consequence of confinement as color charges belonging to different nucleons are not correlated.

By virtue of the above concepts it is possible to calculate correlators for an arbitrary number of color charge densities and, accordingly, explicitly ascertain the weigth function for a large nucleus. The Central Limit Theorem (CLT) establishes that the distribution of color sources tends toward a Gaussian distribution characterized by a two-point correlation function given by

$$\left\langle \rho_a(x^-, \boldsymbol{x}_\perp)\rho_b(y^-, \boldsymbol{y}_\perp)\right\rangle = \delta^{ab}\delta(x^- - y^-)\delta^{(2)}(\boldsymbol{x}_\perp - \boldsymbol{y}_\perp)\mu^2(x^-), \tag{2.79}$$

where μ^2 characterizes the color charge density and, for the sake of simplicity, it is assumed to be independent of the transverse coordinates. In this context, the introduced picture can be reproduced with a Gaussian weight function as

$$W[\rho_a] = \exp\left\{-\int d^2x\; d^2y\; dz^-\; \frac{\rho_a(z^-, \boldsymbol{x}_\perp)\rho_a(z^-, \boldsymbol{y}_\perp)}{2\mu^2(z^-)}\right\}. \tag{2.80}$$

Given the distribution $W[\rho_a]$ defined by the preceding equation within the MV model, the computation of the expectation value of an observable $\mathcal{O}$ is carried out by means of determining the observable in an arbitrary configuration of the color sources, $\mathcal{O}[\rho_a]$, followed by the average over the distribution $W[\rho_a]$,

$$\langle \mathcal{O}\rangle = \int [\mathcal{D}\rho_a]\; W[\rho_a]\; \mathcal{O}[\rho_a]. \tag{2.81}$$

Another important feature is to include quantum evolution within the full picture, which is done by making the distribution function rapidity dependent with its evolution governed by the evolution equation of the two-point correlation function. In this context, however accounting for nonlinear effects, the derivation is performed in a similar fashion as the standard for handling BFKL evolution. After this procedure, the distribution function $W[\rho_a]$ obeys an evolution equation usually known as the Jalilian-Marian-Iancu-McLerran-Weigert-Leonidov-Kovner (JIMWLK) equation [118–125]. As a matter of fact, a generalization of the JIMWLK equation dictates the high-energy evolution responsible for rapidity correlations within the CGC approach [140]. There has been extensive discussion recently pointing out to the nature of correlated particle production, conclusively determining that the wave function of a highly energetic proton might bring with it preexisting correlations that are reflected in the final state [141, 142].

This motivates calculations specifically for this purpose within the CGC framework discussed in this piece. The final chapter of this thesis is precisely devoted to discuss the origin of correlations via studying the more straightforward process containing two-parton correlation functions.

3

Factorized picture of color coherence for gluon radiation off a double QCD antenna

In this chapter it is put forward an extension of the derivations presented in subsection 2.2.4 to multiple emissions with the ultimate goal of extrapolating the results to the subsequent parton branchings that constitute the basis of the full medium-modified parton shower. Turning to substance, the radiation off two antennas – a quark-antiquark and a quark-gluon (antiquark-gluon) dipoles, originated after a first hard splitting assumed to be instantaneous at the origin of the coordinate system within a colored medium, is computed. This study focuses on the interference phenomena that arise from the ensemble of medium-induced modifications after the very first splitting during the branching process. Calculations are performed in its high-energy limit, namely eikonality is assumed in order to fix the trajectories of the partons in the transverse position as they propagate away. The usual small-angle approximation also applies here. Both approximations are expected to be justified for this configuration, thus simplifying enormously the complexity of the problem. The final results provide an extension to previous studies of multi-gluon radiation in an attempt to stress the relevance of interference effects when characterizing the QCD branching process.

3.1 A few remarks on the physical scenario

As was pointed out in the previous piece, dealing with multiple emissions configurations encumbers the discussions mainly owing to the emergence of interferences amongst different processes. On one side is the vacuum shower, where color coherence is preserved in such a way as to lead to angular ordering. In this study, interference patterns may gradually alter the color coherence of the whole system over the decoherence time-scale, what is primarily due to medium-induced radiation. In particular, the focus is now on the process $\gamma^* \to q\bar{q}g_1g_2$, where both the splitting of the photon into the quark-antiquark antenna, $\gamma^* \to q\bar{q}$, and that of the leading partons, $q \to qg_1$ ($\bar{q} \to \bar{q}g_1$), are taken to be very hard, whilst the second gluon emission, g_2, is assumed to be soft – in concrete terms, the energies of all partons involved are much larger than any medium scale except for the last, very soft gluon. These kinematical choices allow for neglecting finite formation time effects for the splittings inside the medium, meaning that dipoles originate at a fixed point in both amplitude and complex-conjugate amplitude, what streamlines cumbersome algebra.

By way of summary, the setup raised here is the soft radiation off a QCD antenna consisting of a quark-gluon (antiquark-gluon) after one of the energetic partons radiates the mentioned hard gluon within a dense medium. This calculation attempts to universalize prior studies conducted on the impact of multiple parton emissions into the final state of a medium-modified parton cascade. More precisely, it aims to go beyond existing standards by seeking to track the coherence record between the consecutive emerging dipoles throughout the entire medium, something that can be controlled by means of the last radiation process naturally occuring in vacuum, just as all partons have already phased out the static medium.

As this scenario works in much the same way that the radiation pattern off a quark-antiquark antenna in the strict soft limit [116, 117], it is instructive to recall the full derivation of that radiation spectrum, which has already been introduced very briefly when reviewing the gluon emission spectrum off the antenna beyond the soft limit (see Fig. 2.10). This considers a color-singlet quark-antiquark pair that emanates from the splitting of a virtual photon occurring on very short-time scales within a medium of size L, namely the antenna is assumed to be created at the origin of the coordinate system in both amplitude and its complex-conjugate. In this regard, the non-radiation probability amplitude simply reads

$$\mathcal{M}_{q\bar{q}} \simeq \bar{u}_i(p) ie_q \gamma_\mu W_{ij}(L, 0; \boldsymbol{r}_1) W^\dagger_{jk}(0, L; \boldsymbol{r}_2) v_k(\bar{p}), \tag{3.1}$$

where $\bar{u}(p)$ and $v(\bar{p})$ are the spinors for the outgoing quark and antiquark, e_q is the quark's electric charge and γ_μ are the Dirac matrices. The fundamental Wilson lines at transverse positions $\boldsymbol{r}_1$ and $\boldsymbol{r}_2$ describe the propagation of the two-parton system from its origin to the end of the medium.

Now, what needs to be noticed is that the actual expression for the medium-modified probability amplitude (3.1) is not required right after since the goal is to factor out the Born-level production amplitude in order to purely discriminate the radiation spectra. There is, however, a need to backtrack the color coding, that is to say, the Wilson lines which account for the restoration of the color coherent structure among the leading partons.

The square of eq. (3.1) averaged over all color profiles is given by

$$\left\langle |\mathcal{M}_{q\bar{q}}|^2 \right\rangle_{\text{med}} = |\mathcal{M}_{q\bar{q}}|^2 \,, \tag{3.2}$$

since it is noticeable that the correlator of the resulting four Wilson lines collapses to unity, $\text{Tr}\left\{W(L,0;\boldsymbol{r}_1)W^\dagger(0,L;\boldsymbol{r}_2)W(L,0;\boldsymbol{r}_2)W^\dagger(0,L;\boldsymbol{r}_1)\right\} = \mathcal{I}$, thus breaking down the phase space for radiation. It is also important to stress that the square of the corresponding vacuum probability amplitude matches with the previous result. Indeed, as is to be expected, it can be explicitly retrieved by squaring eq. (3.1) straight after taking the Wilson lines to be unity. The following chapter sheds further light on this process via allowing the in-medium splitting to display a finite formation time, this way studying the medium modifications that arise as compared to this baseline.

Turning now to the evaluation of the inclusive spectrum for gluon radiation leads to a focus on the radiative interferences between those two emitters. In the strict soft limit, $\omega \to 0$, when the contribution from in-medium radiated gluons can be neglected due to LPM suppression[1], the interference spectrum to be computed is the one pictured in Fig. 3.1. First and foremost, the gluon emission probability amplitudes off each of the partons constituting the singlet antenna are given by

$$\mathcal{M}_{q\bar{q}g(q_g)} \simeq \bar{u}_i(p) i e_q \gamma_\mu t^a_{ij} W_{jk}(L,0;\boldsymbol{r}_1) W^\dagger_{kl}(0,L;\boldsymbol{r}_2) v_l(\bar{p}) \cdot g_s \left(\frac{p\cdot\epsilon}{p\cdot k}\right), \tag{3.3}$$

$$\mathcal{M}_{q\bar{q}g(\bar{q}_g)} \simeq \bar{u}_i(p) i e_q \gamma_\mu W_{ij}(L,0;\boldsymbol{r}_1) W^\dagger_{jk}(0,L;\boldsymbol{r}_2) t^a_{kl} v_l(\bar{p}) \cdot g_s \left(\frac{\bar{p}\cdot\epsilon}{\bar{p}\cdot k}\right), \tag{3.4}$$

where the emitted gluon has energy ω and transverse momentum $\boldsymbol{k}$. In order to proceed with the evaluation of the resulting cross-section, the squared amplitudes (3.3) and (3.4) have to be averaged over the whole ensemble of arbitrary medium color configurations and summed over gluon polarizations.

[1]This limit is remarkably convenient for the purpose of this study as it provides highly relevant information about the degree of color coherence between the two emitters that make up the antenna (see, e.g., [117]), which then is extensively generalized to the case of three emitters.

Accordingly, the direct terms, $\mathcal{R}_q$ and $\mathcal{R}_{\bar{q}}$, turn out to be trivial since the medium averages yield unity – just as for the non-radiation case. As an example, the quark component reads

$$\left\langle \left|\mathcal{M}_{q\bar{q}g(q_g)}\right|^2 \right\rangle_{\text{med}} = \left|\mathcal{M}_{q\bar{q}g(q_g)}\right|^2 = \left|\mathcal{M}_{q\bar{q}}\right|^2 C_F g_s^2 \frac{4}{\boldsymbol{\kappa}^2}, \tag{3.5}$$

which factorizes into the the non-radiation probability amplitude once again, in the same vein as for the vacuum case (for a pedagogical derivation of the vacuum emission pattern off a two-parton system go back to subsection 2.1.1). Here it has also been introduced $\boldsymbol{\kappa}$ as the transverse momentum of the gluon with respect to the quark, $\boldsymbol{\kappa} = \boldsymbol{k} - x\boldsymbol{p}$. The derivation of the antiquark component follows exactly the same steps as the former amplitude. It only implies the swap $\boldsymbol{\kappa} \to \bar{\boldsymbol{\kappa}}$, where $\bar{\boldsymbol{\kappa}}$ is now the transverse momentum of the gluon with respect to the other leg of the antenna, $\bar{\boldsymbol{\kappa}} = \boldsymbol{k} - \bar{x}\bar{\boldsymbol{p}}$.

Dealing now with the interferences amongst both amplitudes (Fig. 3.1), they prove to be the dominant terms for interpreting the radiation pattern off the emitters, and hence also the pieces that reveal the inner coherence picture of the radiation process. As an illustration,

$$\begin{aligned}\left\langle \mathcal{M}_{q\bar{q}g(q_g)}\mathcal{M}^*_{q\bar{q}g(\bar{q}_g)} \right\rangle_{\text{med}} = \left|\mathcal{M}_{q\bar{q}}\right|^2 \frac{1}{N}\sum_{\lambda} \Big\langle \text{Tr}\Big(W^\dagger(0,L;\boldsymbol{r}_1) t^a W(L,0;\boldsymbol{r}_1) W^\dagger(0,L;\boldsymbol{r}_2) \\ \times t^a W(L,0;\boldsymbol{r}_2)\Big)\Big\rangle \cdot g_s^2 \left[\left(\frac{p\cdot\epsilon}{p\cdot k}\right)\left(\frac{\bar{p}\cdot\epsilon^*}{\bar{p}\cdot k}\right)\right],\end{aligned} \tag{3.6}$$

which displays a similar structure to the vacuum result, with the fundamental difference that a color factor different from unity shows up now.

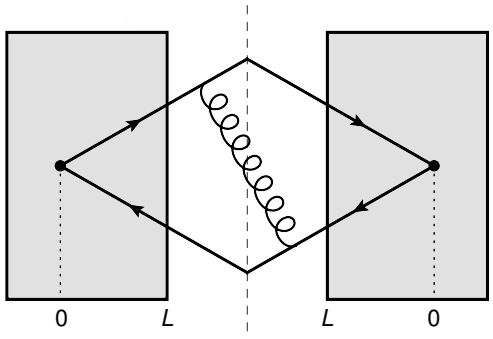

Figure 3.1: Diagrammatic sketch of the *out-out* component to the gluon spectrum off a $q\bar{q}$-antenna propagating within a medium under the soft limit ($\omega \to 0$).

After simple manipulations using both eq. (3.26) and the Fierz identity (3.27) introduced in Appendix 3.B, eq. (3.6) reduces to

$$\left\langle \mathcal{M}_{q\bar{q}g,1}\mathcal{M}^{*}_{q\bar{q}g,2}\right\rangle_{\text{med}} = -\left|\mathcal{M}_{q\bar{q}}\right|^2 C_F \frac{1}{N^2-1}\Big\langle \text{Tr}\left(W_A^{\dagger}(\boldsymbol{r}_2)W_A(\boldsymbol{r}_1)\right)\Big\rangle_{(L,0)} g_s^2 4\frac{\boldsymbol{\kappa}\cdot\bar{\boldsymbol{\kappa}}}{\boldsymbol{\kappa}^2\bar{\boldsymbol{\kappa}}^2}, \quad (3.7)$$

which proves to be directly proportional to the two-parton system interference for the vacuum case, $\mathcal{J} := 4\omega^2\frac{\boldsymbol{\kappa}\cdot\bar{\boldsymbol{\kappa}}}{\boldsymbol{\kappa}^2\bar{\boldsymbol{\kappa}}^2}$.

One can now define the survival probability

$$\mathcal{S}_{(t_2,t_1)} := \frac{1}{N^2-1}\Big\langle \text{Tr}\left(W_A^{\dagger}(\boldsymbol{r}_2)W_A(\boldsymbol{r}_1\right)\Big\rangle_{(t_2,t_1)}, \quad (3.8)$$

which as its name suggests accounts for the probability of the coherence effects surviving the passage across the medium, as previously discussed – see eq. (2.56). It is indeed a redefinition of the decoherence parameter,

$$\Delta_{med}(t_2,t_1) := 1-\mathcal{S}_{(t_2,t_1)}, \quad (3.9)$$

a parameter that characterizes the rate of color decoherence of the pair as a result of color interactions with the deconfined medium [115–117]. In this way, since its origin as a result of the very first splitting inside the medium, the two-parton system spreads over the medium until the very end of it, with the Wilson lines reflecting the color rotation in the wake of an arbitrary number of kicks off the background field[2]. In this interim, the decoherence parameter, implicit in the definition of the survival probability, determines the decoherence time t_d, a physical time-scale that governs the color decoherence of the dipole inside the medium. A more detailed discussion on these ideas will take place a little further down this piece.

At the moment the resulting cross-section is at readiness to be written down,

$$dN^{\text{med}}_{\gamma^*\to q\bar{q}} = \frac{d\sigma^{\text{med}}_{\gamma^*\to q\bar{q}}}{d\sigma_{\text{non-rad}}} = \sum_{\lambda}\left|\mathcal{M}^{\text{tot}}\right|^2\frac{d^3k}{(2\pi)^3\ 2\omega}, \quad (3.10)$$

where $d^3k = \omega^2 d\omega\, d\cos\theta d\phi$, with θ and ϕ the polar and azimuthal angles of the gluon with respect to the emitter, respectively. A glance at eqs. (3.5) and (3.7) suggests that there is scope for casting the spectrum of emitted gluons in the same fashion as is decomposed for the vacuum case,

$$\omega\frac{dN^{med}_{\gamma^*\to q\bar{q}}}{d^3k}\Big|_{\omega\to 0} = \frac{\alpha_s C_F}{(2\pi)^2\omega^2}\Big[\mathcal{R}_q+\mathcal{R}_{\bar{q}}-2\mathcal{S}_{(L,0)}\mathcal{J}\Big], \quad (3.11)$$

[2]A straightforward derivation of *tilted* Wilson lines for in-medium parton propagation is provided in Appendix 3.A.

where $\mathcal{R}_q := 4\omega^2/\boldsymbol{\kappa}^2$ and $\mathcal{R}_{\bar{q}} := 4\omega^2/\bar{\boldsymbol{\kappa}}^2$ are the independent contributions to the radiation off both the quark and the antiquark, respectively, and the last term accounts for the quark-antiquark interference spectrum, with $\mathcal{S}_{(L,0)}$ defined according to eq. (3.8) and $\mathcal{J} := 4\omega^2 \frac{\boldsymbol{\kappa}\cdot\bar{\boldsymbol{\kappa}}}{\boldsymbol{\kappa}^2\bar{\boldsymbol{\kappa}}^2}$. Each of the terms of eq. (3.11) clearly comes from the results derived in eqs. (3.5), (3.5) ($\boldsymbol{\kappa} \to \bar{\boldsymbol{\kappa}}$) and (3.7), respectively. The generalization of the resulting spectrum to the octet case is straightforward and is given by [117]

$$\omega \frac{dN^{med}_{g^*\to q\bar{q}}}{d^3k}\bigg|_{\omega\to 0} = \frac{\alpha_s}{(2\pi)^2\omega^2}\Big[C_F\mathcal{R}_{singlet} + C_A\mathcal{S}_{(L,0)}\mathcal{J}\Big], \tag{3.12}$$

where, in line with the vacuum derivation, $\mathcal{R}_{sing} := \mathcal{R}_q + \mathcal{R}_{\bar{q}} - 2\mathcal{S}_{(L,0)}\mathcal{J}$ is defined to track the singlet component down.

It is worthwhile to recover the corresponding vacuum spectrum to the process under consideration by merely imposing on the survival probability of the coherence effects to tend to unity, so replicating the absence of the medium,

$$\omega \frac{dN^{vac}_{\gamma^*\to q\bar{q}}}{d^3k} = \omega \frac{dN^{med}_{\gamma^*\to q\bar{q}}}{d^3k}\bigg|_{\mathcal{S}_{(L,0)}\to 1} = \frac{\alpha_s C_F}{(2\pi)^2\omega^2}\Big(\mathcal{R}_q + \mathcal{R}_{\bar{q}} - 2\mathcal{J}\Big), \tag{3.13}$$

as explicitly computed in subsection 2.1.1, eq. (2.12). Recapturing the vacuum outcome from the in-medium picture in the dilute limit – $\mathcal{S}_{(L,0)} \to 1$, and accordingly $\Delta_{med} \to 0$ – constitutes a simple test to verify the resulting spectrum, eq. (3.11). This can be done in exactly the same way for the octet case, eq. (3.12).

To close this section, an intelligible interpretation of the physical picture behind eqs. (3.11) and (3.12) is provided. The factorized form of the spectrum allows for tackling two clear limits. The former was already outlined above. It is based on the case when the color correlation length of the medium is larger than the transverse size of the pair, so that the medium cannot resolve the single emitters, thus acting like an individual object with the total charge of the pair. In other words, the antenna radiates coherently, as one would expect in the dilute limit, so the vacuum spectrum is indeed restored as shown above. In a similar spirit, when the medium is able to resolve the antenna, it breaks the color correlation of the pair, then behaving as two independent emitters. The latter limit can be deemed as the opaque limit owing to coherence effects being deeply sensitive to the passage through the medium, $\Delta_{med} \to 1$, in this way leading to total decoherence of the spectrum and breaking the angular ordering pattern.

Thus far it has been introduced an oversimplified picture of color correlations in a few respects. Keeping in mind the above scenario, from here on out the focus is very much on further deeping the understanding of color coherence by working over a multiple medium-induced emissions picture, whereby both two in-medium hard splittings and a very soft gluon emission take place.

3.2 A problem of multiple emitters

As previously highlighted, interference effects as color coherence have significant implications for achieving a greater knowledge on parton cascade standards. Interest is now focusing on the establishment of a more involved QCD partonic evolution picture. The diagrams to be computed are those presented in Fig. 3.2 alongside the analogous ones when making the switch $q \leftrightarrow \bar{q}$.

Just to be clear, here it is derived the spectrum of gluon radiation off two-parton QCD antennas originated after two hard splittings, occurring at times 0 and t, within a static color-deconfined medium of size L. The stress is put on the role of color coherence effects by considering an additional soft gluon emission when the leading emitters have already crossed the entire medium length, as a means of tracing the coherence history of the full picture back. Yet again, neither non-eikonal corrections to parton propagation nor finite formation time effects of the splitting processes are taken into consideration.

From here, the same steps as outlined for the above calculation apply. The partial amplitude for each of the processes presented in the diagrams sketched out in Fig. 3.2 below can be written as

$$\begin{aligned}\mathcal{M}_{q\bar{q}gg(q_g)} \simeq\ & \bar{u}_i(p_1) ie_q \gamma_\mu t^b_{ij} W_{jk}(L,t;\boldsymbol{r}_1) t^a_{kl} W_{lm}(t,0;\boldsymbol{r}_1) W^\dagger_{mi}(0,L;\boldsymbol{r}_2) v_i(p_2) W^{a\alpha}_A(L,t;\boldsymbol{r}_3) \\ & \cdot g_s^2 \left[\left(\frac{p_1\cdot\epsilon(p_3)}{p_1\cdot p_3}\right)\right]\left[\left(\frac{p_1\cdot\epsilon(k)}{p_1\cdot k}\right)\right],\end{aligned} \tag{3.14}$$

$$\begin{aligned}\mathcal{M}_{q\bar{q}gg(\bar{q}_g)} \simeq\ & \bar{u}_i(p_1) ie_q \gamma_\mu W_{ij}(L,t;\boldsymbol{r}_1) t^a_{jk} W_{kl}(t,0;\boldsymbol{r}_1) W^\dagger_{lm}(0,L;\boldsymbol{r}_2) t^b_{mi} v_i(p_2) W^{a\alpha}_A(L,t;\boldsymbol{r}_3) \\ & \cdot g_s^2 \left[\left(\frac{p_1\cdot\epsilon(p_3)}{p_1\cdot p_3}\right)\right]\left[\left(\frac{p_2\cdot\epsilon(k)}{p_2\cdot k}\right)\right],\end{aligned} \tag{3.15}$$

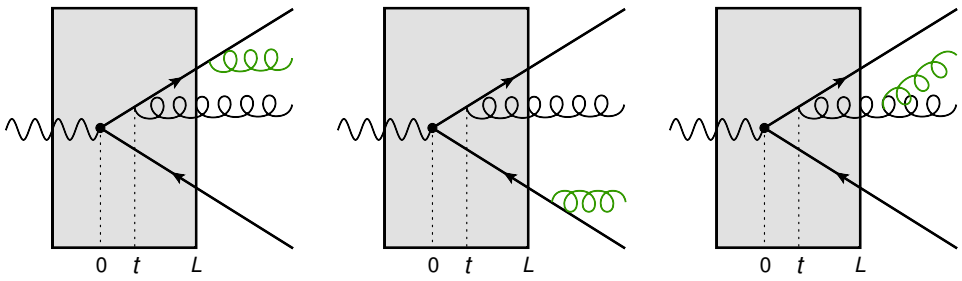

Figure 3.2: Diagrammatic depiction of the probability amplitudes for the general case of three emitters. The green gluon is set outside the medium in order to hold the control of the stage of color coherence through the whole dynamics scenario.

$$\begin{aligned}\mathcal{M}_{q\bar{q}gg(g_g)} \simeq\ & \bar{u}_i(p_1) ie_q \gamma_\mu W_{ij}(L,t;\boldsymbol{r}_1) t^a_{jk} W_{kl}(t,0;\boldsymbol{r}_1) W^\dagger_{li}(0,L;\boldsymbol{r}_2) v_i(p_2) W^{a\alpha}_A(L,t;\boldsymbol{r}_3) \\ & \times (-if^{\alpha yz}) \cdot g_s^2 \left[\left(\frac{p_1\cdot\epsilon(p_3)}{p_1\cdot p_3}\right)\right]\left[\left(\frac{p_3\cdot\epsilon(k)}{p_3\cdot k}\right)\right],\end{aligned} \tag{3.16}$$

up to the phases that are implicit in the definition of the *tilted* Wilson line that generalises eq. (2.21), explicitly derived in Appendix 3.A . Here $\boldsymbol{p}_1$ and $\boldsymbol{p}_2$ represent the quark and antiquark momenta (which follow eikonal paths $\boldsymbol{r}_1$ and $\boldsymbol{r}_2$, respectively). The momenta of the hard and soft gluons are labelled as $\boldsymbol{p}_3$ (following the straight trajectory $\boldsymbol{r}_3$) and $\boldsymbol{k}$ (propagating through the vacuum), respectively.

Moving forward on this, it is necessary to both square the preceding probability amplitudes and compute the radiative interferences. For the purpose of unravelling the coherence physics behind the evolution picture, it is essential to implement the large-N_c limit via keeping only the leading terms in the expansion, as the averaging procedure over the possible configurations entails non-trivial correlation functions among the fields retained within the Wilson lines. This is why from here onwards it suffices to focus on purely developing the color algebra[3]. Technical details on the squaring procedure and the computation of the probability interferences are fully provided in Appendix 3.B.

Following the same reasoning as in the derivation of the squared amplitudes $\mathcal{R}_q$ and $\mathcal{R}_{\bar{q}}$ – eq. (3.5), the direct terms, explicitly schematized in Fig. 3.3, turn out to be trivial under the limit of large number of colors,

$$\begin{aligned}\left\langle \left|\mathcal{M}_{qqgg(q_g)}\right|^2 \right\rangle_{\text{med}} &:= \mathcal{R}_{q_g} \sim C_F^2, \\ \left\langle \left|\mathcal{M}_{qqgg(\bar{q}_g)}\right|^2 \right\rangle_{\text{med}} &:= \mathcal{R}_{\bar{q}_g} \sim C_F^2, \\ \left\langle \left|\mathcal{M}_{qqgg(g_g)}\right|^2 \right\rangle_{\text{med}} &:= \mathcal{R}_{g_g} \sim C_F C_A,\end{aligned} \tag{3.17}$$

meaning that no medium modifications stand out since they are only proportional to the relevant Casimir factors for each radiation process. Noteworthy is the fact that this result is perfectly compatible with expectations as these configurations are indeed not very different from those introduced in Fig. 3.1 when computing the independent components – the Wilson lines collapse to unity once again when finite formation time effects are overlooked.

Likewise, more interesting results are yielded when computing the interference components. Two of the most prominent contributions in the face of identifying a coherence pattern are depicted in Figs. 3.4 and 3.5. In contrast to the direct terms outlined above,

[3]In any case, the kinematic terms are identical to the ones already computed in both the vacuum and the radiation off the antenna in the soft limit derivations.

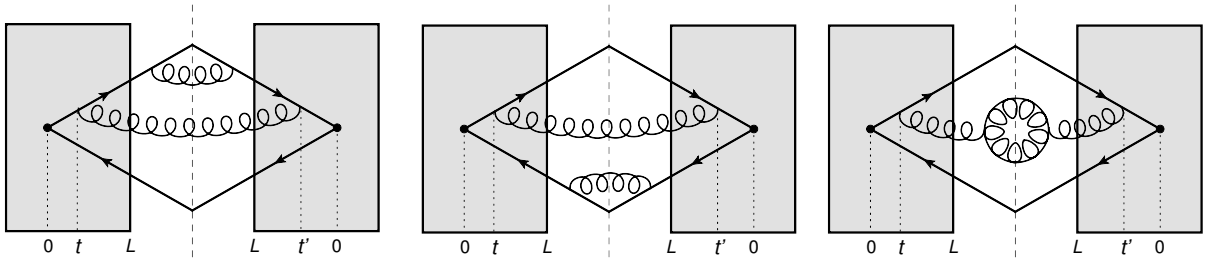

Figure 3.3: Representation of the squared amplitudes for two in-medium hard splittings. Note that $t = t'$ is assumed, meaning that finite formation time effects for the parton splitting processes are discarded.

now the survival probabilities are explicitly reflected in the probability interferences, thus providing valuable insights into the color correlation trend of the emitters. A more elaborated discussion on this point is presented further below. Again, restricted to color algebra, the interference contribution resulting from combining eqs. (3.14) and (3.16), sketched out in Fig. 3.4 (left), reads

$$\left\langle \mathcal{M}_{q\bar{q}gg(q_g)} \mathcal{M}^{*}_{q\bar{q}gg(g_g)} \right\rangle_{\text{med}} \sim \mathcal{S}_{(L,t)}, \tag{3.18}$$

where $\mathcal{S}_{(L,t)}$ is now the survival probability from the second hard splitting, just as the hard gluon is radiated off the quark, to the end of the medium – see eq. (3.8). In order to properly understand the findings for the interferences, it is important to underline the relationship between the survival probability and the decoherence parameter, eq. (3.9). Proceeding analogously for the process presented in Fig. 3.5 (left), this time associating eqs. (3.15) and (3.16), it appears that

$$\left\langle \mathcal{M}_{q\bar{q}gg(\bar{q}_g)} \mathcal{M}^{*}_{q\bar{q}gg(g_g)} \right\rangle_{\text{med}} \sim \mathcal{S}_{(t,0)} \mathcal{S}_{(L,t)}, \tag{3.19}$$

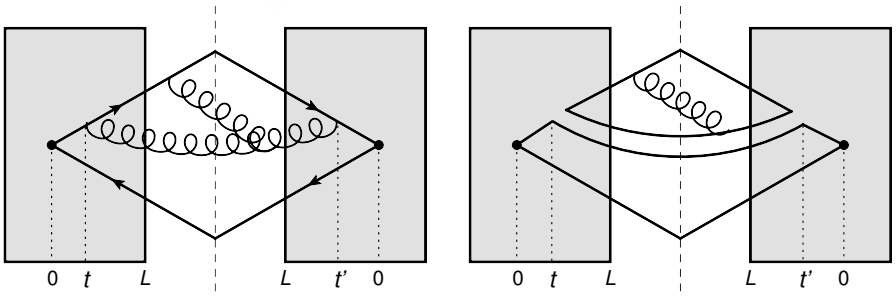

Figure 3.4: Schematic view of one of the interference processes under consideration (left). The corresponding large-N_c limit is shown on the right pane. Recall that $t = t'$ is implemented in order to get eq. (3.18).

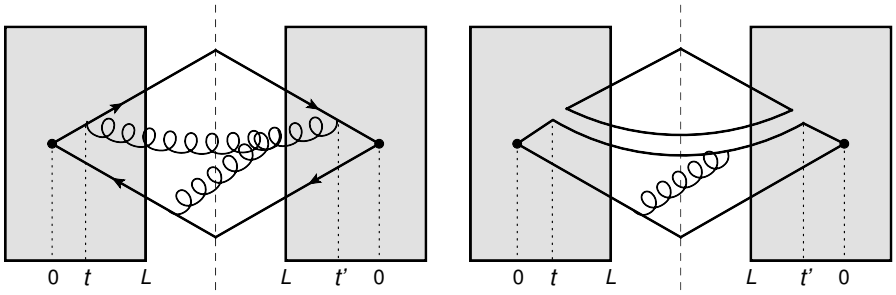

Figure 3.5: Diagrammatic illustration of a probability inteference contributing to the three emitters scenario (left). The large-N_c limit is implemented on the right scheme. Again, $t = t'$ is assumed to obtain eq. (3.19).

so that it shows a factorized scheme in terms of successive survival probabilities, from the origin of the former dipole to the end of the medium. As stated earlier, Appendix 3.B provides details on the actual derivations of eqs. (3.18) and (3.19). The outcomes for the probability interferences delivered above are clearly evident in the right panel of Figs. 3.4 and 3.5, in which the large-N_c limit significantly disentangles the partonic setup. Indeed, the achieved factorizations, eqs. (3.18) and (3.19), admit a nice conceptual interpretation toward deciphering the color coherence puzzle.

As already discussed, the survival probabilities are meant to capture the ability of the medium to break the color correlation between the leading partons along the in-medium evolution. In the present physical picture, the survival probabilities are defined regarding two different regions clearly bounded by the emission time corresponding to the latter hard splitting that takes place within the medium. More precisely, the survival probability emerging in the analytical interferences corresponds exactly to that of the dipole from which the soft gluon is released. As an example to better understand this, looking at Fig. 3.4 (right), the source dipole is originated at emission time t, just when the quark splits up for the very first time during the evolution of the system, while it is born at the origin of the coordinate system in Fig. 3.5 (right). Thus, in the former case, the emission spectrum must be proportional to the survival probability from the hard gluon emission to the end of the medium, as shown by eq. (3.18). Unlike the former, the latter is determined by convolving the survival probabilities of the successive regions, namely from the beginning of the system to the second in-medium hard splitting, and then until the length of the medium, as evidenced by eq. (3.19).

Based on the above study, further conclusions can be drawn at parton evolution level. Having a look at the obtained schemes, it is natural to state that coherence effects in parton branching processes can be assumed as a factorization of single survival probabilities bounded by radiation regions set out during the full development of the shower.

Once the leading partons start spreading, color coherence becomes important. In particular, from the derived schemes it follows that subsequent factored branchings remain in a coherent state as long as the former do it as well. Take, for instance, Fig. 3.4 (right): the factored antenna consisting of the quark and the radiated hard gluon will start its propagation as a whole if and only if $t_d > t$, that is to say, provided the decoherence time from the very first splitting is larger than the time scale that controls the hard gluon emission. The same applies to the next stage of the parton dynamics: the quark-gluon antenna will leave the medium still persisting in a coherent state if the condition $t'_d > L$ is fulfilled, meaning the time scale for decoherence of the new dipole is greater than the length of the medium. In this case, in-medium vacuum-like emissions pop up, what happens as the splittings are predominantly collinear. Once they exit the medium, the subsequent partons shall be subject to the angular ordering condition. On the contrary, if the quark-antiquark pair decoheres before the hard gluon emission takes place, $t_d < t$ – and accordingly $t_d < L$, medium modifications become important and hence all radiation will happen in an incoherent way from this point onward. Typically, coherence is broken when the splitting angle is large.

In short, once coherence effects are broken in a factorized region, successive parton splittings become naturally incoherent, which means ensuring that the development of each splitting marks the onset of the following in terms of color coherence. At the end of the day, coherence displays a knock-on effect in a entirely factorized parton cascade under the large number of colors approach.

Before closing up the discussion, it is worthwhile to make a subtle remark about the major physical time-scales involved in the problem. For the sake of simplicity, the formation time of the dipoles are set to be zero. However, the leading partons spend a considerable length of time within the medium before radiating. This is not as controversial as it may at first sound. Indeed, at high energies, the typical time between two successive splittings reads $\Delta t_{rad} \simeq t_f/\alpha$ [143, 144]. Taking a simple look at this relation, one can appreciate that provided the coupling is small enough, it is possible to bring back the picture of independent splittings since the time between consecutive branchings become remarkably larger than the duration of the splitting itself. Note also that overlapping splittings would be of order α, as it characterizes the strength of the splitting vertex.

As a final comment, although exclusively restricted to a very simple cascading picture, the resulting factorization is meant to hold and become universal for an arbitrary number of antennas. That is to say, further parton branchings do no override the factorized scheme under the large number of colors approach. In this respect, this work provides a reliable description of interference effects in multi-parton scenarios with the ultimate aim of building up a perturbative shower.

3.3 Conclusions and outlook

This work presents a novel setup whose primary objective is to improve knowledge and understanding of jet evolution in matter. Following closely previous references of in-medium radiation off an antenna, the study provides an attempt to widen the scope of color coherence effects in parton propagation when looking toward the whole cascading process.

On this basis, including the possibility of two quasi-instantaneous in-medium hard splittings in the chosen *laboratory*, the main outcome of this project is that it is possible to factorize the subsequent branchings when taking notice of color coherence along the parton shower. This factorization supports a friendly interpretation of the physical picture in terms of interference and color correlation effects. More specifically, each splitting is meant to hold the subsequent in terms of coherence in such a way that each splitting *sees* its corresponding antenna. This leads to a straightforward scene: once coherence is broken in a factorized region, the behaviour spreads throughout the cascading process, thus suppressing coherent radiation as the jet is splitted into two independent (color incoherent) subjets. Again, the time scales that control the dynamics play a key role to better understand parton evolution in matter.

It is worth pointing out that the final results are subject to the eikonal approximation, so that interactions are governed by multiple soft scattering, which is a proper treatment for the leading partons. In fact, a Feynman rule for describing in-medium parton propagation at a fixed angle within the eikonal approximation is derived in Appendix 3.A in order to provide an appropriate framework for further studies in this context. The large-N_c limit was also taken at the end of the calculation as it allows one to present a simple picture, but that does not detract from the validity of the factorized scheme for the successive antennas.

As a final comment, it would be also worthwhile to extend these findings beyond the undertaken approximations, as well as computing a more involved multi-parton radiation picture without limiting the setup to a two-stages scenario. With those developments it will be possible to achieve a reinforced comprehension of the remarkable features of jet evolution within a dense medium.

3.A Deriving the *tilted* Wilson line

Calculations in the presence of an extended medium need, in general, information from space-time coordinates that is absent in the momentum-space representation of the classical Feynman rules.

The derivation of a rule for characterizing the propagation of a parton produced at a fixed angle in a hard vertex inside the medium, written in three dimensional configuration space – with x^+ playing the role of time and the two transverse position coordinates $\boldsymbol{x}$ – is presented here. For simplicity, a process that favor the inference of the rules is addressed, although providing support as regards its general validity.

Three-dimensional vectors in position and momentum representations will be used, $\vec{x} = (x^+, \boldsymbol{x})$ and $\vec{p} = (p^-, \boldsymbol{p})$, respectively, written down in terms of the light-cone variables, in accordance with eq. (2.22).

As previously introduced in subsection 2.2.1, when a parton is very energetic, the Brownian motion described in the transverse plane can be neglected, and this means the trajectories are essentially straight lines. This can clearly be deduced from taking the limit $p^+ \to \infty$ in the expression for the propagator, eq. (2.29), thereby setting the transverse position of the particle along its trajectory, as explicitly establishes eq. (2.30). In general, the initial and final positions of the path integrand do not necessarily have to be the same. Indeed, the computed *tilted* Wilson line will be practical for the cases in which a very energetic quark – or a gluon – is produced at a fixed angle in a hard vertex within the medium.

A way to derive the tilted Wilson line is to come back to the definition of the in-medium quark propagator, eq. (2.29). Considering for simplicity the corresponding term to one scattering and omitting the light-cone energy l^+ gives rise to

$$\mathcal{G}\left(y^+, \boldsymbol{y}; x^+, \boldsymbol{x}\right) = \int_{\vec{x}_1} \mathcal{G}_F\left(y^+, \boldsymbol{y}; x_1^+, \boldsymbol{x}_1\right) igA^-\left(x_1^+, \boldsymbol{x}_1\right) \mathcal{G}_F\left(x_1^+, \boldsymbol{x}_1; x^+, \boldsymbol{x}\right). \tag{3.20}$$

Now assuming that the quark has a certain initial transverse momentum $\boldsymbol{k}$, the free propagator defined as

$$\mathcal{G}_F\left(\vec{y}, \vec{x}|l^+\right) = \int \frac{d^2\boldsymbol{l}}{(2\pi)^2} e^{i\frac{\boldsymbol{l}^2}{2l^+}(x^+ - y^+)} e^{-i\boldsymbol{l}\cdot(\boldsymbol{x}-\boldsymbol{y})}, \tag{3.21}$$

with $\boldsymbol{l} = \boldsymbol{k} + \boldsymbol{\mu}$ for a constant $\boldsymbol{k}$ – understood to be the initial transverse momentum of the quark, turns into

$$\begin{aligned} \mathcal{G}_F\left(y^+, \boldsymbol{y}; x^+, \boldsymbol{x}\right) &= \int \frac{d^2\mu}{(2\pi)^2} e^{i\frac{(\boldsymbol{k}+\boldsymbol{\mu})^2}{2l^+}(x^+ - y^+)} e^{i(\boldsymbol{k}-\boldsymbol{\mu})\cdot(\boldsymbol{x}-\boldsymbol{y})} \\ &\simeq e^{i\frac{\boldsymbol{k}^2}{2l^+}(x^+ - y^+)} e^{-i\boldsymbol{k}\cdot(\boldsymbol{x}-\boldsymbol{y})} \delta^{(2)}\left[\frac{\boldsymbol{k}}{p^+}(x^+ - y^+) - (\boldsymbol{x}-\boldsymbol{y})\right], \end{aligned} \tag{3.22}$$

where the same high-energy limit as that on the derivation of the Wilson line from the Green's function propagator – see eq. (2.30) – has been assumed in the exponential,

$\mu^2/2l^+ \to 0$. Here the Delta function ensures that the propagation is tracked along a straight line with the right slope, $\boldsymbol{k}/p^+$.

The resummation of the diagrams for an arbitrary number of field insertions proves to be simple and leads to

$$\begin{aligned}\mathcal{G}\left(y^+,\boldsymbol{y};x^+,\boldsymbol{x}|p^+\right) \longrightarrow\ & e^{i\frac{\boldsymbol{k}^2}{2p^+}(x^+-y^+)}e^{-i\boldsymbol{k}(\boldsymbol{x}-\boldsymbol{y})}\ W\left[z_{cl}\right]_{x^+}^{y^+} \\ & \times\delta^{(2)}\left[\frac{\boldsymbol{k}}{p^+}(x^+-y^+)-(\boldsymbol{x}-\boldsymbol{y})\right],\end{aligned} \tag{3.23}$$

with the Wilson line evaluated along the classical trajectory

$$W\left[z_{cl}\right]_{x^+}^{y^+} := \mathcal{P}\exp\left\{ig\int_{x^+}^{y^+}d\boldsymbol{z}^+A^-\left(z^+,\boldsymbol{x}+\frac{\boldsymbol{k}}{p^+}(z^+-x^+)\right)\right\}. \tag{3.24}$$

After all, it is possible to define the eikonal trajectory that generalises eq. (2.21) as

$$\begin{aligned}\mathcal{G}_{\text{eik}}\left(y^+,\boldsymbol{y};x^+,\boldsymbol{x}|p^+\right) :=\ & e^{i\frac{\boldsymbol{k}^2}{2p^+}(x^+-y^+)}e^{-i\boldsymbol{k}(\boldsymbol{x}-\boldsymbol{y})}\ W\left[z_{cl}\right]_{x^+}^{y^+} \\ & \times\delta^{(2)}\left[\frac{\boldsymbol{k}}{p^+}(x^+-y^+)-(\boldsymbol{x}-\boldsymbol{y})\right].\end{aligned} \tag{3.25}$$

3.B Technical details on color algebra

This appendix provides insight into the color algebra performed in order to get the results presented in Section 3.2. Specifically, an elaborate development of eqs. (3.17)($\mathcal{R}_{g_g}$) and (3.19) is addressed, this way setting the standard for the derivations not explicitly presented in this manuscript, which prove to show similar or even less difficulty. As a matter of fact, the development of the remaining direct and interference terms is analogous and can be directly brought back from those further elaborated. In the first instance, it is important to recall a couple of recurring relations to be used along the way,

$$W_A^{ab}(\boldsymbol{x}_\perp)t^b = W^\dagger(\boldsymbol{x}_\perp)t^aW(\boldsymbol{x}_\perp), \tag{3.26}$$

and the Fierz identity

$$t^a_{ij}t^a_{kl} = \frac{1}{2}\Big(\delta_{il}\delta_{jk}-\frac{1}{N}\delta_{ij}\delta_{kl}\Big). \tag{3.27}$$

Beginning with the derivation of $\mathcal{R}_{g_g}$, depicted in Fig. 3.3 on the far right pane, and turning the attention to the color flow, the squared amplitude reads

$$\Big\langle|\mathcal{M}_{qqgg(g_g)}|^2\Big\rangle_{\rm med}\sim\frac{1}{N}\Big\langle{\rm Tr}\Big(W_1(t,0)\;t^a\;W_1(L,t)\;W_1^\dagger(t',L)\;t^d\;W_1^\dagger(0,t')\;W_2(L,0)\;W_2^\dagger(0,L)\Big)\\ \times W_4^{a\alpha}(L,t)\;\delta_{\alpha b}\;(-if^{bij})(if^{cij})\;\delta_{c\beta}\;W_4^{\dagger\beta d}(t',L)\Big\rangle,$$

where the subscripts denote the parton trajectories, and the brackets refer to the different regions within the medium in both amplitude and complex-conjugate amplitude.

Now working out separately each of the terms within the trace and those outside it produces

$$W_4^{a\alpha}(L,t)\;\delta_{\alpha b}\;(-if^{bij})(if^{cij})\;\delta_{c\beta}\;W_4^{\dagger\beta d}(t',L)\\ =4N\;{\rm Tr}\Big(t^a\;W_4(L,t)\;t^b\;W_4^\dagger(L,t)\Big)\;Tr\Big(t^b\;W_4^\dagger(t',L)\;t^d\;W_4(t',L)\Big),$$

where the relations $W_A^{ab}(\boldsymbol{x}_\perp)=2\;{\rm Tr}\Big(t^aW(\boldsymbol{x}_\perp)t^bW^\dagger(\boldsymbol{x}_\perp)\Big)$ and $(-if^{bij})(if^{cij})=N\delta_{bc}$ have been used. In this way, this delivers

$$\begin{aligned}
&{\rm Tr}\Big(W_1(t,0)\;t^a\;W_1(L,t)\;W_1^\dagger(t',L)\;t^d\;W_1^\dagger(0,t')\;W_2(L,0)\;W_2^\dagger(0,L)\Big)W_4^{a\alpha}(L,t)\;\delta_{\alpha b}\;(-if^{bij})(if^{cij})\;\delta_{c\beta}\;W_4^{\dagger\beta d}(t',L)\\
&=4N\;{\rm Tr}\Big(W_1(t,0)\;t^a\;W_1(L,t)\;W_1^\dagger(t',L)\;t^d\;W_1^\dagger(0,t')\Big)\;{\rm Tr}\Big(t^a\;W_4(L,t)\;t^b\;W_4^\dagger(L,t)\Big)\;{\rm Tr}\Big(t^b\;W_4^\dagger(t',L)\;t^d\;W_4(t',L)\Big)\\
&=2N\;{\rm Tr}\Big(W_1(t,0)\;t^a\;W_1(L,t)\;W_1^\dagger(t',L)\;t^d\;W_1^\dagger(0,t')\Big)\;{\rm Tr}\Big(W_4^\dagger(L,t)\;t^a\;W_4(L,t)\;W_4^\dagger(t',L)\;t^d\;W_4(t',L)\Big)\\
&=N\;{\rm Tr}\Big(W_1(L,t)\;W_1^\dagger(t',L)\;t^d\;W_1^\dagger(0,t')\;W_1(t,0)\;W_4(L,t)\;W_4^\dagger(t',L)\;t^d\;W_4(t',L)\;W_4^\dagger(L,t)\Big)\\
&=\frac{1}{2}N\;\Big[{\rm Tr}\Big(W_1^\dagger(0,t')\;W_1(t,0)\;W_4(L,t)\;W_4^\dagger(t',L)\Big)\;{\rm Tr}\Big(W_4(t',L)\;W_4^\dagger(L,t)\;W_1(L,t)\;W_1^\dagger(t',L)\Big)\\
&-\frac{1}{N}\;{\rm Tr}\Big(W_1^\dagger(0,t')\;W_1(t,0)\;W_4(L,t)\;W_4^\dagger(t',L)\;W_4(t',L)\;W_4^\dagger(L,t)\;W_1(L,t)\;W_1^\dagger(t',L)\Big)\Big]\\
&=\frac{1}{2}\;\Big[N\;{\rm Tr}\Big(W_1^\dagger(0,t')\;W_1(t,0)\;W_4(L,t)\;W_4^\dagger(t',L)\Big)\;{\rm Tr}\Big(W_4(t',L)\;W_4^\dagger(L,t)\;W_1(L,t)\;W_1^\dagger(t',L)\Big)-1\Big],
\end{aligned}$$

where the Fierz identity (3.27) has been implemented over and over in order to remove the color matrices.

These simplifications have made it possible to reduce the squared amplitude to only two traces of Wilson lines in the fundamental representation,

$$\Big\langle|\mathcal{M}_{qqgg(g_g)}|^2\Big\rangle_{\rm med}\sim\frac{1}{2}\Big\langle{\rm Tr}\Big(W_1^\dagger(0,t')\;W_1(0,t)\;W_4(L,t)\;W_4^\dagger(t',L)\Big)\\ \times{\rm Tr}\Big(W_4(t',L)\;W_4^\dagger(L,t)\;W_1(L,t)\;W_1^\dagger(t',L)\Big)-1\Big\rangle.\tag{3.28}$$

Fixing now the splitting vertices in amplitude and its complex-conjugate to the same time length ($t=t'$), meaning placed one on top of each other, gives rise to

$$\Big\langle|\mathcal{M}_{qqgg(g_g)}|^2\Big\rangle_{\rm med}\sim\frac{1}{2}\Big(N^2-1\Big)=C_FC_A,\tag{3.29}$$

as was previously shown in eq. (3.17).

To end with, the derivation of eq. (3.19) is presented here as an interference contribution example. Proceeding in the same way as for $\mathcal{R}_{g_g}$, it reads

$$\begin{aligned}
&\Big\langle \mathcal{M}_{q\bar{q}gg(\bar{q}_g)} \mathcal{M}^{*}_{q\bar{q}gg(g_g)} \Big\rangle_{\text{med}} \\
&\sim \frac{1}{N} \Big\langle \text{Tr}\Big(W_1(t,0)\; t^a\; W_1(L,t)\; W_1^{\dagger}(t',L)\; t^b\; W_1^{\dagger}(0,t')\; W_2(L,0)\; t^c\; W_2^{\dagger}(0,L) \Big) \\
&\times W_4^{a\alpha}(L,t)\; (-if^{\alpha\beta c})\; W_4^{\dagger \beta b}(t',L) \Big\rangle.
\end{aligned} \tag{3.30}$$

Now, performing the algebra of the aside from the trace expression gives

$$\begin{aligned}
&W_4^{a\alpha}(L,t)\; (-if^{\alpha\beta c})\; W_4^{\dagger \beta b}(t',L) = 2\; \text{Tr}\Big(t^a\; W_4(L,t)\; t^{\alpha}\; W_4^{\dagger}(L,t) \Big) \\
&\times \Big[-2\; \text{Tr}\Big(t^{\alpha} \Big[t^{\beta}, t^{c} \Big] \Big) \Big]\; 2\; \text{Tr}\Big(t^{\beta}\; W_4^{\dagger}(t',L)\; t^b\; W_4(t',L) \Big) \\
&= -8\; \text{Tr}\Big(t^a\; W_4(L,t)\; t^{\alpha}\; W_4^{\dagger}(L,t) \Big)\; \text{Tr}\Big(t^{\alpha} \Big[t^{\beta}, t^{c} \Big] \Big)\; \text{Tr}\Big(t^{\beta}\; W_4^{\dagger}(t',L)\; t^b\; W_4(t',L) \Big) \\
&= -4\; \text{Tr}\Big(W_4^{\dagger}(L,t)\; t^a\; W_4(L,t) \Big[t^{\beta}, t^{c} \Big] \Big)\; \text{Tr}\Big(t^{\beta}\; W_4^{\dagger}(t',L)\; t^b\; W_4(t',L) \Big) \\
&= -4\; \text{Tr}\Big(W_4^{\dagger}(L,t)\; t^a\; W_4(L,t)\; t^{\beta}\; t^{c} \Big)\; \text{Tr}\Big(t^{\beta}\; W_4^{\dagger}(t',L)\; t^b\; W_4(t',L) \Big) \\
&+ 4\; \text{Tr}\Big(W_4^{\dagger}(L,t)\; t^a\; W_4(L,t)\; t^{c}\; t^{\beta} \Big)\; \text{Tr}\Big(t^{\beta}\; W_4^{\dagger}(t',L)\; t^b\; W_4(t',L) \Big) \\
&= -2\; \text{Tr}\Big(t^{c}\; W_4^{\dagger}(L,t)\; t^a\; W_4(L,t)\; W_4^{\dagger}(t',L)\; t^b\; W_4(t',L) \Big) \\
&+ 2\; \text{Tr}\Big(W_4^{\dagger}(L,t)\; t^a\; W_4(L,t)\; t^{c}\; W_4^{\dagger}(t',L)\; t^b\; W_4(t',L) \Big),
\end{aligned}$$

where it has been used that

$$-if^{\alpha\beta c} = (-i)\; \Big(-2i\; \text{Tr}\Big(t^{\alpha} \Big[t^{\beta}, t^{c} \Big] \Big) \Big) = -2\; \text{Tr}\Big(t^{\alpha} \Big[t^{\beta}, t^{b} \Big] \Big). \tag{3.31}$$

Merging now the preceding result with the trace term present in eq. (3.30), and also repeatedly implementing the Fierz identity produces

$$\begin{aligned}
&\text{Tr}\Big(W_1(t,0)\; t^a\; W_1(L,t)\; t^b\; W_1^{\dagger}(t',L)\; t^c\; W_1^{\dagger}(0,t') \Big)\; W_4^{a\alpha}(L,t)\; (-if^{\alpha b\beta})\; W_4^{\dagger \beta c}(t',L) \\
&= -2\; \text{Tr}\Big(W_1(t,0)\; t^a\; W_1(L,t)\; W_1^{\dagger}(t',L)\; t^b\; W_1^{\dagger}(0,t')\; W_2(L,0)\; t^c\; W_2^{\dagger}(0,L) \Big)\; \text{Tr}\Big(t^c\; W_4^{\dagger}(L,t)\; t^a\; W_4(L,t)\; W_4^{\dagger}(t',L)\; t^b\; W_4(t',L) \Big) \\
&+ 2\; \text{Tr}\Big(W_1(t,0)\; t^a\; W_1(L,t)\; W_1^{\dagger}(t',L)\; t^b\; W_1^{\dagger}(0,t')\; W_2(L,0)\; t^c\; W_2^{\dagger}(0,L) \Big)\; \text{Tr}\Big(W_4^{\dagger}(L,t)\; t^a\; W_4(L,t)\; t^c\; W_4^{\dagger}(t',L)\; t^b\; W_4(t',L) \Big) \\
&= -\frac{1}{2}\; \text{Tr}\Big(W_1^{\dagger}(0,t')\; W_2(L,0)\; t^c\; W_2^{\dagger}(0,L)\; W_1(t,0)\; W_4(L,t)\; W_4^{\dagger}(t',L) \Big)\; \text{Tr}\Big(W_4(t',L)\; t^c\; W_4^{\dagger}(L,t)\; W_1(L,t)\; W_1^{\dagger}(t',L) \Big) \\
&+ \frac{1}{2}\; \text{Tr}\Big(W_1^{\dagger}(0,t')\; W_2(L,0)\; t^c\; W_2^{\dagger}(0,L)\; W_1(t,0)\; W_4(L,t)\; t^c\; W_4^{\dagger}(t',L) \Big)\; \text{Tr}\Big(W_4(t',L)\; W_4^{\dagger}(L,t) W_1(L,t)\; W_1^{\dagger}(t',L) \Big) \\
&= -\frac{1}{4}\; \text{Tr}\Big(W_2^{\dagger}(0,L)\; W_1(t,0)\; W_4(L,t)\; W_4^{\dagger}(t',L)\; W_1(0,t')\; W_2(L,0)\; W_4^{\dagger}(L,t)\; W_1(L,t)\; W_1^{\dagger}(t',L)\; W_4(t',L) \Big) \\
&+ \frac{1}{4}\; \text{Tr}\Big(W_2^{\dagger}(0,L)\; W_1(t,0)\; W_4(L,t) \Big)\; \text{Tr}\Big(W_4^{\dagger}(t',L)\; W_1^{\dagger}(0,t')\; W_2(L,0) \Big)\; \text{Tr}\Big(W_4(t',L)\; W_4^{\dagger}(L,t)\; W_1(L,t)\; W_1^{\dagger}(t',L) \Big).
\end{aligned}$$

At this point, the probability interference is

$$\begin{aligned}
&\Big\langle \mathcal{M}_{q\bar{q}gg(\bar{q}_g)}\mathcal{M}^{*}_{q\bar{q}gg(g_g)}\Big\rangle_{\text{med}} \\
&\sim \frac{1}{4N}\,\Big\langle \mathrm{Tr}\Big(W_1(t,0)\;W_4(L,t)\;W_2^{\dagger}(0,L)\Big)Tr\Big(W_1^{\dagger}(0,t')\;W_2(L,0)\;W_4^{\dagger}(t',L)\Big) \\
&\times \mathrm{Tr}\Big(W_1(L,t)\;W_1^{\dagger}(t',L)\;W_4(t',L)\;W_4^{\dagger}(L,t)\Big) \\
&- \mathrm{Tr}\Big(W_2^{\dagger}(0,L)\;W_1(t,0)\;W_4(L,t)\;W_4^{\dagger}(t',L)\;W_1(0,t') \\
&W_2(L,0)\;W_4^{\dagger}(L,t)\;W_1(L,t)\;W_1^{\dagger}(t',L)\;W_4(t',L)\Big)\Big\rangle,
\end{aligned}$$

and, in a similar fashion as the above-derived $\mathcal{R}_{g_g}$, undertaking $t = t'$ gives

$$\begin{aligned}
\Big\langle \mathcal{M}_{q\bar{q}gg(\bar{q}_g)}\mathcal{M}^{*}_{q\bar{q}gg(g_g)}\Big\rangle_{\text{med}} \sim \Big\langle &\mathrm{Tr}\Big(W_1(t,0)\;W_4(L,t)\;W_2^{\dagger}(0,L)\Big) \\
&\mathrm{Tr}\Big(W_1^{\dagger}(0,t)\;W_2(L,0)\;W_4^{\dagger}(t,L)\Big) - 1\Big\rangle.
\end{aligned} \tag{3.32}$$

As a final step, assuming medium averages are local in time in order to hold separately each time-like region, and keeping only the leading terms in the expansion yields

$$\begin{aligned}
\Big\langle \mathcal{M}_{q\bar{q}gg(\bar{q}_g)}\mathcal{M}^{*}_{q\bar{q}gg(g_g)}\Big\rangle_{\text{med}} \sim\; &\frac{1}{N_c}\,\Big\langle \mathrm{Tr}\Big(W(r_1)\;W^{\dagger}(r_2)\Big\rangle_{(t,0)}\Big\langle \mathrm{Tr}\Big(W(r_4)\;W^{\dagger}(r_2)\Big\rangle_{(L,t)} \\
&\times \frac{1}{N_c}\,\Big\langle \mathrm{Tr}\Big(W(r_2)\;W^{\dagger}(r_1)\Big\rangle_{(t,0)}\Big\langle \mathrm{Tr}\Big(W(r_2)\;W^{\dagger}(r_4)\Big\rangle_{(L,t)},
\end{aligned} \tag{3.33}$$

where the convolution of two survival probabilities is clearly identifiable,

$$\Big\langle \mathcal{M}_{q\bar{q}gg(\bar{q}_g)}\mathcal{M}^{*}_{q\bar{q}gg(g_g)}\Big\rangle_{\text{med}} \sim\; \mathcal{S}_{(t,0)}\mathcal{S}_{(L,t)}, \tag{3.34}$$

this way bringing back the corresponding probability interference presented in Section 3.2, eq. (3.19).

USC
UNIVERSIDADE
DE SANTIAGO
DE COMPOSTELA

4

Finite formation time effects for in-medium parton splittings

This piece of work, based on [145], seeks to explore the set of medium-induced modifications that arise from allowing a parton splitting such as those presented in the preceding chapter to occur at a finite formation time. Though the discussion still focuses in the context of a final-state color-singlet splitting, $\gamma \to q\bar{q}$, it shall remain valid for generic splitting processes involving a total color charge. Once again, the high-energy limit is implemented throughout the whole derivation, thereby considerably reducing the complexity of the problem to a semi-classical picture of parton propagation along well-defined trajectories. Contrary to the physical scenarios covered so far in this manuscript, this time the time-like separation of the splitting vertices in amplitude and complex-conjugate amplitude will actually lead to two- and four-point correlation functions of Wilson lines that resum parton-medium interactions. In fact, the dipole and the quadrupole account for the medium's ability to disrupt the color correlation amongst the leading partons at various stages of the process being observed. As evidenced earlier when computing the gluon radiation spectrum off a singlet antenna in the strict soft limit, in the absence of this separation these correlators collapse to unity, this way preventing the possibility to drag the effects of the splitting process throughout the full parton evolution picture. Given that, as previous setups conducted in this thesis have not taken account on a matter as fundamental toward taking notice of accumulated effects of parton-medium interactions over long distances, the formation of the antenna itself is now under examination. To end this study, the findings for the emission spectrum in the presence of a medium are collectively mapped on the already entered Lund plane.

4.1 Introducing the parton splitting setup

The physical scenario considered here consists of the splitting of a *parent* parton with momentum $\vec{p}_0 = [E, \boldsymbol{p}_0]$ into two *daughter* partons with the following final-state kinematics,

$$\vec{p}_1 = [zE, \boldsymbol{p}_1]\,, \;\; \vec{p}_2 = [(1-z)E, \boldsymbol{p}_2]\,, \tag{4.1}$$

with $\boldsymbol{p}_0 = \boldsymbol{p}_1 + \boldsymbol{p}_2$ according to transverse momentum conservation. Again, the notation refers to light-cone kinematics, with $t := x^+$ standing for light-cone time and $E := p^+$ the light-cone energy. The minus component of the momenta is integrated out throughout the derivation, thus producing an explicit time dependence. As stated above, for the moment focus is put on a final-state singlet antenna. More specifically, the splitting of a transversely polarized photon into a quark-antiquark dipole is addressed, as shown in Fig. 4.1. The partial amplitude for the chosen in-medium splitting reads

$$\begin{aligned}\mathcal{M}_{\gamma\to q\bar{q}} = \frac{e}{E} e^{i\frac{\boldsymbol{p}_1^2}{2zE} + i\frac{\boldsymbol{p}_2^2}{2(1-z)E}L} \int_0^\infty dt \int_{\boldsymbol{k}_1,\boldsymbol{k}_2} \left[\mathcal{G}\left(\boldsymbol{p}_1, L; \boldsymbol{k}_1, t|zE\right) \bar{\mathcal{G}}\left(\boldsymbol{p}_2, L; \boldsymbol{k}_2, t|(1-z)E\right)\right]_{ij} \\ \times\, \gamma_{\lambda,s,s'}(z)\; \boldsymbol{k}\cdot\boldsymbol{\epsilon}_\lambda^*\; \mathcal{G}_0\left(\boldsymbol{k}_1+\boldsymbol{k}_2, t|E\right),\end{aligned} \tag{4.2}$$

where $\gamma_{\lambda,s,s'}(z) = i\delta_{s,-s'}\left[z\delta_{\lambda,s} - (1-z)\delta_{\lambda,-s}\right]/\sqrt{z(1-z)}$ is the quark-gluon splitting vertex, with $\lambda = \pm 1$ and $\boldsymbol{k} := (1-z)\boldsymbol{k}_1 - z\boldsymbol{k}_2$. Here $\mathcal{G}$ and $\bar{\mathcal{G}}$ represent the propagators for the quark and the antiquark, respectively. As usual for high-energy processes, parton-medium interactions are assumed to only exchange transverse momentum, so that $\boldsymbol{k}_1$ and $\boldsymbol{k}_2$ correspond to the transverse momentum shared immediately after splitting. For the sake of alleviating notation, the shortcuts $\int_{\boldsymbol{x}} := \int d^2\boldsymbol{x}$ for transverse coordinate and $\int_{\boldsymbol{k}} := \int d^2\boldsymbol{k}/(2\pi)^2$ for transverse momentum integrations are implemented.

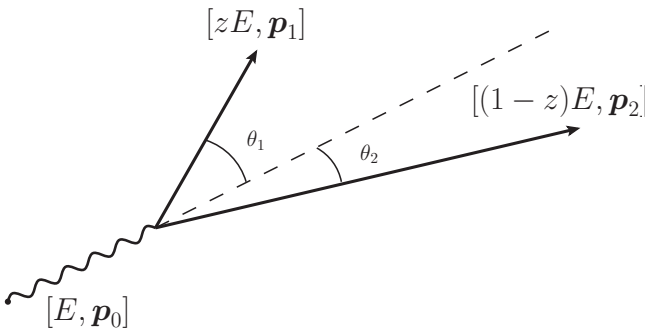

Figure 4.1: Final-state kinematics of the splitting process under consideration. In terms of angular quantities, the antenna opening angle is $\boldsymbol{n}_{12} = \boldsymbol{n}_1 - \boldsymbol{n}_2$, with $|\boldsymbol{n}_1| = \theta_1$, $|\boldsymbol{n}_2| = \theta_2$ and $|\boldsymbol{n}_{12}| = \theta$.

The fully dressed propagator in momentum space transforms to configuration space as

$$\mathcal{G}\left(\boldsymbol{p}_1, t_1; \boldsymbol{p}_0, t_0\right) = \int_{\boldsymbol{x}_1, \boldsymbol{x}_2} e^{-i\boldsymbol{p}_1\cdot\boldsymbol{x}_1 + i\boldsymbol{p}_0\cdot\boldsymbol{x}_0}\, \mathcal{G}(\vec{x}_1, \vec{x}_0), \tag{4.3}$$

where color and energy indices have been suppressed. In configuration space, $\mathcal{G}(\vec{x}_1, \vec{x}_0)$ is described by the Green's function propagator, which has been widely introduced through this manuscript, eq. (2.29).

For propagation outside the medium, the propagator reduces to

$$\mathcal{G}\left(\boldsymbol{p}_1, L; \boldsymbol{k}_1, t|E\right)\Big|_{t>L} = (2\pi)^2\delta(\boldsymbol{k}_1 - \boldsymbol{p}_1)\mathcal{G}_0\left(\boldsymbol{p}_1, L - t|E\right), \tag{4.4}$$

where $\mathcal{G}_0\left(\boldsymbol{k}, t|E\right) = e^{-i\frac{\boldsymbol{k}^2}{2E}t}$, which also corresponds to the photon propagator in eq. (4.2). The expression for the antiquark propagator is analogous.

As the focus of the present study is on the limit of hard splittings inside the medium, meaning that the formation time of the splittings are meant to be much shorter than the typical medium time-scales, a semi-classical picture is expected to dominate the cross-section on general grounds. This situation contrasts with the limit of medium-induced branchings [64, 67, 76, 80, 82, 146, 147], where one considers emissions with transverse momenta dominated by interactions with the medium. The high-energy limit is implemented as well. This in turn means that the energy of the leading partons is infinite, $E \to \infty$, but one can nevertheless trace the finite momentum sharing fraction z back. A two-step approximation process has to be carried out toward establishing this correspondence. The first move fixes the trajectories of the energetic partons, so that they follow classical trajectories determined by the kinematics of the process, whilst the second stage attaches the dipole to a common reference point in transverse space. In fact, both incoming partons are intended to have large enough energy in such a way that fluctuations in transverse position due to scattering with the medium constituents can be overlooked. This contribution can factually be isolated by considering the so-called eikonal expansion of the propagator (2.29) [148,149]. Its zeroth-term, which neglects further transverse momentum broadening in the medium, reads

$$\mathcal{G}^{(0)}(\vec{x}_1, \vec{x}_0) = \mathcal{G}_0(\boldsymbol{x}_1 - \boldsymbol{x}_0, t_1 - t_0)W(t_1, t_0; [\boldsymbol{x}_{cl}]), \tag{4.5}$$

where $\boldsymbol{x}_{cl}(t) = \frac{t_1 - t}{t_1 - t_0}\boldsymbol{x}_0 + \frac{t - t_0}{t_1 - t_0}\boldsymbol{x}_1$ is the classical trajectory. Now, according to the Fourier transformation (4.3), the propagator in mixed representation turns out to be

$$\begin{aligned}\mathcal{G}^{(0)}(\boldsymbol{p}_1, t_1; \boldsymbol{p}_0, t_0) = e^{-i\frac{\boldsymbol{p}_1^2}{2E}(t_1 - t_0)} \int_{\boldsymbol{y}_0, \boldsymbol{y}_1} e^{-i(\boldsymbol{p}_1 - \boldsymbol{p}_0)\cdot\boldsymbol{y}_0} \frac{(t_1 - t_0)E}{2\pi i} e^{i\frac{(t_1 - t_0)E}{2}(\boldsymbol{y}_1 - \boldsymbol{n})^2} \\ \times W(t_1, t_0; [\boldsymbol{y}_0 + (t - t_0)\boldsymbol{y}_1]),\end{aligned} \tag{4.6}$$

where $\boldsymbol{n} := \boldsymbol{p}_1/E$. Imposing $E \gg L^{-1}$ by virtue of the semi-classical limit reduces the kernel of the preceding equation to a Delta function of its argument, this way ensuring that the particles propagate along the classical path. This delivers the following result for the propagator[1],

$$\mathcal{G}^{(0)}(\boldsymbol{p}_1, t_1; \boldsymbol{p}_0, t_0) = e^{-i\frac{\boldsymbol{p}_1^2}{2E}(t_1-t_0)} \int_{\boldsymbol{x}} e^{-i(\boldsymbol{p}_1-\boldsymbol{p}_0)\cdot\boldsymbol{x}} W(t_1, t_0; [\boldsymbol{x} + (t-t_0)\boldsymbol{n}]), \tag{4.7}$$

which corresponds to the S-matrix of a high-energy parton crossing the medium that has been introduced earlier in eq. (2.28).

So far, this procedure removes all non-eikonal broadening effects after the dipole has been formed inside the medium. However, the initial position of the trajectory that describes each leg of the antenna is not yet firmly set, what leads to a *smearing* of the dipole initial position in terms of transverse coordinates[2]. In fact, for physical processes occurring at large time lengths with respect to the initial position, the origin of the Wilson line can be treated as a small correction, thus giving rise to the following result for the quark propagator,

$$\mathcal{G}^{(0)}(\boldsymbol{p}_1, t_1; \boldsymbol{p}_0, t_0) = (2\pi)^2 \delta(\boldsymbol{p}_0 - \boldsymbol{p}_1) e^{-i\frac{\boldsymbol{p}_1^2}{2E}(t_1-t_0)} W(t_1, t_0; [\boldsymbol{n}t]), \tag{4.8}$$

making sure that the Wilson lines are initiated at the same initial transverse position and time.

Now, entering the preceding expression for the propagator into the partial amplitude (4.2), and assuming the splitting takes place within the medium of size L, $0 < t < L$, gives

$$\mathcal{M}^{\text{in}}_{\gamma\to q\bar{q}} = \frac{e}{E}\gamma_{\lambda,s,s'}(z)\ \boldsymbol{p}\cdot\boldsymbol{\epsilon}^*_\lambda \int_0^L dt\ \exp\left(-i\frac{L-t}{t_f}\right)\Big[W_1(L,t)W_2^\dagger(L,t)\Big]_{ij}, \tag{4.9}$$

where $\boldsymbol{p} := (1-z)\boldsymbol{p}_1 - z\boldsymbol{p}_2$ is only related to the final-state momenta. Noteworthy is that the quantum-mechanical formation time can be read off this expression,

$$t_f = \frac{2z(1-z)E}{\boldsymbol{p}^2}. \tag{4.10}$$

This arrangement completes the implementation of the semi-classical approximation, in which the leading partons propagate along certain trajectories determined by their kinematics. This way both Wilson lines correspond to each of the legs of the antenna, such that $W_i(\bar{t}, t) := W(\bar{t}, t; [\boldsymbol{r}_i(s)])$, with $\boldsymbol{r}_i(s) = \boldsymbol{n}_i s$ ($\boldsymbol{n}_1 = \boldsymbol{p}_1/(zE)$ and $\boldsymbol{n}_2 = \boldsymbol{p}_2/[(1-z)E]$).

[1] A similar derivation is performed in [150].

[2] Appendix 4.B provides insight in this respect.

As a matter of fact, the partial amplitude for emissions taking place outside the medium, $t > L$, can be straightforwardly deduced via integrating over the splitting time. It explicitly delivers

$$\mathcal{M}^{\text{out}}_{\gamma\to q\bar{q}} = i\delta_{ij}\frac{z(1-z)}{E}e\gamma_{\lambda,s,s'}(z)\frac{\boldsymbol{p}\cdot\epsilon^*_\lambda}{\boldsymbol{p}^2}. \tag{4.11}$$

The total amplitude will simply be the sum of eqs. (4.9) and (4.11), $\mathcal{M}_{\gamma\to q\bar{q}} = \mathcal{M}^{\text{in}}_{\gamma\to q\bar{q}} + \mathcal{M}^{\text{out}}_{\gamma\to q\bar{q}}$.

4.2 Deriving the spectrum

Turning to the computation of the spectrum of the splittings, it is instructive to recall the following quantities,

$$S_{IJ}(t_1,t_0) := \frac{1}{N}\left\langle \text{Tr}\left(W_I W_J^\dagger\right)\right\rangle, \tag{4.12}$$

the two-point function, already discussed in subsection 2.2.2, which corresponds to the dipole cross-section. Here the extent of the Wilson lines is implicit from the left-hand side of the equation, and $\{I,J\} = \{1,2,\bar{1},\bar{2}\}$. Note that the trajectories in amplitude, $\boldsymbol{r}_1$ and $\boldsymbol{r}_2$, and complex-conjugate amplitude, $\boldsymbol{r}_{\bar{1}}$ and $\boldsymbol{r}_{\bar{2}}$, are only shifted due the difference in the splitting time, and this varies independently, see Fig. 4.2. For its part, the four-point function,

$$Q(t_1,t_0) = \frac{1}{N}\left\langle \text{Tr}\left(W_1 W_2^\dagger W_{\bar{2}} W_{\bar{1}}^\dagger\right)\right\rangle, \tag{4.13}$$

is also referred to as a quadrupole. In the harmonic oscillator approximation (2.41), and for the case of a static medium of size L, the two-point correlator reads

$$S_{IJ}(t_1,t_0) = \exp\left[-\frac{1}{4}\hat{q}\int_{t_0}^{t_1} ds \boldsymbol{r}^2_{IJ}(s)\right], \tag{4.14}$$

with $\hat{q} := C_F\hat{\bar{q}}$ the transport coefficient for fundamental degrees of freedom. $\boldsymbol{r}_{IJ} := \boldsymbol{r}_I - \boldsymbol{r}_J$ describes here the separation between the eikonal trajectories in transverse space. Under the large number of colors approach, the quadrupole can be written as follows [146, 147],

$$Q(t_1,t_0) = S_{1\bar{1}}(t_1,t_0)S_{2\bar{2}}(t_1,t_0) + \int_{t_0}^{t_1} ds\; S_{1\bar{1}}(t_1,s)S_{2\bar{2}}(t_1,s)T(s)S_{12}(s,t_0)S_{\bar{1}\bar{2}}(s,t_0), \tag{4.15}$$

where $T(s)$ is the transition amplitude,

$$T(s) = -\frac{1}{2}\hat{q}\left[\boldsymbol{r}^2_{12}(s) + \boldsymbol{r}^2_{\bar{1}\bar{2}}(s) - \boldsymbol{r}^2_{1\bar{2}}(s) - \boldsymbol{r}^2_{\bar{1}2}(s)\right] = -\hat{q}\;\boldsymbol{r}_{1\bar{1}}(s)\cdot\boldsymbol{r}_{2\bar{2}}(s). \tag{4.16}$$

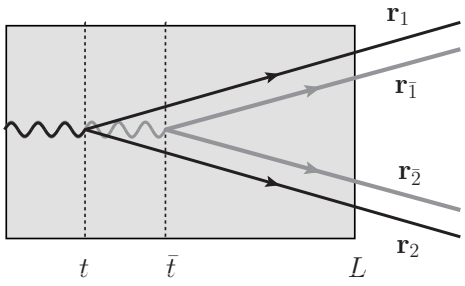

Figure 4.2: The *in-in* component to the spectrum. The amplitude, in black, and its complex-conjugate, in grey, are sketched out on top of each other to emphasize the character of the splitting. The dipole spreads over the region $(\bar{t}, t)$, while the quadrupole does it within the region $(L, \bar{t})$.

Each of the terms in the equation above are the so-called factorizable and non-factorizable pieces of the quadrupole. They describe the propagation of two possible color configurations under the large-N_c limit, such that color is conserved at any given time. In particular, the first term in eq. (4.15) accounts for the propagation of two antennas that separately correlate particles 1 and 2 in amplitude and complex-conjugate amplitude, so that they evolve independently of each other. This is why it is known as the factorizable piece of the quadrupole. The non-factorizable piece, on the other hand, involves a gluon exchange, encapsulated in the transition amplitude, which alters the color correlation of the system from a two-parton correlated state for $t < s$, to the uncorrelated system at times $t > s$.

By virtue of the undertaken approximations, the separations between the leading parton trajectories are either constant or grow linearly with time. Indeed, in its high-energy limit, the separation of the splitting time in amplitude, t, and complex-conjugate amplitude, $\bar{t}$, dictates the precise straight trajectories of the Wilson lines. More specifically,

$$\begin{aligned} &\boldsymbol{r}_{1\bar{1}}(s) = \boldsymbol{n}_1(\bar{t} - t),\ \boldsymbol{r}_{2\bar{2}}(s) = \boldsymbol{n}_2(\bar{t} - t), \\ &\boldsymbol{r}_{12}(s) = \boldsymbol{n}_{12}(s - t),\ \boldsymbol{r}_{\bar{1}\bar{2}}(s) = \boldsymbol{n}_{12}(s - \bar{t}), \end{aligned} \tag{4.17}$$

where $\boldsymbol{n}_{12} := \boldsymbol{n}_1 - \boldsymbol{n}_2$. Noteworthy is to bear in mind its relation with the relative transverse momentum of the pair, $\boldsymbol{n}_{12} = \boldsymbol{p}/[z(1-z)E]$, with $\boldsymbol{p} = (1-z)\boldsymbol{p}_1 - z\boldsymbol{p}_2$. Now, assuming a vanishing initial momentum $\boldsymbol{p}_0$ produces $\boldsymbol{n}_1 = (1-z)\boldsymbol{n}_{12}$ and $\boldsymbol{n}_2 = -z\boldsymbol{n}_{12}$. In angular terms, $\theta := |\boldsymbol{n}_{12}|$ and $\theta_{1(2)} := |\boldsymbol{n}_{1(2)}|$. In this way, the transition amplitude (4.16) takes the simple form

$$T(s) = -\hat{q}\ \boldsymbol{n}_1 \cdot \boldsymbol{n}_2(\bar{t} - t)^2 = -\hat{q}z(1-z)\boldsymbol{n}_{12}^2(\bar{t} - t)^2. \tag{4.18}$$

Having set all these aspects, the inclusive spectrum for the splitting process under consideration can be written as

$$\frac{dN^{\rm med}}{dzd\boldsymbol{p}^2} = \frac{1}{4(2\pi)^2 z(1-z)} \left\langle |\mathcal{M}_{\gamma\to q\bar{q}}|^2 \right\rangle = \frac{1}{4(2\pi)^2 z(1-z)} \left\langle |\mathcal{M}^{\rm in}_{\gamma\to q\bar{q}} + \mathcal{M}^{\rm out}_{\gamma\to q\bar{q}}|^2 \right\rangle , \quad (4.19)$$

where the averaging procedure over the ensemble of medium configurations is implicit. Here, the total spectrum in the presence of a medium can be computed as the sum of three different components. The *in-in* one, which corresponds to the splitting taking place inside the medium in both amplitude and complex-conjugate amplitude; the *in-out* contribution, in the sense of an interference between an emission taking place within the medium in amplitude and outside the medium in its complex-conjugate (or vice versa); and the last contribution corresponding to an emission outside the medium in amplitude and complex-conjugate amplitude. It is therefore intuitive to define the vacuum cross-section from the *out-out* component, $\langle |\mathcal{M}^{\rm out}|^2 \rangle$. It reads

$$\frac{dN^{\rm vac}}{dzd\theta} = \frac{\alpha_{\rm em}}{\pi} \frac{P_{q\gamma}(z)}{\theta}, \quad (4.20)$$

where it has been used that $\boldsymbol{p}^2 = [z(1-z)E\theta]^2$, and the definition of the relevant Altarelli-Parisi splitting function, $P_{q\gamma}(z) = n_f N[z^2 + (1-z)^2]$, with n_f the number of quark flavors. A little algebra gives rise to the following expression for the *in-in* spectrum,

$$\frac{dN^{\text{in-in}}}{dzd\theta} = \frac{dN^{\rm vac}}{dzd\theta}\, 2{\rm Re} \int_0^L \frac{dt}{t_f} \int_t^L \frac{d\bar{t}}{t_f}\, e^{-i\frac{\bar{t}-t}{t_f}}\, Q(L,\bar{t}) S_{12}(\bar{t},t), \quad (4.21)$$

where the quadrupole $Q(L,\bar{t}) := Q(L,\bar{t};t)$ explicitly depends on the splitting time in amplitude. For its part, the *in-out* interference spectrum reads

$$\frac{dN^{\text{in-out}}}{dzd\theta} = -\frac{dN^{\rm vac}}{dzd\theta}\, 2{\rm Im} \int_0^L \frac{dt}{t_f}\, e^{-i\frac{L-t}{t_f}}\, S_{12}(L,t). \quad (4.22)$$

Summing up all three components, the total spectrum can be written in the following manner,

$$\frac{dN^{\rm med}}{dzd\theta} = \frac{dN^{\rm vac}}{dzd\theta} \left[1 + F_{\rm med}(z,\theta)\right], \quad (4.23)$$

where the factor $F_{\rm med}$ encompasses the medium modifications. This function reads

$$F_{\rm med} = 2\int_0^L \frac{d\bar{t}}{t_f} \cos\left(\frac{\bar{t}-t}{t_f}\right) S_{12}(\bar{t},t) Q(L,\bar{t}) - \sin\left(\frac{L-t}{t_f}\right) S_{12}(L,t), \quad (4.24)$$

with $S_{12}(\bar{t},t) := S_{12}(\tau)$ and $Q(L,\bar{t}) := Q(\tau_L,\tau)$ only depending on the differences $\tau := \bar{t}-t$ and $\tau_L := L-\bar{t}$. More explicitly, these functions have the form

$$\begin{aligned} S_{12}(\tau) &= e^{-\frac{1}{12}\hat{q}\theta^2\tau^3}, \\ Q(\tau_L,\tau) &= e^{-\frac{1}{4}\hat{q}\xi\theta^2\tau_L\tau^2} + T(\tau)\int_{\bar{t}}^{L} ds\; e^{-\frac{1}{4}\hat{q}\xi\theta^2(L-s)\tau^2} e^{-\frac{1}{12}\hat{q}\theta^2[(s-\bar{t})^3+(s-t)^3-\tau^3]}, \end{aligned} \tag{4.25}$$

where $s \geq \bar{t} \geq t$, and ξ is defined in terms of the finite momentum fraction z as $\xi = (1-z)^2 + z^2$.

The factorized nature of eq. (4.23) comes from the fact that the kinematics of the antenna is not modified after being formed. Conversely, in the case of medium-induced branchings, the daughter partons experience additional momentum broadening stemming from non-eikonal contributions both during the formation time and afterwards [146, 147].

Looking at the medium modification function, it clearly describes two different stages of the process. The former is governed by the dipole cross-section $S_{12}(t_1,t_0)$ that shows up in both terms. It can be interpreted as the survival probability of a (virtual) pair consisting of the offspring 1 and 2 with increasing transverse size $b_\perp \sim \theta t$, both propagating within the time interval $\Delta t = t_1 - t_0$. This stage is referred to as the decoherence of the dipole. Instead, the quadrupole $Q(\tau_L,\tau)$ only plays a role in contributing to the *in-in* component, see eq. (4.21). Having a look at the expression of the quadrupole, eq. (4.25), the first term accounts for the survival probability of a (real) dipole with fixed transverse size $b_\perp \sim \theta\tau$ at the time of its creation, then propagating the remaining time length till the end of the medium. In this way, it is intuitive and suitable to refer to this stage as the broadening of the antenna, even though in the chosen setup this broadening does not receive contributions from non-eikonal fluctuations regarding changes in the tranverse position of the leading partons along their classical trajectories. The so-called non-factorizable piece, given by the second term in eq. (4.25), is typically a small correction, as will be discussed further below.

Briefly, the terms in eq. (4.24) correspond to the *in-in* probability amplitude and *in-out* interference amplitude components, respectively. Keeping a fixed medium length L, and making the medium density collapse to zero, $\hat{q} \to 0$, reveals a non-trivial cancellation between both terms that leads to $F_{\text{med}} \to 0$, as is expected in the dilute limit.

4.3 The characteristic time-scales of the process

In the same vein as the analysis conducted through this thesis, this piece is intended to discuss the relevant time-scales appearing in the undertaken process.

As evidenced by eq. (4.24), the emission process is characterized by a competition amongst the quantum-mechanical formation time of the antenna, which enforces $\tau \leq t_f$ for the *in-in* and $L - t \leq t_f$ for the *in-out* components, respectively, as well as the suppression factors related to color decoherence and broadening. These conditions arise from avoiding strong oscillations of the trigonometric factors in both terms of eq. (4.24).

Indeed, the relevant scales for the *in-in* spectrum can be directly read off the expressions for the dipole and the factorizable piece of the quadrupole. Explicitly,

$$t_d \sim \left(\frac{1}{\hat{q}\theta^2}\right)^{1/3}, \; t_{\text{broad}} \sim \left(\frac{1}{\hat{q}\theta^2 L}\right)^{1/2}, \tag{4.26}$$

referred to as the decoherence and broadening times, respectively.

As stated above, the non-factorizable piece of the quadrupole constitutes a small correction to this qualitative estimation. This is somewhat clearer after articulating a broader discussion around the physical picture. The decoherence time dictates the color decoherence of the antenna, and for $t_d > L$, the survival probability is close to one and the medium is not able to resolve the dipole until it exits the medium, as was discussed several times throughout this manuscript. In terms of angles, this condition implies that $\theta < \theta_c \sim (\hat{q}L^3)^{-1/2}$. When compared to the formation time, $t_f < t_d$ entails the condition $\boldsymbol{p}^2 > \sqrt{\hat{q}z(1-z)E}$, which is directly related to the transverse momentum broadening accumulated during the formation time. In turn, the broadening time-scale concerns the transverse momentum broadening along the medium length L. In particular, the condition $t_f < t_{\text{broad}}$ implies that $\boldsymbol{p}^2 > Q_s^2 \sim \hat{q}L$, where Q_s is the saturation momentum, entered earlier when computing the radiation spectrum off the antenna in the strict soft limit. Otherwise, the original antenna opening angle would be significantly changed by broadening, and the particles would emerge at a different angle from the initial opening angle. As $t_{\text{broad}} < t_d$ for large angles, $\theta > \theta_c$, the broadening along the whole medium length is typically larger than during the formation time of (relatively) large-angle splittings, such that for small-angle emissions, $\theta < \theta_c$, one should not expect any medium modifications, i.e. $F_{\text{med}} = 0$. More importantly, the kinematical phase-space for in-medium vacuum-like splittings[3] also exists for $t_f < t_{\text{broad}} < t_d$ at large angles, $\theta > \theta_c$.

It is also important to bear in mind that the interference amplitude is not sensitive to the dynamics encoded in the quadrupole, see eq. (4.22). In fact, the *in-out* spectrum results to be only sensitive to the decoherence time in the dipole $S_{12}(L,t)$, as can be seen in eq. (4.24). What is more, according to the range of integration, which is limited by the phase, this term averages to 0 provided that $t_f \ll L$ as $L - t \leq t_f$.

[3]They imply a vanishing F_{med}.

Note, however, that the discussion above only holds for jets with energies larger than the maximal gluon frequency ω_c. As is illustrated in more detail further below, for smaller energies, one finds stronger conditions on the angular phase space, so that one becomes sensitive to two dynamical critical angles given by $t_f|_{z=1} = t_d$, leading to $\theta_d \sim (\hat{q}/E^3)^{1/4}$, and $t_f|_{z=1} = t_{\rm broad}$, what leads to $\theta_{\rm broad} \sim (\hat{q}L)^{1/2}/E$. What is more, since $E < \omega_c \sim \hat{q}L^2$ also implies that $\theta_{\rm broad} < \theta_d$, as long as $\theta_{\rm broad} > R$, or $ER > Q_s$, with R the cone angle of the jet, there exists a regime of in-medium hard splittings.

But to avoid rapid oscillations or exponential suppression of the cross-section as a result of medium modifications, considering the *in-in* component, the difference of emission times in the amplitude and its complex-conjugate has to satisfy

$$\tau \leq \min\left[t_f, t_d, t_{\rm broad}\right]. \tag{4.27}$$

In addition to this condition, the emission time for the *in-in* spectrum itself is of the same order, $t \sim \tau$. To be clear, the actual emission time is dictated by the smallest of the three physical time-scales that are present in the problem. Indeed, as it is always true that $t_{\rm broad} < t_d$, eventually it turns out that $\tau \leq \min\left[t_f, t_{\rm broad}\right]$. Meanwhile, at large formation times, $t_f \gg L$, all factors appearing in the integrand of eqs. (4.21) and (4.22) can be neglected, this way delivering

$$\begin{aligned} \left.\frac{dN^{\text{in-in}}}{dzd\theta}\right|_{t_f\gg L} &\simeq \frac{dN^{\rm vac}}{dzd\theta}\times\left(\frac{L}{t_f}\right)^2, \\ \left.\frac{dN^{\text{in-out}}}{dzd\theta}\right|_{t_f\gg L} &\simeq -\frac{dN^{\rm vac}}{dzd\theta}\times\left(\frac{L}{t_f}\right)^2, \end{aligned} \tag{4.28}$$

so expecting no medium effects at large formation times.

Now, drawing on the discussion conducted throughout this piece, it is enlightening to sketch a kinematical Lund diagram subject to the general constraint $p_\perp := |\boldsymbol{p}| \geq Q_0$, where $Q_0 \sim \Lambda_{QCD}$. As pointed out in subsection 2.1.3, the Lund diagram can be spanned with different variables. In this particular case, it is convenient to exploit it in terms of the logarithmic variables $\left\{\ln\frac{1}{z}, \ln\frac{1}{\theta}\right\}$. Moreover, for simplicity sake, all corrections $\mathcal{O}(1-z)$ are neglected by virtue of the double-logarithmic approximation (DLA) in such a way that regions in the Lund plane are divided by straight lines.

At this stage, there is a subletly that is worthwhile to discuss about. Though the addressed scenario involves a photon splitting which does not encompass any soft divergence, the validity of the factorization property shown in eq. (4.23), as well as the medium modification function (4.24), remains for an arbitrary splitting process. In fact, the generalization of these findings to colored splittings is outlined in Appendix 4.A.

At fixed coupling, the total phase-space (PS) available for radiation off a jet with energy E and a cone angle R is therefore given by

$$(PS)_{\text{tot}} = \frac{1}{\bar{\alpha}} \int_0^1 dz \int_0^R d\theta \; \frac{d\sigma^{DLA}}{dz d\theta} \Theta(zE\theta > Q_0) = \frac{1}{2} \ln^2 \frac{ER}{Q_0}, \tag{4.29}$$

where $d\sigma^{DLA}/dzd\theta$ accounts for the probability that one splitting takes place, eq. (2.19). Explicitly recalling it here,

$$d\sigma^{DLA} = \bar{\alpha} \cdot d\ln\frac{1}{z} \; d\ln\frac{1}{\theta}, \tag{4.30}$$

where $\bar{\alpha} := 2\alpha_s C_F/\pi$, with C_R the total charge of the dipole. Accordingly, at leading order the Lund plane is uniformly filled with density $\rho \sim \bar{\alpha}$.

In essence, four different competing time-scales pop up in the presence of a medium: (a) the kinematical formation time t_f; (b) the decoherence time t_d; (c) the broadening time t_{broad}; and (d) the medium length L. While primarily related to the formation of the dipole itself and its propagation through the medium, these time-scales will also play a role in the further evolution of the system due to the fixed kinematical choices, e.g. acting as a source for subsequent radiation.

4.4 Mapping out the phase-space onto the Lund plane

In this piece, a thorough discussion around the relevant time-scales regarding the Lund diagram drawn in Fig. 4.3 is presented. In particular, it is sketched for one in-medium splitting within the context of two possible energy regimes: $E > \omega_c$ (on the left-hand pane) and $E < \omega_c$ (on the right side). The different ordering of the time-scales outlined above correspond to the marked areas on the plane. More specifically, the straight lines are given by the following set of equations

$$\begin{aligned} \ell &= \ln EL - 2y \qquad (t_f = L), \\ \ell &= \ln \frac{E}{\hat{q}^{1/3}} - \frac{4}{3}y \qquad (t_f = t_d), \\ \ell &= \ln \frac{E}{Q_s} - y \qquad (t_f = t_{\text{broad}}), \end{aligned} \tag{4.31}$$

where $\ell := \ln 1/z$ and $y := \ln 1/\theta$. In the high-energy case, $E > \omega_c$, the critical angle θ_c is also marked with a vertical line.

In a first step, the high-energy regime is reviewed regarding Fig. 4.3 (left). The quantities $L_R := \ln R/\theta_c$ and $L_E := \ln E/\omega_c$ are entered in order to ease the interpretation of the phase-space for the different regions. Explicitly,

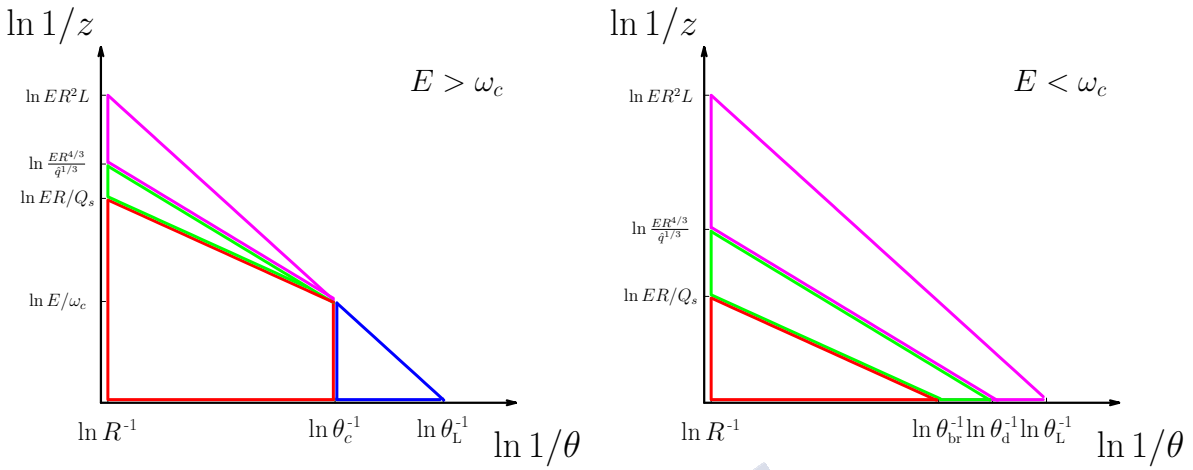

Figure 4.3: The Lund diagram for one soft and collinear vacuum splitting. The main phase-space regimes, bounded by the straight lines depicted on the figures, are interpreted as follows (starting from the uppermost line and going down): (i) the first line (magenta-blue on the left, purely magenta on the right) stands for the boundary in which the quantum-mechanical formation time is of the order of the medium length, $t_f = L$; (ii) the magenta-green line represents the boundary where the formation time is of the order of the decoherence time, $t_f = t_d$; (iii) the green-red line accounts for the boundary that matches the formation time and the time-scale for medium-induced broadening; (iv) finally, the vertical red-blue line (only in the left pane) represents the critical angle $\theta = \theta_c$.

(A.1) $\mathbf{t_f < t_{broad} < t_d < L}$ **(red region):** Particles are created early in the medium, governed by the quantum-mechanical formation time; that corresponds to vacuum-like emissions inside the medium [101, 150]. The phase-space reads

$$(\mathrm{PS})_1 = L_R \left(L_E + \frac{1}{2} L_R \right), \tag{4.32}$$

which is single-logarithmic in the jet energy. The leading term arises for the case when $zE > \omega_c$. All other contributions are subleading in the jet energy provided that $t_d < L$, starting from the second term in the preceding equation. In terms of decoherence of the pair, $t_d < L$ implies that the antenna decoheres in color at a finite distance inside the medium, which opens up for the possibility of incoherent energy loss due to secondary medium-induced radiation.

(A.2) $\mathbf{t_{broad} < t_f < t_d < L}$ **(green region):** In this case, medium modifications are expected to show up to a large extent since the broadening time is the shortest scale controlling the evolution of the system. The phase-space is given by

$$(\mathrm{PS})_2 = \frac{1}{6} L_R^2, \tag{4.33}$$

which is not logarithmically enhanced by the jet energy. This region involves relatively soft splittings, with $zE < \omega_c$ and $\boldsymbol{p}^2 < Q_s$.

(A.3) $\mathbf{t_{broad} < t_d < t_f < L}$ **(magenta region):** In this region, the results follow the same trend as the previous one. In particular, with the decoherence time regulating the stage before formation, a strong suppression of the formation of the two-parton system is appreciated on general grounds. This time ordering entails $\omega/L < \boldsymbol{p}^2 < (\hat{q}zE)^{1/2}$. Here the phase-space is

$$(\mathrm{PS})_3 = \frac{1}{3} L_R^2, \tag{4.34}$$

which is neither enhanced by logarithms of the jet energy.

(A.4) $\mathbf{t_f < L < t_d < t_{broad}}$ **(blue region):** Here, the splitting takes places inside the medium, but the created partons remain coherent. This occurs whether the splitting angle is small enough, $\theta < \theta_c$ [117], what supports again the idea of vacuum-like emissions. The phase-space reads

$$(\mathrm{PS})_4 = \frac{1}{4} L_E^2, \tag{4.35}$$

and is double-logarithmic in the jet energy. This time ordering implies that the medium is not able to resolve the splitting and, for the non-singlet case, the jet experiences coherent quenching due to the presence of a total color charge [150,151]. Also noteworthy is the fact that this scheme only exists within the high-energy regime, $E > \omega_c$. Due to the restriction on the energy, the characteristic decoherence and broadening time-scales are always shorter than the medium length, and all radiation inside the medium, i.e. $t_f < L$, actually occurs at angles larger than the critical angle θ_c, as $(\omega_c\theta^2)^{-1} < (zE\theta^2)^{-1} < L$.

(B) $\mathbf{t_f > L}$ **(beyond the** $t_f = L$ **line):** Medium effects are suppressed by the fact that the splitting occurs outside the medium.

In brief, medium effects are expected to be visible within two different areas, **(A.2)** and **(A.3)**. For its part, two regions of vacuum-like emissions inside the medium can also be identified, $t_f < L$, namely regions **(A.1)** and **(A.4)**. However, the fate of the dipole after splitting is expected to be very different as regards these two regions. In fact, it appears appropriate to denote regions **(A.1)** and **(A.4)** as incoherent and coherent radiation, respectively.

As is to be expected, the total phase-space for emissions inside the medium is the sum of the four contributions,

$$(\mathrm{PS})_{t_f<L} = \sum_{i=1}^{4} (\mathrm{PS})_i = \frac{1}{4} \ln^2 ER^2L. \tag{4.36}$$

Hence, there is a relatively large probability for a splitting taking place inside the medium, i.e. $(\mathrm{PS})_{t_f<L}/(\mathrm{PS})_{\mathrm{tot}} \sim 1/2$ asymptotically when $E \to \infty$. In the context of Monte Carlo simulations, the ratio is slowly varying and lies close to $\sim 40 - 45\%$ [152].

To end with, it is also enlightening to consider the low-energy regime, i.e. $E < \omega_c$. Here, the logarithmic contributions are automatically restricted and significant corrections to the leading-logarithmic approximation should be included. Nevertheless, it is interesting to point out that the region bounded by the condition $t_f < t_{\mathrm{broad}} < t_d$, corresponding to the **(A.1)** area, scales like

$$(\mathrm{PS})_{t_f<t_{\mathrm{broad}}(E<\omega_c)} = \frac{1}{2} \ln^2 \frac{ER}{Q_s}. \tag{4.37}$$

This regime will not be discussed further than this, however the impact of the remaining phase-space regimes can be systematically implemented following the steps above.

4.5 Numerical evaluation of the phase-space

As the main result of this work is to demonstrate the factorization property of the medium spectrum given by eq. (4.23), a numerical evaluation of the medium modification function onto the kinematical Lund plane is presented here. In particular, $Q_0 = 0.2$ GeV and $\hat{q} = 1.5$ GeV^2/fm are taken as reference values. The following jet and medium parameters are used for two different evaluations: for the high-energy regime, $E = 1000$ GeV and $L = 2$ fm, while for the low-energy regime $E = 240$ GeV and $L = 8$ fm[4]. The final results are shown in Fig. 4.4, with F_{med} defined in eq. (4.24). The plot at the left displays the result of evaluating the medium modification function into the Lund diagram defined in Fig. 4.3 for the high-energy regime, whereas the one on the right side represents the scheme within the low-energy regime. Lines are equivalent in both maps. As stated earlier when developing the Lund diagram, the full shaded area corresponds to the available phase-space given the constraint $k_\perp > Q_0$, and the lines correspond to the result of imposing $t_f = L$, $t_f = t_d$ and $t_f = t_{\mathrm{broad}}$ (from top to bottom).

[4]The reason behind this choice is to map the same in-medium phase-space $t_f < L$, so that the characteristic angle θ_c in the high-energy regime is approximately located at the same absolute angle as θ_{broad} in the low-energy regime.

It is therefore worthwhile to trace the medium modification function for different limits. Looking first at the high-energy regime (see Fig. 4.4, left pane), in the region where vacuum-like emissions are expected to take place, $t_f < t_{\text{broad}} < L$ with $t_d > L$ ($\theta < \theta_c$) and $t_f > L$, medium effects are negligible. Indeed, the onset of medium modifications follow the line $t_f = t_d$, and they are more pronounced within the regime bounded by $t_{\text{broad}} < t_f < t_d$, as predicted in Section 4.3. This is of little surprise as t_{broad} is related to the transverse momentum broadening along the medium length L, this way making sense for larger media.

In the low-energy regime (Fig. 4.4, right panel), on the other hand, medium effects are much larger. In fact, the scaling behaviour stated above can only be thought to hold in a parametric sense, and care has to be taken with the assumptions regarding the importance of the transverse momentum broadening. In fact, this parameter choice illustrates that part of the jet, i.e. large-angle and soft emissions, happen to reach the non-perturbative scale while still being inside the medium (in terms of time-scales, $t_f < L$). This constitutes a new category of in-medium modifications that goes beyond the scope of this work.

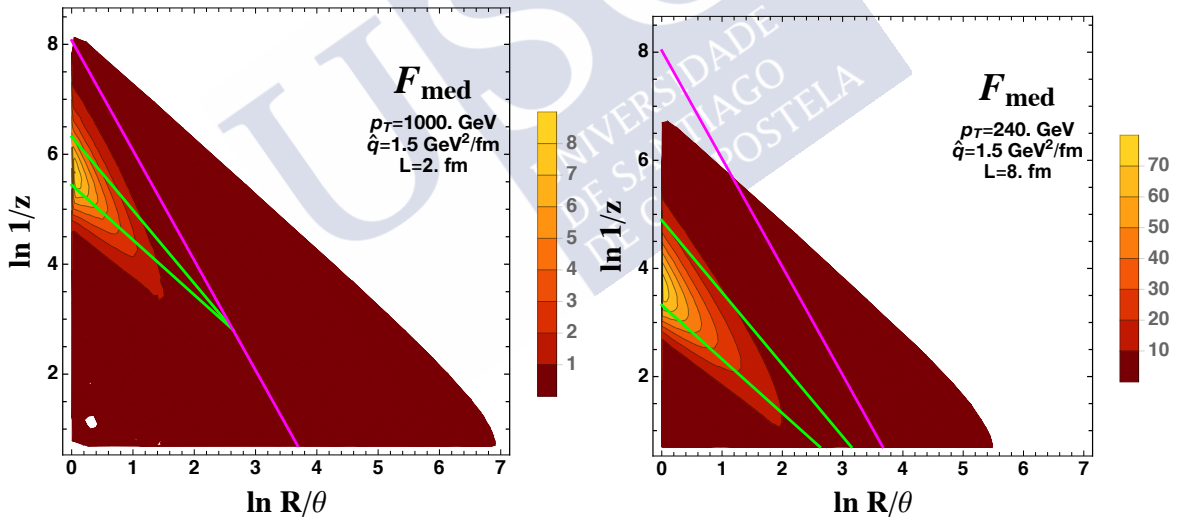

Figure 4.4: Numerical evaluation of the medium modification function F_{med} for the high- ($E > \omega_c$, left pane) and low-energy regimes ($E < \omega_c$, right panel). Notice that the scale of the color coding on the right-hand side is rescaled by a factor 10 with respect to the left one. The shaded area corresponds to the available phase-space given the constraint $k_\perp > Q_0$. The boundaries for the different regions are the same as those depicted in Fig. 4.3.

4.6 Summary and outlook

This work is intended to extend studies on the production of hard radiation in the presence of hot and dense matter. However, two regimes of vacuum-like emissions are found inside the medium. These schemes include the regime of short formation times (in particular $t_f < t_{\text{broad}} < L$, corresponding to the region **(A.1)** in Fig. 4.3), and small angles ($\theta < \theta_c$, region **(A.4)** in Fig. 4.3). Even so, the fate of these two types of emissions is different as only in the former scheme do the splitting products lose their color coherence before reaching the end of the medium. As a result of this prompt decoherence, the splitted partons should therefore become subject to independent energy loss processes. For its part, emissions in region **(A.4)** are color coherent when they exit the medium and should behave as an individual object.

The border at which long-distance medium effects start to play a role in the splitting process was also identified. This takes place at $t_f \geq t_{\text{broad}}$ and is also recovered in the numerical evaluation of the medium modification function onto the kinematical Lund plane, shown in Fig. 4.4. This study therefore confirms the notion of purely vacuum-like emissions inside the medium, meaning that the in-medium splitting function is equal to the one in vacuum, $F_{\text{med}} \approx 0$.

Finally, computing higher-order splitting processes goes beyond the scope of this analysis. Yet despite this, the discussion presented around the time-scales further corroborates the validity of the undertaken assumptions for the regions of vacuum-like emissions.

4.A Considering colored splittings

Generalizing the nature of the addressed splitting process to arbitrary color representations is straightforward, and does not modify the general structure of eq. (4.23). One simply has to replace the coupling constant $\alpha_{\text{em}} \to \alpha_s$, and the Altarelli-Parisi splitting function for the relevant one, e.g. $P_{q\gamma}(z) \to P_{ij}(z)$ in the vacuum spectrum, eq. (4.20). The laborious part is rather incurred by working out the color algebra, which this time turns out to be more involved when computing the medium modification function F_{med}. Taken as a concrete example the splitting process $q \to q+g$, the expressions for the dipole and the quadrupole have to be replaced by the following ones,

$$\begin{aligned} S_{12}(\bar{t},t) \to \frac{1}{N^2-1}\Big\langle \text{Tr}\left(W_2^\dagger(t,\bar{t})W_1(\bar{t},t)\right)\text{Tr}\left(W_0^\dagger(t,\bar{t})W_2(\bar{t},t)\right) \\ - \frac{1}{N}\text{Tr}\left(W_0^\dagger(t,\bar{t})W_1(\bar{t},t)\right)\Big\rangle, \end{aligned} \tag{4.38}$$

$$Q \to \frac{1}{N^2-1}\Big\langle \mathrm{Tr}\left(W_{\bar{1}}^{\dagger}(\bar{t},L)W_1(L,\bar{t})W_{\bar{2}}^{\dagger}(\bar{t},L)W_{\bar{2}}(L,\bar{t})\right)\mathrm{Tr}\left(W_{\bar{2}}^{\dagger}(\bar{t},L)W_2(L,\bar{t})\right) - \frac{1}{N}\mathrm{Tr}\left(W_{\bar{1}}^{\dagger}(\bar{t},L)W_1(L,\bar{t})\right)\Big\rangle. \tag{4.39}$$

Now, the second term in both expressions above can be neglected under the large-N_c limit, thus remaining

$$S_{12}(\bar{t},t) \to S_{12}(\bar{t},t)S_{20}(\bar{t},t), \tag{4.40}$$

$$Q \to Q(L,\bar{t})S_{2\bar{2}}(L,\bar{t}). \tag{4.41}$$

The emergence of these new dipole structures, $S_{20}(\bar{t},t)$ and $S_{2\bar{2}}(L,\bar{t})$, does not preclude transferring the qualitative insight regarding color-singlet dipole splittings to color-charged ones. In the harmonic oscillator approximation, they read

$$S_{20}(\bar{t},t) = e^{-\frac{1}{12}\hat{q}(1-z)^2\theta^2\tau^3}, \tag{4.42}$$

$$S_{2\bar{2}}(L,\bar{t}) = e^{-\frac{1}{4}\hat{q}z^2\theta^2(L-t')\tau^2}, \tag{4.43}$$

where now the differences amongst the trajectories described by the Wilson lines are given by $\boldsymbol{r}_{20}(s) = \boldsymbol{n}_1(s-t)$ and $\boldsymbol{r}_{2\bar{2}} = \boldsymbol{n}_2(t'-t)$.

Focusing on the dynamics during formation, in the large-N_c limit the scheme $S_{12}S_{20}$ only depends on the jet quenching parameter through the combination $\hat{q}_{\text{eff}} = \hat{q}[1+(1-z)^2] \approx [(1-z)N + z^2 C_F]\hat{\bar{q}}$, with $\hat{q} = C_F\hat{\bar{q}}$. Indeed, this effective $\hat{q}_{\text{eff}}$ has been previously identified for medium-induced quark-gluon splitting, see e.g. [147].

Similar conclusions can be reached as regards the correction to the quadrupole. Therefore, on balance, though the general outcome of this study is based on the calculation of a color-singlet splitting, the discussion above establishes that it can be straightforwardly extrapolated to splittings involving a non-zero total color charge via carefully considering the color dependence of $\hat{q}_{\text{eff}}$, together with the expected replacements in the vacuum spectrum, what also validates the discussion of soft and collinear radiation applied to the building of the Lund plane performed in Section 4.4.

4.B Beyond the classical picture

By implementing the high-energy limit, $E \to \infty$, and using the propagator previously introduced in eq. (4.7), the amplitude is given by

$$\mathcal{M}^{\text{in}}_{\gamma\to q\bar{q}} = \frac{e}{E}\gamma^{\gamma\to q\bar{q}}_{\lambda,s,s'}(z)\int_0^L dt\; e^{-i\frac{L-t}{t_f}} \times \Big[\boldsymbol{p} + i[(1-z)\boldsymbol{\partial}_{x_1} - z\boldsymbol{\partial}_{x_2}]\Big]\cdot\boldsymbol{\epsilon}_\lambda\Big[W_1(t_L,t)W_2^\dagger(t_L,t)\Big]_{ij}\Big|_{\boldsymbol{x}_1=\boldsymbol{x}_2=\boldsymbol{n}_0 t}, \tag{4.44}$$

up to factors that cancel out when computing the cross-section. Here $\boldsymbol{n}_0 = (\boldsymbol{p}_1+\boldsymbol{p}_2)/E$, and the trajectories followed by the antenna constituents are described by $\boldsymbol{r}_i := \boldsymbol{x}_i + (s-t)\boldsymbol{n}_i$, whereas in the derivation presented in Section 4.2 it was assumed that $\boldsymbol{x}_i = 0$.

The *in-in* spectrum then becomes

$$\frac{dN^{\text{in-in}}}{dzd\boldsymbol{p}^2} = \frac{dN^{\text{vac}}}{dzd\boldsymbol{p}^2}\,2\text{Re}\int_0^L\frac{dt}{t_f}\int_t^L\frac{d\bar{t}}{t_f}e^{-i\frac{\bar{t}-t}{t_f}}\hat{\mathcal{V}}_1\Big[Q(L,\bar{t})S_{12}(\bar{t},t)\Big]_{\substack{\boldsymbol{x}_2=\boldsymbol{x}_1=\boldsymbol{n}_0 t\\ \bar{\boldsymbol{x}}_2=\bar{\boldsymbol{x}}_1=\boldsymbol{n}_0 t}}, \tag{4.45}$$

and, in the same spirit, the *in-out* spectrum reads

$$\frac{dN^{\text{in-out}}}{dzd\boldsymbol{p}^2} = \frac{dN^{\text{vac}}}{dzd\boldsymbol{p}^2}\,2\text{Im}\int_0^L\frac{dt}{t_f}e^{-i\frac{L-t}{t_f}}\hat{\mathcal{V}}_2\Big[S_{12}(L,t)\Big]_{\boldsymbol{x}_2=\boldsymbol{x}_1=\boldsymbol{n}_0 t}, \tag{4.46}$$

where $t_f = 2z(1-z)E/\boldsymbol{p}^2$. Here the following operators have also been introduced,

$$\hat{\mathcal{V}}_1 = \frac{1}{\boldsymbol{p}^2}\Big(\boldsymbol{p} + i[(1-z)\boldsymbol{\partial}_{x_1} - z\boldsymbol{\partial}_{x_2}]\Big)\cdot\Big(\boldsymbol{p} - i[(1-z)\boldsymbol{\partial}_{\bar{x}_1} - z\boldsymbol{\partial}_{\bar{x}_2}]\Big), \tag{4.47}$$

$$\hat{\mathcal{V}}_2 = \frac{\boldsymbol{p}}{\boldsymbol{p}^2}\Big(\boldsymbol{p} + i[(1-z)\boldsymbol{\partial}_{x_1} - z\boldsymbol{\partial}_{x_2}]\Big). \tag{4.48}$$

The dipole term, which encompasses the additional shift of the initial positions of the Wilson lines, is now

$$S_{12}(t_1,t_0) = \exp\left\{-\frac{1}{4}\hat{q}\Delta t\left[\Big(\boldsymbol{x}_{12}+\frac{1}{2}\Delta t\boldsymbol{n}_{12}\Big)^2 + \frac{1}{12}\Delta t^2\boldsymbol{n}_{12}^2\right]\right\} \tag{4.49}$$

for generic time intervals, $\Delta t := t_1 - t_0$, and $\boldsymbol{x}_{12} := \boldsymbol{x}_1 - \boldsymbol{x}_2$, while the missing terms in the quadrupole, eq. (4.15), read

$$S_{I\bar{I}}(t_1,t_0) = \exp\left[-\frac{1}{4}\hat{q}\Delta t\Big(\boldsymbol{x}_{I\bar{I}} + \boldsymbol{n}_I\tau\Big)^2\right] \tag{4.50}$$

by virtue of eq. (4.12).

As a result of the constraints on the initial transverse position in amplitude and complex-conjugate amplitude, what leads to both $\boldsymbol{x}_1 = \boldsymbol{x}_2$ and $\bar{\boldsymbol{x}}_1 = \bar{\boldsymbol{x}}_2$, respectively,

the resulting spectra are similar to the terms derived to obtain eq. (4.23), except for a unique prefactor emerging under the integrals of the *in-in* and *in-out* components that arises from the more involved vertices presented just above.

Taking a closer look at these terms for the factorizable piece of the *in-in* component, the correction factor appearing under the integral reads

$$1 - i\frac{\hat{q}\tau^2}{4z(1-z)E} - i\frac{\hat{q}\tau_L\tau\xi}{z(1-z)E} - \left(\frac{\hat{q}\tau_L\tau\xi}{2z(1-z)E}\right)^2\left(1+\frac{\tau}{2\xi\tau_L}\right) + \frac{\hat{q}\tau_L\xi}{[z(1-z)E\theta]^2}, \quad (4.51)$$

with $\tau_L := L - \bar{t}$ and $\xi := (1-z)^2 + z^2$.

For the *in-out* component, the correction factor is $1 - i\hat{q}(L-t)^2/[4z(1-z)E]$, which closely resembles the two first terms in the preceding expression when exchanging τ by $L - t$. Neglecting all finite-z corrections, and assuming short times, $t, \bar{t} \ll L$, these terms scale as

$$1 - i\frac{t_f}{t_d}\left(\frac{\tau}{t_d}\right)^2 - i\left(\frac{t_f}{t_{\text{broad}}}\right)\left(\frac{\tau}{t_{\text{broad}}}\right) - \left(\frac{t_f}{t_{\text{broad}}}\right)^2\left(\frac{\tau}{t_{\text{broad}}}\right)^2 + \left(\frac{t_f}{t_{\text{broad}}}\right)^2, \quad (4.52)$$

what explicitly proves that corrections due to the vertex start to play a role whenever the kinematical formation time ceases to be the shortest time-scale to which compare the difference of emission times τ. In particular, this is starting to occur when $\tau \leq t_{\text{broad}} < t_f$.

USC
UNIVERSIDADE
DE SANTIAGO
DE COMPOSTELA

5

Embedding color coherence into the probabilistic picture of a partonic cascade

This chapter, the last one in this thesis devoted to the study of final state effects, is set up as a first attempt to embed the notion of color coherence into the evolution equation describing the branching processes that make up a medium-induced parton shower. As shall be seen later, this implementation of coherence effects into the rate equations scene takes, as a baseline, a parton configuration not so different from those addressed in Chapters 3 and 4. Then, after computing the relevant diagrams within the BDMPS-Z approach, the latest step towards eliciting an approachable probabilistic cascading picture which now encompasses color connections amongst the leading partons is to manipulate the emission kernel so that one can factor the coherence scheme out.

5.1 The partonic setup

As repeatedly stated throughout this manuscript, the intrinsic motivation of the studies presented in this thesis comprises a more detailed description and knowledge regarding a real-life parton shower. This means going a step beyond the main approximations undertaken in previous studies under this subject, as laid down in both Chapter 3 and 4.

These chapters accomplish this via handling multiple emissions configurations and taking notice of finite formation time effects for the splittings inside the medium, respectively. The partonic setup addressed here is not much different from those referred to. In particular, the double inclusive gluon production process occurring in a dense medium is raised now, where the extra gluon compared to the BDMPS-Z baseline is assumed to be very soft and, thus, the last splitting naturally takes place outside the medium – otherwise the gluon could no longer survive. In the same vein as the above calculation, the formation time of the quark-gluon dipole inside the medium is taken as finite.

As is clear given the above choices for the starting partonic configuration, only the two diagrams shown in Fig. 5.1 become significant for this study. What is more, as the right-hand diagram in Fig. 5.1 is nothing more than a mere color charge correction to the *in-in* component of the BDMPS-Z gluon radiation spectrum, the focus here is put on computing the interference contribution depicted on the left panel. The following section provides a detailed account of the computation of the spectrum according to these considerations.

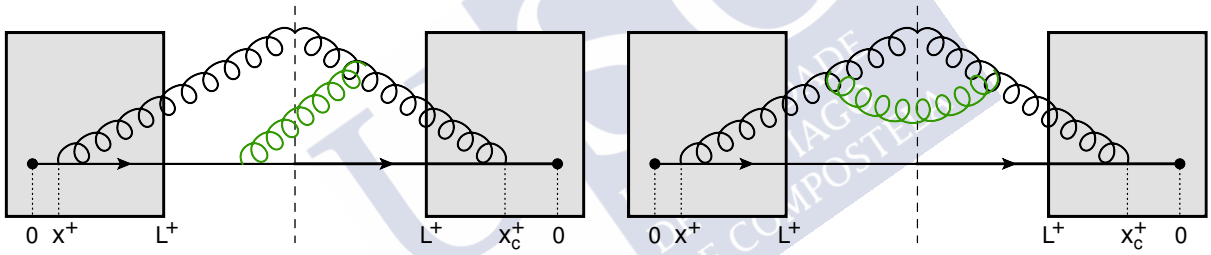

Figure 5.1: Diagrammatic representation of the relevant contributions to the process set forth above. The leading-eikonal quark, which emanates at $t = 0$ as a result of the hard process that materializes inside the medium, splits at $t = x^+$ in probability amplitude, whilst the splitting takes place at $t = x_c^+$ in complex-conjugate amplitude. For its part, eikonality restrictions are eased for the emerging gluon inside the medium – hereafter referred to as the BDMPS-Z gluon, this way allowing the parton to spread over the transverse plane. In a similar fashion as to the interference components corresponding to the processes derived in Chapter 3, the green gluon, laid again outside the medium, serves as means of tracking the coherence history of the partonic system, what, as will be seen later, is essential for the ultimate aim of this study. The plus component of the light-cone momentum for this soft gluon is fixed to the same in both amplitude and its complex-conjugate. As noted above, here the emphasis is on deriving the interference between the probability amplitudes $\langle \mathcal{M}_q \mathcal{M}_g^\dagger \rangle$ (left pane), while the direct component $\langle \mathcal{M}_g \mathcal{M}_g^\dagger \rangle$ (right panel) does not have much to say when looking towards embodying coherence effects into the rate equation for describing medium-induced partonic splittings.

5.2 Computing the spectrum

As discussed above, emphasis is put on the computation of the interference contribution displayed on the left-hand side of Fig. 5.1. By following the same standards as for deriving the spectrum of the processes presented under the preceding chapters, the probability amplitudes for the two branches making up this component can be written as

$$\begin{aligned}\mathcal{M}_q = -\frac{2g^2}{\omega}\int_{\boldsymbol{z}_\perp,x^+} & e^{-i\boldsymbol{k}_\perp\cdot\boldsymbol{z}_\perp}\ \partial_{\boldsymbol{x}_\perp}|_0\ \mathcal{G}^{ab}(L^+,\boldsymbol{z}_\perp;x^+,\boldsymbol{x}_\perp|k^+)\ t^c_{mi}W_{ij}(L^+,x^+;\boldsymbol{0})\\ & \times t^b_{jk}W_{kl}(x^+,0;\boldsymbol{0})\frac{\boldsymbol{k'}_\perp\cdot\boldsymbol{\epsilon'}_\perp}{\boldsymbol{k'}^2_\perp},\end{aligned} \tag{5.1}$$

$$\begin{aligned}\mathcal{M}_g = -\frac{2ig^2}{\omega}\int_{\boldsymbol{z}_\perp,x^+} & e^{-i\boldsymbol{k}_\perp\cdot\boldsymbol{z}_\perp}\ \partial_{\boldsymbol{x}_\perp}|_0\ f^{cda}\mathcal{G}^{ab}(L^+,\boldsymbol{z}_\perp;x^+,\boldsymbol{x}_\perp|k^+)\ W_{ij}(L^+,x^+;\boldsymbol{0})\\ & \times t^b_{jk}W_{kl}(x^+,0;\boldsymbol{0})\frac{\boldsymbol{k'}_\perp\cdot\boldsymbol{\epsilon'}_\perp}{\boldsymbol{k'}^2_\perp},\end{aligned} \tag{5.2}$$

where the shortcuts $\int_{x^+} := \int_0^L dx^+$ and $\int_{\boldsymbol{x}} := \int d^2\boldsymbol{x}$ have been implemented. Thus, the interference between the probability amplitudes above is given by

$$\begin{aligned}\left\langle \mathcal{M}_q\mathcal{M}_g^\dagger\right\rangle = \frac{4ig^4}{\omega^2\boldsymbol{k'}^2}\int_{\boldsymbol{z}_\perp,\boldsymbol{z'}_\perp,x^+,x_c^+} & e^{-i\boldsymbol{k}_\perp\cdot(\boldsymbol{z'}_\perp-\boldsymbol{z}_\perp)}\partial_{\boldsymbol{x}_\perp}\cdot\partial_{\boldsymbol{x'}_\perp}\Big\langle t^c_{mi}W_{ij}t^a_{jk}\mathcal{G}^{ab}W_{kl}\\ & \times f^{dcb}W^\dagger_{l\bar{k}}\mathcal{G}^{\dagger d\bar{a}}t^{\bar{a}}_{\bar{k}\bar{j}}W^\dagger_{\bar{j}\bar{m}}\Big\rangle_{\boldsymbol{x}_\perp=\boldsymbol{x'}_\perp=0},\end{aligned} \tag{5.3}$$

where all the position boundaries have been removed in order to shorten the expression. Now performing the color algebra over the objects inside the brackets delivers

$$\mathrm{Tr}\left(W^\dagger_{(L^+,x_c^+)}t^cW_{(L^+,x_c^+)}t^{a'}t^{\bar{a}}\right)W^{a'a}_{(x_c^+,x^+)}\mathcal{G}^{ab}(L^+,\boldsymbol{z}_\perp;x^+,\boldsymbol{x}_\perp)f^{dcb}\mathcal{G}^{\dagger d\bar{a}}(L^+,\boldsymbol{z'}_\perp;x_c^+,\boldsymbol{x'}_\perp), \tag{5.4}$$

which eventually reduces to

$$\begin{aligned}&\frac{i}{4}f^{a'\bar{a}A}f^{bcd}W^{cA}_{(L^+,x_c^+)}W^{a'a}_{(x_c^+,x^+)}\mathcal{G}^{ab}_{(L^+,x^+)}(\boldsymbol{z}_\perp,\boldsymbol{x}_\perp)\mathcal{G}^{\dagger d\bar{a}}_{(L^+,x_c^+)}(\boldsymbol{z'}_\perp,\boldsymbol{x'}_\perp)\\ &=\frac{i}{4}\int_{\boldsymbol{y}_\perp}f^{a'\bar{a}A}f^{bcd}W^{cA}_{(L^+,x_c^+)}W^{a'a}_{(x_c^+,x^+)}\mathcal{G}^{al}_{(x_c^+,x^+)}(\boldsymbol{y}_\perp,\boldsymbol{x}_\perp)\mathcal{G}^{lb}_{(L^+,x_c^+)}(\boldsymbol{z}_\perp,\boldsymbol{y}_\perp,)\mathcal{G}^{\dagger d\bar{a}}_{(L^+,x_c^+)}(\boldsymbol{z'}_\perp,\boldsymbol{x'}_\perp).\end{aligned} \tag{5.5}$$

This last step involves the use of the identity

$$t^a_{ij}t^b_{jk} = \frac{1}{2N}\delta^{ab}\delta_{ij} + \frac{1}{2}d^{abc}t^c_{ij} + \frac{i}{2}f^{abc}t^c_{ik}. \tag{5.6}$$

After these manipulations, averaging over initial polarization and color states and summing over final states gives rise to the following radiation spectrum,

$$\begin{aligned}\omega\omega'\frac{dI}{d^2\boldsymbol{k}d^2\boldsymbol{k}'d\omega d\omega'} = \frac{2C_FC_A\alpha_s^2}{(2\pi)^2\omega^2N(N^2-1)^2\boldsymbol{k}'^2}\,\mathrm{Re}\Bigg[\int_{\boldsymbol{z}_\perp,\boldsymbol{z}'_\perp,x^+,x_c^+,\boldsymbol{y}_\perp} e^{i\boldsymbol{k}_\perp\cdot(\boldsymbol{z}'_\perp-\boldsymbol{z}_\perp)} \\ \times\partial_{\boldsymbol{x}_\perp}|_0\cdot\partial_{\boldsymbol{x}'_\perp}|_0\,\mathrm{Tr}\Big\langle\mathcal{G}(\boldsymbol{y}_\perp,\boldsymbol{x}_\perp|k^+)W(\boldsymbol{0})\Big\rangle_{(x_c^+,x^+)} \\ \times f^{jia}f^{cbd}\Big\langle W^{ac}(\boldsymbol{0})\mathcal{G}^{jb}(\boldsymbol{z}_\perp,\boldsymbol{y}_\perp,|k^+)\mathcal{G}^{\dagger id}(\boldsymbol{z}'_\perp,\boldsymbol{x}'_\perp|k^+)\Big\rangle_{(L^+,x_c^+)}\Bigg],\end{aligned} \tag{5.7}$$

where ω' accounts for the frequency of the softer gluon. Here the introduced shorthands explicitly read $\int_{x^+,x_c^+} := \int_0^{L^+}dx^+\int_{x^+}^{L^+}dx_c^+$. Not surprinsingly, it is noticeable that the gluon radiation spectrum for the vacuum case can be factored out from the computed spectrum. Explicitly,

$$\begin{aligned}\frac{\left(\omega\omega'\frac{dI}{d^2\boldsymbol{k}d^2\boldsymbol{k}'d\omega d\omega'}\right)}{\left(\omega'\frac{dI^{\mathrm{vac}}}{d\omega' d^2\boldsymbol{k}'}\right)} = \frac{2C_F\alpha_s}{(2\pi^2)\omega^2N(N^2-1)^2}\,\mathrm{Re}\Bigg[\int_{\boldsymbol{z}_\perp,\boldsymbol{z}'_\perp,x^+,x_c^+,\boldsymbol{y}_\perp} e^{i\boldsymbol{k}_\perp\cdot(\boldsymbol{z}'_\perp-\boldsymbol{z}_\perp)} \\ \times\partial_{\boldsymbol{x}_\perp}|_0\cdot\partial_{\boldsymbol{x}'_\perp}|_0\,\mathrm{Tr}\Big\langle\mathcal{G}(\boldsymbol{y}_\perp,\boldsymbol{x}_\perp|k^+)W(\boldsymbol{0})\Big\rangle_{(x_c^+,x^+)} \\ \times f^{jia}f^{cbd}\Big\langle W^{ac}(\boldsymbol{0})\mathcal{G}^{jb}(\boldsymbol{z}_\perp,\boldsymbol{y}_\perp|k^+)\mathcal{G}^{\dagger id}(\boldsymbol{z}'_\perp,\boldsymbol{x}'_\perp|k^+)\Big\rangle_{(L^+,x_c^+)}\Bigg],\end{aligned} \tag{5.8}$$

with

$$\omega'\frac{dI^{\mathrm{vac}}}{d^2\boldsymbol{k}d\omega} = \frac{\alpha_sC_A}{(2\pi^2)\boldsymbol{k}^2}. \tag{5.9}$$

It is also insightful to compare the above expression for the spectrum, eq. (5.8), with the *in-in* component of the pure BDMPS-Z configuration that is present in the previously entered eq. (2.47) [72],

$$\begin{aligned}\omega\frac{dI^{in-in}}{d^2\boldsymbol{k}d\omega} = \frac{2C_F\alpha_s}{(2\pi^2)\omega^2(N^2-1)^2}\,\mathrm{Re}\Bigg[\int_{\boldsymbol{z}_\perp,\boldsymbol{z}'_\perp,x^+,x_c^+,\boldsymbol{y}_\perp} e^{i\boldsymbol{k}_\perp\cdot(\boldsymbol{z}'_\perp-\boldsymbol{z}_\perp)} \\ \times\partial_{\boldsymbol{x}_\perp}|_0\cdot\partial_{\boldsymbol{x}'_\perp}|_0\,\mathrm{Tr}\Big\langle\mathcal{G}(\boldsymbol{y}_\perp,\boldsymbol{x}_\perp|k^+)W(\boldsymbol{0})\Big\rangle_{(x_c^+,x^+)} \\ \times\mathrm{Tr}\Big\langle\mathcal{G}(\boldsymbol{z}_\perp,\boldsymbol{y}_\perp|k^+)\mathcal{G}^\dagger(\boldsymbol{z}'_\perp,\boldsymbol{x}'_\perp|k^+)\Big\rangle_{(L^+,x_c^+)}\Bigg].\end{aligned} \tag{5.10}$$

As can be seen, both expressions display the same kernel structure until the BDMPS-Z gluon is emitted in both amplitude and complex-conjugate amplitude. At this stage,

the soft gluon embodied in the novel configuration gives rise to a more sophisticated color ensemble than the standard two-point correlator that pops up when addressing the original setup.

The following presents the detailed solution of the spectrum (5.8). This requires carefully working out the two- and three-point correlation functions. The two-point correlator, which kept recurring in the above chapters, is given by the path-integral of a two-dimensional harmonic oscillator [153, 154],

$$\begin{aligned}\mathcal{K}(\boldsymbol{x}_\perp,\boldsymbol{y}_\perp)_{(x_c^+,x^+)} &= \frac{1}{N^2-1}\Big\langle \mathcal{G}(\boldsymbol{y}_\perp,\boldsymbol{x}_\perp)W(\mathbf{0})\Big\rangle_{(x_c^+,x^+)} \\ &= \frac{A(x_c^+,x^+)}{i\pi}\exp\Big[iA(x_c^+,x^+)B(x_c^+,x^+)(\boldsymbol{x}_\perp^2-\boldsymbol{y}_\perp^2)-2iA(x_c^+,x^+)\;\boldsymbol{x}_\perp\cdot\boldsymbol{y}_\perp\Big],\end{aligned} \tag{5.11}$$

with

$$A(x_c^+,x^+)=\frac{\omega\Omega}{2\sin[\Omega(x_c^+-x^+)]},\;\; B(x_c^+,x^+)=2\cos[\Omega(x_c^+-x^+)], \tag{5.12}$$

and

$$\Omega=\frac{1-i}{2}\sqrt{\frac{\hat{q}}{\omega}} \tag{5.13}$$

accounting for the imaginary frequency.

The three-point function that appears in eq. (5.8), on the other hand, requires more thorough treatment. Explicitly, it can be written as follows within the harmonic oscillator approximation,

$$\begin{aligned}&\int_{\boldsymbol{y}_\perp}^{\boldsymbol{z}_\perp}\mathcal{D}\boldsymbol{r}_1(t)\int_{\boldsymbol{x}'_\perp}^{\boldsymbol{z}'_\perp}\mathcal{D}\boldsymbol{r}_2(t)\;\exp\left\{\frac{i\omega}{2}\int_{x_c^+}^{L^+}dt\;\left(\dot{\boldsymbol{r}}_1^2-\dot{\boldsymbol{r}}_2^2\right)-\frac{\hat{q}}{8}\int_{x_c^+}^{L^+}dt\Big(\boldsymbol{r}_1^2+\boldsymbol{r}_2^2+(\boldsymbol{r}_1-\boldsymbol{r}_2)^2\Big)\right\} \\ &=\int_{\boldsymbol{y}_\perp}^{\boldsymbol{z}_\perp}\mathcal{D}\boldsymbol{r}_1(t)\int_{\boldsymbol{x}'_\perp}^{\boldsymbol{z}'_\perp}\mathcal{D}\boldsymbol{r}_2(t)\;\exp\left\{\frac{i\omega}{2}\int_{x_c^+}^{L^+}dt\;\left(\dot{\boldsymbol{r}}_1^2-\dot{\boldsymbol{r}}_2^2\right)-\frac{\hat{q}}{4}\int_{x_c^+}^{L^+}dt\Big(\boldsymbol{r}_1^2+\boldsymbol{r}_2^2-\boldsymbol{r}_1\cdot\boldsymbol{r}_2\Big)\right\},\end{aligned}$$

with $\boldsymbol{r}_1$ and $\boldsymbol{r}_2$ capturing the trajectories of the gluon within the transverse plane in amplitude and its complex-conjugate, respectively.

At this point, proceeding in the same manner as is done in [146], the boost-like transformation

$$\begin{pmatrix}\boldsymbol{r}_1\\ \boldsymbol{r}_2\end{pmatrix}=\gamma\begin{pmatrix}1&\beta\\ \beta&1\end{pmatrix}\begin{pmatrix}\hat{\boldsymbol{r}}_1\\ \hat{\boldsymbol{r}}_2\end{pmatrix},\quad \gamma=\frac{1}{\sqrt{1-\beta^2}}, \tag{5.14}$$

leaves the Lagrangian unchanged, and then, by choosing

$$\beta = 2 - \sqrt{3}, \quad \gamma = \frac{1}{\sqrt{6 - 4\sqrt{3}i}}, \tag{5.15}$$

the path-integral above is reduced to

$$\begin{aligned} &\int \mathcal{D}\hat{\boldsymbol{r}}_1(t)\ \mathcal{D}\hat{\boldsymbol{r}}_2(t)\ \exp\left\{ i\omega \int_{x_c^+}^{L^+} dt\ \left(\frac{\dot{\hat{\boldsymbol{r}}}_{\mathbf{1}}^2}{2} + i\frac{\sqrt{3}}{8}\frac{\hat{q}}{\omega}\hat{\boldsymbol{r}}_{\mathbf{1}}^2 \right) \right\} \\ &\times \exp\left\{ i\omega \int_{x_c^+}^{L^+} dt\ \left(-\frac{\dot{\hat{\boldsymbol{r}}}_{\mathbf{2}}^2}{2} + i\frac{\sqrt{3}}{8}\frac{\hat{q}}{\omega}\hat{\boldsymbol{r}}_{\mathbf{2}}^2 \right) \right\}. \end{aligned} \tag{5.16}$$

The above expression is now the product of two path-integrals of the same kind as the one emerging from the two-point correlator, eq. (5.11). In the same vein, the solution reads [146]

$$\mathcal{J}(\hat{\boldsymbol{r}}_{1x}, \hat{\boldsymbol{r}}_{1y})\bar{\mathcal{J}}(\hat{\boldsymbol{r}}_{2x}, \hat{\boldsymbol{r}}_{2y}), \tag{5.17}$$

where

$$\begin{aligned} \mathcal{J}(\hat{\boldsymbol{r}}_{1x}, \hat{\boldsymbol{r}}_{1y})_{(L^+, x_c^+)} = &\frac{k_{br}^2(1-i)}{4\pi \sinh[\Omega(L^+ - x_c^+)]} \\ &\times \exp\left\{ \frac{(i-1)k_{br}^2}{4\sinh[\Omega(L^+ - x_c^+)]} \left[(\hat{\boldsymbol{r}}_{1x}^2 + \hat{\boldsymbol{r}}_{1y}^2) - 2\hat{\boldsymbol{r}}_{1x}\cdot\hat{\boldsymbol{r}}_{1y} \right] \right\}, \end{aligned} \tag{5.18}$$

with

$$\Omega := \frac{1+i}{2}\sqrt{\frac{\hat{q}_{eff}}{\omega}}, \tag{5.19}$$

and $\hat{q}_{eff} = \frac{\sqrt{3}}{2}\hat{q}$ an average version of the jet quenching parameter.

Finally, entering the outlined results for the correlators (5.11) and (5.17) into the radiation spectrum (5.8), the outcome is

$$\begin{aligned} \omega\omega' \frac{dI}{d^2\boldsymbol{k}d^2\boldsymbol{k}'d\omega d\omega'} = &\frac{2C_F C_A \alpha_s^2}{(2\pi^2)\omega^2 \boldsymbol{k}'^2}\ \mathrm{Re}\Bigg[\int_{\boldsymbol{z}_\perp, \boldsymbol{z}'_\perp, x^+, x_c^+, \boldsymbol{y}_\perp} e^{i\boldsymbol{k}_\perp\cdot(\boldsymbol{z}'_\perp - \boldsymbol{z}_\perp)} \\ &\times \partial_{\boldsymbol{x}_\perp}\cdot\partial_{\boldsymbol{x}'_\perp}\ \mathcal{K}(\boldsymbol{x}_\perp, \boldsymbol{y}_\perp)_{(x_c^+, x^+)}\ \mathcal{J}(\hat{\boldsymbol{r}}_{1x}, \hat{\boldsymbol{r}}_{1y})_{(L^+, x_c^+)} \\ &\times \mathcal{J}(\hat{\boldsymbol{r}}_{2x}, \hat{\boldsymbol{r}}_{2y})_{(L^+, x_c^+)} \Bigg]_{\boldsymbol{x}_\perp = \boldsymbol{x}'_\perp = 0}. \end{aligned} \tag{5.20}$$

As is apparent, convoluting the three kernel structures shown just above leads to a cumbersome output. Though a full treatment of the preceding expression was conducted,

the endpoint helps little to the real intent of this study. Some general conclusions can however be drawn as regards the coherence trend of the partonic system. For example, color coherence is preserved provided the BDMPS-Z gluon is emitted collinearly to the leading quark, this way overriding the impact of the soft gluon. Accordingly, the radiation spectrum collapses to the pure BDMPS-Z result under the collinear limit, eq. (5.10). Conversely, color coherence gradually fades as the emission angle of the BDMPS-Z gluon increases, eventually reaching the point at which the phase-space for the soft gluon emission is quantum suppressed since both leading partons would have lost its color connection.

On balance, as seen from the above, the resulting spectrum makes discussing methods considerably challenging. For that reason, what follows is the implementation of some approximations which pave the way for embedding the notion of color coherence into a standard probabilistic approach that describes medium-induced branchings, the ultimate aim of this project. More specifically, in line with the partonic picture introduced in Chapter 4, gluon trajectories can be treated within the semi-classical limit. Classically, the gluon transverse trajectories $\boldsymbol{r}_1$ and $\boldsymbol{r}_2$ are regarded as straight lines that have the same slope, so that they can be configured as

$$\boldsymbol{r}_1(t) \sim \boldsymbol{x}_\perp + (t+\tau)\theta,\ \boldsymbol{r}_2(t) \sim \boldsymbol{x}'_\perp + t\theta, \tag{5.21}$$

where $\tau = x_c^+ - x^+$ is the difference of gluon emission times in amplitude and complex-conjugate amplitude, namely the formation time of the BDMPS-Z gluon, while θ accounts for its emission angle. In this way, the following relation is fulfilled,

$$(\boldsymbol{r}_1 \cdot \boldsymbol{r}_2)(t) \sim (\boldsymbol{x}_\perp + (t+\tau)\theta) \cdot (\boldsymbol{x}'_\perp + t\theta)\,. \tag{5.22}$$

Now, since the current focus is on capturing the overall contribution of this piece, it can also be set that $\boldsymbol{x}_\perp \sim \boldsymbol{x}'_\perp \sim 0$. Furthermore, as the formation time of the BDMPS-Z gluon is assumed to be much smaller than the further propagation from formation time to the end of the medium, $\Delta t := L - x_c^+ \gg \tau$, the scalar product of both trajectories reduces to

$$(\boldsymbol{r}_1 \cdot \boldsymbol{r}_2)(\Delta t) \sim (\Delta t)^2\theta^2. \tag{5.23}$$

This approach allows to encapsulate coherence into a simplified estimation of the decoherence parameter, Δ_{med}, which have been emerging on a recurring basis throughout this manuscript. Explicitly,

$$\Delta_{med} = 1 - \exp\left(-\frac{\hat{q}}{12}\theta^2(\Delta t)^3\right). \tag{5.24}$$

As shown in the following section, this coherence piece can be intuitively inset into the context of a probabilistic cascade, thus adding a missing piece to the whole picture.

5.3 A color coherence correction to the medium-induced parton evolution picture

5.3.1 Implementing parton showering from a probabilistic perspective

The computation of the gluon radiation spectrum performed in the section above evidences that the arising three-point correlator contains all the physics of color coherence between the leading partons, namely the quark and gluon making up the antenna that propagates away until the end of the medium, just before the soft gluon emission takes place.

A procedure is now being introduced according to previous studies on the resummation of in-medium parton splittings occurring in the context of a democratic branching approach [101, 143, 146], as the gateway to enter coherence physics into the probabilistic picture for medium-induced partonic evolution. To put it clearly, the basis of this approach relies on starting with the basic assumption that the emission process can be regarded as a Markov chain so that one can neglect both momentum exchanges and broadening over the short-lived splittings, thus leading to a simple dependence of the splitting kernel. What is more, within this framework, the late-time color structure of the parton dynamics can be restricted to that of two independent emitters spreading out throughout the medium. Albeit some basic elements for a democratic treatment of the parton shower are discussed below, for the purpose of this study there is no need to substantially revisit the background underpinning the derivation of the evolution equation. For details, refer to [143, 146].

Opening up the subject, one can use the generating functional evolution method as a way to generate an iterative parton cascade based on $1 \to 2$ processes [1, 2, 155]. The generating functional, containing the branching probabilities for a parton originated at light-cone time t_0 with 3-momentum[1] $\vec{p}_0 = (p_0^+, \boldsymbol{p}_0)$ reads

$$\mathcal{Z}_{p_0}[t, t_0|u] = \sum_{n=1}^{\infty} \frac{1}{n!} \int \left(\prod_{i=1}^{n} d\Omega_i \right) P_n(\vec{k}_1, ..., \vec{k}_n; t, t_0) u(\vec{k}_1) ... u(\vec{k}_n), \tag{5.25}$$

with $t_0 \leq t \leq L$, and $P_n(\vec{k}_1, ..., \vec{k}_n)$ accounting for the probability of measuring n final state gluons with momenta $\vec{k}_1, ..., \vec{k}_n$ at time t – it therefore encapsulates all the physical information as regards the branching process. As shall be seen in greater detail below, under the specific scenario to be addressed the entire evolution is completely set via defining a broadening probability and a splitting probability for a $1 \to 2$ process. Here $u(\vec{k})$ is a generic function of $\vec{k}$. In particular, the functional derivative is defined as

[1] Again, parton evolution is restricted to the transverse plane and, accordingly, the + component of the incoming parton momentum is conserved, $p_0^+ = \sum_{i=1}^{n} k_i^+$.

$$\frac{\delta u(\vec{p})}{\delta u(\vec{q})} = \delta(p^+ - q^+)\delta^2(\boldsymbol{p}-\boldsymbol{q}). \tag{5.26}$$

Once this is introduced, the probabilities P_n can be retrieved via taking the n-th functional derivative of $\mathcal{Z}_{p_0}[t,t_0|u]$ evaluated at $u=0$, what delivers

$$P_n(\vec{k}_1,...,\vec{k}_n;t,t_0) = \left[\prod_{i=1}^{n}(2\pi)^3 2k_i^+ \frac{\delta}{\delta u(\vec{k}_i)}\right]\mathcal{Z}_{p_0}(t,t_0|u)\Big|_{u=0}. \tag{5.27}$$

Now considering the configuration in which the incoming parton does not split within the time interval (L,t_0), the broadening probability P_1 must read

$$P_1(\vec{k};L,t_0) = 2p_0^+ 2\pi\delta(k^+ - p_0^+)\mathcal{P}_1(\boldsymbol{k};L,t_0), \tag{5.28}$$

where $\mathcal{P}_1(\boldsymbol{k};L,t_0)$ comprises the probability of finding a parton with momentum $\boldsymbol{k}$ that has gained a transverse momentum $\boldsymbol{k}-\boldsymbol{p}_0$ during its propagation, to wit, the classical broadening piece. Taking the derivative of the preceding expression with respect to t gives rise to the following evolution equation,

$$\partial_t\mathcal{P}_1(\boldsymbol{k};t,t_0) = \int_{\boldsymbol{l}}\mathcal{C}(\boldsymbol{l})\mathcal{P}_1(\boldsymbol{k}-\boldsymbol{l};t,t_0), \tag{5.29}$$

with the broadening kernel $\mathcal{C}(\boldsymbol{l})$ defined as

$$\mathcal{C}(\boldsymbol{l}) = -\frac{1}{2}Nn\sigma(\boldsymbol{l}). \tag{5.30}$$

As was already underlined on several occasions throughout this manuscript, n and $\sigma(\boldsymbol{l})$ are the density of scattering centers and the dipole cross-section, respectively. Here $\boldsymbol{l}$ is the transferred momentum acquired via medium rescattering.

It now appears appropriate to define the probability of finding two outgoing partons with momenta $\vec{k}$ and $\vec{q}$ according to a similar principle, but this time, on top of the transverse momentum broadening, the splitting probability for a $1\to 2$ branching needs to be brought into the picture. Explicitly,

$$P_2(\vec{k},\vec{q};L,t_0) = 2p_0^+\delta(k^+ + q^+ - p_0^+)\mathcal{P}_2(\boldsymbol{k},\boldsymbol{q},z;L,t_0), \tag{5.31}$$

with

$$\begin{aligned}\mathcal{P}_2(\boldsymbol{k},\boldsymbol{q},z;L,t_0) = 2g^2z(1-z)\int_{t_0}^{L}dt\ \mathcal{K}(z,p_0^+)\\ \times\int_{\boldsymbol{l}}\mathcal{P}_1(\boldsymbol{k}-z\boldsymbol{l};L,t)\mathcal{P}_1(\boldsymbol{q}-(1-z)\boldsymbol{l};L,t)\mathcal{P}_1(\boldsymbol{l}-\boldsymbol{p}_0;t,t_0)\end{aligned} \tag{5.32}$$

describing the parton propagation from t_0 until the point the branching process takes place. The splitting, assumed to be time independent, is given by[2] [143]

$$\mathcal{K}(z,p_0^+)=\frac{P_{gg}}{2\pi}\sqrt{\frac{\hat{q}(1-z+z^2)}{z(1-z)p_0^+}}, \tag{5.33}$$

where P_{gg} is the leading-order Altarelli-Parisi gluon splitting function.

It is important to stress that the derivation above was carried out under the assumption that the energetic parton does not experience a branching process during the time interval (L,t_0), so that one is only left with the broadening piece. During this interim, however, the transverse momentum of the high-energy parton can undergo broadening, and then a $1\to 2$ parton splitting can take place, eventually to be followed by an additional broadening course experienced by the daughter partons. Hence, in the latter case, there is a need to enter a change into eq. (5.32). In particular, the second building block now reads

$$\tilde{\mathcal{P}}_2(\boldsymbol{k},\boldsymbol{q},z;L,t_0)=2g^2z(1-z)\int_{t_0}^{L}dt\;\mathcal{K}(z,p_0^+)(2\pi)^4\delta^{(2)}(\boldsymbol{k}-z\boldsymbol{p}_0)\delta^2(\boldsymbol{q}-(1-z)\boldsymbol{p}_0), \tag{5.34}$$

where it has been set the initial momentum of the incoming parton as the momentum just after it was created. This produces the following expression for the time evolution,

$$\partial_t\tilde{\mathcal{P}}_2(\boldsymbol{k},\boldsymbol{q},z;t,t_0)=2g^2z(1-z)\mathcal{K}(z,p_0^+)(2\pi)^4\delta^{(2)}(\boldsymbol{k}-z\boldsymbol{p}_0)\delta^{(2)}(\boldsymbol{q}-(1-z)\boldsymbol{p}_0), \tag{5.35}$$

while the linear variation of $\tilde{\mathcal{P}}_2$ is given by

$$\begin{aligned}\tilde{\mathcal{P}}_2(\boldsymbol{k},\boldsymbol{q},z;t_0+dt,t_0)=\tilde{\mathcal{P}}_2(t_0,t_0)+2g^2z(1-z)\mathcal{K}(z,p_0^+)(2\pi)^4\delta^{(2)}(\boldsymbol{k}-z\boldsymbol{p}_0)\\ \times\delta^{(2)}(\boldsymbol{q}-(1-z)\boldsymbol{p}_0)dt,\end{aligned} \tag{5.36}$$

with $\tilde{\mathcal{P}}_2(t_0,t_0)=0$.

Combining now this result with the time evolution equation derived for $\mathcal{P}_1$, and writing down the linear variation of the generating functional as

$$\begin{aligned}\mathcal{Z}_{p_0}(t_0+dt,t_0)=&\int d\Omega_k\;P_1(\vec{k},t_0+dt,t_0)u(\vec{k})\\ &+\frac{1}{2}\int d\Omega_{k_1}d\Omega_{k_2}P_2(\vec{k}_1,\vec{k}_2;t_0+dt,t_0)u(\vec{k}_1)u(\vec{k}_2),\end{aligned} \tag{5.37}$$

[2]As mentioned earlier in this manuscript, the splitting kernel can be generalized to any other flavors.

it is possible to infer the master equation for the generating functional. It reduces to

$$\begin{aligned}\partial_t \mathcal{Z}_{p_0}(t,t_0|u) = &\int_l \mathcal{C}(\boldsymbol{l},t_0)u(p_0^+,\boldsymbol{p}_0+\boldsymbol{l}) \\ &+\alpha_s\int_z \mathcal{K}(z,p_0^+)\left[u(z\vec{p}_0)u\left((1-z)\vec{p}_0\right)-u(\vec{p}_0)\right],\end{aligned} \tag{5.38}$$

where the last term, proportional to $u(\vec{p}_0)$, ensures conservation of probability during the evolution.

At this point, the master equation enables one to straightforwardly determine the inclusive one-gluon distribution $D(x,\boldsymbol{k},t)$ that accounts for the probability of finding a gluon with energy fraction x and transverse momentum $\boldsymbol{k}$ produced at time t via the decay of an ancestor parton. Explicitly,

$$D(x,\boldsymbol{k},t) := k^+\left.\frac{\delta\mathcal{Z}_{p_0}[t,t_0|u]}{\delta u(\vec{k})}\right|_{u=1}. \tag{5.39}$$

Finally, entering eq. (5.38) into the preceding expression for the inclusive one-gluon distribution and taking its time derivative produces [143]

$$\begin{aligned}\partial_t D(x,\boldsymbol{k},t) = &\int_l \mathcal{C}(\boldsymbol{l})D(x,\boldsymbol{k}-\boldsymbol{l},t) \\ &+\alpha_s\int_z\left[\frac{2}{z^2}\mathcal{K}\left(z,\frac{x}{z}p_0^+\right)D\left(\frac{x}{z},\frac{\boldsymbol{k}}{z}\right)\Theta(z-x)-\mathcal{K}(z,xp_0^+)D(x,\boldsymbol{k},t)\right],\end{aligned} \tag{5.40}$$

a rate equation that favours a friendly interpretation in the light of the meaning of each of the terms that make it up. In particular, the first term accounts for the transverse momentum broadening via medium rescattering between successive in-medium splittings, while the two terms within the square brackets correspond to the production of a new gluon with energy fraction x and transverse momentum $\boldsymbol{k}$ emitted off a parton with energy fraction x/z and transverse momentum $\boldsymbol{k}/z$, and the absortion of a gluon with energy fraction x and transverse momentum $\boldsymbol{k}$ via an in-medium splitting, respectively.

To complete this study, the following piece explores the possibility of embodying the notion of color coherence amongst the leading partons into the rate equation sketched at the end of this subsection.

5.3.2 Embedding color coherence into the medium-modified parton shower evolution equations

To recapitulate, after computing the spectrum of the addressed scenario, an estimation of the corresponding coherence factor was accomplished at the bottom of Section 5.2, which provides a sound basis to somehow link the coherence piece to the building blocks that shape the evolution equation for the inclusive one-gluon spectrum outlined right above. Indeed, it seems intuitively plausible to embed this image as a correction into one of the basic elements that are used to develop the resulting rate equation.

More specifically, the decoherence parameter shown in eq. (5.24) naturally enters into the basic skeleton as a correction to the splitting kernel. Explicitly, the coherence-modified kernel reads

$$\mathcal{K}(z,p_0^+) \to \mathcal{K}'(z,p_0^+;t-t_0) = \int_{\boldsymbol{l}} \mathcal{K}(\boldsymbol{l})\Delta_{med}(\boldsymbol{l}), \tag{5.41}$$

where

$$\Delta_{med}(\boldsymbol{l},z,p_0^+;L-t) := 1-\exp\left(-\frac{\hat{q}}{12}\theta^2(\boldsymbol{l},z,p_0^+)(L-t)^3\right). \tag{5.42}$$

Here the emission angle is given by

$$\theta(\boldsymbol{l},z,p_0^+) = \frac{\boldsymbol{l}}{z(1-z)p_0^+}, \tag{5.43}$$

this way depending on the transferred momentum $\boldsymbol{l}$ and both the energy fraction z and the energy of the leading parton p_0^+.

Given the coherence-modified kernel estimated above, it will now be possible to take a further step towards achieving an evolution equation of the same substance as eq. (5.40). In fact, the same steps undertaken above for the Markov shower must be followed, namely deriving the time evolution equation for the two-particle broadening piece as well as the coherence-modified master equation for the generating functional, which ultimately leads to the desired evolution equation for the one-gluon distribution.

Some estimates developed via comparing the relevant time-scales involved in the big picture suggest that there is broad agreement with established principles on jet propagation in a dense medium, many of which have been widely discussed throughout this manuscript.

5.4 Discussion and outlook

This study represents a first attempt to implement coherence effects into the standard resummation formula for a medium-induced QCD cascade. In particular, under the framework of the BDMPS-Z approach, a novel configuration involving an extra soft gluon emission with respect to the standard BDMPS-Z scheme is computed as a baseline for quantifying color coherence, with the ultimate aim of achieving a coherence-modified evolution equation for the inclusive one-gluon distribution. Not surprisingly, the computed emission spectrum displays a friendly structure to be fitted into the splitting kernel $\mathcal{K}$ since the coherence piece can be straightforwardly factored out.

After introducing the basic elements for the derivation of the standard evolution equation some insights on the expected outcome are discussed. Specifically, the coherence-modified rate equation features an only major change that rests upon swapping the original splitting kernel by a modified branching kernel that is composed by the coherence piece – deduced when computing the total radiation spectrum. Preliminary evidences are very much in line with baseline studies in this respect.

Lastly, it should be noted that the fact that the computation is framed in the context of the Markovian approximation may lead to confusion as this approach disregards interference effects. For this reason, certain corrections concerning the branching and broadening pieces are being performed in order to alleviate this mismatch. However, further studies will be necessary to get closer to a robust coherence-modified evolution equation for the medium-induced partonic showering. Numerical tests will also evidence the reliability of the final outcome.

USC
UNIVERSIDADE
DE SANTIAGO
DE COMPOSTELA

6

Deciphering the origin of angular correlations in high-energy collisions

This final piece is aiming to supplement already existing studies on rapidity and angular correlations between produced particles in high-energy collisions. More specifically, considering a high-energy scattering of a hadronic projectile on a stationary target in the lab frame, one seeks to provide a simple picture around the origin of final-state particle correlations via studying a two-gluon final state.

6.1 General remarks

One of the main observations of the CMS collaboration was the detection of long-range correlations in pp collisions at $\sqrt{s} = 7$ TeV between two charged hadrons emerging from the collision collimated in their azimuthal angle ϕ, while at the same time being separated in rapidity η [156]. Remarkably, these correlations recall those seen in relativistic heavy-ion data from RHIC [157, 158]. The phenomenon was called *ridge* because of its shape on the $\phi - \eta$ data graph.

As correlations spread over a wide rapidity interval, arguments around causality issues lead to the conclusion that they have their roots in the very early stages of the collision.

The thinking behind this is that relativistic particles propagating out of the interaction region would otherwise be causally disconnected and, eventually, uncorrelated [141, 142]. As becomes clear, particle correlations might provide support to the development of better knowledge in order to disentangle initial and final state effects. Additionally, albeit long-range rapidity correlations may not be associated with the formation of the QGP at all, they could indeed compete to go beyond to enhance the dynamics underlying final-state jet quenching [159, 160].

A number of mechanisms designed for justifying the ridge in pp and AA collisions have been proposed ([161–164], among others). In particular, it is thought that a hydrodynamical evolution starting in the aftermath of the scattering leads to a collective behaviour of the final state of the gluons cloud, which will then be accountable for the rise of this phenomenon in the context of HIC. Although there is broad consensus on the origin of the correlations in heavy-ion collisions, the puzzle mechanism remains outstanding when it comes to pp and pA collisions. This logic above has also been proposed as an attemp to understand the source of the correlations in small systems [165]. Based on the aforementioned causality argument, there is also a great deal of debate around the so-called *glasma* approximation, founded on the dilute-dilute limit of the earlier introduced CGC framework [141, 142, 166].

The framework of this study is exactly the same to that presented in [167], where the focus is not placed on the physics behind the glasma approach, but instead a straight logical reasoning is proposed with no reference being made to any specific model of high-energy evolution. Considering the high-energy scattering of a hadronic projectile on a stationary target in the lab frame, one can observe two final-state projectile gluons with rapidities Y_1 and Y_2 that scattered on the target. As is well known according to the BFKL dynamics entered in subsection 2.3.1, at high energies the hadronic wave function is gluon dominated and, in consecuence, their Lorentz transformation properties are homogeneously distributed in rapidity in a boost invariant state. This means the same projectile gluon distribution at rapidities Y_1 and Y_2, so that, given an impact parameter and a target field configuration, a gluon is as likely to emerge at Y_1 as it is at Y_2, what is reminiscent of the rise of particle correlations. Similarly, if one of the gluons is likely to acquire a transverse momentum $\boldsymbol{q}$, the same holds true for the other. Hence, one clearly expects forward gluon correlations to be very generic within this scenario. This is particularly true for a projectile wave function dominated by the classical Weizsacker-Williams (WW) field, as in this context fluctuations in the wave function are small and the gluon density is almost the same at all rapidities.

More explicitly, using light-cone Hamiltonian perturbation theory, the hadronic wave function at high energy reads [168, 169]

$$|\Psi\rangle = \exp\left\{ i \int d^2x \; b_i^a(x) \int d\eta \left(a_i^{\dagger a}(x,\eta) + a_i^a(x,\eta) \right) \right\} B(a, a^\dagger)|\psi\rangle, \tag{6.1}$$

where ψ is the wave function of valence charges that determines the distribution of fast partons responsible for the color charge density ρ. Here B is a Bogolyuvov-type operator of the soft gluon fields a, and b accounts for the WW field depending on ρ via classical Yang-Mills equations of motion. In the dilute projectile limit is given by

$$b_i^a = \frac{g}{\pi} \int_y f_i(x-y)\rho^a(y), \text{ with } f_i(x-y) = \frac{(x-y)_i}{(x-y)^2}. \tag{6.2}$$

Though the above debate on the roots of angular correlations is greatly simplified in a few respects, it paves the way for performing realistic calculations when computing high-energy multigluon amplitudes as a way to unlock valuable information about the source of such correlations. As an example, both gluons do not scatter off the target with the exact same momentum transfers as, even setting both the same impact parameter and a fixed target fields configuration, this leads to a non-trivial probability distribution of momentum transfers. Besides that, observing a gluon in the final state not only requires that it acquires some transverse momentum, but it must also decorrelate from the source valence charge of the incoming wave function. Therefore, and with a view to better understanding the expected features of angular correlations within the high-energy QCD work frame discussed above, the two-gluon inclusive cross-section is recapped on a very detailed level.

6.2 Revisiting the double inclusive gluon production probability

Although calculating multigluon amplitudes has already been the subject of much debate, there still seems to be no definite results regarding high-energy pp collisions. Both the dense-dense [170] and dense-dilute [171,172] configurations for the colliding hadrons have already been covered, but the situation which comes closer to the LHC collisions scenario is probably one where the density in the proton wave function is neither parametrically large nor perturbatively small, so that the scope of [172] is the one that fits best with this line. However, this in depth analysis takes as its starting point the two-gluon probability amplitude provided by [171]. To be more specific, the most general expression for the double-gluon probability amplitude displayed in [171], which is built upon the single-gluon production amplitude in a dense-dilute scattering, is given by

$$\begin{aligned} A_{ij}^{ab}(k,p) = \int_{u,z} e^{ikz+ipu} \int_{x_1,x_2} \Big\{ & f_i(z-x_1)[S_z - S_{x_1}]^{ac} f_j(u-x_2)[S_u - S_{x_2}]^{bd} \hat{\rho}_{x_2}^d \hat{\rho}_{x_1}^c + \\ & + f_i(z-x_1)[S_z - S_{x_1}]^{ac} f_j(u-x_2)[S_u \delta_{ux_1} - S_{x_2}\delta_{x_2x_1}]^{bm} T_{md}^c \hat{\rho}_{x_2}^d \Big\}, \end{aligned} \tag{6.3}$$

where $\hat{\rho}^a(x)$ is the operator of the color charge density, and $S^{ab}(x)$ is the eikonal scattering matrix determined by the target color fields. Then, performing the symmetrization of the operators within the preceding amplitude,

$$\hat{\rho}^a\hat{\rho}^{a_1} = \frac{1}{2}\{\hat{\rho}^a, \hat{\rho}^{a_1}\} + \frac{1}{2}T^c_{aa_1}\hat{\rho}^c, \tag{6.4}$$

leads to get the two-gluon probability amplitude outlined in [172] back. Explicitly,

$$\begin{aligned} A^{ab}_{ij}(k,p) = \int_{u,z} e^{ikz+ipu} \int_{x_1,x_2} \Big\{ & f_i(z-x_1)[S_z - S_{x_1}]^{ac} f_j(u-x_2)[S_u - S_{x_2}]^{bd} \frac{1}{2}\{\rho^d_{x_2}, \rho^c_{x_1}\} \\ & + f_i(z-x_1)[S_z - S_{x_1}]^{ac} f_j(u-x_2)[S_u - S_{x_2}]^{bd} \frac{1}{2} T^e_{dc}\rho^e_{x_1}\delta(x_1-x_2) \\ & + f_i(z-x_1)[S_z - S_{x_1}]^{ac} f_j(u-x_2)[S_u\delta_{ux_1} - S_{x_2}\delta_{x_2x_1}]^{bm} T^c_{md}\rho^d_{x_2} \Big\}. \end{aligned} \tag{6.5}$$

The first term of the above equation straightforwardly produces

$$A^{ab}_{ij}(k,p)_{[1]} = \int_{u,z} e^{ikz+ipu} \int_{x_1,x_2} \Big\{ f_i(z-x_1)[S_z - S_{x_1}]^{ac}\rho^c_{x_1} \Big\} \Big\{ f_j(u-x_2)[S_u - S_{x_2}]^{bd}\rho^d_{x_2} \Big\}. \tag{6.6}$$

Now integrating once the third line of eq. (6.5) and renaming $x_2 \to x_1$ gives

$$\begin{aligned} A^{ab}_{ij}(k,p)_{[3]} = \int_{u,z} e^{ikz+ipu} \int_{x_1} \Big\{ & f_i(z-u)[S_z - S_u]^{ac} f_j(u-x_1) S^{bm}_u T^c_{md}\rho^d_{x_1} \\ & - f_i(z-x_1)[S_z - S_{x_1}]^{ac} f_j(u-x_1) S^{bm}_{x_1} T^c_{md}\rho^d_{x_1} \Big\}, \end{aligned} \tag{6.7}$$

where the first term can be reorganised in a more compact manner as follows,

$$A^{ab}_{ij}(k,p)_{[3(i)]} = \int_{u,z} e^{ikz+ipu} \int_{x_1} f_i(z-u) f_j(u-x_1) \Big\{ [S_z - S_u]\bar{\rho}(x_1) S^\dagger_u \Big\}^{ab}, \tag{6.8}$$

with $\bar{\rho} := T^a\rho^a$.

Hence, all that remains is to work out the second line of both eq. (6.5) and (6.7). Combining the two delivers

$$\begin{aligned} A^{ab}_{ij}(k,p)_{[2+3(ii)]} &= \int_{u,z} e^{ikz+ipu} \int_{x_1} \Big\{ f_i(z-x_1)[S_z - S_{x_1}]^{ac} f_j(u-x_1)[S_u - S_{x_1}]^{bd} \frac{1}{2} T^e_{dc}\rho^e_{x_1} \\ &\quad - f_i(z-x_1)[S_z - S_{x_1}]^{ac} f_j(u-x_1) S^{bm}_{x_1} T^c_{md}\rho^d_{x_1} \Big\} \\ &= \int_{u,z} e^{ikz+ipu} \int_{x_1} \Big[f_i(z-x_1) f_j(u-x_1) \Big] \Big\{ -\frac{1}{2}[S_z - S_{x_1}]^{ac} T^e_{cd}\rho^e_{x_1}[S^\dagger_u - S^\dagger_{x_1}]^{db} \\ &\quad - [S_z - S_{x_1}]^{ac} T^d_{cm}\rho^d_{x_1} S^{mb\dagger}_{x_1} \Big\} \\ &= -\int_{u,z} e^{ikz+ipu} \int_{x_1} \Big[f_i(z-x_1) f_j(u-x_1) \Big] \Big\{ [S_z - S_{x_1}]\bar{\rho}_{x_1} \Big(\frac{1}{2}[S^\dagger_u - S^\dagger_{x_1}] + S^\dagger_{x_1} \Big) \Big\}, \end{aligned}$$

which finally gives rise to

$$A_{ij}^{ab}(k,p)_{[2+3(ii)]} = -\frac{1}{2}\int_{u,z} e^{ikz+ipu}\int_{x_1}\Big[f_i(z-x_1)f_j(u-x_1)\Big]\Big\{[S_z-S_{x_1}]\bar{\rho}_{x_1}[S_u^\dagger+S_{x_1}^\dagger]\Big\}^{ab}. \quad (6.9)$$

Putting the results (6.6), (6.9) and (6.8) all together, the two-gluon production probability amplitude eventually reduces to

$$\begin{aligned} A_{ij}^{ab}(k,p) = &\int_{u,z} e^{ikz+ipu}\int_{x_1,x_2}\Big\{f_i(z-x_1)[S_z-S_{x_1}]^{ac}\rho_{x_1}^c\Big\}\Big\{f_j(u-x_2)[S_u-S_{x_2}]^{bd}\rho_{x_2}^d\Big\}\\ &-\frac{1}{2}\int_{x_1} f_i(z-x_1)f_j(u-x_1)\Big\{[S_z-S_{x_1}]\bar{\rho}_{x_1}[S_u^\dagger+S_{x_1}^\dagger]\Big\}^{ab}\\ &+\int_{x_1} f_i(z-u)f_j(u-x_1)\Big\{[S_z-S_u]\bar{\rho}(x_1)S_u^\dagger\Big\}^{ab}, \end{aligned} \quad (6.10)$$

which reveals a clear physical picture when looking at each of the terms separately. In particular, the first line corresponds to independent production of the two gluons. The second term, on the other hand, accounts for the emission of the two gluons off the same color source in the projectile wave-function. The third one comprises the remaining configuration, the process in which both gluons are subsequently produced in the collision: the softer gluon is emitted in the wave-function on the hands of the former hard gluon. It might be also insightful to interpret them in terms of BFKL ladders – see Fig. 2.12, as the square of the first line would represent a piece of a diagram including two independent ladders, whilst the square of the other two terms would match with the emission of two gluons within the same BFKL ladder.

Squaring eq. (6.10) gives rise to several terms in the cross-section,

$$\frac{dN}{d^2p d^2k d\eta d\xi} = \left\langle \sigma^4+\sigma^3+\sigma^2\right\rangle_{P,T}. \quad (6.11)$$

As a matter of fact, it is possible to identify them according to the physical setup they account for in the same vein as just discussed for the full amplitude. As an example, the square of the first line of eq. (6.10), concerning the independent production of the two gluons, reads

$$\begin{aligned} \sigma^4 = &\int_{u,z,\bar{u},\bar{z}} e^{ik(z-\bar{z})+ip(u-\bar{u})}\int_{x_1,x_2,\bar{x}_1,\bar{x}_2}\vec{f}(\bar{z}-\bar{x}_1)\cdot\vec{f}(z-x_1)\;\vec{f}(\bar{u}-\bar{x}_2)\cdot\vec{f}(u-x_2)\\ &\times\Big\{\rho_{x_1}[S_z^\dagger-S_{x_1}^\dagger][S_{\bar{z}}-S_{\bar{x}_1}]\rho_{\bar{x}_1}\Big\}\Big\{\rho_{x_2}[S_u^\dagger-S_{x_2}^\dagger][S_{\bar{u}}-S_{\bar{x}_2}]\rho_{\bar{x}_2}\Big\}. \end{aligned} \quad (6.12)$$

Not surprisingly, this expression reveals angular correlations since, even though both gluons are actually produced independently from each other, they are emitted off exactly the same sources configuration via scattering on the same target field. It turns out simple to analytically prove this by means of eq. (6.12). One way is to write it as follows [167],

$$\sigma^4 = \langle \sigma(k)\sigma(p) \rangle_{P,T} \,, \tag{6.13}$$

with

$$\sigma(k) = \int_{z,\bar{z}} e^{ik(z-\bar{z})} \int_{x_1,\bar{x}_1} \vec{f}(\bar{z}-\bar{x}_1)\cdot\vec{f}(z-x_1)\Big\{\rho_{x_1}[S_z^\dagger - S_{x_1}^\dagger][S_{\bar{z}} - S_{\bar{x}_1}]\rho_{\bar{x}_1}\Big\}, \tag{6.14}$$

so that for a fixed configuration of both projectile sources $\rho(x)$ and target fields $S(x)$, $\sigma(k)$ displays a maximum at some value $\boldsymbol{k} = \boldsymbol{q}$, as eq. (6.13) does it too for $\boldsymbol{k} = \boldsymbol{p} = \boldsymbol{q}$. In this way, $\sigma^4(k,p)$ exhibits a maximum at relative zero angle between both momenta as $\boldsymbol{k}$ and $\boldsymbol{p}$ are parallel regardless of the configuration.

The other two contributions to the total cross-section are further complicated, thus hindering the discussion regarding the emergence of correlations. Unlike σ^4, the most enlightening term in this context, in σ^2 and σ^3 both gluons are originally correlated with each other in the incoming wave function, steadily reaching the conclusion that the nature of the correlations must retain extra physics. Explicitly,

$$\begin{aligned}
\sigma^2 = \int_{u,z,\bar{u},\bar{z}} e^{ik(z-\bar{z})+ip(u-\bar{u})} \int_{x_1,\bar{x}_1} & \\
& \frac{1}{4}\vec{f}(\bar{z}-\bar{x}_1)\cdot\vec{f}(z-x_1)\vec{f}(\bar{u}-\bar{x}_1)\cdot\vec{f}(u-x_1) \\
& \times \mathrm{Tr}\Big\{[S_u + S_{x_1}]\bar{\rho}_{x_1}[S_z^\dagger - S_{x_1}^\dagger][S_{\bar{z}} - S_{\bar{x}_1}]\bar{\rho}_{\bar{x}_1}[S_{\bar{u}}^\dagger + S_{\bar{x}_1}^\dagger]\Big\} \\
& + \vec{f}(\bar{z}-\bar{u})\cdot\vec{f}(z-u)\vec{f}(\bar{u}-\bar{x}_1)\cdot\vec{f}(u-x_1) \\
& \times \mathrm{Tr}\Big\{S_u\bar{\rho}_{x_1}[S_z^\dagger - S_u^\dagger][S_{\bar{z}} - S_{\bar{u}}]\bar{\rho}_{\bar{x}_1}S_{\bar{u}}^\dagger\Big\} \\
& - \frac{1}{2}\vec{f}(\bar{z}-\bar{x}_1)\cdot\vec{f}(z-u)\vec{f}(\bar{u}-\bar{x}_1)\cdot\vec{f}(u-x_1) \\
& \times \mathrm{Tr}\Big\{S_u\bar{\rho}_{x_1}[S_z^\dagger - S_u^\dagger][S_{\bar{z}} - S_{\bar{x}_1}]\bar{\rho}_{\bar{x}_1}[S_{\bar{u}}^\dagger + S_{\bar{x}_1}^\dagger]\Big\} \\
& - \frac{1}{2}\vec{f}(\bar{z}-\bar{u})\cdot\vec{f}(z-x_1)\vec{f}(\bar{u}-\bar{x}_1)\cdot\vec{f}(u-x_1) \\
& \times \mathrm{Tr}\Big\{[S_u + S_{x_1}]\bar{\rho}_{x_1}[S_z^\dagger - S_{x_1}^\dagger][S_{\bar{z}} - S_{\bar{u}}]\bar{\rho}_{\bar{x}_1}S_{\bar{u}}^\dagger\Big\},
\end{aligned} \tag{6.15}$$

and similarly,

$$\begin{aligned}\sigma^3 = &\int_{u,z,\bar{u},\bar{z}} e^{ik(z-\bar{z})+ip(u-\bar{u})} \int_{x_1,\bar{x}_1,x_2(\bar{x}_2)} \\ &-\frac{1}{2}\vec{f}(\bar{z}-\bar{x}_1)\cdot\vec{f}(z-x_1)\vec{f}(\bar{u}-\bar{x}_1)\cdot\vec{f}(u-x_2) \\ &\times \mathrm{Tr}\Big\{\bar{\rho}_{x_1}[S_z^\dagger - S_{x_1}^\dagger][S_{\bar{z}}-S_{\bar{x}_1}]\bar{\rho}_{\bar{x}_1}[S_{\bar{u}}^\dagger + S_{\bar{x}_1}^\dagger][S_u - S_{x_2}]\bar{\rho}_{x_2}\Big\} \\ &-\frac{1}{2}\vec{f}(\bar{z}-\bar{x}_1)\cdot\vec{f}(z-x_1)\vec{f}(\bar{u}-\bar{x}_2)\cdot\vec{f}(u-x_1) \\ &\times \mathrm{Tr}\Big\{\bar{\rho}_{\bar{x}_2}[S_{\bar{u}}^\dagger - S_{\bar{x}_2}^\dagger][S_u + S_{x_1}]\bar{\rho}_{x_1}[S_z^\dagger - S_{x_1}^\dagger][S_{\bar{z}}-S_{\bar{x}_1}]\bar{\rho}_{\bar{x}_1}\Big\} \\ &+\vec{f}(\bar{z}-\bar{u})\cdot\vec{f}(z-x_1)\vec{f}(\bar{u}-\bar{x}_1)\cdot\vec{f}(u-x_2) \\ &\times \mathrm{Tr}\Big\{\bar{\rho}_{x_1}[S_z^\dagger - S_{x_1}^\dagger][S_{\bar{z}}-S_{\bar{u}}]\bar{\rho}_{\bar{x}_1}S_{\bar{u}}^\dagger[S_u - S_{x_2}]\bar{\rho}_{x_2}\Big\} \\ &+\vec{f}(\bar{z}-\bar{x}_1)\cdot\vec{f}(z-u)\vec{f}(\bar{u}-\bar{x}_2)\cdot\vec{f}(u-x_1) \\ &\times \mathrm{Tr}\Big\{\bar{\rho}_{\bar{x}_2}[S_{\bar{u}}^\dagger - S_{\bar{x}_2}^\dagger]S_u\bar{\rho}_{x_1}[S_z^\dagger - S_u^\dagger][S_{\bar{z}}-S_{\bar{x}_1}]\bar{\rho}_{\bar{x}_1}\Big\}.\end{aligned} \tag{6.16}$$

So far, the contribution σ^4, the more prominent term for the discussion, enabled angular correlations to be identified in an accessible fashion within this context. Notwithstading the difficulty in retrieving the physics of correlations behind the latter two terms present in the total cross-section, next is detailed the procedure to obtain the full cross-section again, but instead the probability amplitude is squared first and the full symmetrization between the operators $\hat{\rho}$ is carried out afterwards. This would make it possible to better evaluate the magnitude of the correlations arising from the remaining messy terms which still have to be discussed.

To get started, it is convenient to introduce some notation to shorten the long expressions that will pop up. In particular,

$$\begin{aligned} N_{zx_1\bar{z}\bar{x}_1} &:= \vec{f}(z-x_1)\cdot\vec{f}(\bar{z}-\bar{x}_1) \\ F^{ab}_{zx_1\bar{z}\bar{x}_1} &:= N_{zx_1\bar{z}\bar{x}_1}[(S_z^\dagger - S_{x_1}^\dagger)(S_{\bar{z}}-S_{\bar{x}_1})]^{ab}, \\ F^{ab}_{x_1\bar{x}_1}(k) &:= \int_{z,\bar{z}} e^{ik(z-\bar{z})}F^{ab}_{zx_1\bar{z}\bar{x}_1}, \quad F^{ab}_{x_1\bar{x}_1}(k) = F^{ba}_{\bar{x}_1x_1}(-k), \\ G^{ab}_{zx_1\bar{z}\bar{x}_1} &:= N_{zx_1\bar{z}\bar{x}_1}[(S_{x_1}^\dagger(S_{\bar{z}}-S_{\bar{x}_1})]^{ab}, \\ G^{ab}_{x_1\bar{x}_1}(k) &:= \int_{z,\bar{z}} e^{ik(z-\bar{z})}G^{ab}_{zx_1\bar{z}\bar{x}_1}, \\ M^{ab}_{zx_1\bar{z}\bar{x}_1} &:= N_{zx_1\bar{z}\bar{x}_1}[(S_z^\dagger(S_{\bar{z}}-S_{\bar{x}_1})]^{ab}. \end{aligned} \tag{6.17}$$

As an example, in terms of these shorthands, σ^4, given by eq. (6.12), reads

$$\sigma^4 = [\rho F(k)\rho][\rho F(p)\rho], \tag{6.18}$$

and, likewise, σ^3, provided by eq. (6.12), can be expressed as

$$\begin{aligned}\sigma^3 =& -\frac{1}{4}\bar{\rho}_{x_1}F_{x_1\bar{x}_1}(k)\bar{\rho}_{\bar{x}_1}F_{\bar{x}_1x_2}(-p)\bar{\rho}_{x_2}+\frac{1}{4}\bar{\rho}_{\bar{x}_1}F_{\bar{x}_1x_1}(-k)\bar{\rho}_{x_1}F_{x_1\bar{x}_2}(p)\bar{\rho}_{\bar{x}_2}\\ &+\frac{1}{2}\bar{\rho}_{\bar{x}_1}F_{\bar{x}_1x_1}(-k)\bar{\rho}_{x_1}G_{x_1\bar{x}_2}(p)\bar{\rho}_{\bar{x}_2}-\frac{1}{2}\bar{\rho}_{x_1}F_{x_1\bar{x}_1}(k)\bar{\rho}_{\bar{x}_1}G_{\bar{x}_1x_2}(-p)\bar{\rho}_{x_2}\\ &-\int_{u,\bar{u}}e^{ip(u-\bar{u})}\Big[\bar{\rho}_{\bar{x}_1}F_{\bar{x}_1u}(-k)\bar{\rho}_{x_1}M_{ux_1\bar{u}\bar{x}_2}\bar{\rho}_{\bar{x}_2}-\bar{\rho}_{x_1}F_{x_1\bar{u}}(k)\bar{\rho}_{\bar{x}_1}M_{\bar{u}\bar{x}_1ux_2}\bar{\rho}_{x_2}\Big].\end{aligned}\tag{6.19}$$

As noted above, the goal from here on is to compute the total cross-section via squaring the amplitude first and performing the full symmetrization among the $\hat{\rho}$ operators afterwards. In this way, squaring the original amplitude, eq. (6.3), delivers

$$\frac{dN}{d^2pd^2kd\eta d\xi}=\left\langle\Sigma^4+\Sigma^3+\Sigma^2\right\rangle_{P,T},\tag{6.20}$$

with

$$\Sigma^4=\bar{A}^{ab}_{ij[1]}(k,p)A^{ab*}_{ij[1]}(k,p)=F^{ab}_{x_1\bar{x}_1}(k)F^{cd}_{x_2\bar{x}_2}(p)\hat{\rho}^c_{x_2}\hat{\rho}^a_{x_1}\hat{\rho}^d_{\bar{x}_2}\hat{\rho}^b_{\bar{x}_1},\tag{6.21}$$

$$\begin{aligned}\Sigma^3 &= \bar{A}^{ab}_{ij[1]}(k,p)A^{ab*}_{ij[2]}(k,p)+A^{ab*}_{ij[1]}(k,p)\bar{A}^{ab}_{ij[2]}(k,p)\\ &=\Big[\int_{u,\bar{u}}e^{ip(u-\bar{u})}F^{ab}_{u\bar{x}_1}(k)M^{md}_{ux_2\bar{u}\bar{x}_2}T^a_{mc}-F^{ab}_{x_2\bar{x}_1}(k)G^{md}_{x_2\bar{x}_2}(p)T^a_{mc}\Big]\hat{\rho}^c_{x_2}\hat{\rho}^d_{\bar{x}_2}\hat{\rho}^b_{\bar{x}_1}\\ &+\Big[\int_{u,\bar{u}}e^{ip(u-\bar{u})}F^{ab}_{x_1\bar{u}}(k)M^{mc}_{\bar{u}\bar{x}_2ux_2}T^b_{md}-F^{ab}_{x_1\bar{x}_2}(k)G^{mc}_{\bar{x}_2x_2}(-p)T^b_{md}\Big]\hat{\rho}^c_{x_2}\hat{\rho}^a_{x_1}\hat{\rho}^d_{\bar{x}_2},\end{aligned}\tag{6.22}$$

and

$$\begin{aligned}\Sigma^2 &= \bar{A}^{ab}_{ij[2]}(k,p)A^{ab*}_{ij[2]}(k,p)\\ &=\int_{u,\bar{u}}e^{ip(u-\bar{u})}F^{ab}_{x_1\bar{x}_1}(k)N_{ux_2\bar{u}\bar{x}_2}T^a_{mc}[(S^\dagger_u\delta_{ux_1}-S^\dagger_{x_2}\delta_{x_1x_2})(S_{\bar{u}}\delta_{\bar{u}\bar{x}_1}-S_{\bar{x}_2}\delta_{\bar{x}_1\bar{x}_2})]^{mn}\\ &\times T^b_{nd}\hat{\rho}^c_{x_2}\hat{\rho}^d_{\bar{x}_2}.\end{aligned}\tag{6.23}$$

The focus now is set in particular on working out eqs. (6.21) and (6.22) in order to obtain compact expressions for Σ^4 and Σ^3 that favour a friendly interpretation looking to acquire more thorough knowledge of how correlations arise in this scenario.

Commencing with eq. (6.21), the $\hat{\rho}$ operators can be expanded as follows by virtue of eq. (6.4),

$$\hat{\rho}^c_{x_2}\hat{\rho}^a_{x_1}\hat{\rho}^d_{\bar{x}_2}\hat{\rho}^b_{\bar{x}_1}=\hat{\rho}^c_{x_2}\hat{\rho}^a_{x_1}\Big[\frac{1}{2}\{\hat{\rho}^d_{\bar{x}_2},\hat{\rho}^b_{\bar{x}_1}\}+\frac{1}{2}T^e_{db}\hat{\rho}^e_{(\bar{x}_2,\bar{x}_1)}\Big].\tag{6.24}$$

Using now

$$\hat{\rho}^a \frac{1}{2}\{\hat{\rho}^{a_1}\hat{\rho}^{a_2}\} = \frac{1}{6}\{\hat{\rho}^a\hat{\rho}^{a_1}\hat{\rho}^{a_2}\} + \frac{1}{2}\Big[\frac{1}{2}T^c_{aa_1}\{\hat{\rho}^{a_2}\hat{\rho}^c\} + \frac{1}{2}T^c_{aa_2}\{\hat{\rho}^{a_1}\hat{\rho}^c\}\Big] + \frac{1}{12}\{T^{a_1}T^{a_2}\}_{ac}\hat{\rho}^c, \quad (6.25)$$

where $\{\hat{\rho}^{a_1}\cdots\hat{\rho}^{a_n}\}$ denotes a fully symmetrized product of n charge density operators, and eq. (6.4) once again, eq. (6.24) reads

$$\begin{aligned}\hat{\rho}^c_{x_2}\hat{\rho}^a_{x_1}\hat{\rho}^d_{\bar{x}_2}\hat{\rho}^b_{\bar{x}_1} = \hat{\rho}^c_{x_2}\Big\{&\frac{1}{6}\{\hat{\rho}^a_{x_1}\hat{\rho}^d_{\bar{x}_2}\hat{\rho}^b_{\bar{x}_1}\} + \frac{1}{2}\Big[\frac{1}{2}T^e_{ad}\{\hat{\rho}^b_{\bar{x}_1}\hat{\rho}^e_{(x_1,\bar{x}_2)}\} + \frac{1}{2}T^e_{ab}\{\hat{\rho}^d_{\bar{x}_2}\hat{\rho}^e_{(x_1,\bar{x}_1)}\}\Big] \\ &+ \frac{1}{12}\{T^dT^b\}_{ae}\hat{\rho}^e\Big\} + \Big[\frac{1}{2}\{\hat{\rho}^c_{x_2},\hat{\rho}^a_{x_1}\} + \frac{1}{2}T^e_{ca}\hat{\rho}^e_{(x_2,x_1)}\Big]\frac{1}{2}T^e_{db}\hat{\rho}^e_{(\bar{x}_2,\bar{x}_1)}.\end{aligned} \quad (6.26)$$

Having a look at the preceding expression, one can easily realise that neither the fourth nor the sixth term will contribute to σ^4 or $\bar{\sigma}^3$ as they include a combination of only two $\hat{\rho}$ operators. Thus, it simply remains

$$\begin{aligned}\hat{\rho}^c_{x_2}\hat{\rho}^a_{x_1}\hat{\rho}^d_{\bar{x}_2}\hat{\rho}^b_{\bar{x}_1} = \hat{\rho}^c_{x_2}\Big\{&\frac{1}{6}\{\hat{\rho}^a_{x_1}\hat{\rho}^d_{\bar{x}_2}\hat{\rho}^b_{\bar{x}_1}\} + \frac{1}{2}\Big[\frac{1}{2}T^e_{ad}\{\hat{\rho}^b_{\bar{x}_1}\hat{\rho}^e_{(x_1,\bar{x}_2)}\} + \frac{1}{2}T^e_{ab}\{\hat{\rho}^d_{\bar{x}_2}\hat{\rho}^e_{(x_1,\bar{x}_1)}\}\Big]\Big\} \\ &+ \frac{1}{4}T^e_{db}\{\hat{\rho}^c_{x_2},\hat{\rho}^a_{x_1}\}\hat{\rho}^e_{(\bar{x}_2,\bar{x}_1)}.\end{aligned} \quad (6.27)$$

Now expanding again the equation above by virtue of the following expression,

$$\begin{aligned}\hat{\rho}^a\frac{1}{6}\{\hat{\rho}^{a_1}\hat{\rho}^{a_2}\hat{\rho}^{a_3}\} = \frac{1}{24}\{\hat{\rho}^a\hat{\rho}^{a_1}\hat{\rho}^{a_2}\hat{\rho}^{a_3}\} + \frac{1}{2}\Big[&\frac{1}{6}T^c_{aa_1}\{\hat{\rho}^{a_2}\hat{\rho}^c\hat{\rho}^{a_3}\} + \frac{1}{6}T^c_{aa_2}\{\hat{\rho}^{a_1}\hat{\rho}^c\hat{\rho}^{a_3}\} \\ &+ \frac{1}{6}T^c_{aa_3}\{\hat{\rho}^{a_2}\hat{\rho}^c\hat{\rho}^{a_1}\}\Big] + \frac{1}{12}\Big[\frac{1}{2}\{T^{a_1}T^{a_2}\}_{ac}\{\hat{\rho}^c\hat{\rho}^{a_3}\} + \frac{1}{2}\{T^{a_1}T^{a_3}\}_{ac}\{\hat{\rho}^c\hat{\rho}^{a_2}\} \\ &+ \frac{1}{2}\{T^{a_2}T^{a_3}\}_{ac}\{\hat{\rho}^c\hat{\rho}^{a_1}\}\Big],\end{aligned} \quad (6.28)$$

and implementing eq. (6.25) over again, eq. (6.27) eventually reduces to

$$\begin{aligned}\hat{\rho}^c_{x_2}\hat{\rho}^a_{x_1}\hat{\rho}^d_{\bar{x}_2}\hat{\rho}^b_{\bar{x}_1} = &\frac{1}{24}\{\hat{\rho}^c_{x_2}\hat{\rho}^a_{x_1}\hat{\rho}^d_{\bar{x}_2}\hat{\rho}^b_{\bar{x}_1}\} + \frac{1}{2}\Big[\frac{1}{6}T^e_{ca}\{\hat{\rho}^d_{\bar{x}_2}\hat{\rho}^e_{(x_2,x_1)}\hat{\rho}^b_{\bar{x}_1}\} + \frac{1}{6}T^e_{cd}\{\hat{\rho}^a_{x_1}\hat{\rho}^e_{(x_2,\bar{x}_2)}\hat{\rho}^b_{\bar{x}_1}\} \\ &+ \frac{1}{6}T^e_{cb}\{\hat{\rho}^d_{\bar{x}_2}\hat{\rho}^e_{(x_2,\bar{x}_1)}\hat{\rho}^a_{x_1}\}\Big] + \frac{1}{2}\hat{\rho}^c_{x_2}\Big[\frac{1}{2}T^e_{ad}\{\hat{\rho}^b_{\bar{x}_1}\hat{\rho}^e_{(x_1,\bar{x}_2)}\} + \frac{1}{2}T^e_{ab}\{\hat{\rho}^d_{\bar{x}_2}\hat{\rho}^e_{(x_1,\bar{x}_1)}\}\Big] \\ &+ \frac{1}{2}T^e_{db}\frac{1}{6}\{\hat{\rho}^e_{(\bar{x}_2,\bar{x}_1)}\hat{\rho}^c_{x_2}\hat{\rho}^a_{x_1}\}.\end{aligned} \quad (6.29)$$

Note that eqs. (6.4), (6.25) and (6.28) can be explicitly inferred from

$$\langle\hat{\rho}^a_x\{\hat{\rho}^{a_1}...\hat{\rho}^{a_n}\}\rangle = \Big[1 + \frac{1}{2}\Big(T^b\frac{\delta}{\delta\rho^b_x}\Big) + \frac{1}{12}\Big(T^b\frac{\delta}{\delta\rho^b_x}\Big)^2\Big]_{ca}\langle\langle\rho^c_y\rho^{a_1}...\rho^{a_n}\rangle\rangle \quad (6.30)$$

for $n=1$, $n=2$ and $n=3$, respectively. Similarly,

$$\langle\{\hat{\rho}^{a_1}...\hat{\rho}^{a_n}\}\hat{\rho}^a_y\rangle = \Big[1-\frac{1}{2}\Big(T^b\frac{\delta}{\delta\rho^b_x}\Big)+\frac{1}{12}\Big(T^b\frac{\delta}{\delta\rho^b_x}\Big)^2\Big]_{ac}\langle\langle\rho^c_y\rho^{a_1}...\rho^{a_n}\rangle\rangle. \tag{6.31}$$

Hence, after the algebra performed above, eq. (6.21) can be written as

$$\begin{aligned}\Sigma^4 &= F^{ab}_{x_1\bar{x}_1}(k)F^{cd}_{x_2\bar{x}_2}(p)\hat{\rho}^c_{x_2}\hat{\rho}^a_{x_1}\hat{\rho}^d_{\bar{x}_2}\hat{\rho}^b_{\bar{x}_1} = \\ &= F^{ab}_{x_1\bar{x}_1}(k)F^{cd}_{x_2\bar{x}_2}(p)\Big[\frac{1}{24}\{\hat{\rho}^c_{x_2}\hat{\rho}^a_{x_1}\hat{\rho}^d_{\bar{x}_2}\hat{\rho}^b_{\bar{x}_1}\}_{[1]}+\frac{1}{2}\Big[\frac{1}{6}T^e_{ca}\{\hat{\rho}^d_{\bar{x}_2}\hat{\rho}^e_{(x_2,x_1)}\hat{\rho}^b_{\bar{x}_1}\}_{[2.1]} \\ &+\frac{1}{6}T^e_{cd}\{\hat{\rho}^a_{x_1}\hat{\rho}^e_{(x_2,\bar{x}_2)}\hat{\rho}^b_{\bar{x}_1}\}_{[2.2]}+\frac{1}{6}T^e_{cb}\{\hat{\rho}^d_{\bar{x}_2}\hat{\rho}^e_{(x_2,\bar{x}_1)}\hat{\rho}^a_{x_1}\}_{[2.3]}\Big]+\frac{1}{2}\Big[T^e_{ad}\frac{1}{6}\{\hat{\rho}^c_{x_2}\hat{\rho}^b_{\bar{x}_1}\hat{\rho}^e_{(x_1,\bar{x}_2)}\}_{[3.1]} \\ &+T^e_{ab}\frac{1}{6}\{\hat{\rho}^c_{x_2}\hat{\rho}^d_{\bar{x}_2}\hat{\rho}^e_{(x_1,\bar{x}_1)}\}_{[3.2]}\Big]+\frac{1}{2}T^e_{db}\frac{1}{6}\{\hat{\rho}^e_{(\bar{x}_2,\bar{x}_1)}\hat{\rho}^c_{x_2}\hat{\rho}^a_{x_1}\}_{[4]}\Big],\end{aligned} \tag{6.32}$$

where each of the terms are tagged with a subscript to keep a clear picture in mind from then on. Below they are worked out in order to make the expressions more compact:

$$\begin{aligned}\Sigma^4_{[1]} &= F^{ab}_{x_1\bar{x}_1}(k)F^{cd}_{x_2\bar{x}_2}(p)\frac{1}{24}\{\hat{\rho}^c_{x_2}\hat{\rho}^a_{x_1}\hat{\rho}^d_{\bar{x}_2}\hat{\rho}^b_{\bar{x}_1}\} = \rho^a_{x_1}F^{ab}_{x_1\bar{x}_1}(k)\rho^b_{\bar{x}_1}\rho^c_{x_2}F^{cd}_{x_2\bar{x}_2}(p)\rho^d_{\bar{x}_2} \\ &= [\rho^a_{x_1}F^{ab}_{x_1\bar{x}_1}(k)\rho^b_{\bar{x}_1}][\rho^c_{x_2}F^{cd}_{x_2\bar{x}_2}(p)\rho^d_{\bar{x}_2}] = [\rho F(k)\rho]\,[\rho F(p)\rho]\,,\end{aligned} \tag{6.33}$$

$$\begin{aligned}\Sigma^4_{[2.1]} &= F^{ab}_{x_1\bar{x}_1}(k)F^{cd}_{x_2\bar{x}_2}(p)\frac{1}{12}T^e_{ca}\{\hat{\rho}^d_{\bar{x}_2}\hat{\rho}^e_{(x_2,x_1)}\hat{\rho}^b_{\bar{x}_1}\} \\ &= -\frac{1}{2}\rho^b_{\bar{x}_1}F^{ba}_{\bar{x}_1x_1}(-k)T^e_{ac}\rho^e_{(x_2,x_1)}F^{cd}_{x_2\bar{x}_2}(p)\rho^d_{\bar{x}_2} \\ &= -\frac{1}{2}\rho_{\bar{x}_1}F_{\bar{x}_1x_1}(-k)\bar{\rho}_{(x_2,x_1)}F_{x_2\bar{x}_2}(p)\rho_{\bar{x}_2} = -\frac{1}{2}\rho_xF_{xy}(-k)\bar{\rho}_yF_{yw}(p)\rho_w,\end{aligned} \tag{6.34}$$

$$\begin{aligned}\Sigma^4_{[2.2]} &= F^{ab}_{x_1\bar{x}_1}(k)F^{cd}_{x_2\bar{x}_2}(p)\frac{1}{12}T^e_{cd}\{\hat{\rho}^a_{x_1}\hat{\rho}^e_{(x_2,\bar{x}_2)}\hat{\rho}^b_{\bar{x}_1}\} \\ &= \frac{1}{2}\left[\rho^a_{x_1}F^{ab}_{x_1\bar{x}_1}(k)\rho^b_{\bar{x}_1}\right]\left[-T^e_{dc}\rho^e_{(x_2,\bar{x}_2)}F^{cd}_{x_2\bar{x}_2}(p)\right] \\ &= -\frac{1}{2}\left[\rho_{x_1}F_{x_1\bar{x}_1}(k)\rho_{\bar{x}_1}\right]\mathrm{Tr}\left[\bar{\rho}_{(x_2,\bar{x}_2)}F_{x_2\bar{x}_2}(p)\right] = -\frac{1}{2}\left[\rho_xF_{xy}(k)\rho_y\right]\mathrm{Tr}\left[\bar{\rho}_xF_{xx}(p)\right],\end{aligned} \tag{6.35}$$

$$\begin{aligned}\Sigma^4_{[2.3]} &= F^{ab}_{x_1\bar{x}_1}(k)F^{cd}_{x_2\bar{x}_2}(p)\frac{1}{12}T^e_{cb}\{\hat{\rho}^a_{\bar{x}_2}\hat{\rho}^e_{(x_2,\bar{x}_1)}\hat{\rho}^a_{x_1}\} = -\frac{1}{2}\rho^a_{x_1}F^{ab}_{x_1\bar{x}_1}(k)T^e_{bc}\rho^e_{(x_2,\bar{x}_2)}F^{cd}_{x_2\bar{x}_2}(p)\rho^d_{\bar{x}_2} \\ &= -\frac{1}{2}\rho_{x_1}F_{x_1\bar{x}_1}(k)\bar{\rho}_{(x_2,\bar{x}_1)}F_{x_2\bar{x}_2}(p)\rho_{\bar{x}_2} = -\frac{1}{2}\rho_xF_{xy}(k)\bar{\rho}_yF_{yw}(p)\rho_w,\end{aligned} \tag{6.36}$$

$$\begin{aligned}\Sigma^4_{[3.1]} &= F^{ab}_{x_1\bar{x}_1}(k)F^{cd}_{x_2\bar{x}_2}(p)\frac{1}{12}T^e_{ad}\{\hat{\rho}^c_{x_2}\hat{\rho}^b_{\bar{x}_1}\hat{\rho}^e_{(x_1,\bar{x}_2)}\}\\ &= \frac{1}{2}\rho^b_{\bar{x}_1}F^{ba}_{\bar{x}_1x_1}(-k)T^e_{ad}\rho^e_{(x_1,\bar{x}_2)}F^{dc}_{\bar{x}_2x_2}(-p)\rho^c_{x_2}\\ &= \frac{1}{2}\rho_{\bar{x}_1}F_{\bar{x}_1x_1}(-k)\bar{\rho}_{(x_1,\bar{x}_2)}F_{\bar{x}_2x_2}(-p)\rho_{x_2} = \frac{1}{2}\rho_xF_{xy}(-k)\bar{\rho}_yF_{yw}(-p)\rho_w,\end{aligned} \tag{6.37}$$

$$\begin{aligned}\Sigma^4_{[3.2]} &= F^{ab}_{x_1\bar{x}_1}(k)F^{cd}_{x_2\bar{x}_2}(p)\frac{1}{12}T^e_{ab}\{\hat{\rho}^c_{x_2}\hat{\rho}^d_{\bar{x}_2}\hat{\rho}^e_{(x_1,\bar{x}_1)}\}\\ &= \frac{1}{2}\left[-T^e_{ba}\rho^e_{(x_1,\bar{x}_1)}F^{ab}_{x_1\bar{x}_1}(k)\right]\left[\hat{\rho}^c_{x_2}F^{cd}_{x_2\bar{x}_2}(p)\rho^d_{\bar{x}_2}\right]\\ &= -\frac{1}{2}\mathrm{Tr}\left[\bar{\rho}_{(x_1,\bar{x}_1)}F_{x_1\bar{x}_1}(k)\right]\left[\rho_{x_2}F_{x_2\bar{x}_2}(p)\rho_{\bar{x}_2}\right] = -\frac{1}{2}\mathrm{Tr}\left[\bar{\rho}_xF_{xx}(k)\right]\left[\rho_yF_{yw}(p)\rho_w\right],\end{aligned} \tag{6.38}$$

$$\begin{aligned}\Sigma^4_{[4]} &= F^{ab}_{x_1\bar{x}_1}(k)F^{cd}_{x_2\bar{x}_2}(p)\frac{1}{12}T^e_{db}\{\hat{\rho}^e_{(\bar{x}_2,\bar{x}_1)}\hat{\rho}^c_{x_2}\hat{\rho}^a_{x_1}\} = -\frac{1}{2}\rho^a_{x_1}F^{ab}_{x_1\bar{x}_1}(k)T^e_{bd}\rho^e_{(\bar{x}_2,\bar{x}_1)}F^{dc}_{\bar{x}_2x_2}(-p)\rho^c_{x_2}\\ &= -\frac{1}{2}\rho_{x_1}F_{x_1\bar{x}_1}(k)\bar{\rho}_{(\bar{x}_2,\bar{x}_1)}F_{\bar{x}_2x_2}(-p)\rho_{x_2} = -\frac{1}{2}\rho_xF_{xy}(k)\bar{\rho}_yF_{yw}(-p)\rho_w.\end{aligned} \tag{6.39}$$

Finally, summing up all the contributions to Σ^4 produces

$$\begin{aligned}\Sigma^4 &= \left[\rho F(k)\rho\right]\left[\rho F(p)\rho\right] + \frac{1}{2}\rho_xF_{xy}(-k)\bar{\rho}_yF_{yw}(-p)\rho_w - \frac{1}{2}\rho_xF_{xy}(k)\bar{\rho}_yF_{yw}(p)\rho_w\\ &- \frac{1}{2}\mathrm{Tr}[\bar{\rho}_xF_{xx}(k)][\rho_yF_{yw}(p)\rho_w] - \frac{1}{2}[\rho_xF_{xy}(k)\rho_y]\mathrm{Tr}[\bar{\rho}_xF_{xx}(p)] - \frac{1}{2}\rho_xF_{xy}(k)\bar{\rho}_yF_{yw}(-p)\rho_w\\ &- \frac{1}{2}\rho_xF_{xy}(-k)\bar{\rho}_yF_{yw}(p)\rho_w.\end{aligned}$$

It now appears that all but the first term from the preceding equation include a combination of three color charge densities, clearly suggesting a redefinition of Σ^4 as $\Sigma^4 = \sigma^4 + \sigma^{3(4)}$, with

$$\sigma^4 = \left[\rho F(k)\rho\right]\left[\rho F(p)\rho\right], \tag{6.40}$$

and

$$\begin{aligned}\sigma^{3(4)} &= \frac{1}{2}\rho_xF_{xy}(-k)\bar{\rho}_yF_{yw}(-p)\rho_w - \frac{1}{2}\rho_xF_{xy}(k)\bar{\rho}_yF_{yw}(p)\rho_w\\ &- \frac{1}{2}\mathrm{Tr}[\bar{\rho}_xF_{xx}(k)][\rho_yF_{yw}(p)\rho_w] - \frac{1}{2}[\rho_xF_{xy}(k)\rho_y]\mathrm{Tr}[\bar{\rho}_xF_{xx}(p)]\\ &- \frac{1}{2}\rho_xF_{xy}(k)\bar{\rho}_yF_{yw}(-p)\rho_w - \frac{1}{2}\rho_xF_{xy}(-k)\bar{\rho}_yF_{yw}(p)\rho_w,\end{aligned} \tag{6.41}$$

this way opening the door to direct comparison with the results obtained for σ^4 and σ^3 when symmetrizing first and squaring afterwards, namely eqs. (6.18) and (6.19).

As might be expected, eqs. (6.40) and (6.18) are just the same, as is also its interpretation regarding the appearance of angular correlations, already well-founded earlier. For its part, eq. (6.41) accounts for some extra terms arising when carrying out the symmetrization right after squaring the probability amplitude. Accordingly, the last two terms of eq. (6.41) match with the first two ones obtained in eq. (6.19). The remaining four emanate from labouring the original expression for Σ^3. Indeed, below is performed the same procedure followed for drawing σ^4 and $\sigma^{3(4)}$ off the original expression of Σ^4, eq. (6.21), but now to get the contributions to σ^3 out of Σ^3, eq. (6.22), which, obviously, have to fit with those last four terms derived in eq. (6.19). Explicitly,

$$\begin{aligned}\Sigma^3 = &\Big[\int_{u,\bar{u}} e^{ip(u-\bar{u})} F^{ab}_{u\bar{x}_1}(k) M^{md}_{ux_2\bar{u}\bar{x}_2} T^a_{mc\ [1.1]} - F^{ab}_{x_2\bar{x}_1}(k) G^{md}_{x_2\bar{x}_2}(p) T^a_{mc\ [1.2]}\Big] \hat{\rho}^c_{x_2}\hat{\rho}^d_{\bar{x}_2}\hat{\rho}^b_{\bar{x}_1} \\ &+ \Big[\int_{u,\bar{u}} e^{ip(u-\bar{u})} F^{ab}_{x_1\bar{u}}(k) M^{mc}_{\bar{u}\bar{x}_2 ux_2} T^b_{md\ [2.1]} - F^{ab}_{x_1\bar{x}_2}(k) G^{mc}_{\bar{x}_2 x_2}(-p) T^b_{md\ [2.2]}\Big] \hat{\rho}^c_{x_2}\hat{\rho}^a_{x_1}\hat{\rho}^d_{\bar{x}_2},\end{aligned} \tag{6.42}$$

with

$$\begin{aligned}\Sigma^3_{[1.1]} &= \int_{u,\bar{u}} e^{ip(u-\bar{u})} F^{ab}_{u\bar{x}_1}(k) M^{md}_{ux_2\bar{u}\bar{x}_2} T^a_{cm} \rho^c_{x_2}\rho^d_{\bar{x}_2}\rho^b_{\bar{x}_1} \\ &= -\int_{u,\bar{u}} e^{ip(u-\bar{u})} \rho^b_{\bar{x}_1} F^{ba}_{\bar{x}_1 u}(-k) T^c_{am}\rho^c_{x_2} M^{md}_{ux_2\bar{u}\bar{x}_2}\rho^d_{\bar{x}_2} \\ &= -\int_{u,\bar{u}} e^{ip(u-\bar{u})} \rho_{\bar{x}_1} F_{\bar{x}_1 u}(-k)\bar{\rho}_{x_2} M_{ux_2\bar{u}\bar{x}_2}\rho_{\bar{x}_2},\end{aligned} \tag{6.43}$$

$$\begin{aligned}\Sigma^3_{[1.2]} &= -F^{ab}_{x_2\bar{x}_1}(k) G^{md}_{x_2\bar{x}_2}(p) T^a_{cm}\rho^c_{x_2}\rho^d_{\bar{x}_2}\rho^b_{\bar{x}_1} = \rho^b_{\bar{x}_1} F^{ba}_{\bar{x}_1 x_2}(-k) T^c_{am}\rho^c_{x_2} G^{md}_{x_2\bar{x}_2}(p)\rho^d_{\bar{x}_2} \\ &= \rho_{\bar{x}_1} F_{\bar{x}_1 x_2}(-k)\bar{\rho}_{x_2} G_{x_2\bar{x}_2}(p)\rho_{\bar{x}_2} = \rho_x F_{xy}(-k)\bar{\rho}_y G_{yw}(p)\rho_w,\end{aligned} \tag{6.44}$$

$$\begin{aligned}\Sigma^3_{[2.1]} &= \int_{u,\bar{u}} e^{ip(u-\bar{u})} F^{ab}_{x_1\bar{u}}(k) M^{mc}_{\bar{u}\bar{x}_2 ux_2} T^b_{md}\rho^c_{x_2}\rho^a_{x_1}\rho^d_{\bar{x}_2} \\ &= \int_{u,\bar{u}} e^{ip(u-\bar{u})} \rho^a_{x_1} F^{ab}_{x_1\bar{u}}(k) T^d_{bm}\rho^d_{\bar{x}_2} M^{mc}_{\bar{u}\bar{x}_2 ux_2}\rho^c_{x_2} \\ &= \int_{u,\bar{u}} e^{ip(u-\bar{u})} \rho_{x_1} F_{x_1\bar{x}_1}(k)\bar{\rho}_{\bar{x}_2} M_{\bar{u}\bar{x}_2 ux_2}\rho_{x_2},\end{aligned} \tag{6.45}$$

$$\begin{aligned}\Sigma^3_{[2.2]} &= -F^{ab}_{x_1\bar{x}_2}(k) G^{mc}_{\bar{x}_2 x_2}(-p) T^b_{md}\rho^c_{x_2}\rho^a_{x_1}\rho^d_{\bar{x}_2} = -\rho^a_{x_1} F^{ab}_{x_1\bar{x}_2}(k) T^b_{md}\rho^d_{\bar{x}_2} G^{mc}_{\bar{x}_2 x_2}(p)\rho^c_{x_2} \\ &= -\rho_{x_1} F_{x_1\bar{x}_2}(k)\bar{\rho}_{\bar{x}_2} G_{\bar{x}_2 x_2}(p)\rho_{x_2} = -\rho_x F_{xy}(k)\bar{\rho}_y G_{yw}(-p)\rho_w.\end{aligned} \tag{6.46}$$

Taken all together delivers

$$\begin{aligned}\sigma^3 = &\hat{\rho}_x F_{xy}(-k)\bar{\rho}_y G_{yw}(p)\rho_w - \rho_x F_{xy}(k)\hat{\bar{\rho}}_y G_{yw}(-p)\rho_w - \\ &- \int_{u,\bar{u}} e^{ip(u-\bar{u})}\Big[\rho_{\bar{x}_1} F_{\bar{x}_1 u}(-k)\bar{\rho}_{x_2} M_{ux_2\bar{u}\bar{x}_2}\rho_{\bar{x}_2} - \rho_{x_1} F_{x_1\bar{u}}(k)\bar{\rho}_{\bar{x}_2} M_{\bar{u}\bar{x}_2 ux_2}\rho_{x_2}\Big],\end{aligned} \tag{6.47}$$

what, as stated above, is in accordance with the last four terms of eq. (6.19).

Finally, after this cumbersome algebra procedure, the fully ordered expression for the double inclusive gluon production reads

$$\frac{dN}{d^2pd^2kd\eta d\xi} = \left\langle \sigma^4 + \bar{\sigma}^3 + \bar{\sigma}^2 \right\rangle_{P,T}, \tag{6.48}$$

where

$$\sigma^4 = [\rho F(k)\rho][\rho F(p)\rho], \tag{6.49}$$

$$\bar{\sigma}^3 = \sigma^{3(4)} + \sigma^3, \tag{6.50}$$

with

$$\begin{aligned}\sigma^{3(4)} = &\frac{1}{2}\rho_x F_{xy}(-k)\bar{\rho}_y F_{yw}(-p)\rho_w - \frac{1}{2}\rho_x F_{xy}(k)\bar{\rho}_y F_{yw}(p)\rho_w \\ &- \frac{1}{2}\mathrm{Tr}[\bar{\rho}_x F_{xx}(k)][\rho_y F_{yw}(p)\rho_w] - \frac{1}{2}[\rho_x F_{xy}(k)\rho_y]\mathrm{Tr}[\bar{\rho}_x F_{xx}(p)] \\ &- \frac{1}{2}\rho_x F_{xy}(k)\bar{\rho}_y F_{yw}(-p)\rho_w - \frac{1}{2}\rho_x F_{xy}(-k)\bar{\rho}_y F_{yw}(p)\rho_w,\end{aligned} \tag{6.51}$$

$$\begin{aligned}\sigma^3 = &\rho_x F_{xy}(-k)\bar{\rho}_y G_{yw}(p)\rho_w - \rho_x F_{xy}(k)\bar{\rho}_y G_{yw}(-p)\rho_w \\ &- \int_{u,\bar{u}} e^{ip(u-\bar{u})}\Big[\rho_{\bar{x}_1} F_{\bar{x}_1 u}(-k)\bar{\rho}_{x_2} M_{ux_2\bar{u}\bar{x}_2}\rho_{\bar{x}_2} - \rho_{x_1} F_{x_1\bar{u}}(k)\bar{\rho}_{\bar{x}_2} M_{\bar{u}\bar{x}_2 ux_2}\rho_{x_2}\Big].\end{aligned} \tag{6.52}$$

For now, contributions involving a combination of two $\hat{\rho}$ operators, $\bar{\sigma}^2$, which come from both Σ^4 and Σ^3, as well as from the original expression of Σ^2, eq. (6.23), are disregarded, since major cancelations amongst the vast number of terms that arise are not expected, thus making it very difficult to draw relevant conclusions about the origin of the aforementioned correlations. Furthermore, noticing the similarity between the emerging contributions with the ones obtained for $\bar{\sigma}^3$, correlations are very likely to belong to the same nature.

As a final step, given the similarity between the terms that make up $\bar{\sigma}^3$, it is well worth attempting to simplify even more eq. (6.50) in such a way as to streamline the procedure for averaging. More specifically, writing down the expression for $\bar{\sigma}^3$ above as follows leads to non-trivial cancellations that can make it much easier to compute the remaining correlators arising in the final expression,

$$
\begin{aligned}
\bar{\sigma}^3 = &-\frac{1}{2}\rho_x F_{xy}(k)\bar{\rho}_y\Big[F_{yw}(p)+F_{yw}(-p)+2G_{yw}(-p)\Big]\rho_w \\
&-\frac{1}{2}\rho_x F_{xy}(-k)\bar{\rho}_y\Big[F_{yw}(p)-F_{yw}(-p)-2G_{yw}(p)\Big]\rho_w \\
&-\int_{u,\bar{u}} e^{ip(u-\bar{u})}\Big[\rho_{\bar{x}_1}F_{\bar{x}_1 u}(-k)\bar{\rho}_{x_2}M_{ux_2\bar{u}\bar{x}_2}\rho_{\bar{x}_2}-\rho_{x_1}F_{x_1\bar{u}}(k)\bar{\rho}_{\bar{x}_2}M_{\bar{u}\bar{x}_2 ux_2}\rho_{x_2}\Big] \\
&-\frac{1}{2}\mathrm{Tr}[\bar{\rho}_x F_{xx}(k)][\rho_y F_{yw}(p)\rho_w]-\frac{1}{2}[\rho_x F_{xy}(k)\rho_y]\mathrm{Tr}[\bar{\rho}_x F_{xx}(p)].
\end{aligned}
\tag{6.53}
$$

Now rewriting $G_{yw}(p)$ and $G_{yw}(-p)$ in terms of M and F as

$$
\begin{cases}
G_{yw}(p) = M_{uy\bar{u}w} - F_{yw}(p), \\
G_{yw}(-p) = M_{\bar{u}wuy} - F_{yw}(-p),
\end{cases}
\tag{6.54}
$$

gives rise to

$$
\begin{aligned}
\bar{\sigma}^3 = &-\frac{1}{2}\rho_x F_{xy}(k)\bar{\rho}_y\Big[F_{yw}(p)+F_{yw}(-p)-2F_{yw}(-p)\Big]\rho_w \\
&-\frac{1}{2}\rho_x F_{xy}(-k)\bar{\rho}_y\Big[F_{yw}(p)-F_{yw}(-p)+2F_{yw}(p)\Big]\rho_w \\
&-\int_{u,\bar{u}} e^{ip(u-\bar{u})}\Big\{\rho_{\bar{x}_1}\Big[F_{\bar{x}_1 u}-F_{\bar{x}_1 x_2}\Big](-k)\bar{\rho}_{x_2}M_{ux_2\bar{u}\bar{x}_2}\rho_{\bar{x}_2} \\
&-\rho_{x_1}\Big[F_{x_1\bar{u}}-F_{x_1\bar{x}_2}\Big](k)\bar{\rho}_{\bar{x}_2}M_{\bar{u}\bar{x}_2 ux_2}\rho_{x_2}\Big\} \\
&-\frac{1}{2}\mathrm{Tr}[\bar{\rho}_x F_{xx}(k)][\rho_y F_{yw}(p)\rho_w]-\frac{1}{2}[\rho_x F_{xy}(k)\rho_y]\mathrm{Tr}[\bar{\rho}_x F_{xx}(p)].
\end{aligned}
\tag{6.55}
$$

Finally, arguing that both contributions within the explicit integral cancel each other out owing to symmetry reasons delivers

$$
\begin{aligned}
\bar{\sigma}^3 = &-\frac{1}{2}\rho_x\Big[F_{xy}(k)+F_{xy}(-k)\Big]\bar{\rho}_y\Big[F_{yw}(p)-F_{yw}(-p)\Big]\rho_w \\
&-\rho_x F_{xy}(-k)\bar{\rho}_y F_{yw}(p)\rho_w \\
&-\frac{1}{2}\mathrm{Tr}[\bar{\rho}_x F_{xx}(k)][\rho_y F_{yw}(p)\rho_w]-\frac{1}{2}[\rho_x F_{xy}(k)\rho_y]\mathrm{Tr}[\bar{\rho}_x F_{xx}(p)].
\end{aligned}
\tag{6.56}
$$

Eq. (6.56) constitutes a more friendly expression in pursuit of averaging this specific contribution with respect to the projectile color charge distribution via the MV model, earlier introduced in subsection 2.3.3, which establishes that the distribution of color sources can be reproduced with a Gaussian weight function. This last step is planned to be carried out in a future study that could provide an insightful picture regarding the understanding of the correlations this component can lead to.

6.3 Conclusions and outlook

This chapter was intended to showcase that, in high-energy collisions, the appearance of angular correlations between emerging particles can be tested under very simple standards. More precisally, for this purpose it is appropriate to address the computation of the double inclusive gluon production probability within the framework in which one of the objects is dense and the other dilute.

In this sense, as the cross-section can be split into three different pieces accounting for three very clear configurations, each of these contributions can be addressed independently in the face of interpreting the origin of the correlations. In particular, the final expression for σ^4 straightforwardly reveals the backstory behind the physics of correlations without going into state-of-the-art approaches. For its part, a cumbersome algebraic workout leads to a large extent simplified expression for one of the remaining terms making up the cross-section, this way setting the stage for a feasible averaging process over the projectile wave function, what might unveil different evidences on the source of these correlations.

To finish off, it must be noted that this work seeks to provide a way out of the results presented in [167], study on which this work is fully based. To be quite specific, when calculating the fully ordered expression for the probability via performing the full symmetrization between the color charge density operators after squaring the amplitude, [167] mismatches the origin of the different terms contributing to σ^3 – coming from both Σ^4 and Σ^3, what prevents a substantial simplification of the resulting formulae and, consequently, severely complicates the averaging procedure. It will be seen if this novel development status gives renewed insights in this regard.

USC
UNIVERSIDADE
DE SANTIAGO
DE COMPOSTELA

Summary

Heavy-ion collisions provide an accessible way to better understand the physics behind the strong interaction sector of the Standard Model of particle physics, as heavy-ion physics encompasses a wide range region from highly energetic partons described by pQCD to strong interactions between partons at lower scales. In particular, strongly interacting matter undergoes a phase transition from a confined phase to a deconfined Quark-Gluon Plasma under extremely high conditions, which is a very lively topic in the research community. Experimental measurements show that the collimated multiparticle sprays called jets lose considerable energy as they propagate through QGP, referred to as jet quenching, the main research topic of this doctoral thesis. Jet quenching can be used to probe the QGP properties by looking at different observables related to parton energy loss. Indeed, a total comprehension of in-medium jet evolution depends largely upon being capable of capturing jets' behaviour when they spread through hot and dense matter. It is for this reason that this phenomenon is potentially one of the most versatile experimental tools for characterizing the QGP. The broad kinematical reach of the LHC and the much larger luminosities expected for the near future open the door to both completely redesigned and new jet tools which may then be used to somehow isolate the different scales at different stages of the evolution, including initial stages. Here, a key piece for making sense of the data depends on a sound control of the splitting process within the relevant domain. The problem of elementary parton splittings in fact constitutes an important consideration in this context as is one of the key ingredients that enter the formulation of a Monte Carlo parton shower. In a diagrammatic language, final-state in-medium emissions are described via a classical current representing high-energy particles that act as sources of soft gluons and originate from a fixed position in probability amplitude and complex-conjugate amplitude. Likewise, the interference spectrum off multiple emitters has been performed assuming an instantaneous splitting of the current, giving rise to the well-known antenna radiation pattern, one of the cornerstones upon which this thesis was built. Three of the four research studies carried out in this manuscript are indeed further developments in this issue.

The first of these was presented in Chapter 3, where the radiation spectrum off two-parton QCD antennas originated after two hard splittings within a static color-deconfined medium was derived. Strong emphasis was placed on the role of the color coherence phenomenon via considering an additional soft gluon emission when the emitters have already traversed the entire medium, this way opening up the possibility of tracing the coherence history of the whole scenario back. Neither non-eikonal corrections to parton propagation nor finite formation time effects of the splitting processes were taken into consideration throughout the entire derivation. As a warm-up exercise, the derivation of the radiation pattern off a $q\bar{q}$-antenna in the strict soft limit is revisited since the major issue in this piece runs along the same lines, but it does attempt nonetheless to open up some new insight into the description of a final-state medium-induced partonic cascade.

Right from the very beginning, it is easy to realise that the survival probabilities corresponding to the parton configurations concerning the splittings under consideration will play a significant role in the face of conducting a qualitative discussion in terms of two-point correlation functions, objects that emerge on a recurring basis. More specifically, writing the probability amplitudes as a function of the survival probabilities of the leading dipoles enables one to find a factorization in the large-N_c limit that allows establishing a clear physical picture concerning the full coherence picture of the presented setup. To be more precise, the main qualitative outcome can be summarized as follows within the limit of large number of colors: color coherence factorizes along the parton shower. In other words, if coherence is preserved after the very first in-medium splitting, the subsequent smaller antennas will radiate coherently too. Conversely, when interferences wash out coherence completely, multiple emissions may be considered as a probabilistic shower of independent branchings. It is worth noting, however, that beyond the large-N_c limit the proof of this factorization is spoiled since subleading n-point correlation functions pop up – what would require a more involved implementation. Additionally, a straightforward derivation of tilted Wilson lines is performed, meant for the cases in which a very energetic quark – or a gluon – is produced at a fixed angle in a hard vertex inside the medium.

The objectives of the study carried out in Chapter 4 are in line with those described just above. More precisely, it also looks at a collinear parton splitting inside a color-deconfined medium, but now particular focus is put on studying the medium-modifications that emerge from allowing this splitting to take place at a finite distance within the medium. Unlike the preceding work, where the dipole was assumed to be formed quasi-instantaneously close to the origin of the coordinate system, here the study concentrates on looking further at the formation of the antenna itself, for the moment without considering additional radiative processes afterwards. A key challenge here entails deciphering whether the properties of the antenna are set at the moment of formation or whether those still can undergo modifications over large distances until the end of the medium. The findings point to the importance of both regimes. In particular, the main outcome of this study, namely the emission spectrum in a medium, proves to be factorable as a product of the vacuum cross-section and a function as for the medium-induced modification, this way allowing for an ongoing discrimination of medium effects. This function, named F_{med}, encapsulates all information regarding the medium modification factor corresponding to a $1 \to 2$ splitting function. As with earlier works on this subject, it is of great help to map the spectrum of a $1 \to 2$ parton splitting inside a medium onto the kinematical Lund plane, what enables one to conduct an straightforward discussion concerning the different regimes and relevant time-scales arising in the map for in-medium splittings. Especially worth mentioning is the appearance of two regimes of vacuum-like emissions within the medium, meaning that the in-medium splitting function is equal to the one in vacuum in these areas. The project was completed with a numerical study that largely verifies the performed analysis and the generalization of the process under consideration to be valid for arbitrary splitting processes.

Chapter 5 is the last piece of this manuscript dedicated to the study of final state effects via giving attention to the relevance of color coherence in the description of the partonic showering within the context of HIC. Specifically, the analysis carried out seeks evidences to design a coherence-modified evolution equation describing the medium-induced partonic cascade. To this end, a partonic scheme not dissimilar from those dealt with already in the thesis is developed. This involves the double inclusive gluon production process taking place inside a medium, with the added difficulty of allowing the splitting to display a finite formation time, in close analogy with the preceding study. Explicitly computing the radiation spectrum associated to this process leads to a cumbersome output involving the convolution of three kernel structures that makes standard discussing methods not quite useful. It is possible, however, to implement some approximations prior to find the exact solution which reveals a more favourable analytical environment in order to embed the notion of color coherence into the original rate equations built upon a Markov-like branching approach. In particular, the novel rate equation would only exhibit a significant modification that would affect the splitting kernel, now comprising a coherence piece which is exactly a simplified estimation of the decoherence parameter Δ_{med}. Preliminary findings point out to a close concordance with baseline studies in this respect. Just to be clear on the inconsistency that implies the sense of attempting to insert coherence effects into a pure Markovian showering picture, certain modifications are being carried out through the branching and broadening pieces as a way to lighten this mismatch, whilst further developments will be required for achieving a more reliable description of a real-life parton emission rate.

Finally, even though this thesis is mainly focused on in-depth studies as regards final state effects, initial state effects also take part here. In this vein, Chapter 6, the concluding chapter of this manuscript, falls within the CGC effective theory work frame. Its object is to pursue a holistic explanation about the origin of final-state particle correlations, which may hold a key to disentangle initial and final state effects. To achieve this end, the double inclusive gluon production probability is computed within the dense-dilute context, in which some pieces reveal angular correlations whose origin can be straightforwardly argued under basic principles. The next step, planned for a future analysis, includes performing the medium averaging procedure so as to give a renewed perspective concerning the roots of such correlations.

As a final remark, the works presented in this thesis have been devised to both reinforce existing studies on jet evolution in matter and provide new insights in the face of deciphering the puzzle of how jet constituents lose energy in a QCD medium. Achieving a sound knowledge in this respect will lead to a complete understanding of the cascading of a jet, this way allowing for the development of reliable Monte Carlo event generators as well.

USC
UNIVERSIDADE
DE SANTIAGO
DE COMPOSTELA

Resumen

En las últimas décadas se ha generado un interés creciente alrededor del estudio de las colisiones de iones pesados, ya que estas brindan una forma completamente nueva de entender la exitosa teoría de las interacciones fuertes en condiciones extremas, lo que se conoce como QCD a alta temperatura y densidad. Esta teoría se sometió a numerosas pruebas en aceleradores de partículas durante más de 40 años con el objeto de estudiar el comportamiento de los hadrones en el vacío. Más recientemente, la interacción fuerte ha comenzado también a ser probada en un medio, alcanzando valores críticos de temperatura y densidad que llevan a una escala de energía que favorece el deconfinamiento de quarks y gluones. Estas condiciones dan paso a la formación del llamado Plasma de Quarks y Gluones (QGP), un nuevo estado de la materia que puede comportarse de manera inesperada debido a efectos colectivos.

De acuerdo con la descripción actual de la evolución del universo primitivo, la teoría del Big Bang, 10^{-5} s después de la explosión, una sopa de QGP experimentó una transición de fase a hadrones confinados, la primera pista de una transición de QCD. Profundizar y ampliar el conocimiento sobre esta transición implica estudiar la estructura interna de la materia en condiciones extremas de temperatura y densidad. Desde una perspectiva teórica, el desafío principal al que se enfrenta la comunidad científica no es otro que lograr una formulación sólida alrededor de una teoría cuántica de campos en el medio utilizando QCD. Sin embargo, esta teoría no es perturbativa en torno a las escalas relevantes, lo que limita el uso de métodos analíticos. Una forma de avanzar en el conocimiento de sus propiedades es abordar el QGP como un líquido casi perfecto cuyos ingredientes interactúan fuertemente.

El estudio del plasma se ha establecido durante mucho tiempo como uno de los principales objetivos del Relativistic Heavy Ion Collider (RHIC) en el Brookhaven National Laboratory (BNL) y del programa del Large Hadron Collider (LHC) en el Conseil Européen pour la Recherche Nucléaire (CERN). Para caracterizar esta nueva fase de la materia en condiciones de laboratorio se manejan distintas *probes* en el contexto de las colisiones de iones de pesados. Las *hard probes* (HP) se crean en las primeras etapas de la colisión después de los procesos de dispersión *hard* y, por lo tanto, son *probes* clave para inferir las propiedades del medio. Los *jets* son *hard probes* naturales ya que las secciones eficaces de producción pueden abordarse exclusivamente dentro del dominio perturbativo de la QCD (pQCD). Mientras los *jets* se propagan por el medio QCD deconfinado, la dispersión múltiple que sufren los partones *hard* que los componen con los componentes del medio da lugar a la modificación de su dinámica y conduce a la pérdida de energía de los mismos, comúnmente conocida como *jet quenching*. Concretamente, el *jet quenching* se puede usar para probar las propiedades del QGP por medio del estudio de distintos observables relacionados con la pérdida de energía de los partones.

Una comprensión total de la evolución de los *jets* en un medio pasa por ser capaces de capturar su comportamiento cuando se propagan a través de materia a alta temperatura y densidad. Es por esta razón que este fenómeno es potencialmente uno de las instrumentos experimentales más versátiles para caracterizar el QGP. El amplio alcance cinemático del LHC y las incluso mayores luminosidades esperadas para el futuro próximo abren la puerta a herramientas completamente rediseñadas y nuevas para el estudio de los *jets*, herramientas que pueden usarse también para aislar de alguna manera las diferentes escalas correspondientes a diferentes etapas de la evolución, incluidas las etapas iniciales justo después de la colisión. Históricamente, los éxitos del *jet quenching* confirman el poder de las *hard probes* a la hora de describir el QGP. En particular, la detección de la asimetría *di-jet* en el LHC fue una de las primeras evidencias experimentales de esta supresión.

A pesar de que varios modelos intentan proporcionar un enfoque completo de la propagación de los *jets* a través de la materia, aún queda mucho por hacer para lograr una comprensión más profunda de los mecanismos subyacentes responsables de sus interacciones cuando se propagan por un medio. En términos generales, esta tesis apunta precisamente a arrojar luz sobre los mecanismos responsables del *jet quenching* y de la respuesta del medio a la propagación de las *hard probes*. Una de las fuentes clave detrás de las modificaciones sufridas por un *jet* energético como resultado de su interacción con los ingredientes del medio es la radiación inducida por el propio medio, que se puede calcular en el marco de diferentes aproximaciones generales dentro de la pQCD, como el formalismo BDMPS-Z/ASW, GLV o AMY, entre otros. Estos modelos no son más que la generalización del efecto Landau-Pomeranchuk-Migdal (LPM) al contexto de la pQCD. Además de todo esto, los generadores Monte Carlo (MC) de *jet quenching* resultaron ser herramientas extremadamente efectivas para conseguir una conexión mejor entre implementaciones teóricas y experimentos.

Dada su capacidad de cálculo perturbativa, los procesos que involucran transferencias de momento altas se calculan a partir de primeros principios en ausencia de los efectos del medio. En presencia de un medio la formulación no es tan diferente, lo que motiva a utilizar técnicas de subestructura de *jets* para dar más detalles sobre la interacción de acuerdo a características esenciales como la pérdida de energía, la radiación inducida por el medio o la coherencia de color. Concretamente, la coherencia de color entre partones es uno de los aspectos básicos del proceso de cascada de partones y constituye un desafío central presente en el state-of-the-art de la teoría y la fenomenología de la evolución de los *jets* y los procesos radiativos en la materia. En los últimos años se han llevado a cabo muchos intentos para avanzar en este sentido. En particular, una serie de trabajos sobre la radiación producida por una *antena* quark-antiquark establecieron una visión relevante sobre la descripción de la propagación partónica en el medio, poniendo de relieve así los efectos de interferencia a la hora de analizar la cascada de partones dentro del medio denso.

El cuerpo principal de este manuscrito ofrece una visión más amplia y novedosa del fenómeno de la coherencia de color en el marco del estudio de la radiación múltiple de gluones y sus efectos en los estados finales mediante una extensión de las derivaciones anteriores realizadas en este contexto. Tratar con configuraciones que involucran múltiples emisiones dificulta las discusiones ya que las interferencias entre los diferentes procesos pueden llegar a ser importantes. En el caso de la cascada de partones en el vacío se conserva el color, lo que conduce al conocido *angular ordering*. En los estudios que se presentan aquí, motivados por la radiación de gluones inducida por el medio, los patrones de interferencia pueden alterar gradualmente la coherencia de color del sistema en una escala de tiempo conocida como tiempo de decoherencia, escala que gobierna el denominado régimen de decoherencia. Dentro de este régimen, las antenas experimentan una rápida decorrelación de color a medida que viajan por el medio, perdiendo así la noción de memoria de su origen.

Como ya se mencionó anteriormente, esta tesis está destinada principalmente a estudiar el estado final de las colisiones de iones pesados a través del análisis de efectos como los indicados en los dos párrafos anteriores. Sin embargo, las etapas iniciales que tienen lugar justo después de la colisión también tienen su lugar en este manuscrito. La relación entre los dos tipos de efectos relacionados con las colisiones se discute también aquí.

Con respecto a estos últimos, la comprensión de la estructura de las funciones de onda de los núcleos que colisionan es de suma importancia, y se encuentra codificada en las funciones de distribución partónicas nucleares (nPDFs), que caracterizan la estructura y la dinámica partónica de los núcleos. A altas energías, los núcleos no se comportan como una mera superposición incoherente de sus nucleones constituyentes, sino que los efectos de coherencia resultan ser importantes. No solo modifican su contenido partónico, sino también la dinámica subyacente de las partículas producidas en los procesos de dispersión. En consecuencia, las PDFs (nPDFs) no son calculables perturbativamente ya que involucran dominios de la sección eficaz que corresponden a largas distancias – energías bajas. Por lo general, se ajustan a partir de datos experimentales. Existe una distinción entre tales efectos de estado inicial (IS), que son un preludio de la termalización, de aquellos que dan lugar a la presencia del QGP, los efectos de estado final (FS). Destacar la diferencia entre ambos es de vital importancia para una caracterización adecuada de la materia producida en las colisiones de iones pesados, ya que a veces pueden conducir a fenómenos cualitativos similares con respecto a observables interesantes.

Otra línea fundamental es el análisis de los fenómenos colectivos enmarcados en el contexto de la teoría efectiva *Color Glass Condensate* (CGC), que actualmente es un modelo universalmente aceptado para describir la física a *small Bjorken-x*. Esta aproximación incorpora efectos de recombinación no lineal tanto a nivel de producción de partículas como también en la evolución cuántica de las funciones de onda hadrónicas. Por lo tanto, separar el marco CGC de otros efectos exige el análisis de observables más exclusivos.

Una de las primeras y más interesantes observaciones en este sentido fue el hallazgo de correlaciones de largo alcance entre dos partículas en colisiones *pp* en el LHC, aunque ya se habían observado correlaciones similares en RHIC. Una explicación aceptada para los eventos observados está relacionada con el flujo colectivo en el QGP. Sin embargo, esta sigue siendo una pregunta abierta. Las correlaciones de largo alcance podrían no estar vinculadas con el origen del QGP ya que se extienden en un intervalo de rapidez muy grande, concluyendo que pueden originarse en una etapa muy temprana de la colisión. Apoyando este punto de vista, en la parte final de esta tesis se realiza también un análisis de correlaciones angulares entre gluones producidos en colisiones hadrónicas a altas energías dentro del modelo CGC. En particular se prueba que los gluones emitidos están necesariamente correlacionados tanto en rapidez como en ángulo de emisión.

Entrando un poco más en los detalles de cada uno de los capítulos, el Capítulo 1 tiene como objetivo contextualizar los estudios que se presentan mediante una visión amplia de la teoría y la fenomenología de la QCD. Por su parte, en el Capítulo 2 se presenta una descripción formal del marco general que se aplica para describir la propagación de partículas altamente energéticas a través de la materia. En este capítulo se destacan también antecedentes en torno a herramientas y métodos teóricos habituales en *jet quenching* y CGC, prestando particular atención a las diferentes técnicas requeridas para desarrollar las derivaciones realizadas en el cuerpo principal de esta tesis, en la que se llevan a cabo tres trabajos diferentes enfocados en profundizar en el estudio de *jet quenching*. Tanto el primero como el segundo tienen como objeto entender mejor la evolución de la cascada de partones en todas sus etapas. Dado que estos plantean una generalización de estudios previos sobre el problema de la coherencia de color, se recuperan resultados anteriores al establecer los límites apropiados. En el tercero de ellos se presenta un primer intento de introducir los efectos de coherencia de color en la ecuación de evolución para *splittings* que tienen lugar dentro de un medio. Por último, la sección final tiene como objetivo descifrar el origen de las correlaciones que surgen entre partículas producidas a altas energías. Los cálculos que se presentan en este capítulo están enmarcados en el contexto de CGC. A continuación se repasan los puntos clave y los resultados más relevantes de cada uno de estos cálculos.

En el Capítulo 3 se calcula el espectro de radiación de dos antenas que se originan como resultado de dos *hard splittings* dentro de un medio estático deconfinado. El énfasis general se encuentra en el papel del fenómeno de coherencia de color al considerar la emisión de un gluón *soft* cuando los emisores ya han abandonado el medio, abriendo así la posibilidad de rastrear el historial de coherencia del escenario físico completo. No se tienen en consideración aquí ni correcciones no eikonales a la propagación de los partones ni efectos de tiempos de formación finitos de los *splittings*. Como ejercicio de calentamiento, se repasa la derivación del patrón de radiación de una antena $q\bar{q}$ en el límite *soft*, ya que aunque se intenta generar una visión nueva en torno a la descripción de una cascada partónica inducida por el medio, la forma de desarrollar el problema no es muy diferente.

Es fácil darse cuenta de que las probabilidades de supervivencia correspondientes a las configuraciones partónicas relativas a los *splittings* que se consideran desempeñarán un papel importante de cara a una discusión cualitativa en términos de las funciones de correlación de dos puntos, objetos que emergen de forma recurrente durante toda la derivación. Más específicamente, escribir las amplitudes de probabilidad en función de las probabilidades de supervivencia de los dipolos principales permite encontrar una factorización en el límite de *large-*N_c que conduce a una imagen física muy clara en términos de la coherencia del sistema. Para ser más precisos, el resultado cualitativo principal se puede resumir de la siguiente manera bajo el límite mencionado: la coherencia de color factoriza a lo largo de la cascada. En otras palabras, si se preserva la coherencia de color después del primer *splitting* dentro del medio, las antenas que se originan posteriormente también se propagarán en un estado coherente. Por el contrario, cuando las interferencias destruyen completamente la coherencia, las emisiones pueden considerarse como una cascada probabilística de *splittings* independientes. Así y todo, merece la pena señalar que más allá del límite de *large-*N_c esta factorización deja de ser válida, ya que aparecen funciones de correlación subdominantes en N_c, lo que requeriría una implementación más complicada. Para completar, al final del capítulo se realiza una derivación directa de líneas de Wilson inclinadas, pensada para los casos en los que se produce un quark o un gluón muy energético a un ángulo fijo en un vértice *hard* dentro del medio.

Por su parte, los objetivos del estudio realizado en el Capítulo 4 están en línea con los descritos en el párrafo anterior. Concretamente, se hace ahora hincapié en las modificaciones que surgen al permitir que los procesos de *splitting* tengan lugar a una distancia finita dentro del medio. A diferencia del trabajo anterior, dónde se suponía que el dipolo se forma casi instantáneamente cerca del origen del sistema de coordenadas, se observa más a fondo aquí la formación de la antena, sin considerar por el momento procesos radiativos adicionales. Un punto clave radica en descifrar si las propiedades de la antena se establecen en el momento de su formación o si todavía pueden sufrir modificaciones a grandes distancias dentro del propio medio. Los hallazgos apuntan a la importancia de ambos regímenes. En particular, el espectro de emisión resulta ser factorizable como el producto de la sección eficaz en el vacío por una función que cuantifica la modificación inducida por el medio, permitiendo así discriminar sus efectos. Esta función, denominada F_{med}, condensa toda la información sobre el factor de modificación del medio correspondiente a una función de *splitting* de tipo $1 \to 2$. En analogía con trabajos similares sobre este tema, resulta de gran ayuda mapear el espectro de un *splitting* $1 \to 2$ que tiene lugar dentro del medio en el plano cinemático de Lund, ya que este permite llevar a cabo una discusión directa sobre los diferentes regímenes y escalas de tiempo que surgen en el mapa para tales *splittings*. Digna de mención es la aparición de dos regímenes de emisiones similares a las que ocurren en el vacío dentro del medio, lo que significa que en estas áreas la función de *splitting* en el medio es igual a la del vacío. En la parte final del proyecto se presenta un estudio numérico que verifica en gran medida el análisis realizado, así como una generalización del proceso bajo consideración para *splittings* arbitrarios.

El Capítulo 5 es la última pieza de esta tesis dedicada al estudio de estados finales en el contexto de las colisiones de iones pesados. Específicamente, el análisis realizado busca evidencias para diseñar una ecuación de evolución modificada que describa la cascada partónica inducida por el medio incluyendo efectos de coherencia de color. Con este fin, se aborda un esquema partónico que consiste en el proceso de producción de dos gluones dentro de un medio estático, con la dificultad añadida de que el tiempo de formación del proceso de *splitting* se considera finito, en estrecha analogía con el estudio resumido en el párrafo anterior. El cálculo explícito del espectro de radiación asociado a este proceso resulta bastante engorroso a nivel algebraico, ya que involucra la convolución de tres estructuras que hace que los métodos de discusión estándar no sean del todo útiles. Es posible, sin embargo, implementar algunas aproximaciones antes de encontrar la solución exacta que revelan un entorno analítico más favorable para incorporar la noción de coherencia de color en las ecuaciones de evolución originales basadas en el concepto de cascada Markoviana. En particular, la nueva ecuación de evolución solo exhibiría una modificación significativa que afectaría a la estructura que describe el *splitting*, ahora comprendiendo un término de coherencia que no es otro que una estimación simplificada del parámetro de decoherencia Δ_{med}. Hallazgos preliminares apuntan a una estrecha concordancia con estudios de referencia llevados a cabo en este mismo escenario.

Finalmente, a pesar de que esta tesis se centra en el estudio de los estados finales de las colisiones, los efectos de estado inicial también cobran importancia en el último capítulo de la misma. Concretamente, el Capítulo 6 se enmarca en el contexto de la teoría efectiva CGC, y el objetivo pasa por buscar una explicación sobre el origen de las correlaciones de partículas en el estado final, que pueden ser la clave para desenlazar los efectos de estado inicial y final. Con este objeto se calcula aquí la probabilidad de producción de dos gluones en el límite denso-diluido. Algunas piezas revelan correlaciones angulares cuyo origen puede argumentarse directamente bajo principios básicos. El siguiente paso, planeado para un análisis futuro, incluye realizar el procedimiento de promediado sobre las posibles configuraciones del medio para dar una perspectiva renovada sobre las raíces de tales correlaciones.

Como observación final, los trabajos presentados en esta tesis han sido diseñados para reforzar estudios existentes sobre la evolución de los *jets* en la materia, así como proporcionar nuevas ideas para descifrar el puzzle de cómo los componentes de un *jet* pierden energía en un medio QCD denso. Alcanzar un conocimiento sólido en este respecto conducirá a una comprensión completa de la cascada partónica que experimenta un *jet*, permitiendo también el desarrollo de generadores de eventos Monte Carlo más optimizados.

Bibliography

[1] Y. L. Dokshitzer, V. A. Khoze, A. H. Mueller and S. I. Troian, "Basics of perturbative QCD". Gif-sur-Yvette, France: Ed. Frontieres (1991) 274 p. (Basics of).

[2] R. K. Ellis, W. J. Stirling and B. R. Webber, "QCD and Collider Physics". Cambridge University Press, 1996.

[3] F. J. Ynduráin, "QCD: The Theory of Quark and Gluon Interactions". Springer-Verlag, 2006.

[4] W. Greiner, S. Schramm and E. Stein, "Quantum Chromodynamics". Springer, 2007.

[5] S. Fadin, L. N. Lipatov, "Quantum Chromodynamics: Perturbative and Nonperturbative Aspects". Cambridge University Press, 2010.

[6] A. V. Smilga, "Lectures on Quantum Chromodynamics", World Scientific, London, 2001 [arXiv:hep-ph/9901412].

[7] D. J. Gross and F. Wilczek, "Ultraviolet Behavior of Non-Abelian Gauge Theories", Phys. Rev. Lett. **30** (1973) 1343-1346.

[8] H. D. Politzer, "Reliable Perturbative Results for Strong Interactions?", Phys.Rev.Lett. **30** (1973) 1346-1349.

[9] H. Fritzsch, M. Gell-Mann and H. Leutwyler, "Advantages of the Color Octet Gluon Picture", Phys.Lett. B**47** (1973) 365-368.

[10] N. Armesto and C. Pajares, "Cromodinámica Cuántica", Revista Española de Física (2011) Vol. **25**, no. 4.

[11] S. Bethke, "The 2009 World Average of alpha(s)", Eur.Phys.J. C**64** (2009) 689-703 [arXiv:0908.1135 [hep-ph]].

[12] G. F. Sterman and S. Weinberg, "Jets from Quantum Chromodynamics", Phys.Rev.Lett. **39** (1977) 1436.

[13] S. Durr *et al*, "Lattice QCD at the physical point: light quark masses", Phys.Lett. B**701** (2011) 265-268 [arXiv:1011.2403 [hep-lat]]

[14] J. D. Bjorken, "Asymptotic Sum Rules at Infinite Momentum", Phys.Lett. **179** (1969) 1547-1553.

[15] R. P. Feynman, "Very high-energy collisions of hadrons", Phys.Rev.Lett. **23** (1969) 1415-1417.

[16] V. N. Gribov, "Interaction of gamma quanta and electrons with nuclei at high-energies", Sov.Phys.JETP **30** (1970) 709-717.

[17] V. N. Gribov and L. N. Lipatov, "Deep inelastic ep scattering in perturbation theory", Sov.J.Nucl.Phys. **15** (1972) 438-450.

[18] K. J. Eskola, H. Paukkunen and C. A. Salgado, "EPS09: A New Generation of NLO and LO Nuclear Parton Distribution Functions", JHEP **0904** (2009) 065 [arXiv:0902.4154 [hep-ph]].

[19] K. J. Eskola, P. Paakkinen, H. Paukkunen and C. A. Salgado, "EPPS16: Nuclear parton distributions with LHC data", Eur.Phys.J. C**77** (2017) no.3, 163 [arXiv:1612.05741 [hep-ph]].

[20] J. C. Collins, D. E. Soper and G. F. Sterman, "Factorization of Hard Processes in QCD", Adv.Ser.Direct.High Energy Phys. **5** (1989) 1-91 [arXiv:hep-ph/0409313].

[21] G. Altarelli and G. Parisi, "Asymptotic Freedom in Parton Language", Nucl.Phys. B**126** (1977) 298-318.

[22] Y. L. Dokshitzer, "Calculation of the Structure Functions for Deep Inelastic Scattering and e+ e- Annihilation by Perturbation Theory in Quantum Chromodynamics", Sov.Phys.JETP **46** (1977) 641-653.

[23] T. D. Lee and G. C. Wick, "Vacuum Stability and Vacuum Excitation in a Spin 0 Field Theory", Phys.Rev. D**9** (1974) 2291-2316.

[24] J. C. Collins and M. J. Perry, "Superdense Matter: Neutrons Or Asymptotically Free Quarks?", Phys.Rev.Lett. **34** (1975) 1353.

[25] F. Karsch, "Lattice QCD at High Temperature and Density", Lect.Notes Phys. **583** (2002) 209-249 [arXiv:hep-lat/0106019].

[26] F. Gelis, "The Initial Stages of High Energy Heavy Ion Collisions", Institut de Physique Théorique (IPhT) Habilitation Thesis [https://www.ipht.fr/Pisp/francois.gelis/Physics/].

[27] R. Pasechnik and M. Sumbera, "Phenomenological Review on Quark–Gluon Plasma: Concepts vs. Observations", Universe **3** (2017) no.1, 7 [arXiv:1611.01533 [hep-ph]].

[28] J. Adams *et al.* [STAR Collaboration], "Experimental and Theoretical Challenges in the Search for the Quark Gluon Plasma: The STAR Collaboration's Critical Assessment of the Evidence from RHIC Collisions", Nucl.Phys. A**757** (2005) 102-183 [arXiv:nucl-ex/0501009].

[29] K. Adcox *et al.* [PHENIX Collaboration], "Formation of dense partonic matter in relativistic nucleus-nucleus collisions at RHIC: Experimental evaluation by the PHENIX collaboration", Nucl.Phys. A**757** (2005) 184-283 [arXiv:nucl-ex/0410003].

[30] B. B. Back *et al.* [PHOBOS Collaboration], "The PHOBOS Perspective on Discoveries at RHIC", Nucl.Phys. A**757** (2005) 28-101 [arXiv:nucl-ex/0410022].

[31] I. Arsene *et al.* [BRAHMS Collaboration], "Quark Gluon Plasma and Color Glass Condensate at RHIC? The Perspective from the BRAHMS experiment", Nucl.Phys. A**757** (2005) 1-27 [arXiv:nucl-ex/0410020].

[32] D. d'Enterria, "Jet quenching", Landolt-Bornstein **23** (2010) 471 [arXiv:0902.2011 [nucl-ex]].

[33] R. Baier, D. Schiff and B. G. Zakharov, "Energy loss in perturbative QCD", Ann.Rev.Nucl.Part.Sci. **50** (2000) 37-69 [arXiv:hep-ph/0002198].

[34] M. Gyulassy, I. Vitev, X. N. Wang and B. W. Zhang, "Jet Quenching and Radiative Energy Loss in Dense Nuclear Matter", in R. C. Hwa and X.-N. Wang (eds.), "Quark-Gluon Plasma 3" 123-191 (World Scientific, 2004) [arXiv:nucl-th/0302077].

[35] J. Casalderrey-Solana and C. A. Salgado, "Introductory lectures on jet quenching in heavy ion collisions", Acta Phys.Polon. B**38** (2007) 3731-3794 [arXiv:0712.3443 [hep-ph]].

[36] A. H. Mueller and J.-w. Qiu, "Gluon Recombination and Shadowing at Small Values of x", Nucl.Phys. B**268** (1986) 427-452.

[37] L. D. McLerran and R. Venugopalan, "Computing Quark and Gluon Distribution Functions for Very Large Nuclei", Phys.Rev. D**49** (1994) 2233-2241 [arXiv:hep-ph/9309289].

[38] L. D. McLerran and R. Venugopalan, "Gluon Distribution Functions for Very Large Nuclei at Small Transverse Momentum", Phys.Rev. D**49** (1994) 3352-3355 [arXiv:hep-ph/9311205].

[39] L. D. McLerran and R. Venugopalan, "Green's Functions in the Color Field of a Large Nucleus", Phys.Rev. D**50** (1994) 2225-2233 [arXiv:hep-ph/9402335].

[40] R. Venugopalan, "The Color Glass Condensate: A Summary of key ideas and recent developments", Lectures given at Conferences C04-08-29.2, C04-06-22.2 and C04-06-01.2 [arXiv:hep-ph/0412396].

[41] R. C. Hwa (ed.), "Quark-Gluon Plasma, Advanced Series on Directions in High Energy Physics: Volume 6". World Scientific, 1990.

[42] R. C. Hwa (ed.), "Quark-Gluon Plasma 2". World Scientific, 1995.

[43] R. C. Hwa and X.-N. Wang (eds.), "Quark-Gluon Plasma 3". World Scientific, 2004.

[44] R. C. Hwa and X.-N. Wang (eds.), "Quark-Gluon Plasma 4". World Scientific, 2010.

[45] X.-N. Wang (ed.), "Quark-Gluon Plasma 5". World Scientific, 2016.

[46] B. I. Ermolaev and V. S. Fadin, "Doubly logarithmic asymptotic behavior of exclusive cross sections in quantum chromodynamics", JETP Lett. **33** (1981) 269-272.

[47] A. H. Mueller, "On the Multiplicity of Hadrons in QCD Jets", Phys.Lett. B**104** (1981) 161-164.

[48] G. P. Salam, "Elements of QCD for hadron colliders", Lectures given at Conference C09-06-14.1 [arXiv:1011.5131 [hep-ph]].

[49] Y. Yilmaz, "Jet quenching in heavy-ion collisions at LHC with CMS detector", Massachusetts Institute of Technology (MIT) Ph. D. Thesis (2013) [http://web.mit.edu/mithig/theses/Yetkin-Yilmaz-thesis.pdf].

[50] G. Luisoni and S. Marzani, "QCD resummation for hadronic final states", J.Phys. G**42** (2015) no.10, 103101 [arXiv:1505.04084 [hep-ph]].

[51] J. D. Bjorken, "Energy Loss of Energetic Partons in Quark-Gluon Plasma: Possible Extinction of High p_T Jets in Hadron-Hadron Collisions", FERMILAB-PUB-82-059-THY.

[52] S. Jeon and G. D. Moore, "Energy Loss of Leading Partons in a Thermal QCD Medium", Phys.Rev. C**71** (2005) 034901 [arXiv:hep-ph/0309332].

[53] A. Peshier, "The QCD collisional energy loss revised", Phys.Rev.Lett. **97** (2006) 212301 [arXiv:hep-ph/0605294].

[54] S. Peigné, P.-B. Gossiaux and T. Gousset, "Retardation Effect for Collisional Energy Loss of Hard Partons Produced in a QGP", JHEP **0604** (2006) 011 [arXiv:hep-ph/0509185].

[55] M. Djordjevic, "Collisional Energy Loss in a Finite Size QCD Matter", Phys.Rev. C**74** (2006) 064907 [arXiv:nucl-th/0603066].

[56] S. Peigné and A. Peshier, "Collisional energy loss of a fast heavy quark in a quark-gluon plasma", Phys.Rev. D**77** (2008) 114017 [arXiv:0802.4364 [hep-ph]].

[57] B. Schenke, C. Gale and G.-Y. Qin, "The evolving distribution of hard partons traversing a hot strongly interacting plasma", Phys.Rev. C**79** (2009) 054908 [arXiv:0901.3498 [hep-ph]].

[58] M. G. Mustafa, "Energy Loss of Charm Quarks in the Quark-Gluon Plasma: Collisional vs Radiative", Phys.Rev. C**72** (2005) 014905 [arXiv:hep-ph/0412402].

[59] S. Cao, G.-Y. Qin, S. A. Bass and B. Müller, "Collisional vs. Radiative Energy Loss of Heavy Quark in a Hot and Dense Nuclear Matter", Nucl.Phys. A**904-905** (2013) 653c-656c [arXiv:1209.5410 [nucl-th]].

[60] P. L. Anthony *et al.*, "An Accurate measurement of the Landau-Pomeranchuk-Migdal effect", Phys.Rev.Lett. **75** (1995) 1949-1952.

[61] L. D. Landau and I. Pomeranchuk, "Limits of applicability of the theory of bremsstrahlung electrons and pair production at high-energies", Dokl.Akad.Nauk Ser.Fiz. **92** (1953) 535-536.

[62] A. B. Migdal, "Bremsstrahlung and pair production in condensed media at high-energies", Phys.Rev. **103** (1956) 1811-1820.

[63] H. Bethe and W. Heitler, "On the stopping of fast particles and on the creation of positive electrons", Proc.Roy.Soc.Lond. A**146** (1934) 83-112.

[64] R. Baier, Y. L. Dokshitzer, A. H. Mueller, S. Peigne and D. Schiff, "Radiative energy loss of high-energy quarks and gluons in a finite volume quark-gluon plasma", Nucl.Phys. B**483** (1997) 291-320 [arXiv:hep-ph/9607355].

[65] R. Baier, Y. L. Dokshitzer, A. H. Mueller, S. Peigne and D. Schiff, "Radiative energy loss and $p_\perp$-broadening of high energy partons in nuclei", Nucl.Phys. B**484** (1997) 265-282 [arXiv:hep-ph/9608322].

[66] B. G. Zakharov, "Fully quantum treatment of the Landau–Pomeranchuk–Migdal effect in QED and QCD", JETP Lett. **63** (1996) 952-957 [arXiv:hep-ph/9607440].

[67] B. G. Zakharov, "Radiative energy loss of high-energy quarks in finite size nuclear matter and quark-gluon plasma", JETP Lett. **65** (1997) 615-620 [arXiv:hep-ph/9704255].

[68] R. Baier, Y. L. Dokshitzer, A. H. Mueller and D. Schiff, "Medium-induced radiative energy loss: Equivalence between the BDMPS and Zakharov formalisms", Nucl.Phys. B**531** (1998) 403-425 [arXiv:hep-ph/9804212].

[69] U. A. Wiedemann, "Transverse dynamics of hard partons in nuclear media and the QCD dipole", Nucl.Phys. B**582** (2000) 409-450 [arXiv:hep-ph/0003021].

[70] U. A. Wiedemann, "Gluon radiation off hard quarks in a nuclear environment: opacity expansion", Nucl.Phys. B**588** (2000) 303-344 [arXiv:hep-ph/0005129].

[71] U. A. Wiedemann, "Jet Quenching versus Jet Enhancement: a quantitative study of the BDMPS-Z gluon radiation spectrum", Nucl.Phys. A**690** (2001) 731-751 [arXiv:hep-ph/0008241].

[72] C. A. Salgado and U. A. Wiedemann, "Calculating Quenching Weights", Phys.Rev. D**68** (2003) 014008 [arXiv:hep-ph/0302184].

[73] N. Armesto, C. A. Salgado and U. A. Wiedemann, "Medium-Induced Gluon Radiation off Massive Quarks Fills the Dead Cone", Phys.Rev. D**69** (2004) 114003 [arXiv:hep-ph/0312106].

[74] M. Gyulassy, P. Levai and I. Vitev, "Jet Quenching in Thin Quark-Gluon Plasmas I: Formalism", Nucl.Phys. B**571** (2000) 197-233 [arXiv:hep-ph/9907461].

[75] M. Gyulassy, P. Levai and I. Vitev, "Non-Abelian Energy Loss at Finite Opacity", Phys.Rev.Lett. **85** (2000) 5535-5538 [arXiv:nucl-th/0005032].

[76] M. Gyulassy, P. Levai and I. Vitev, "Reaction operator approach to non-Abelian energy loss", Nucl.Phys. B**594** (2001) 371-419 [arXiv:nucl-th/0006010].

[77] M. Gyulassy, P. Levai and I. Vitev, "Jet Tomography of Au+Au Reactions Including Multi-gluon Fluctuations", Phys.Lett. B**538** (2002) 282-288 [arXiv:nucl-th/0112071].

[78] P. B. Arnold, G. D. Moore and L. G. Yaffe, "Photon Emission from Ultrarelativistic Plasmas", JHEP **0111** (2001) 057 [arXiv:hep-ph/0109064].

[79] P. B. Arnold, G. D. Moore and L. G. Yaffe, "Photon Emission from Quark-Gluon Plasma: Complete Leading Order Results", JHEP **0112** (2001) 009 [arXiv:hep-ph/0111107].

[80] P. B. Arnold, G. D. Moore and L. G. Yaffe, "Photon and Gluon Emission in Relativistic Plasmas", JHEP **0206** (2002) 030 [arXiv:hep-ph/0204343].

[81] X.-f. Guo and X.-N. Wang, "Multiple Scattering, Parton Energy Loss and Modified Fragmentation Functions in Deeply Inelastic eA Scattering", Phys.Rev.Lett. **85** (2000) 3591-3594 [arXiv:hep-ph/0005044].

[82] X.-N. Wang and X.-f. Guo, "Multiple Parton Scattering in Nuclei: Parton Energy Loss", Nucl.Phys. A**696** (2001) 788-832 [arXiv:hep-ph/0102230].

[83] B.-W. Zhang and X.-N. Wang, "Multiple Parton Scattering in Nuclei: Beyond Helicity Amplitude Approximation", Nucl.Phys. A**720** (2003) 429-451 [arXiv:hep-ph/0301195].

[84] A. Majumder, R. J. Fries and B. Müller, "Photon bremsstrahlung and diffusive broadening of a hard jet", Phys.Rev. C**77** (2008) 065-209 [arXiv:0711.2475 [nucl-th]].

[85] A. Majumder, "Hard collinear gluon radiation and multiple scattering in a medium", Phys.Rev. D**85** (2012) 014023 [arXiv:0912.2987 [nucl-th]].

[86] N. Armesto *et al.*, "Comparison of Jet Quenching Formalisms for a Quark-Gluon Plasma 'Brick' ", Phys.Rev. C**86** (2012) 064904 [arXiv:1106.1106 [hep-ph]].

[87] S. Wicks, "Up to and beyond ninth order in opacity: Radiative energy loss with GLV", arXiv:0804.4704 [nucl-th].

[88] S. Caron-Huot and C. Gale, "Finite-size effects on the radiative energy loss of a fast parton in hot and dense strongly interacting matter", Phys.Rev. C**82** (2010) 064902 [arXiv:1006.2379 [hep-ph]].

[89] G. Marchesini, B. R. Webber, G. Abbiendi, I. G. Knowles and M. H. Seymour, "HERWIG: a Monte Carlo event generator for simulating hadron emission reactions with interfering gluons. Version 5.1", Comput.Phys.Commun. **67** (1992) 465-508.

[90] T. Sjostrand, S. Mrenna and P. Z. Skands, "PYTHIA 6.4 Physics and Manual", JHEP **0605** (2006) 026 [arXiv:hep-ph/0603175].

[91] A. Dainese, C. Loizides and G. Paic,"Leading-particle suppression in high energy nucleus–nucleus collisions", Eur.Phys.J. C**38** (2005) 461-474 [arXiv:hep-ph/0406201].

[92] I.P. Lokhtin and A.M. Snigirev, "A model of jet quenching in ultrarelativistic heavy ion collisions and high-p_T hadron spectra at RHIC", Eur.Phys.J. C**45** (2006) 211-217 [arXiv:hep-ph/0506189].

[93] N. Armesto, L. Cunqueiro and C. A. Salgado, "Implementation of a medium-modified parton shower algorithm", Eur.Phys.J. C**61** (2009) 775-778 [arXiv:0809.4433 [hep-ph]].

[94] K. C. Zapp, F. Krauss and U. A. Wiedemann, "A perturbative framework for jet quenching", JHEP **1303** (2013) 080 [arXiv:1212.1599 [hep-ph]].

[95] B. Schenke, C. Gale, and S. Jeon, "MARTINI: An event generator for relativistic heavy-ion collisions", Phys.Rev. C**80** (2009) 054913 [arXiv:0909.2037 [hep-ph]].

[96] B. Schenke, C. Gale, and S. Jeon, "Hydrodynamic evolution and jet energy loss in Cu+Cu collisions", Phys.Rev. C**83** (2011) 044907 [arXiv:1101.0425 [hep-ph]].

[97] F. A. Dreyer, G. P. Salam and G. Soyez, "The Lund Jet Plane", JHEP **1812** (2018) 064 [arXiv:1807.04758 [hep-ph]].

[98] B. Andersson, G. Gustafson, L. Lonnblad and U. Pettersson, "Coherence effects in deep inelastic scattering", Z.Phys. C**43** (1989) 625.

[99] H. A. Andrews *et al.*, "Novel tools and observables for jet physics in heavy-ion collisions", J.Phys. G**47** (2020) 6, 065102 [arXiv:1808.03689 [hep-ph]].

[100] S. Marzani, G. Soyez and M. Spannowsky, "Looking inside jets: an introduction to jet substructure and boosted-object phenomenology", Lect.Notes Phys. **958** (2019) pp. [arXiv:1901.10342 [hep-ph]].

[101] P. Caucal, E. Iancu, A. H. Mueller and G. Soyez, "Vacuum-like jet fragmentation in a dense QCD medium", Phys.Rev.Lett. **120** (2018) 232001 [arXiv:1801.09703 [hep-ph]].

[102] M. Cacciari, G. P. Salam and G. Soyez, "FastJet user manual", Eur.Phys.J. C**72** (2012) 1896, [arXiv:1111.6097 [hep-ph]].

[103] S. Catani, Y. L. Dokshitzer, M. H. Seymour and B. R. Webber, "Longitudinally invariant $k_\perp$ clustering algorithms for hadron hadron collisions", Nucl.Phys. B**406** (1993) 187-224.

[104] S. D. Ellis and D. E. Soper, "Successive Combination Jet Algorithm For Hadron Collisions", Phys. Rev. D**48** (1993) 3160–3166 [arXiv:hep-ph/9305266].

[105] Y. L. Dokshitzer, G. Leder, S. Moretti and B. R. Webber, "Better Jet Clustering Algorithms", JHEP **9708** (1997) 001 [arXiv:hep-ph/9707323].

[106] M. Cacciari, G. P. Salam and G. Soyez, "The anti-k_t jet clustering algorithm", JHEP **0804** (2008) 063 [arXiv:0802.1189 [hep-ph]].

[107] S. A. Bass, C. Gale, A. Majumder, C. Nonaka, G.-Y. Qin, T. Renk and J. Ruppert, "Systematic Comparison of Jet Energy-Loss Schemes in a Realistic Hydrodynamic Medium", Phys.Rev. C**79** (2009) 024901 [arXiv:0808.0908 [nucl-th]].

[108] N. Armesto, M. Cacciari, T. Hirano, J. Nagle and C. A. Salgado, "Constraint fitting of experimental data with a jet quenching model embedded in a hydrodynamical bulk medium", J.Phys. G**37** (2010) 025104 [0907.0667 [hep-ph]].

[109] R. Baier and Y. Mehtar-Tani, "Jet quenching and broadening: the transport coefficient $\hat{q}$ in an anisotropic plasma", Phys.Rev. C**78** (2008) 064906 [arXiv:0806.0954 [hep-ph]].

[110] Y. Mehtar-Tani and K. Tywoniuk, "Improved opacity expansion for medium-induced parton splitting", [arXiv:1910.02032 [hep-ph]].

[111] J. Barata and Y. Mehtar-Tani, "Improved opacity expansion at NNLO for medium induced gluon radiation", [arXiv:2004.02323 [hep-ph]].

[112] L. Apolinário, C. Andrés and F. Domínguez, "Medium-induced gluon radiation with full resummation of multiple scatterings for realistic parton-medium interactions", JLAB-THY-20-3143 [arXiv:2002.01517 [hep-ph]].

[113] A. Kovner and U. A. Wiedemann, "Gluon Radiation and Parton Energy Loss", in R. C. Hwa and X.-N. Wang (eds.), "Quark-Gluon Plasma 3" 192-248 (World Scientific, 2004) [arXiv:hep-ph/0304151]

[114] J. Casalderrey-Solana and E. Iancu, "Interference effects in medium–induced gluon radiation", JHEP **1108** (2011) 015 [arXiv:1105.1760 [hep-ph]].

[115] Y. Mehtar-Tani, C. A. Salgado and K. Tywoniuk, "The radiation pattern of a QCD antenna in a dilute medium", JHEP **1204** (2012) 064 [arXiv:1112.5031 [hep-ph]].

[116] Y. Mehtar-Tani, C. A. Salgado and K. Tywoniuk, "The radiation pattern of a QCD antenna in a dense medium", JHEP **1210** (2012) 197 [arXiv:1205.5739 [hep-ph]].

[117] Y. Mehtar-Tani, C. A. Salgado and K. Tywoniuk, "Jets in QCD media: from color coherence to decoherence", Phys.Lett. B**707** (2012) 156-159 [arXiv:1102.4317 [hep-ph]].

[118] J. Jalilian-Marian, A. Kovner, L. D. McLerran and H. Weigert, "The Intrinsic Glue Distribution at Very Small x", Phys.Rev. D**55** (1997) 5414-5428 [arXiv:hep-ph/9606337].

[119] J. Jalilian-Marian, A. Kovner, A. Leonidov and H. Weigert, "The BFKL Equation from the Wilson Renormalization Group", Nucl.Phys. B**504** (1997) 415-431 [arXiv:hep-ph/9701284].

[120] J. Jalilian-Marian, A. Kovner, A. Leonidov and H. Weigert, "The Wilson renormalization group for low x physics: towards the high density regime", Phys.Rev. D**59** (1998) 014014 [arXiv:hep-ph/9706377].

[121] J. Jalilian-Marian, A. Kovner and H. Weigert, "The Wilson renormalization group for low x physics: Gluon evolution at finite parton density", Phys.Rev. D**59** (1998) 014015 [arXiv:hep-ph/9709432].

[122] J. Jalilian-Marian, A. Kovner, A. Leonidov and H. Weigert, "Unitarization of Gluon Distribution in the Doubly Logarithmic Regime at High Density", Phys.Rev. D**59** (1999) 034007, Phys.Rev. D**59** (1999) 099903 (erratum) [arXiv:hep-ph/9807462].

[123] E. Iancu, A. Leonidov and L. D. McLerran, "Nonlinear Gluon Evolution in the Color Glass Condensate: I", Nucl.Phys. A**692** (2001) 583-645 [arXiv:hep-ph/0011241].

[124] E. Iancu, A. Leonidov and L. D. McLerran, "The Renormalization Group Equation for the Color Glass Condensate", Phys.Lett. B**510** (2001) 133-144 [arXiv:hep-ph/0102009].

[125] E. Ferreiro, E. Iancu, A. Leonidov and L. D. McLerran, "Nonlinear Gluon Evolution in the Color Glass Condensate: II", Nucl.Phys. A**703** (2002) 489-538 [arXiv:hep-ph/0109115].

[126] F. Gelis, E. Iancu, J. Jalilian-Marian and R. Venugopalan, "The Color Glass Condensate", Ann.Rev.Nucl.Part.Sci. **60** (2010) 463-489 [arXiv:1002.0333 [hep-ph]].

[127] F. Gelis, "Color Glass Condensate and Glasma", Int.J.Mod.Phys. A**28** (2013) 1330001 [arXiv:1211.3327 [hep-ph]].

[128] F. D. Aaron *et al.* [H1 and ZEUS Collaborations], "Combined Measurement and QCD Analysis of the Inclusive $e^{\pm}p$ Scattering Cross Sections at HERA", JHEP **1001** (2010) 109 [arXiv:0911.0884 [hep-ex]].

[129] L. V. Gribov, E. M. Levin and M. G. Ryskin, "Semihard Processes in QCD", Phys.Rept. **100** (1983) 1-150.

[130] E. A. Kuraev, L. N. Lipatov and V. S. Fadin, "The Pomeranchuk Singularity in Nonabelian Gauge Theories", Sov.Phys.JETP **45** (1977) 199-204, Zh.Eksp.Teor.Fiz. **72** (1977) 377-389.

[131] I. I. Balitsky and L. N. Lipatov, "The Pomeranchuk Singularity in Quantum Chromodynamics", Sov.J.Nucl.Phys. **28** (1978) 822-829, Yad.Fiz. **28** (1978) 1597-1611.

[132] A. H. Mueller, "Soft gluons in the infinite momentum wave function and the BFKL pomeron", Nucl.Phys. B**415** (1994) 373-385.

[133] F. Domínguez, "Unintegrated Gluon Distributions at Small-x", Columbia University Ph. D. Thesis (2011).

[134] V. S. Fadin, E. A. Kuraev and L. N. Lipatov, "On the Pomeranchuk Singularity in Asymptotically Free Theories", Phys.Lett. B**60** (1975) 50-52.

[135] H. Navelet and S. Wallon, "Onium-Onium scattering at fixed impact parameter: exact equivalence between the color dipole model and the BFKL Pomeron", Nucl.Phys. B**522** (1998) 237-281 [arXiv:hep-ph/9705296].

[136] I. Balitsky, "Operator expansion for high-energy scattering", Nucl.Phys. B**463** (1996) 99-160 [arXiv:hep-ph/9509348].

[137] I. Balitsky, "Factorization and high-energy effective action", Phys.Rev. D**60** (1999) 014020 [arXiv:hep-ph/9812311].

[138] Y. V. Kovchegov, "Small-x F_2 Structure Function of a Nucleus Including Multiple Pomeron Exchanges", Phys.Rev. D**60** (1999) 034008 [arXiv:hep-ph/9901281].

[139] Y. V. Kovchegov, "Unitarization of the BFKL Pomeron on a Nucleus", Phys.Rev. D**61** (2000) 074018 [arXiv:hep-ph/9905214].

[140] E. Iancu and D. N. Triantafyllopoulos, "JIMWLK evolution for multi-particle production in Langevin form", JHEP **1311** (2013) 067 [arXiv:1307.1559 [hep-ph]].

[141] A. Dumitru, F. Gelis, L. D. McLerran and R. Venugopalan, "Glasma flux tubes and the near side ridge phenomenon at RHIC", Nucl.Phys. A**810** (2008) 91-108 [arXiv:0804.3858 [hep-ph]].

[142] A. Dumitru, K. Dusling, F. Gelis, J. Jalilian-Marian, T. Lappi and R. Venugopalan, "The ridge in proton-proton collisions at the LHC", Phys.Lett. B**697** (2011) 21-25 [arXiv:1009.5295 [hep-ph]].

[143] J.-P. Blaizot, F. Dominguez, E. Iancu and Y. Mehtar-Tani, "Probabilistic picture for medium-induced jet evolution", JHEP **1406** (2014) 075 [arXiv:1311.5823 [hep-ph]].

[144] P. Arnold, S. Iqbal and T. Rase, "Strong- vs. weak-coupling pictures of jet quenching: a dry run using QED", JHEP **1905** (2019) 004 [arXiv:1810.06578 [hep-ph]].

[145] F. Domínguez, J. G. Milhano, C. A. Salgado, K. Tywoniuk and V. Vila, "Mapping collinear in-medium parton splittings", Eur.Phys.J. C**80** (2020) 1, 11 [arXiv:1907.03653 [hep-ph]].

[146] J.-P. Blaizot, F. Domínguez, E. Iancu and Y. Mehtar-Tani, "Medium-induced gluon branching", JHEP **1301** (2013) 143 [arXiv:1209.4585 [hep-ph]].

[147] L. Apolinário, N. Armesto, J. G. Milhano and C. A. Salgado, "Medium-induced gluon radiation and colour decoherence beyond the soft approximation", JHEP **1502** (2013) 119 [arXiv:1407.0599 [hep-ph]].

[148] T. Altinoluk, N. Armesto, G. Beuf, M. Martínez and C. A. Salgado, "Next-to-eikonal corrections in the CGC: gluon production and spin asymmetries in pA collisions", JHEP **1407** (2014) 068 [arXiv:1404.2219 [hep-ph]].

[149] T. Altinoluk, N. Armesto, G. Beuf and A. Moscoso, "Next-to-next-to-eikonal corrections in the CGC", JHEP **1601** (2016) 114 [arXiv:1505.01400 [hep-ph]].

[150] Y. Mehtar-Tani and K. Tywoniuk, "Radiative energy loss of neighboring subjets", Nucl.Phys. A**979** (2018) 165-203 [arXiv:1706.06047 [hep-ph]].

[151] J. Casalderrey-Solana, Y. Mehtar-Tani, C. A. Salgado and K. Tywoniuk, "New picture of jet quenching dictated by color coherence", Phys.Lett. B**725** (2013) 357-360 [arXiv:1210.7765 [hep-ph]].

[152] J. Casalderrey-Solana, J. G. Milhano and P. Quiroga-Arias, "Out of Medium Fragmentation from Long-Lived Jet Showers", Phys.Lett. B**710** (2012) 175-181 [arXiv:1111.0310 [hep-ph]].

[153] B. G. Zakharov, "Light-cone path integral approach to the Landau–Pomeranchuk–Migdal effect", Phys.Atom.Nucl. **61** (1998) 838-854, Yad.Fiz. **61** (1998) 924-940 [arXiv:hep-ph/9807540].

[154] L. Apolinário, N. Armesto and C. A. Salgado, "Medium-induced emissions of hard gluons", Phys.Lett. B**718** (2012) 160-168 [arXiv:1204.2929 [hep-ph]].

[155] P. Cvitanovic, P. Hoyer and K. Zalewski, "Parton Evolution as a Branching Process", Nucl.Phys. B**176** (1980) 429-448.

[156] V. Khachatryan *et al.* [CMS Collaboration], "Observation of Long-Range, Near-Side Angular Correlations in Proton-Proton Collisions at the LHC", JHEP **1009** (2010) 091 [arXiv:1009.4122 [hep-ex]].

[157] B. I. Abelev *et al.* [STAR Collaboration], "Long range rapidity correlations and jet production in high energy nuclear collisions", Phys.Rev. C**80** (2009) 064912 [arXiv:0909.0191 [nucl-ex]].

[158] B. Alver *et al.* [PHOBOS Collaboration],"High transverse momentum triggered correlations over a large pseudorapidity acceptance in Au+Au collisions at $\sqrt{s_{NN}}$ = 200 GeV", Phys.Rev.Lett. **104** (2010) 062301 [arXiv:0903.2811 [nucl-ex]].

[159] C. A. Salgado and U. A. Wiedemann, "Medium Modification of Jet Shapes and Jet Multiplicities", Phys.Rev.Lett. **93** (2004) 042301 [arXiv:hep-ph/0310079].

[160] C. A. Salgado and U. A. Wiedemann, "Measuring the Collective Flow with Jets", Phys.Rev.Lett. **93** (2004) 242301 [arXiv:hep-ph/0405301].

[161] I. O. Cherednikov and N. G. Stefanis, "On correlations in high-energy hadronic processes and the CMS ridge: A manifestation of quantum entanglement?", Int.J.Mod.Phys. A**27** (2012) 1250008 [arXiv:1010.4463 [hep-ph]].

[162] K. Werner, Iu. Karpenko and T. Pierog, "The "Ridge" in Proton-Proton Scattering at 7 TeV", Phys.Rev.Lett. **106** (2011) 122004 [arXiv:1011.0375 [hep-ph]].

[163] I. Bautista, J.Dias de Deus and C. Pajares, "The "Ridge" in Proton-Proton Scattering at 7 TeV", AIP Conf.Proc. **1343** (2011) 495-497 [arXiv:1011.1870 [hep-ph]].

[164] B. A. Arbuzov, E. E. Boos and V.I. Savrin, "CMS ridge effect at LHC as a manifestation of bremstralung of gluons due to the quark-anti-quark string formation", Eur.Phys.J. C**71** (2011) 1730 [arXiv:1104.1283 [hep-ph]].

[165] P. Bozek and W. Broniowski, "Correlations from hydrodynamic flow in p-Pb collisions", Phys.Lett. B**718** (2013) 1557-1561 [arXiv:1211.0845 [nucl-th]].

[166] T. Lappi and L. D. McLerran, "Some Features of the Glasma", Nucl.Phys. A**772** (2006) 200-212 [arXiv:hep-ph/0602189].

[167] A. Kovner and M. Lublinsky, "Angular Correlations in Gluon Production at High Energy", Phys.Rev. D**83** (2011) 034017 [arXiv:1012.3398 [hep-ph]].

[168] A. Kovner and M. Lublinsky, "In pursuit of Pomeron loops: the JIMWLK equation and the Wess-Zumino term", Phys.Rev. D**71** (2005) 085004 [arXiv:hep-ph/0501198].

[169] A. Kovner, M. Lublinsky and U. Wiedemann, "From bubbles to foam: dilute to dense evolution of hadronic wave function at high energy", JHEP **0706** (2007) 075 [arXiv:0705.1713 [hep-ph]].

[170] F. Gelis, T. Lappi and R. Venugopalan, "High energy factorization in nucleus-nucleus collisions II - Multigluon correlations", Phys.Rev. D**78** (2008) 054020 [arXiv:0807.1306 [hep-ph]].

[171] A. Kovner and M. Lublinsky, "One gluon, two gluon: multigluon production via high energy evolution", JHEP **0611** (2006) 083 [arXiv:hep-ph/0609227].

[172] R. Baier, A. Kovner, M. Nardi and U. A. Wiedemann, "Particle Correlations in Saturated QCD Matter", Phys.Rev. D**72** (2005) 094013 [arXiv:hep-ph/0506126].

USC
UNIVERSIDADE
DE SANTIAGO
DE COMPOSTELA